Ultrafine and Nano-Size Welding Fume Exposure Assessment:

Size, Shape and Chemical Characterization

BY

JOHN DANIEL BRESKEY
B.A., Oberlin College, 1998
M.S., University of Illinois at Chicago, 2008

THESIS

Submitted as partial fulfillment of the requirements
For the degree of Doctor of Philosophy in Public Health Sciences
In the Graduate College of the
University of Illinois at Chicago 2011

Chicago, Illinois

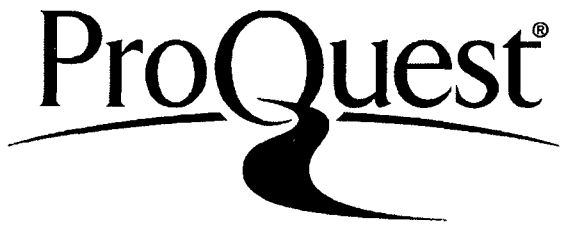

ProQuest LLC
789 East Eisenhower Parkway
P.O. Box 1346
Ann Arbor, MI 48106-1346

ACKNOWLEDGMENTS

The research presented in this thesis was supported in part by the National Institute for Occupational Safety and Health (NIOSH) grant K01-OH008298-01A1.

I would like to thank my committee for their support during this process. Thank you to my research advisor Dr. Serap Erdal, for all of her efforts getting my through graduate school.

Thank you to my friends and colleagues in EOHS for making these years a wonderful experience. Anders Abelmann for all of your help in the welding laboratory.

And thank you to my family for your unwavering support through all these years of graduate school. And of course to love of my life, Mandy, thank you for getting me through the thick of it. I love you!

JDB

TABLE OF CONTENTS

TABLE OF CONTENTS (continued)

TABLE OF CONTENTS (continued)

TABLE OF CONTENTS (continued)

LIST OF TABLES

LIST OF TABLES (continued)

LIST OF TABLES (continued)

LIST OF TABLES (continued)

LIST OF FIGURES

LIST OF FIGURES (continued)

LIST OF FIGURES (continued)

LIST OF ABBREVIATIONS

AAS	Atomic Absorption Spectroscopy
ACGIH	American Conference of Governmental Industrial Hygienists
AWS	American Welding Society
CMD	Count Median Diameter
EDS	X-ray Energy Dispersive Spectroscopy
EELS	Electron Energy Loss Spectroscopy
ELPI	Electronic Low Pressure Impactor
EM	Electron Microscopy
FCAW	Flux-Cored Arc Welding
GMAW	Gas Metal Arc Welding
GSD	Geometric Standard Deviation
GTAW	Gas Tungsten Arc Welding
HR-ICP-MS	High Resolution Inductively Coupled Mass Spectroscopy
IARC	International Agency for Research on Cancer
IR	Infrared
MMD	Mass Median Diameter
MOUDI	Micro-Orifice Uniform Deposit Impactor
MS	Mild Steel
NIOSH	National Institute of Occupational Safety and Health
OSHA	US Occupational Safety and Health Administration
PCIS	Personal Cascade Impactor Sampler
PSD	Particle Size Distribution
PTFE	Polytetrafluoroethylene
RF	Radio Frequency
SMAW	Shielded Metal Arc Welding
SS	Stainless Steel

TG/DTA	Thermo-gravimetric/Differential Thermal Analyzer
TLV	Threshold Limit Value
TWA	Time-Weighted Average
UV	Ultraviolet
XRD	X-ray Diffraction Spectroscopy
XRF	X-ray Fluorescence Spectroscopy

SUMMARY

A laboratory-based characterization study of stainless steel welding fume emitted from a shielded metal arc welding process was conducted. Fume was characterized on the basis of particle size, chemistry and shape. Welding was performed in both an isokinetic emission chamber to capture total fume emission characteristics and within an exposure chamber, incorporating a breathing thermal manikin, to study personal exposure characteristics. Particle size of welding fume was determined as size-fractionated mass concentrations collected using three unique cascade impactor instruments. Metal composition and hexavalent chromium content of size-fractionated welding fume samples were determined using inductively coupled plasma mass spectroscopy and atomic absorption spectroscopy, respectively. Particle shape characterization across size-fractionated samples was determined using scanning and transmission electron microscopy.

The mass-based size characterization revealed a bimodal particle size distribution with a primary mode diameter of approximately 0.3 μm and a secondary mode diameter between 1 and 5 μm. The measured particle size distribution parameters were generally robust across experimental systems suggesting that previous studies that characterized welding fume under emission conditions may be applicable to confined space exposure conditions similar to those implemented in the exposure chamber. Particle size distribution parameters obtained with personal cascade impactor samplers did not agree well with larger ambient-type cascade impactors and thus should not be used to characterize welding fume size distributions in occupational settings.

Metal compositional analysis of size fractionated welding fume samples revealed a spike in the alkali metal species sodium and potassium in particles between 0.1 μm and 1.0 μm, while transition metal species of iron, chromium, manganese and nickel did not vary substantially across particle size fractions. Hexavalent chromium analysis also revealed a spike in particles sizes between 0.1 and 1.0 μm diameter suggesting a chemical dependence of hexavalent content with alkali metal content of welding fume samples, however, specific correlation between species could not be verified because composition of the two species was not conducted on the same sample. Further exploration on the size dependence of alkali metal and hexavalent chromium content of welding fume should be completed.

Particle shape and morphology characterization with electron microscopy revealed three distinct size groups of primary particles classified as small medium and large which corresponded to physical diameter ranges of less than 10 nm, between 10 nm and 100 nm and larger than 100 nm, respectively. Analysis of the morphological characteristics of welding fume revealed that fume particles agglomerate into primarily chainlike structures or densely packed structures. The smallest primary particle size groups were more often associated with chain-like agglomerates while larger primary particle size groups were more often associated with densely packed agglomerates. Overall differences in the distribution of morphology types across particle size fractions were not observed. The classification of morphologies presented herein can provide a standardized system for future single particle chemical analysis studies.

1. INTRODUCTION

1.1 Welding Processes

Welding metal pieces together is an ancient practice. Forge welding, diffusion bonding, brazing and soldering were techniques developed before and during the Bronze Age. These welding processes are considered solid-phase welding because the metal pieces to be joined are not melted in the process. Instead, mechanical action or solder materials are used to create the bond. In contrast to solid-phase welding processes are the fusion welding processes, which use a heat source intense enough to melt the edges of the metal joint. Fusion welding, in general, provides a commonly and frequently used manufacturing tool for the joining of metallic components, especially for metal plate pieces. There are many different welding processes employed for joining of various metals such as mild steel, aluminum, and stainless steels, the most important of which in industry is the electric arc welding process.

1.1.1 Electric Arc Welding

Electric arc welding can be described as the process wherein a power supply is used to create an electric arc between an electrode and the base material. The heat generated in the electric arc is enough to melt the material to be joined (base metal) as well as the electrode (consumable). The electrode contributes sufficient filler material to the joint area so that the resulting weld has the proper metallurgical and mechanical properties. Different arc welding

techniques have developed over time and a discussion of the most common is pertinent for this research.

1.1.1.1 Gas-Tungsten Arc Welding

Gas-Tungsten Arc Welding (GTAW) is the process wherein the joining of metals is accomplished through heating with an electric arc between a non-consumable tungsten electrode and the base metal (Kou, 1987). To prevent oxidation of the welded material, often an inert shielding gas, such as argon or helium is used to protect the welding area. Figure 1 below represents the GTAW process in diagram. The electrode is usually water cooled to prevent overheating and, although not required in all instances, a filler wire is applied to the weld area to complete the joining process. GTAW is sometimes referred to as Tungsten Inert Gas (TIG) welding process.

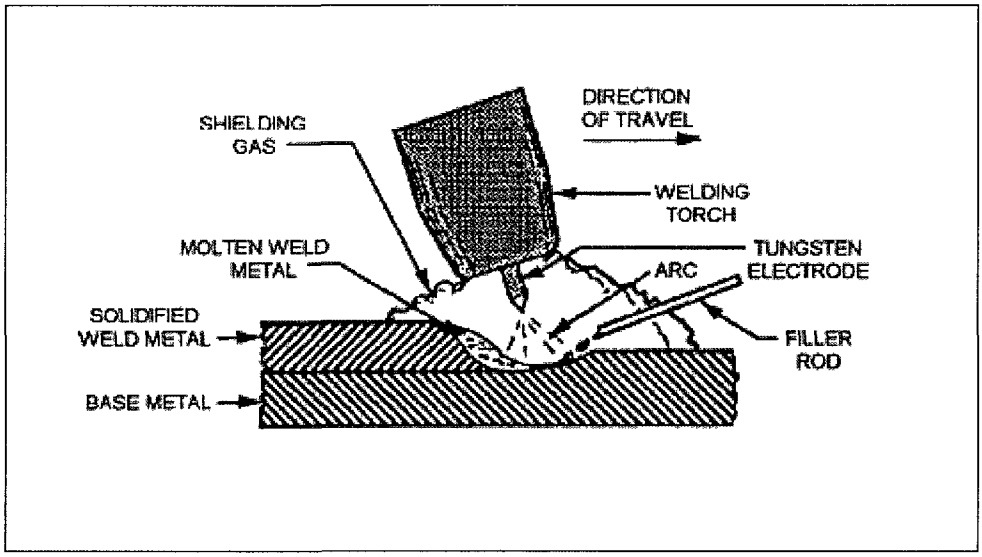

Figure 1: Diagram of gas-tungsten arc welding process.

The GTAW process is a "clean" welding process, meaning it leaves no slag, and is used for welding metals such as titanium, zirconium, magnesium and aluminum (Kou, 1987). An advantage of the GTAW process is a higher level of weld pool control because the welding current is low and the filler material is fed separately by hand. A disadvantage to the process is that filler material deposition rate is slow and joining large pieces together becomes time consuming.

1.1.1.2 Gas-Metal Arc Welding

Gas-Metal Arc Welding (GMAW) is the process wherein the joining of materials is accomplished through heating with an electric arc established between a continuous consumable metal electrode and the base metal. Similar to GTAW, a shielding gas is used to protect the weld

area from oxidation; however, inert gases (e.g. argon or helium), active gas (e.g. carbon dioxide) or a mixture of the two can be used. The GMAW process is sometimes referred to as Metal Inert Gas (MIG) welding or Metal Active Gas (MAG) welding, depending on the type of shielding gas used. An inert gas flushes oxygen away from the arc-zone to prevent oxidation of the weld metal while an active gas is added to improve arc stability and metal deposition. Figure 2 below represents the GMAW process in diagram. The consumable filler wire electrode is constantly fed through the welding machine while the shielding gas is pumped through the nozzle to the electrode tip.

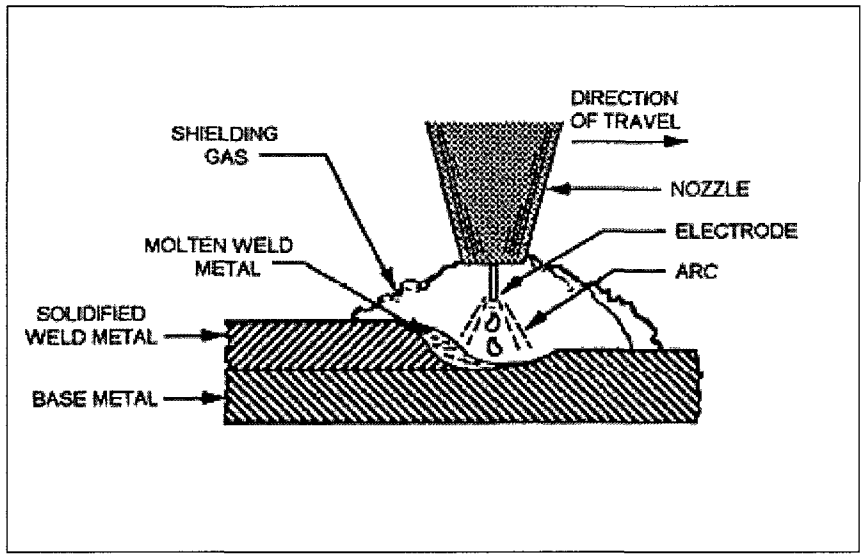

Figure 2: Diagram of gas metal arc welding process.

Due to continuous feeding consumable wire, the GMAW process is an easy and time efficient method of joining metal materials together. The use of shielding gases from compressed gas

cylinders, however, limits the portability of the welding equipment and requires the close proximity of the welder, welding machine and work-piece.

1.1.1.3 Flux-Cored Arc Welding

Flux-Cored Arc Welding (FCAW) is the process wherein the joining of metals is accomplished through heating with an electric arc created between a consumable flux-filled metal tube electrode and the base metal. Figure 3 represents the FCAW process. The FCAW is very similar to the GMAW process, the main difference being the fluxing material incorporated within the metal electrode. The decomposition of the flux material provides a shielding gas around the weld area once the electrode begins to melt. Additional shielding gas (inert, active, or combination of the two) can be used in the FCAW process depending on the materials to be welded. Like GMAW, the filler wire is fed through the welding machine at a constant rate and shielding gas, if used, is pumped through the nozzle across the electrode tip in the weld area.

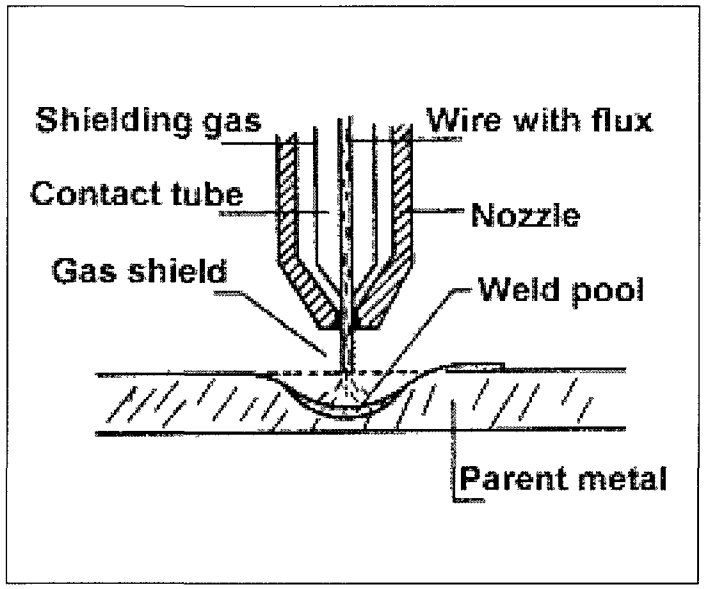

Figure 3: Diagram of flux-cored arc welding process

1.1.1.4 Shielded-Metal Arc Welding

Shielded-Metal Arc Welding (SMAW) is the process wherein joining of metals is accomplished through heating with an electric arc created between a flux covered consumable electrode and the base metal. The SMAW process is different from the GMAW and FCAW processes in that the consumable electrode is approximately 30 cm in length and must be replaced by hand once consumed. Figure 4 below represents the SMAW process in diagram. Similar to FCAW, the decomposition of flux coating of the SMAW electrode provides the shielding gas around the weld area as well as provides a slag coating to the completed weld.

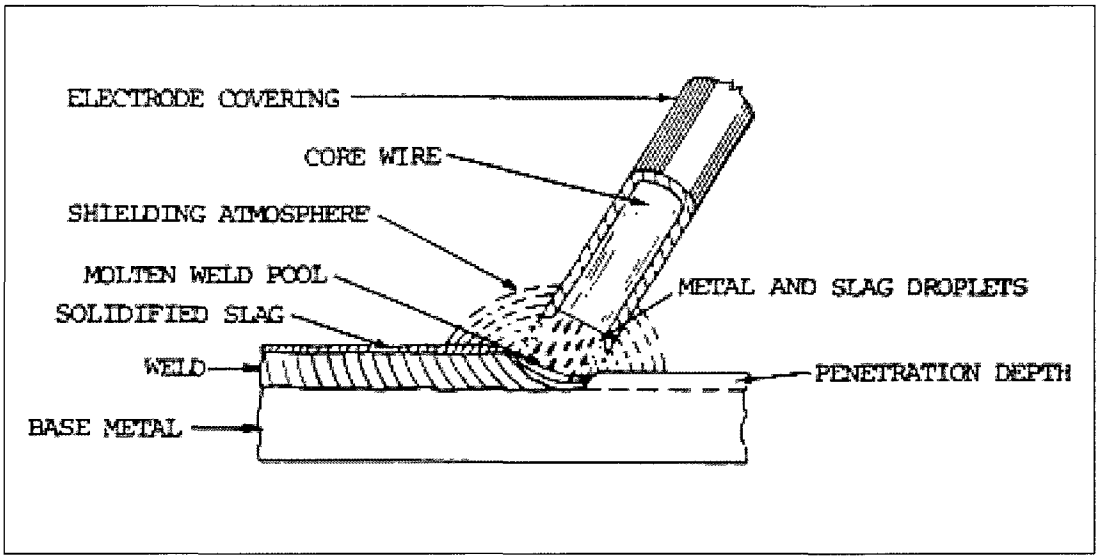

Figure 4: Diagram of shielded metal arc welding process.

The SMAW process requires simple equipment, which makes it inexpensive and portable, ideal for maintenance, repair and field construction activities. However, frequent changing of the electrodes decreases the production efficiency as compared to GMAW and FCAW processes. The SMAW process is sometimes referred to as Manual Metal Arc (MMA) welding due to the manual manipulation of the electrode.

1.1.2 Welding Process Dynamics

There are many variables that come together during the arc welding process, which must be maintained in strict tolerances for the proper joining characteristics. The welding parameters selected ultimately influence the metal transfer from electrode to work-piece and the metallurgical soundness of the weld.

1.1.2.1 Welding Parameters

A Current/Voltage

Welding machines are used to supply the electric power to the process in Direct Current (DC), Alternating Current (AC) or both DC and AC. The DC mode can also be specified as electrode positive (DCEP) or electrode negative (DCEN), based on the whether the positive or negative lead is attached to the electrode. The current used in arc welding ranges from 50-350 amperes depending on the type or welding employed and the type of electrode used. The heat generated by the arc is determined by the amount of current used, and welders often vary the current setting to match the conditional aspects of the welding project. Voltage is related to current via Ohm's law, and any change in current will change the voltage. Electrode manufacturers specify optimal current settings to be used with specific electrode types and sizes.

A welding parameter closely associated with current and voltage is the Heat Input (HI), which is typically calculated as the ratio of power (voltage × current) to the velocity of the heat source (i.e., the arc). The velocity of the heat source can be measured as the travel speed of the welding rod. This parameter is useful comparing welding performed with different electrode types and sizes.

B Electrode Type

Electrodes used in arc welding are classified based on operational characteristics, quality of deposition metal and flux coating characteristics. The American Welding Society (AWS)

classification system describes mild steel SMAW electrodes by a four or five-digit code proceeded by the letter 'E'. The "E" stands for electrode. The first two or three digits of the code stand for the tensile strength given in pounds per square inch. The third (or fourth) digit stands for the position to be welded. In stainless steel SMAW electrode classification the first 3 digits are based on the composition while the last two digits are based on the welding position. Additional compositional information can also be classified with a letter between the third and fourth digit (e.g., "L" standing for low-carbon).

C Electrode Size

Electrode size is classified by the diameter of the electrode not including the electrode coating. Diameter is usually measured and reported in standard units (inches). The most common diameters used are 3/32" (2.4 mm), 1/8" (3.2 mm) and 5/32" (4.0 mm). The selection of electrode diameter is dependent upon the sizing of the nature of the joint to be welded. In addition, the current settings necessary for proper welding increase with increasing electrode diameter.

D Shielding Gas Composition

In GTAW, GMAW and FCAW, shielding gas composition is an additional parameter to be controlled during welding. Shielding gases include inactive gases like argon or helium or active gases like carbon dioxide or oxygen. The selection of shielding gas blends depends on the materials to be welded as well as the required arc properties.

1.1.2.2 Metal Transfer Modes

Consumable electrodes in fusion welding act not only as the conductor of the arc current, and thereby the heat source, but also as the source of filler metal for the joint to be fused (J. Lancaster, 1984). The proper transfer of that metal from the electrode to the weld pool is essential for weld integrity. The three major types of metal transfer modes have been identified as short-circuiting transfer, globular transfer and spray type transfer.

In short-circuiting mode (also referred to as dip transfer mode), metal is transferred from the electrode to the weld pool when they are in contact with each other (Kou, 1987). In globular transfer mode, large droplets of liquid metal, the size of the electrode diameter or bigger, grow at the tip of the electrode, detach and fall through the arc to the molten weld pool due to gravimetric forces (Bracarense & Liu, 1993). In spray transfer mode, a shower spray of small droplets of liquid metal and slag fly across the arc due mainly to electromagnetic forces (Bracarense & Liu, 1993; Kou, 1987).

1.2 Welding Environment

Arc welding has been a prominent industrial technique beginning in the 1930's and 1940's with an explosion of applied uses developing after the Second World War (J. F. Lancaster, 1987). Although welding has developed as a certified profession in this same time frame, many industrial environments employ welders with no formal training.

1.2.1 Welding in Industry

Welding is a versatile engineering process and its applications span many industrial settings. In 2008, 466,400 workers in the U.S. were employed as welders, cutters, solderers, and brazers (BLS, 2008) and the most recent census data suggests that over 496,540 workers in the United States are involved in welding or allied processes (Day & Rosenthal, 2008). Additionally, because welding applications can be easily learned and performed, many more workers perform welding not as their primary task but as part of their job for maintenance and other activities. This raises an uncertainty as to the number of people performing welding occupationally. According to International Agency for Research on Cancer (IARC), the number of workers worldwide whose work involves some welding is about three million (IARC, 1990a).

1.2.2 Hazards of Welding

Worksites where welding is performed may pose specific hazards associated with the industrial process, while the arc welding process itself poses mainly chemical and physical hazards not only to welders but also to other workers in the vicinity.

1.2.2.1 Physical Hazards

Physical hazards associated with arc welding processes include noise, vibration, heat, electrical current and infrared (IR), ultraviolet (UV), and radio frequency (RF) radiation (NIOSH, 1988a). Physical hazards associated with arc welding should be mitigated or minimized with proper engineering, administrative and personal protective equipment controls.

The personal protective equipment used by welders should be discussed briefly. It is recommended that welders wear suitable fire and heat resistant clothing (e.g., leather) that covers as much bare skin as possible to protect against burns and excessive UV radiation. Eye and face protection is accomplished with the use of a welding helmet/mask. Many types and designs of helmets exist and all provide full-face protection, as well as a viewing window with UV filter glass, but does not provide respiratory protection (NIOSH, 1988b).

1.2.2.2 Chemical Hazards

Chemical hazards associated with arc welding processes are noxious gases and metal fumes generated from the welding itself (J. Antonini, 2003). Gases generated during welding include carbon dioxide, carbon monoxide, nitrogen oxide, nitrogen dioxide and ozone. Composition of the generated fume varies by type of welding process and the materials (filler and base metal) being used. Metals often found in welding fume include Aluminum (Al), Cadmium (Cd), Chromium (Cr), Copper (Cu), Iron (Fe), Lead (Pb), Manganese (Mn), Magnesium (Mg), Molybdenum (Mo), Nickel (Ni), Silicon (Si), Titanium (Ti) and Zinc (Zn).

Control of chemical hazards from welding should include engineering controls (e.g., general and local ventilation) as well personal protective equipment (e.g., respiratory protection) when engineering controls are infeasible.

1.3 Occupational Health Issues with Welding

Frequent inhalation exposures of high concentrations of fumes and gases during welding have been associated with a variety of health effects in various organ systems. Thus, a large body of research and scientific literature on the health effects associated with welding, including several review articles, has emerged. Most recently, Antonini (2003) categorized the state of scientific knowledge of welding exposure and related respiratory and non-respiratory health effects. A summary of those finding is presented below.

1.3.1 Non-Respiratory Health Issues

Manganism, a neurological disease similar to Parkinson's disease caused by chronic exposure to manganese, has been documented in welders exposed mainly to mild steel (J. Antonini, 2003). Additionally, epidemiological studies have observed that welders with Parkinson's disease had a earlier onset of the disease as compared to non-welders with the disease (Sadak, Schulz, Racette, & Perlmutter, 2001). Manganese could not be verified as the causative agent for this observed difference.

1.3.2 Respiratory Health Issues

Epidemiological studies on the effect of welding fume exposure in regards to the pulmonary function of welders have had variable results (J. Antonini, 2003). No studies have indicated that usual day-to-day welding exposure leads to severe or clinically apparent lung function impairment (J. Antonini, 2003; Sferlazza & Beckett, 1991). Many of the cross-sectional studies do not indicate

an effect of welding fume exposure on lung function; however, studies of welders in shipyards, whose exposure is often greater due to primarily confined space welding, show more negative effects on lung function (Sferlazza & Beckett, 1991). Other studies have demonstrated the effects of confined space versus non-confined space welding has similar lung function impairment results outside of the shipyard industry as well (J. Antonini, 2003).

Acute transient effects on welders' pulmonary function have also been investigated epidemiologically. A three-year case control study of mild steel and stainless steel welders found a significant across shift negative change in lung function of stainless steel and welders using SMAW process (Sobaszek, et al., 2000). Additionally, it was observed that welders with 20 years or more of stainless steel welding experience had more significant across-shift (i.e., pre-shift to post-shift) reductions in lung function. Exposure to high levels of chromium and nickel in stainless steel welders as compared to mild steel welders was suggested as the reason for the difference between cohorts (Sobaszek, et al., 2000).

Occupational asthma develops from the exposure of sensitizing agents in the workplace and is different from non-occupational asthma by a later onset and lack of seasonal variation of symptoms (J. Antonini, 2003). The welding of stainless steel poses the most risk for the development of occupational asthma because of the respiratory sensitizing agents chromium and nickel found in stainless steel welding fume. One epidemiology study observed significant negative changes in subclinical respiratory functions indicative for asthma over a 9 year period but was unable to correlate exposure to a single metal (Beach, et al., 1996). Authors concluded that although a specific mechanism of toxicity could not be established, the hypersensitivity of chromium and nickel appear plausible.

Industrial bronchitis entails swelling (inflammation) of the large airways of the lungs that occurs in some people who work around certain dusts, fumes, smoke, or other substances. A higher prevalence of chronic bronchitis symptoms is the most frequently found abnormality between welders and non-welders in regards to respiratory health (Sferlazza & Beckett, 1991). Epidemiological studies of bronchitis and welding often find that differences in chronic bronchitis prevalence cannot be distinguished from the prevalence of smoking in welding cohorts, although a proposed synergistic effect of smoking and welding has been proposed (J. Antonini, 2003).

To date, lung cancer associated with welding has not been definitively linked in epidemiological studies (J. Antonini, 2003). The IARC has classified welding fumes as a possible human carcinogen based on *limited evidence* in humans and *inadequate evidence* in experimental animals for the carcinogenicity of welding fumes and gases (IARC, 1990b). The difficulty in relating welding fume exposure to lung cancer lies in inadequate exposure characterization and the mixed exposures often experienced by welders (e.g., cigarette smoke, asbestos). Risk of lung cancer associated with welding is often linked to stainless steel welding because of the carcinogenic potential of chromium and nickel that are components in the welding fume.

1.4 Welding Fume Exposure Assessment and Characterization

Although occupational exposure to welding fumes has been linked to neurological and respiratory health effects, the available epidemiological data are too limited to provide conclusive answers as to the underlying mechanisms of such toxicity. It has been pointed out that historic exposure assessments reported in the literature have been lacking in enough detail for the ability to link exposure to toxicity or health effects assessments (J. M. Antonini, 2003). Stainless steel

welding specifically poses more health risks because it has significant chromium and nickel (both known human carcinogens) content as well as other toxic metals (aluminum, copper, manganese, molybdenum, titanium) with chronic effects. However, most of the exposure data reported in the literature are total fume measurements obtained in different workplaces, with sparse results of specific chemical characterization. Determining whether welders are exposed to fume components at levels that could trigger health effects is paramount in understanding the mechanisms of toxicity associated with welding fume exposure.

Welding fume is a complex mixture of gases and particulate matter. It has been shown that particles with aerodynamic diameter of 1 μm or less can account for approximately 95% of the total measured mass in the fume, with mass-median diameter (MMD) ranging from 0.6 to 0.25 μm (Paul Hewett, 1995). Additionally, number concentrations of particles maximize within the nanometer range (Zimmer & Biswas, 2001). Experimental work demonstrated that about 95% of the total/respirable welding fume mass is less than 250 nm in aerodynamic size and about 30% of total/respirable welding fume mass is less than 100 nm in aerodynamic size (Erdal, Schauer, Breskey, & Indacochea, 2008). Understanding the characteristics of nano-size particles within welding aerosols, therefore, may serve as an important factor in bridging the gap between exposure assessment and toxicological effects. The role of nano-size particles within the fume on observed health effects is currently not known.

Nano-size particles have been associated with adverse health effects in humans, mainly because smaller particles penetrate deeper into the alveolar space within the lungs where normal mechanisms of mucosocilliary removal do not apply (Ibald-Mulli A, 2002). Toxicological research on ultrafine particles has revealed evidence for significant correlation between surface area as a

metric of dose and adverse pulmonary effects including inflammation and tissue damage (Borm, 2006). This suggests that equivalent mass dose concentrations of nanoparticles have a higher response than particles of similar chemistry with larger aerodynamic diameters.

We postulate that poor exposure assessment and characterization of the nano-particle fraction of welding fume is major gap in linking welding fume exposures to observed health effects. Understanding toxicological potential of and human exposure to chemical agents are keys to any human health risk assessment. This research intends to characterize welding fume exposure in terms of the nano-particle fraction. Specific attention will be paid to the factors of the welding process and exposure scenario that affect the physical and chemical characteristics of welding fume.

2. PARTICLE SIZE DISTRIBUTIONS OF WELDING FUME IN THE BREATHING-ZONE AND IN ISOKINETIC CHAMBER, MEASURED UNDER LABORATORY-CONTROLLED CONDITIONS

2.1 Background

Welding fume is composed of both gases and solid particulate; however, in this research the term fume is used exclusively to describe the solid particulates.

2.1.1 Particle Size Distribution

The hazard posed by inhaled welding fume depends on the site within the respiratory system at which it deposits. The deposition of particles within the human respiratory system is dependent on particle size, and the fume emitted during the welding process has a wide distribution of particle sizes ranging from only a few nanometers to tens of microns in diameter. The Particle Size Distribution (PSD) is one of the metrics used to evaluate the hazards posed to humans by any inhaled aerosol. A PSD describes the frequency (i.e., number or mass) of particles as a function of particle size. Often, aerosols generated from industrial processes follow a lognormal distribution that can be described by the parameters of that distribution, i.e., median diameter (either count [CMD] or mass [MMD]) and geometric standard deviation (GSD). Knowledge of the underlying frequency distribution parameters of a given aerosol allows one to predict the extent that particles may enter and deposit within the human respiratory system.

Where particles deposit within the lung is a critical factor in whether adverse health outcomes are associated with a given aerosol exposure. The human respiratory system is classified into three regions based on particle deposition which are described as the extrathoracic region, which includes the nasopharynx and mouth, tracheobronchial region which includes the trachea, bronchi and bronchioles, and alveolar region, which includes the alveolar ducts and alveolar sacs. Particle deposition to each of these regions is dependent upon many factors including whether mouth or nose breathing is used, flow rate (i.e., breathing rate and volume) and particle size. Figure 5 below represents the theoretical deposition of nose breathing in the different pulmonary regions as a function of particle size (Oberdorster, et al., 2004). As can be seen from this graph, ultrafine particles are most efficient at penetrating to and depositing within the alveolar region of the lungs. Once in the alveolar spaces, these particles may pass to the bloodstream and become agents of systemic toxicity.

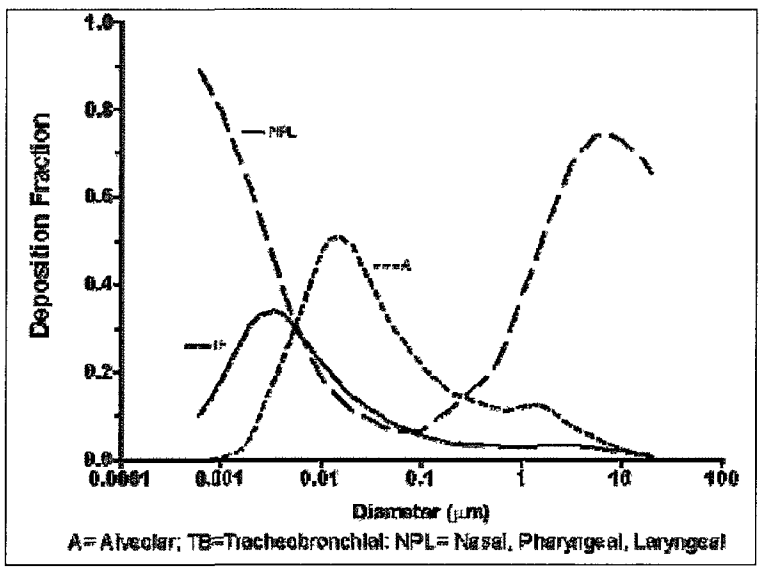

Figure 5: Predicted regional deposition for nose breathing.

There are many methods used to measure PSD of aerosols. In this research, three different cascade impactors were used to measure mass-based PSDs of aerosol generated from SMAW/SS welding operations performed in two different experimental systems. A cascade impactor is a sampling instrument that employs a series of nozzles with decreasing diameter from top to bottom, coupled with individual impaction plates to capture aerosols by taking advantage of particle inertia (Hinds, 1999b). As the aerosol passes through the nozzle at a given velocity, the output flow stream is directed at the flat impaction plate, which deflects the flow to form an abrupt 90° bend in the flow streamlines. Particles whose inertia exceeds a certain value are unable to follow the streamlines and impact on the flat impaction stage, while smaller particles do follow the streamlines and can move to the next set of nozzles and impaction plate. Thus, airflow is accelerated to higher velocities in successive impaction stages by forcing the flow to pass through smaller surface area nozzles, leading to collection of smaller particles on each subsequent stage. This allows separation of particles by their momentum differences into a number of size ranges and collection of these size ranges on impaction stages simultaneously. The particle size measured using a cascade impactor is not physical but rather aerodynamic diameter.

Lognormal distributions often mathematically characterize particle size distributions in aerosols found in occupational and environmental settings and the specification of the mathematical form of the particle size distribution is a prerequisite for the estimation of the distribution parameters (de Ruiter & Oeseburg, 1987). There is no theoretical basis for the log-normality of particle size distributions of aerosols in many cases, and the rationale for using this type of distribution is merely based on empirical considerations (de Ruiter & Oeseburg, 1987).

The frequency function of the lognormal distribution has the form:

$$df = \frac{1}{\sqrt{2\pi}\, d_p \ln \sigma_g} \exp\left(-\frac{\left(\ln d_p - \ln MMD\right)^2}{2\left(\ln \sigma_g\right)^2} \right) dd_p \qquad \textbf{Eq 1}$$

where

d_p = particle size (μm)
MMD = mass median diameter (μm)
σ_g = geometric standard deviation (GSD)

For a mass-based particle size distribution, the average size of a poly-disperse aerosol is the Mass Median Diameter (MMD). This means that half of the total mass of the particles is in the size range smaller than MMD, and half of the mass is in the size range larger than MMD. The Geometric Standard Deviation (GSD) is a measure that indicates the spread of a PSD. Estimation of distribution parameters, MMD and GSD, is easily accomplished using a log-probability plot where particle size is plotted as a function of cumulative mass probability (i.e., percent weight less than stated particle size). The median particle size corresponds to size at 50% cumulative probability ($d_{50\%}$ = MMD) and the GSD is calculated by:

$$\sigma_g = \frac{d_{84\%}}{d_{50\%}} \qquad \textbf{Eq 2}$$

The GSD, being the ratio of two sizes, has no units and must always be greater than or equal to 1.0. The MMD and GSD can be determined directly from a log-probability plot and completely define the mathematical form of a lognormal distribution. One attribute of the lognormal distribution is that the GSD remains constant for all moment (e.g., count, surface area, mass) distributions. Therefore, if a mass-based size distribution is known, it is possible to calculate the other moment distributions using the Hatch-Choate conversion equations (Hinds, 1999b).

2.1.2 Measurements of Welding Fume Particle Size Distribution in the Literature

Welding fume PSD measurements have been reported for a variety of welding processes in the literature. However, data that describe the PSD of the SMAW process have been limited.

Berner and Berner (1982) measured mass-based PSD of an SMAW process (base metal type unspecified) with an 11-stage low pressure impactor in a laboratory experiment. Researchers measured an MMD of 0.35 μm with a GSD of 1.6. The authors reported that 93% of the mass was contained in particles less than 1 μm in aerodynamic diameter and only 0.65% of the mass was in particles smaller than 0.1 μm in aerodynamic diameter. Authors noted that the size distribution was not exactly unimodal logarithmic and suggested that it might be trimodal. Furthermore, they suggested that the measured MMD was associated with the accumulation mode but that a

nucleation mode was only partially observed due to inadequate mass collection on lower stages of the impactor.

Narayana (1995) used an ambient pressure Andersen Sampler (8 stages) coupled with a low pressure assembly (5 stages) to measure the PSD of SMAW-SS in a laboratory experimental system. The cascade impactor instrument was able to capture a particle size range of 0.08 – 35 μm, however, authors reported that all fume fell below 10.5 μm in aerodynamic diameter. Further, a "significant fraction" of the fume mass distribution was collected in the 0.08 – 2.0 μm size range. It is reported that the distribution is bimodal in nature, but neither median diameters of each mode nor mass concentration values are reported by the authors.

Hewett (1995) also conducted a laboratory study in an emission chamber and measured parameters of the PSD of SMAW-MS and SMAW-SS using a Micro Orifice Uniform Deposit Impactor (MOUDI), which is one of the impactors used in our experiments. PSD parameters of SMAW-MS were MMD of 0.59 μm and GSD of 1.80. PSD parameters of SMAW-SS were calculated as MMD of 0.46 μm and GSD of 1.55. The author also measured the bulk density of the welding fume and reported as 3.4 g/cm^3 for both MS and SS.

Most recently, Sowards et al. (2008) completed a laboratory-based study aimed at characterizing SMAW electrodes, including the E308-16 SS electrode utilized in our experiments. The researchers measured number and mass distributions of SMAW using an Electrical Low Pressure Impactor (ELPI), which is also one of the instruments used in our experiments. The count median diameter for the E308-16 electrode was 0.21 μm (GSD=1.18) and 0.25 μm (GSD=1.15) for low (11.1 kJ/in.) and high (17.3 kJ/in.) heat inputs, respectively. The measured mass median

diameters were 0.62 μm (GSD=1.11) and 0.56 μm (GSD=1.11) for low and high inputs, respectively. Mass of fume below particle size of 0.1 μm accounted for 1.5% of total mass based on the constructed particle size distribution.

The previous studies generally describe the PSD parameters of SMAW under laboratory conditions, but do not offer insight into how these reported PSD parameters may represent welding fume in actual welder exposure scenarios. One field study measured the mass- and count-based PSD of SMAW-MS (3.2 mm diameter, type E6011) within a large welding shop (Stephenson, Seshadri, & Veranth, 2003). An 8-stage Andersen cascade impactor collected mass-based size-fractionated fume samples 3 m above the floor of the shop. This sampling location was chosen to best estimate the PSD of the fume in a well-mixed occupational setting and serve as representative of exposures experienced by workers not specifically performing welding tasks. A canning mobility particle sizer (SMPS) and an optical particle counter (OPC) were located at tabletop level at a distance of 8.5 m from the welding operation, again to estimate the size distribution indicative of exposures to other workers in the vicinity of welding operations. The mass-based measurements revealed a bimodal distribution with modes at approximately 0.3 μm (GSD=1.5) and 5 μm (GSD=2.75) with 80% of the mass falling below 1 μm diameter particles. (Distribution parameters estimated from log-probability plot within article.) The count-based PSD parameters obtained with the SMPS and OPC were reported as CMD of 0.12 μm (GSD = 2.07).

Beyond SMAW, other researchers have explored the PSD of other welding processes. One emission chamber-based laboratory study of GMAW and FCAW used an SMPS and a Condensation Particle Counter (CPC) to measure an overall CMD of 0.352 μm during fume generation (Zimmer & Biswas, 2001). These researchers also measured the count-based PSDs at 15, 120, and 480 seconds

after a short burst of welding (~2 s) in order to understand how aging affects the PSD. At 15 s, they measured a multimodal distribution with modes at 90 and 246 nm. At 120 s, they measured modes at 104 and 264 nm. At 480 s, they measured modes at 200 and 352 nm. The authors suggest that this multi-modal evolution of the count-based PSD over time is a function of either chemistry differences between particles being formed and/or the differences in the formation rate of fume generated from the arc-zone and fume generated from microspatter.

The same research group continued their studies of GMAW fume and extended their research to particles greater than 1 μm in diameter in the welding fume (A. T. Zimmer, P. A. Baron, & P. Biswas, 2002). This research in the same laboratory emission chamber incorporated an Aerosizer (TSI Inc., Model 3220) to measure micrometer-scale particles. With this additional instrumentation, researchers identified a count-based primary mode of 6.8 μm. This portion of the welding aerosol was attributed to the microspatter from the welding process. When comparing the count-based distribution statistics from both the Aerosizer and the SMPS, the micrometer-size aerosol is roughly five-orders of magnitude smaller than the sub-micron aerosol and therefore contributes significantly less to a respirable aerosol exposure.

Another laboratory-based study examined the mass-based PSD of FCAW-MS using the Andersen 8-stage cascade impactor (N. T. Jenkins, Pierce, & Eagar, 2005). Here, aerosol distribution parameters were measured as a MMD of 0.33 μm and GSD of 4.0. Researchers noted that the distribution was more bimodal in nature, corresponding to nucleation and accumulation modes, and was not adequately described by a single set of MMD and GSD parameters. To overcome this lack of fit, the data collected from the cascade impactor was grouped according to lower stages (nucleation mode) and upper stages (accumulation mode) in an attempt to define the two modes of

the distribution. Using this method, authors calculated mode diameters of 0.43 μm (GSD = 1.4) and 6.8 μm (GSD = n.a.). Ninety percent of the mass was contained in particles greater than 1 μm in aerodynamic diameter.

2.1.3 Particle charge measurement reported in the Literature

The inherent static electrical charge on workplace aerosols has been critically reviewed in the occupational hygiene field previously (J. Vincent, 1985, 1986; J. H. Vincent, Johnston, Jones, & McIathlan, 1983). These reviews document that particles in workplace aerosols do exhibit a significant static charge and may have practical significance in terms of aerosol sampling considerations (i.e., sampling media), deposition and retention within the human respiratory tract and contaminant removal via filtration.

Particle charge is quantified in terms of the median magnitude of charge per particle ($|q|_m$) and generally, all aerosols become charged during the process of being made airborne (J. Vincent, 1986). It has been found that the median magnitude of charge per particle for isometric particles may be expressed as a function of particle aerodynamic diameter (d_{ae}) by:

$$\left|q/e\right|_m = A\, d_{ae}^{n} \qquad \textbf{Eq 3}$$

Here, A and n are numerical coefficients (J. Vincent, 1986). For d_{ae} expressed in micrometers, A is the median number of charges equivalent in magnitude to the elementary charge e (=1.6 x 10^{-19} C) carried by particles of aerodynamic diameter 1 μm. Measurements of particle charge in workplaces revealed a spread of coefficient values depending on the type of particle and the mechanism of dispersal. For instance, drilling of sandstone resulted in A = 40 and n = 1.4, Compressed air blowing of mineral dusts (quartz and sulfur) resulted in A = 20 and n = 1.0 – 1,4. Automated dust dispersal of coal dust resulted in A = 40 – 126 and n = 1.0 – 1.6.

In terms of welding aerosols, one study did attempt to measure the charge on welding aerosols from GMAW and SMAW processes (Johnston, Vincent, & Jones, 1985). In this experiment, a specialty split flow elutriator (Johnston, 1983) in combination with an OPC was used to measure the polarity and magnitude of particle charge as well as the size-distribution of the aerosol. There was a difficulty, however, when trying to relate the particle charge measurements to the size distribution of the aerosol because the optical particle counter used could only gauge particles greater than 0.5 μm in diameter. To overcome this limitation, authors estimated a median diameter particle of 0.2 μm based on scanning electron microscopy of welding samples. Based on this particle size, they were able to estimate A = ~10 but could not estimate the coefficient n because of the lack of size distribution data..

More recently, aerosol instrumentation has advanced in terms of charge measurement capabilities of small particles, and applications to medical aerosols have arisen in the scientific literature (Glover & Chan, 2004; Young, et al., 2007). The method uses a modified ELPI to measure the charge on aerosols from metered dose inhalers (MDIs) (Glover & Chan, 2004). The basic configuration of the ELPI used for this particle charge measurement is turning the corona charger

and trap voltage off during experimentation. Application of the ELPI method to welding aerosols may better characterize the charge represented across the entire distribution, which this dissertation research attempts to accomplish. With the modified ELPI method, the particle charge characterization of welding aerosols previously attempted (J. Vincent, 1986) may be completed to particle sizes less than 0.5 μm in aerodynamic diameter.

2.2 Study Objectives

The general goal of this research is to determine the parameters and form of the particle size distribution and the charge per particle of welding fume generated during SMAW process on stainless steel under laboratory-controlled conditions by advancing the research in this area to the study of ultra-fine/nano-size fractions (<0.1 μm) found in welding fume. The particle size and charge information is essential component of human exposure assessment for welding fume and necessary for designing future health effects studies for welders.

Specifically this study aims to:

1) determine the parameters and form of the mass-based particle size distribution measured in an isokinetic emission chamber using three different cascade impactors (ELPI, MOUDI, PCIS) and assess consistency of results across measurement tools;

2) determine the parameters and form of the mass-based particle size distribution within the breathing-zone of a manikin simulating a welder located in an exposure chamber using three

different cascade impactors (ELPI, MOUDI, PCIS) and assess consistency of results across instruments;

3) uncover potential differences in the character and form of PSD measured in isokinetic emission chamber and in the breathing-zone in order to gain insight into representation of emission chamber fume PSD measurements for inhaled welding fume; ;

4) determine the parameters and form of the count-based PSD measured within the breathing-zone of the manikin simulating a welder located in the exposure chamber using the ELPI as a function of under different welding parameters (i.e., electrode size and amperage setting); and assess the relationship between parameters of mass-based and count-based distribution for welding fume;

5) estimate the charge per particle of welding aerosol using the ELPI within the breathing-zone of the manikin simulating a welder located in the exposure chamber; and

2.3 Study Methods

The two laboratory-based experimental systems (emission and exposure chambers) used in this research have been described and characterized previously (Breskey, 2008; Durgam, 2004) and only a short description of each experimental system is provided here.

2.3.1 Isokinetic Emission Chamber

An emission chamber constructed of stainless steel with an approximate volume of 0.23 m^3 was designed and fabricated to conduct welding fume characterization experiments under laboratory-controlled conditions. The design attributes and dimensions of the emission chamber and its components are schematically illustrated in Figure 6. The chamber has two main components, with a conical hood section in which welding experiments can be conducted, and a straight flanged duct section with a sampling platform.

The base diameter of the conical hood is 1m and it has two glove ports that are 17.8 cm in diameter and spaced with a center-to-center distance of 43.2 cm. This allows access and ample room for a welder to reach the welding gun and operate the equipment with ease. The hood also has provision for two view ports so that the operator may see the welding being performed within the chamber. A slotted welding table is placed underneath the chamber to facilitate the placement of base metal for welding experiments and an electrically controlled turntable is also employed to move the base metal piece during welding and control variability in welding speed.

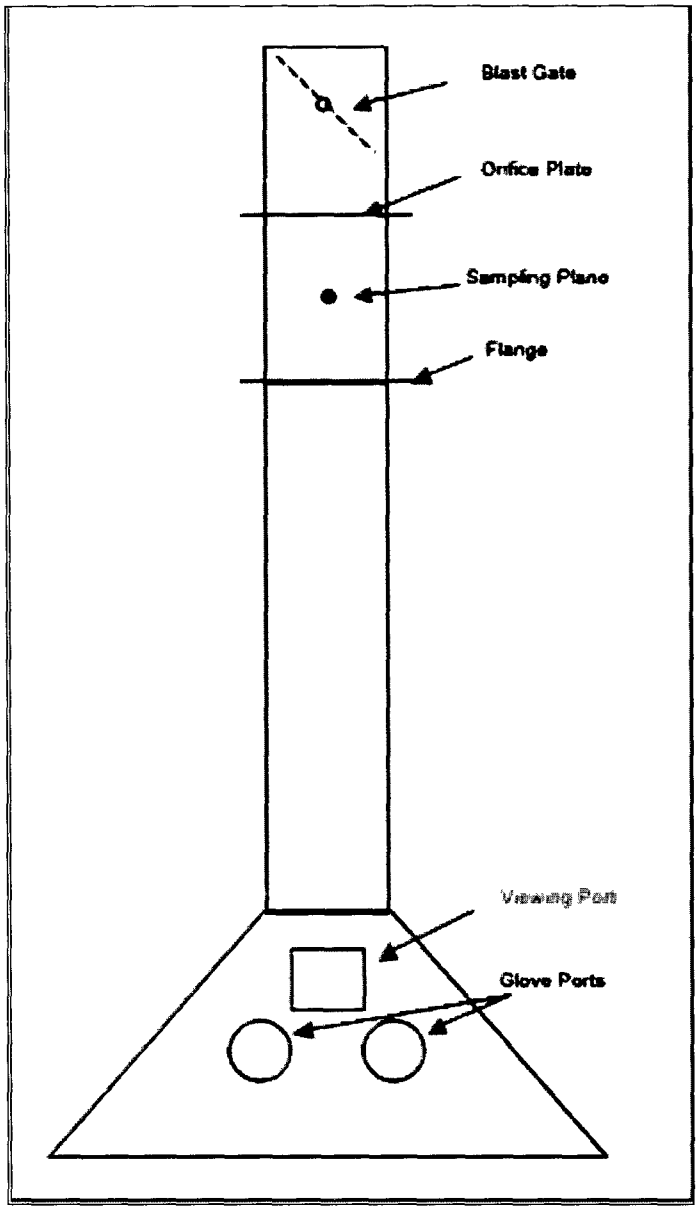

Figure 6: Emission chamber.

The straight duct has a total length of 2.3 m and the inner diameter of 18.7 cm. The sampling plane is at a distance of eight duct diameters upstream of the apex of the conical section. An orifice plate is located two duct diameters downstream of the sampling plane and allows for the

quick measurement of the airflow rate through the system. At the top of the straight duct section is a butterfly blast gate that is used to regulate the airflow through the chamber. The straight duct is connected to the existing exhaust ventilation ductwork in the laboratory and welding fumes are vented to building air quality control systems. The chamber allows samples to be collected isokinetically in the sampling plane of the straight duct section. At isokinetic conditions velocity and flow rate are controlled and concentration is expected to be uniform in the sampling section (Durgam, 2004).

2.3.2 Exposure Chamber

The exposure chamber (Figure 7) consists of the three sections: 1) cubic, 2) pyramidal, and 3) circular straight duct. The cubic portion has the dimensions of 1.2 m in length, 1.2 m width and 1.1 m in height and is the portion that contains the manikin and semi-automated welding process. The front side of the cubic section has a small window (17.8x17.8 cm) and two glove ports through which the researcher can reach and perform welding inside the chamber. The backside of cubic section contains a door (66x31 cm), which is hinged at the top and allows access to the manikin and welding turntable in between experimental runs. The door has a window with dimensions of 51x17.8 cm. The pyramidal section measures 1.2x1.2 m at the base and tapers to the circular straight duct section (with inner diameter of 18.7 cm) at a 45-degree angle. The sides of the pyramidal section measure 99 cm. The total volume of the cubic and pyramidal sections combined is 1.87 m^3.

The circular straight duct section extends from the top of the pyramidal section to the main exhaust plenum of the laboratory air quality ventilation system and has an inner diameter of 18.7

cm. The straight duct section is broken into three smaller sections. The first of these is 25.4 cm long and contains a small hole to allow insertion of a sampling probe for collection of fresh welding fume exiting the system (which was not used for sample collection in this research). The second section is 22.9 long and acts as a spacing element. The third straight duct section is 83.8 cm long and contains a hinged blast gate that allows for airflow rate control through the chamber. In addition, there is an orifice plate between the second and third portions of the straight duct with horse barbed pressure taps located one inch above and below the plate. A manometer connected to these pressure taps allows measurement of the pressure differential across the orifice. Each smaller portion of the circular straight duct section is secured together by flanges and bolts.

All components of the exposure chamber were constructed of stainless steel and are welded together at the seams. The chamber is supported and held in position by an outer cage constructed of Unistrut (type P1100). The bottom of the chamber is 50.8 cm above the floor and 48.3 from the wall of the laboratory on the left side of the chamber. The bottom of the chamber is open and allows air from the laboratory to enter and flow through to the exhaust plenum.

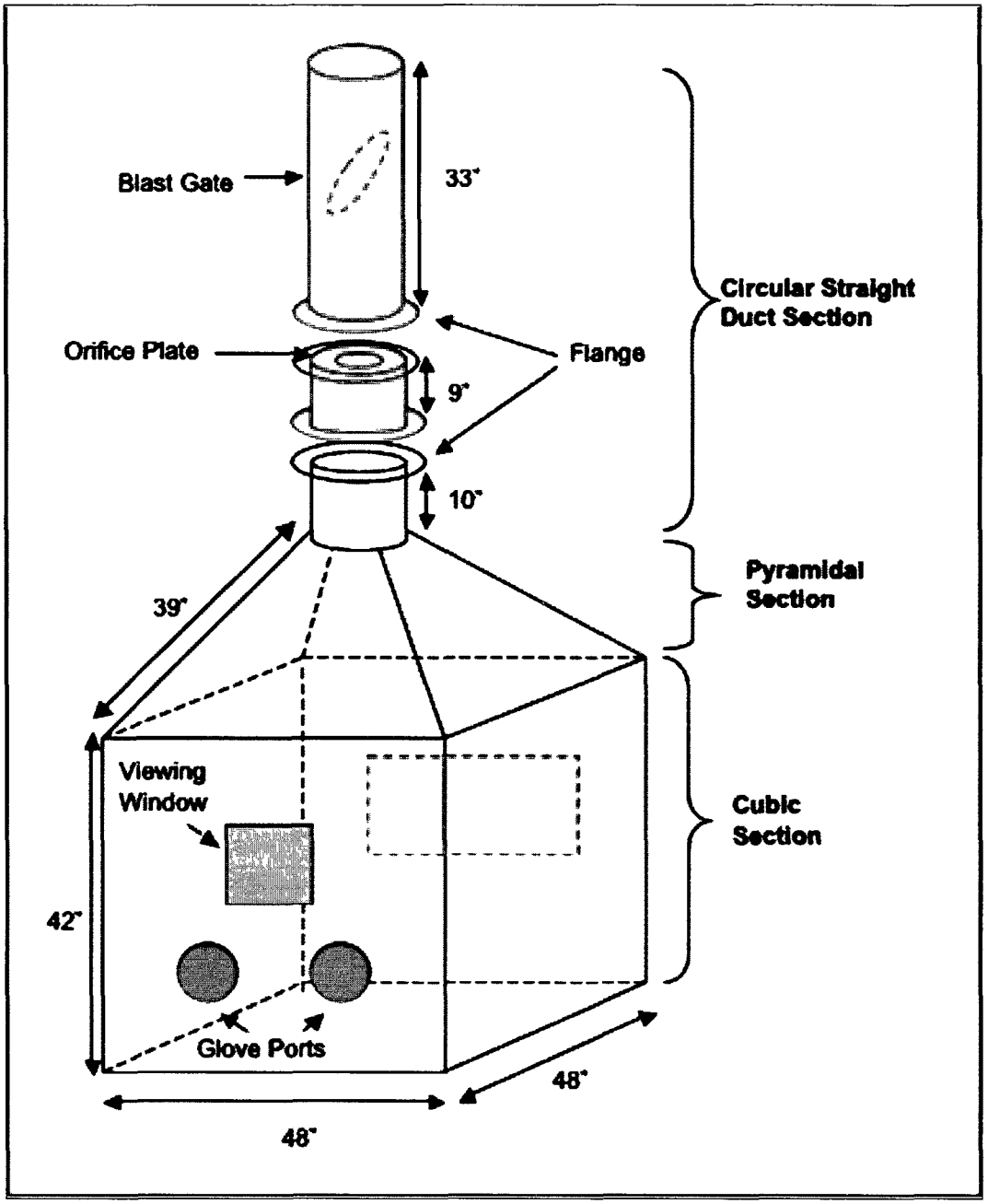

Figure 7: Exposure chamber.

The exposure chamber system incorporates a breathing thermal manikin as a tool to represent an actual welder performing the work task. The manikin is a thermal respirating torso

developed by Measurement Technology Northwest (MTNW) of Seattle, WA, and consists of head, torso (to the waist), and arms (to the elbow). It includes nose and mouth openings that can be connected to an external breathing apparatus. Additionally, an external heating apparatus connects to the manikin and raises the skin temperature, thereby simulating the human thermal plume. Aerosol collection filters can be installed inside the head at nose or mouth inhalation points, depending on the specific test being conducted. The inhalation and exhalation points can be changed as needed, but cannot be overlapped - thus maintaining test integrity. The manikin head is designed to open at the back for easy access to the integrated filtering unit.

The breathing is controlled by computer software that controls parameters, which define the mode of operation. The basic parameters that can be controlled are the tidal volume (range: 0.1-2.5 L), breathing rate (range: 20-40 cycles/min.), and inhalation:exhalation ratio (1:5 or 5:1). The control system monitors these user inputs and adjusts the motion of the air cylinders accordingly. The tidal volume is controlled through the distance traveled by the pistons in the cylinder and the breathing rate is determined by the speed by which the piston moves. The piston speed can be different on the inhale and exhale cycles, producing an I:E ratio matching the user input. Airflow measurements (inhaled and exhaled air) are controlled by integrated spirometers.

The heating system consists of an external heater, along with a power cable and sensor cables that connect to the manikin. The manikin is comprised of two independently heated thermal zones – the head, and the torso/arms. Each of the two zones has independently controlled heaters that allow the user to select a temperature set point for the manikin. The sensor cables connect to thermocouples placed within the manikin close to the skin at points on the chest and the head to maintain constant temperature, which simulates human body temperature.

The manikin is mounted onto a plate on a stand, enabling varying the torso angle between 0 – 30 degrees. Since the head angle was adjustable from 0 – 30 degrees, a strap was added to secure the desired head position/angle. Both angles/positions were checked before and after each experiment using a protractor. The manikin was placed in the middle of the exposure chamber to allow airflow around it. The distance of the manikin to the welding piece (i.e., 27.9 cm) was chosen to mimic a typical welding scenario. The location of the manikin was directly opposite that of the welding operator, thus a right-handed welding operator outside the chamber would technically simulate the welding of a left-handed operator inside the chamber.

In order to mimic an actual welder, the manikin was clothed in a heavy-duty leather welding jacket. Various custom straps were added to the jacket's front and back to assist in stabilizing and consistently positioning the air sampling devices across different experimental runs. The manikin was also outfitted with a standard welding helmet held in place by extra chin and neck straps to ensure consistent positioning of manikin and sampler within the helmet from one experimental run to the next.

2.3.3 Welding Equipment/Consumables

The welding equipment setup consisted of a welding machine and a welding turntable. The welding machine (Miller Electric Mfg Co., Model 330A/BP, Appleton, Wisconsin) is a combined SMAW/GTAW apparatus. The turntable (M.B.C. Company model BP-2-A, Mukwonago, Wisconsin) was used in order to ensure constant welding speed and was bolted onto the frame of the exposure chamber, to ensure stability and consistent position of the welding piece. During welding experiments the turntable was set to a speed dial setting of 1.3, which was determined to be about

0.16 revolutions per minute. The setting corresponds to a theoretical travel speed of 15.7 cm per minute based on circular diameter of 30.5 cm (roughly the size of base metal plates used. The experimental average travel speeds varied between 17.5 and 9.1 cm per minute across experimental runs depending on the diameter of the circle welded. Specific welding speeds varied during experiments based on the location of the electrode, either closer or further from the edge of the base metal, which ultimately determined the diameter of the circle to be welded. The position and speed setting of the turntable was chosen such that the welding operator could perform the welding in a consistent manner, within a comfortable working distance using the chamber glove ports, at a speed ensuring standard weld quality. A standard SMAW welding gun was used for all experiments.

All experiments were performed on certified S.S. 304 grade, 0.635 cm stainless steel sheet metal pieces ('base metals') with an approximate size of 35.5 by 35.5 cm. All metal was purchased certified from Metal Management, Inc. (Chicago, Illinois). The welding electrodes used were 2.6 mm, 3.2 mm and 4.0 mm diameter E308H-16 (Midalloy Chromax, St. Louis, MO), purchased from Wisco Welding Company located in Chicago, Illinois. These diameters were chosen to reflect common welding applications in industry. Whenever electrodes from an open package were used, they were always heated at 120 °C for at least three hours prior to the initiation of experiments in order to remove potential moisture.

2.3.4 Sampling Devices

Size and charge characteristics of welding aerosol were investigated in this research by employing different cascade impactor instruments. Although each of these instruments operates

under the same theoretical principles, the actual performance of the instruments varies depending on the sampling conditions, sampler design and efficiency. The aerosol samplers employed and associated sampling media are described in the following sections.

2.3.4.1 Electronic Low Pressure Impactor

The Electrical Low-Pressure Impactor (ELPI) is an instrument used to measure airborne particle size distribution and concentration in real-time (Keskinen, Pietarinen, & Lehtimaki, 1992; Marjamaki, Keskinen, Chen, & Pui, 2000; Marjamaki, Lemmetty, & Keskinen, 2005; Marjamaki, et al., 2002; Virtanen, Marjamaki, Ristimaki, & Keskinen, 2001). The operating principle of the ELPI is based on particle charging, inertial classification in a cascade impactor, and electrical detection of the aerosol particles. The ELPI's cascade impactor fractionates aerosol into 13 different size ranges with 50% collection efficiency cut-off points of: 10, 6.8, 4.4, 2.5, 1.6, 1.0, 0.65, 0.40, 0.26, 0.17, 0.108, 0.06 and 0.030 μm. Additionally, the impactor may be operated in particle charging and electrical detection mode, which allows measurement of size-segregated number concentration in real-time. The ELPI operated at a flow rate of 10 lpm using a calibrated high-volume sampling pump. The impaction stages of the ELPI accommodate 25-mm filters or impaction plates.

The main components of the instrument are a corona charger, a low-pressure cascade impactor and a multi-channel electrometer. When using the ELPI for number concentration measurements, the sample first passes through a unipolar positive polarity charger where the particles in the sample are charged electrically by small ions produced in a corona discharge. After the charger, the charged particles are size fractionated according to aerodynamic properties in a low-pressure impactor. The stages of the impactor are insulated electrically and each stage is

connected individually to an electrometer current amplifier. The charged particles collected in a specific impactor stage produce an electrical current, which is recorded by the respective electrometer channel. A larger charge correlates to a higher particle population.

The electrical current value of each channel is proportional to the number of particles collected on a stage, and thus to the particle number concentration in the particular size range specific to that stage. The current values are converted to an aerodynamic size distribution using particle size dependent relations describing the properties of the charger and the impactor stages. The instrument can also be operated with particle charging mode in the off position as a conventional impactor, which allows measurement of size-segregated mass-based concentration.

During emission chamber experiments, a 14 mm diameter isokinetic sampling probe was fitted to the ELPI sampler inlet. During exposure experiments, the instrument could not be placed within the exposure chamber due to its size. Instead, a SS sampling probe of 60 cm in length was fitted to the ELPI inlet and passed through the exposure chamber wall and positioned within the right side of manikin's breathing-zone (outside the welding helmet) in the exposure chamber experiments (see Figure 8).

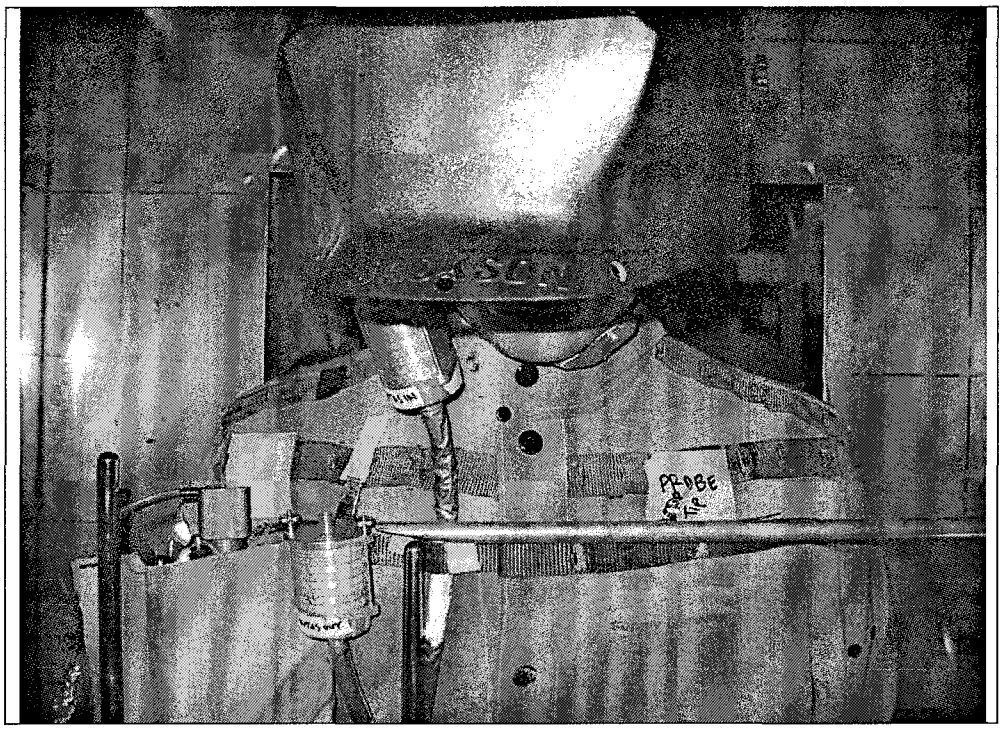

Figure 8: Exposure chamber sampling set-up.

2.3.4.2 Micro-Orifice Uniform-Deposit Impactor

The Micro Orifice Uniform Deposit Impactor (MOUDI) (MSP Corporation, Model 110, Shoreview, Minnesota) is primarily designed as an ambient air sampling device (Marple, Rubow, & Behm, 1991). The MOUDI fractionates aerosols into 11 size ranges with 50% collection efficiency cut-off points of 18, 10, 5.6, 3.2, 1.8, 1.0, 0.56, 0.32, 0.18, 0.10, 0.056 μm and has a back-up filter which collects aerosols <0.056 μm in aerodynamic size. The MOUDI uses 47 mm filters on impaction plates and a 37 mm back-up filter. The MOUDI is operated at a flow rate of 30 lpm using a calibrated high-volume sampling pump.

During emission experiments, a 25 mm diameter isokinetic sampling probe was fitted to the sampler inlet and positioned within the sampling plane. During exposure experiments, the MOUDI was located within the breathing-zone of the manikin (on the right side of manikin's torso) outside the welding helmet in the exposure chamber experiments (see Figure 8).

2.3.4.3 Personal Cascade Impactor Sampler

The Personal Cascade Impactor Sampler (PCIS), a personal exposure sampling instrument, is a small cascade impactor that can be worn on the body (Misra, Singh, Shen, Sioutas, & Hall, 2002). The PCIS separates and collects airborne particles into five aerosol size ranges: > 2.5 μm, 1.0 to 2.5 μm, 0.50 to 1.0 μm, 0.25 to 0.50 μm, and < 0.25 μm. The PCIS was connected to a 14 mm diameter isokinetic sampling probe to collect welding fume samples during emission chamber experiments. Also, two PCIS instruments were placed within the manikin's breathing-zone during exposure chamber experiments: one sampler outside and one sampler inside the welding helmet on the right side of manikin's head (see Figure 8). The PCIS is operated at approximately 9 lpm and one calibrated sampling pump was used to operate both samplers simultaneously. The impaction stages of the PCIS accommodate 25 mm filters while the backup filter is a 37 mm filter.

2.3.5 Experimental Design

There are three rounds of experiments performed in this research: 1) mass-based concentration measurements in the emission chamber; 2) mass-based concentration measurements in the exposure chamber; and 3) -number-based concentration measurements in

the exposure chamber. Experiment setup and conditions for each round of experiments are defined in the following sections.

2.3.5.1 Mass-Based Concentration Measurements in Emission Chamber

Four experiments were performed within the emission chamber to obtain data to construct the mass-based PSD. During these experiments, welding process parameters (electrode size= 3.2mm; welding current=100A) were held constant. The ELPI, MOUDI and PCIS were fitted with isokinetic sampling probes (with sampling nozzle diameters of 14, 25, and 14 corresponding to sampling flow rates of 10 lpm, 30 lpm and 9 lpm, respectively) that were positioned in the sampling plane of the emission chamber system. The ELPI was operated with the corona charger turned off, thus allowing for unbiased mass collection. Both the ELPI and the MOUDI were operated with polytetrafluoroethylene (PTFE) filters with 0.5 μm pore size on the impaction plates (25 mm diameter for ELPI and PCIS and 47 mm diameter for MOUDI). The MOUDI and PCIS backup filters were 37 mm diameter PTFE with 2.0 μm pore size.

2.3.5.2 Mass-Based Measurements in Exposure Chamber

Four experiments were performed within the exposure chamber to construct the mass based PSD and to determine the mass-based PSD parameters. During these experiments, welding process parameters (electrode size=3.2 mm; welding current=100A) were held constant. The MOUDI was placed within the breathing-zone of the manikin with the instrument's inlet at the right shoulder. The ELPI was positioned outside of the exposure chamber while the sampling probe fitted to the inlet of the ELPI passed through the chamber wall. The inlet of the sampling probe

reached across the body of the manikin and was positioned parallel to the MOUDI inlet, 5 cm to the left of the MOUDI inlet. The ELPI was operated with the corona charger turned off, thus allowing for unbiased mass collection. Both the ELPI and MOUDI were operated with 0.5 μm pore-size PTFE filters on impaction plates (25 mm diameter for ELPI and PCIS and 47 mm diameter for MOUDI). The MOUDI and PCIS backup filters were 37 mm diameter 2.0 μm pore-size PTFE. During exposure experiments, two PCIS instruments were placed within the manikin's breathing-zone (on the right side of manikin's torso): one sampler outside and another sampler inside the welding helmet.

The manikin was positioned within the center of the exposure chamber at a distance of 28 cm from the closest edge of the base metal piece on the turntable. Physiological (breathing rate=16 breaths per minute; breathing volume=0.85 liters per breath) and subject-specific posturing (torso angle=20 degree torso tilt; head angle=20 degree head tilt) parameters were held constant during exposure experiments. A 47 mm diameter 0.5 μm pore-size PTFE filter was used in the filter assembly in the manikin head to collect inhaled fume.

2.3.5.3 Real Time Number Concentration and Particle Charge Measurement

The real time number concentration of particles found in welding fume was measured in the breathing-zone of the manikin in the exposure chamber using the ELPI instrument. A set of nine experiments were performed in the exposure chamber to explore the variability of number concentration within the breathing-zone as a function welding electrode diameter 2.4 mm, 3.2 mm, 4.0 mm and the welding amperage setting. For each electrode size, a low, a medium and a high amperage setting was selected that are within the optimum and recommended operating range of that electrode size. Specifically, for electrode sizes of 2.4 mm, 3.2 mm, 4.0 mm, the experiments

were performed at low [60 A, 90 A, 110 A], medium [70 A, 100 A, 120 A] and high [80 A, 110 A, 130 A]) amperage settings, respectively. Welding time (thus, number of electrodes burned) during experiments was adjusted from one experimental run to the next to ensure adequate sample collection by in-situ examination of particle loading within the ELPI. The welding time varied from 8:34 to 32:27 minutes and the number of electrodes burned ranged from to 7 to 40 across nine experiments. **TABLE** I summarizes parameters and conditions of the number concentration measurement experiments conducted within the exposure chamber. In order to obtain the number concentration readings with the ELPI, the corona charger was turned on to allow the electrometers to record the count data. Aluminum impaction plates were employed in the ELPI to simultaneously obtain mass-based concentration data. A PTFE filter was used in the manikin's head assembly during these experimental runs.

TABLE I: NUMBER CONCENTRATION EXPERIMENTAL SUMMARY

Experiment #	Electrode Size (mm)	Amperage (A)	# of Electrodes Burned	Welding Time (mm:ss)	# of Pulsed Electrodes
1	2.4	60 (L)	20	22:01	3
2	2.4	70 (M)	40	32:27	4
3	2.4	80 (H)	31	20:59	4
4	3.2	85 (L)	20	23:03	3
5	3.2	95 (M)	16	17:08	3
6	3.2	105 (H)	16	15:27	3
7	4.0	110 (L)	10	13:30	3
8	4.0	120 (M)	9	11:03	0
9	4.0	130 (H)	7	8:34	0

During each of the experiments (except Experiment # 8 and 9), a small subset of the electrodes burned was used as a basis to calculate the particle charge of the welding fume. While burning these few electrodes, the corona charger was cycled on and off (pulsed) approximately in every 10 seconds during the experiments. This procedure allowed the recording of 10 seconds of number concentration measurement followed by 10 seconds of inherent particle charge measurement followed by another 10 seconds of particle number concentration measurement, and so on until the entire electrode is consumed. Assuming that the measured number concentrations stayed the same during the 10 seconds that the inherent particle charge was being measured, we can apply that inherent charge to the number concentration and, then, calculate the charge per particle.

2.3.6 Sampling Procedures

All filter media, as described in previous sections, were prepared over the course of several days. Filters were desiccated for at least 72 hours and weighed at intervals of at least 24 hours to achieve a stable weight. A stable weight is defined as the standard deviation of all weighing events for each filter, divided by the average weight of each filter, corresponding to a value less than or equal to 5%. For values greater than 5%, additional measurements were taken until the desired level of stability is achieved.

Every morning, upon arrival, the facilities were firstly inspected for any substantial changes or abnormalities, in equipment, inventory, or laboratory ventilation system. The welding electrode oven was turned on, allowing electrodes from unsealed containers to be heated at 250 °F for at least 2 hours prior to initiating an experiment.

While the ventilation properties of our experimental system was thoroughly characterized in a prior study (Breskey, 2008), the system was validated every day. This was performed by taking center line Pitot tube measurements at ten different pressure drop settings, 0.1 – 3.1 mm H_2O, spanning well across the design operating range of the ventilation rate (i.e., 315 – 945 cfm). To ensure consistent operation of the system, all other blast gates/ventilation hoods in the laboratory was always firmly closed during calibration of the system and during all subsequent experiments.

On any given day, a total number of one to four experimental runs were performed, the number depending on start-time, duration of each run, potential problems encountered during each day, etc. A master list of run order and parameter settings was posted in the welding laboratory, and all input values for each run were continuously verified against this list. A package of extensive recording sheets was used, where all parameters for each run, filter IDs, pump IDs, electrode weights, etc. were recorded.

Operators were instructed to wash their hands prior to handling any filter media. Nitrile gloves were to be worn and all filter media were handled using clean tweezers. A separate clean work area was setup for filter handling where a covered lab bench provided a clean environment. Here, each of the four samplers was loaded with proper filter media. Before and after each run, filter media were stored in Petri dishes labeled with filter ID, run number, and date. Upon loading a filter into a sampler, the corresponding filter ID was noted in the appropriate field on the recording sheets. A second operator verified the filter IDs.

Each filter was paired with an appropriate pump. Each sampler-pump assembly was then calibrated using a primary flow meter (BIOS Dry-Cal, model DC-Lite; Bios International Corp,

Butler, NJ): the first five readings (of which each is an average of ten instrument readings) were recorded to allow for the instrument to stabilize, the subsequent ten readings were recorded to determine the pre-run pump flow rate. An external breathing unit serves the filter cassette located in the manikin's head.

The power supply to the welding unit was always shut off at the wall switch in-between runs. Before each run, the welding machine ground cable connection to the positioner was checked to ensure tightness and thus adequate and safe contact. The welding gun was placed inside the chamber within reach of the welder.

The travel speed of the positioner was kept at a constant setting of 1.3, equivalent of a weld speed of about 11.7 – 17.5 cm/min. The varying weld speed was due to the fact that the welds were placed in a circular pattern with decreasing radius. The welding machine control panel was marked using colored tape to ensure consistent and precise setting of the welding amperage for each run.

The manikin outfit was modified to ensure consistent placement of each sampler throughout experiments. Photos were used for further comparison and for ensuring compliance of sampler placement in previous runs. The samplers were checked to ensure that the sampler inlet was always facing outward, including the sampler inside the helmet. The manikin's posture was adjusted for each run and secured with bolts. A guide for the torso angle was attached to the manikin's seat post and verified using a protractor. The head angle was determined by measuring the gap in the "neck" between the torso and the head with the following criteria:

Attaching straps to the manikin's head and seat post secured the position of the head of the manikin. The manikin's position inside the chamber was made permanent by bolting the seat post to the massive frame of the chamber. This position was verified on a regular basis to ensure a distance of 27.9 cm (11 in) from seat post to the anchor point. The manikin operating parameters (breathing rate and volume) were noted on the recording sheets and corresponding values were set in the control software. All hose connections were checked to verify proper setup of the manikin.

The welding operator followed a careful and systematic scheme to ensure proper operation of the system. With the power off an electrode was placed in the welding gun. During exposure chamber experiments, the operator ensured that the manikin's helmet was in welding position (down) and that all sampler locations remained intact. At the operator's signal, the welding machine was turned on. At all times, the welding time (also known as the arc time) was recorded using a stopwatch. The welding time for each electrode was recorded, as was the welding amperage as measured on the welding machine, as well as the manikin torso and head temperatures at the end of each electrode welding time. After each electrode, the welding machine was shut off to ensure safety for the operator to (1) drop the electrode stub into a container, (2) to flip the manikin's welding helmet into an "up" position, and (3) to load a new electrode in the welding gun.

Throughout each experimental run, the welding operator was responsible for maintaining consistent welds, while the other operator(s) were responsible for monitoring all equipment to ensure proper operation of pumps, manikin temperature, etc. and for recording experimental data.

Upon achieving a desired welding time for a given experiment, the welding machine was switched off. All sampling equipment was allowed to run for one additional minute, whereupon they were all switched off and the total sampling time and the stop time were recorded. The orifice pressure drop reading was also recorded. After an additional two minutes to allow all fume to be ventilated from the chamber, the rear chamber door was opened and all samplers retrieved, including the manikin filter cassette within the manikin's head. The samplers were then allowed to cool down before repeating the calibration described in the pre-run procedure. All filter media were then removed from the samplers using the same, rigorous protocol.

When disassembling the samplers to retrieve the filters, much care was put into not losing any mass from the filters. The filter media was handled solely with clean tweezers and immediately placed in Petri dishes. The Petri dishes were then lined up next to each other on a white background to allow for thorough visual evaluation. Observations such as color of sample, degree of load, and possible loose particles were recorded in data recording sheets for qualitative evaluation. At the end of each day, all used filters were put back into a desiccator for at least one week, before being post-weighed according to the same protocol.

2.3.7 Mass Concentration Calculation

The fundamental metric of the construction of mass-based PSD is the mass concentration (mg/m^3) of welding aerosol measured during the experiment. The mass concentration is calculated by:

$$M = \frac{m \cdot k}{Q \cdot t} \quad \textbf{Eq 4}$$

where

M = mass concentration (mg/m^3)
m = mass gain on filter (mg)
Q = flow rate of air sampling instrument (lpm)
t = sampling time of experiment (min)
k = conversion factor (10^3 L/m^3)

A mass concentration is calculated for each stage of the cascade impactor for each experiment conducted. Each set of experiments in the two systems (emission and exposure) had four replicates. The average of each particle size fraction across all four replicates was used to calculate the average mass concentration, which formed the basis of PSD data shown below.

2.3.8 Estimation of Particle Size Distribution Parameters

To estimate the PSD parameters, log-probability plots of cascade impactor data were created using Microsoft Excel spreadsheet software. The general method for creating a log-probability plot is to: 1) Calculate the mass-based concentration for each impaction stage with a given 50% cut-off point aerodynamic diameter (μm); 2) Sort the concentrations from lowest stage (smaller particle size) to highest stage (larger particle size); 3) Sum all mass-based concentrations across stages together to calculate the total mass-based concentration; 4) Divide each stage-specific mass-based concentration by the total mass concentration to calculate percent mass for each particle size fraction; 6) Consecutively, sum the percent mass fractions to obtain the cumulative

percent mass fraction for each stage; 7) Convert the cumulative percent mass fractions (as probabilities) to a z-score (i.e., inverse of standard normal cumulative distribution) using the "NORMSINV()" function; 8) Plot the z-score on the x-axis against the particle size on the y-axis on a logarithmic scale. Once the log-probability plot is created, a visual interpretation of linearity must be performed. If the data follow a linear trend, log-normality of the distribution may be assumed and a best fit line may be applied to the data. The MMD may be represented by the intercept and the GSD represented by the exponential transformation of the slope. If the data does not prove linear when plotted, then a different distribution or bimodal/multi-modal distribution may be present.

The bimodal log-normal distribution has been described previously (de Ruiter & Oeseburg, 1987) can be defined mathematically as:

$$\psi(d) = \frac{\gamma_1}{d\sqrt{(2\pi)\ln\sigma_{g1}}}\exp\left[\frac{-(\ln d - \ln d_{g1})^2}{2\ln^2\sigma_{g1}}\right] + \frac{\gamma_2}{d\sqrt{(2\pi)\ln\sigma_{g2}}}\exp\left[\frac{-(\ln d - \ln d_{g2})^2}{2\ln^2\sigma_{g2}}\right] \quad \textbf{Eq 5}$$

Where

$\psi(d)$ = probability density,
γ_1 = weight factor for first subdistribution,
γ_2 = weight factor for second subdistribution,
d_{g1} = geometric mean of first subdistribution,
d_{g2} = geometric mean of second subdistribution,
σ_{g1} = geometric standard deviation of first subdistribution,
σ_{g2} = geometric standard deviation of second subdistribution.

The factors, γ_1 and γ_2, add up to unity, so the probability density function is normalized. This implies that the distribution is fully described by means of five parameters (de Ruiter & Oeseburg, 1987). Estimating the parameters of the bimodal distribution is not as straight forward as the log-probability plot method and requires the aid of computer software. One such approach has been described previously (Phillips, Esmen, Hall, & Lynch, 2004) and is used here to estimate the bimodal parameters of the measured size-fractionated welding fume concentration data. The method involves adjusting the derivatives to minimize the residuals of the likelihood function. The software is developed and run using the Microsoft QuickBasic software.

Although log-probability plots are the easiest method to determine PSD parameters, care must be given to the limitations of the method. Because of the expansion of the scale at the upper and lower portions of the log-probability plot, an error in cumulative frequency is about four times wider on the graph at 5% and 95% (z-score = -1.96 and 1.96, respectively) than it is at 50%. The rule of thumb for fitting a straight line on a log-probability plot is to give the most weight to the data points lying in the range extending from 20% to 80% probability (z-score = ±0.84) and little weight to the points lying less than 5% and greater than 95% regions. Least squares regression for the entire data set is not recommended for this application because it overemphasizes the tails of the distribution (Hinds, 1999b).

2.4 Results

Raw data generated from the scientific experiments is presented in the Appendix. Experimental data presented in this section represent average mass-based concentrations (i.e., average of four replicates) measured using each aerosol sampler (ELPI, MOUDI and PCIS) within each experimental system.

2.4.1 Mass-Based Particle Size Distribution of Welding Fume

The size-fractionated mass-based concentrations measured during the isokinetic emission and exposure chamber experiments are presented in TABLE II and TABLE III, respectively. During the emission chamber experiments, while the total mass-based concentration measured by the ELPI was 6.8 mg/m^3, experiments with MOUDI resulted in lower total mass-based concentration measurement of 4.4 mg/m^3. During exposure chamber experiments, the total mass-based concentration measured using the ELPI was 5.0 mg/m^3, whereas the same measured obtained using the MOUDI was much lower, 0.7 mg/m^3. The log-probability plot of particle size distribution data generated using the ELPI and the MOUDI in the emission and exposure chamber experiments is presented together in Figure 9 and Figure 10, respectively.

TABLE II: MASS CONCENTRATIONS FROM EMISSION CHAMBER

ELPI		MOUDI	
Particle Size (μm)	**Conc. (mg/m³)**	**Particle Size (μm)**	**Conc. (mg/m³)**
0.028	0.04	0.010	0.02
0.055	0.04	0.056	0.05
0.094	0.07	0.100	0.08
0.157	0.20	0.180	0.78
0.266	1.22	0.320	1.33
0.387	3.14	0.560	1.35
0.622	1.42	1.00	0.50
0.961	0.26	1.80	0.09
1.62	0.08	3.20	0.08
2.42	0.11	5.60	0.05
4.05	0.06	10.0	0.04
6.77	0.06	18.0	0.07
10.04	0.05	-	-
Sum	6.76	Sum	4.45

TABLE III: MASS CONCENTRATIONS FROM EXPOSURE CHAMBER

ELPI		MOUDI	
Particle Size (μm)	**Conc. (mg/m³)**	**Particle Size (μm)**	**Conc. (mg/m³)**
0.028	0.03	0.010	0.02
0.055	0.09	0.056	0.00
0.094	0.06	0.100	0.01
0.157	0.13	0.180	0.09
0.266	0.66	0.320	0.26
0.387	2.08	0.560	0.21
0.622	1.02	1.00	0.03
0.961	0.32	1.80	0.01
1.62	0.15	3.20	0.01
2.42	0.12	5.60	0.00
4.05	0.12	10.0	0.02
6.77	0.13	18.0	0.03
10.04	0.08	-	-
Sum	5.01	Sum	0.69

Upon inspection of the log-probability plots (Figure 9 and Figure 10), it is observed that the data are not linear and the PSD parameters may not be interpreted from a best-fit line through the center region of the data (i.e., 20%-80%). However, the data do fit a bimodal lognormal distribution and the parameters of this distribution were estimated using the software application of Phillips, Esmen et al. 2004 (as described in section 0). The generated lognormal bimodal distribution parameters are presented in **TABLE** IV and associated models for each distribution are plotted in Figure 9 and Figure 10 for the emission chamber experiments and the exposure chamber experiments, respectively.

TABLE IV: PARAMETERS OF BIMODAL LOGNORMAL MASS-BASED CONCENTRATION DISTRIBUTION

Sampler/System	d_{g1} (μm)	σ_{g1}	d_{g2} (μm)	σ_{g2}	γ_1	γ_2
ELPI Emission	0.30	1.50	2.60	2.80	0.94	0.06
ELPI Exposure	0.30	1.36	1.39	3.30	0.80	0.20
MOUDI Emission	0.27	1.60	1.90	3.50	0.90	0.10
MOUDI Exposure	0.27	1.55	4.50	3.56	0.88	0.12
Average	0.29	1.50	2.60	3.29	0.88	0.12

The bimodal parameters estimated using the particle size distribution data generated by operating each instrument under both emission and exposure chamber experimental conditions are similar. The MMD of the first mode (d_{g1}) for all distributions is virtually identical where a median aerodynamic diameter of 0.30 μm and 0.27 μm was obtained using the ELPI and the MOUDI in both chambers, respectively. Similarly, the GSD for the primary mode (σ_{g1}) is very close to one another across instruments and experimental systems albeit slightly smaller GSD for the data generated by operating the ELPI (1.50 for emission chamber; 1.36 for exposure chamber) as compared to those generated by operating the MOUDI (1.60 for emission chamber; 1.55 for exposure chamber). However, these results should be interpreted with caution due to small sample size. The MMD (d_{g2}) and the GSD (σ_{g2}) of the minor second mode is more variable across instruments and experimental systems.

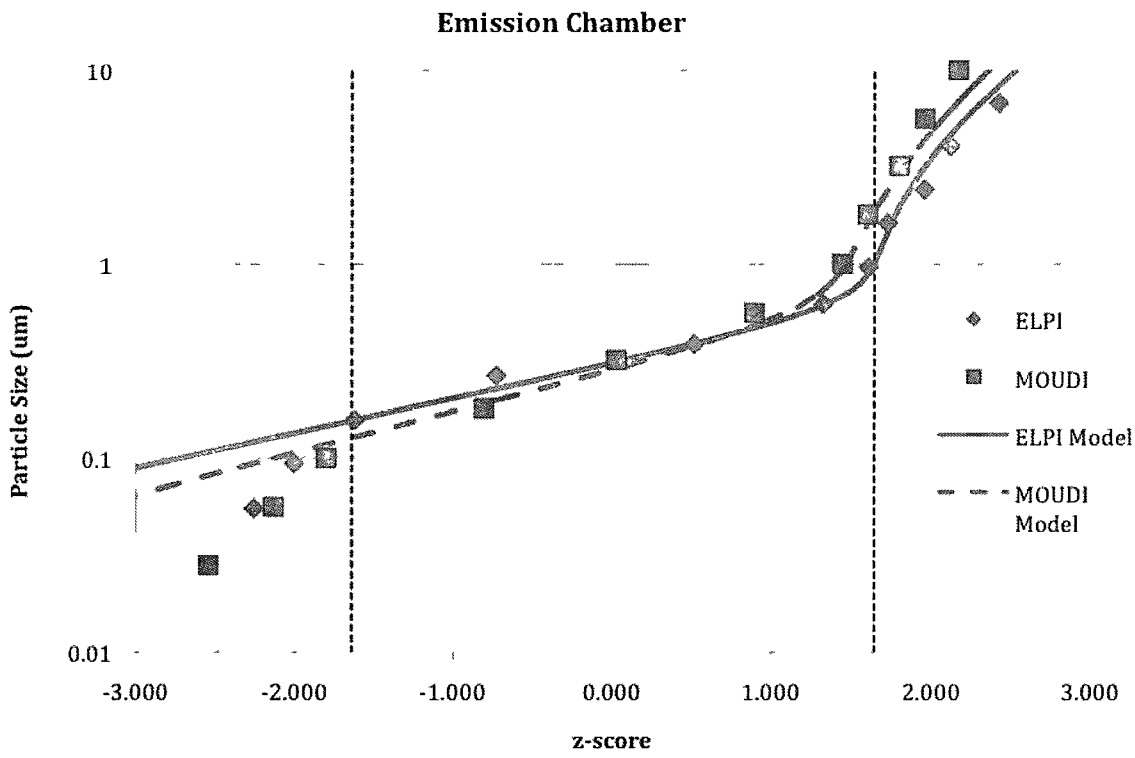

Note: Dashed lines represent lower and upper 5% of mass-based concentration distribution

Figure 9: Log-probability plot, emission chamber.

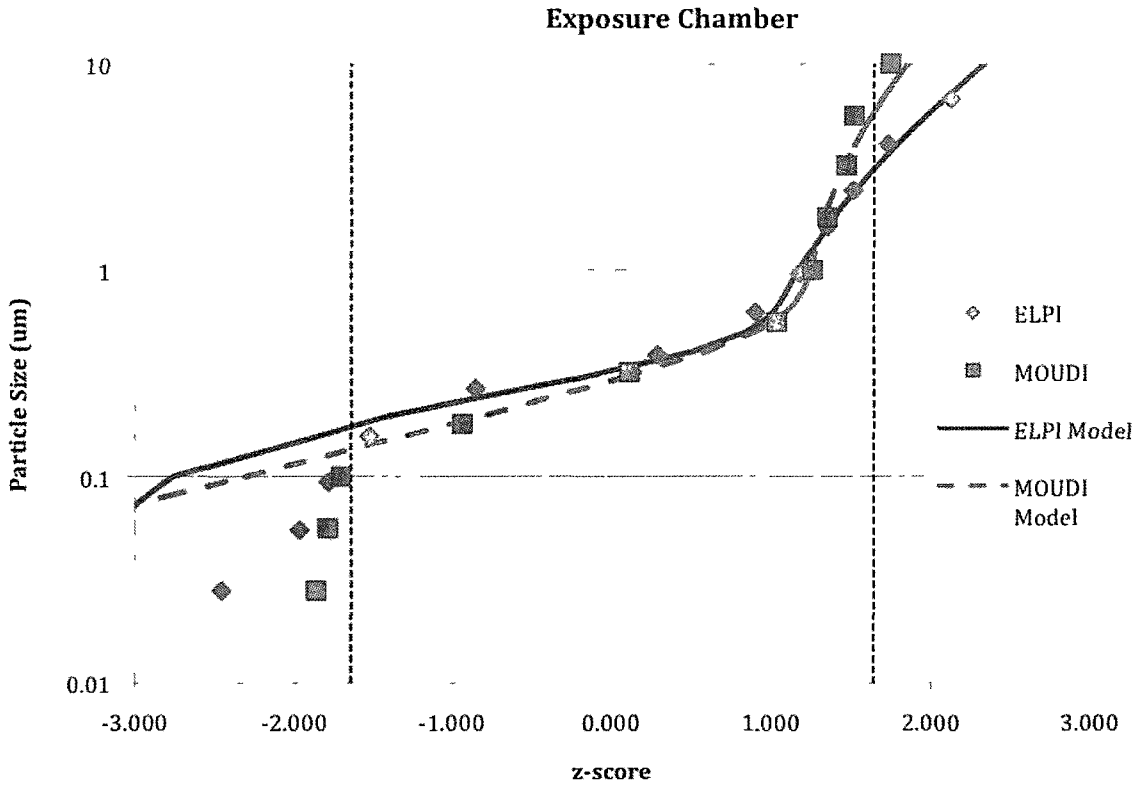

Note: Dashed lines represent lower and upper 5% of mass-based concentration distribution

Figure 10: Log-probability plot, exposure chamber.

The log-probability plots (Figure 9 and Figure 10) demonstrate that the bimodal distribution model used predict the measured data relatively well for the upper 95% of the distribution and estimated distribution parameters are not substantially different from one another across experimental systems. Thus, the numerical parameters were averaged across all instruments and experimental systems to define an aggregate bimodal distribution that represents all collected data (**TABLE** IV). The log-probability plot of the aggregate mass-based concentration data across all instruments and experimental systems along with the aggregate distribution parameters model is presented in Figure 11.

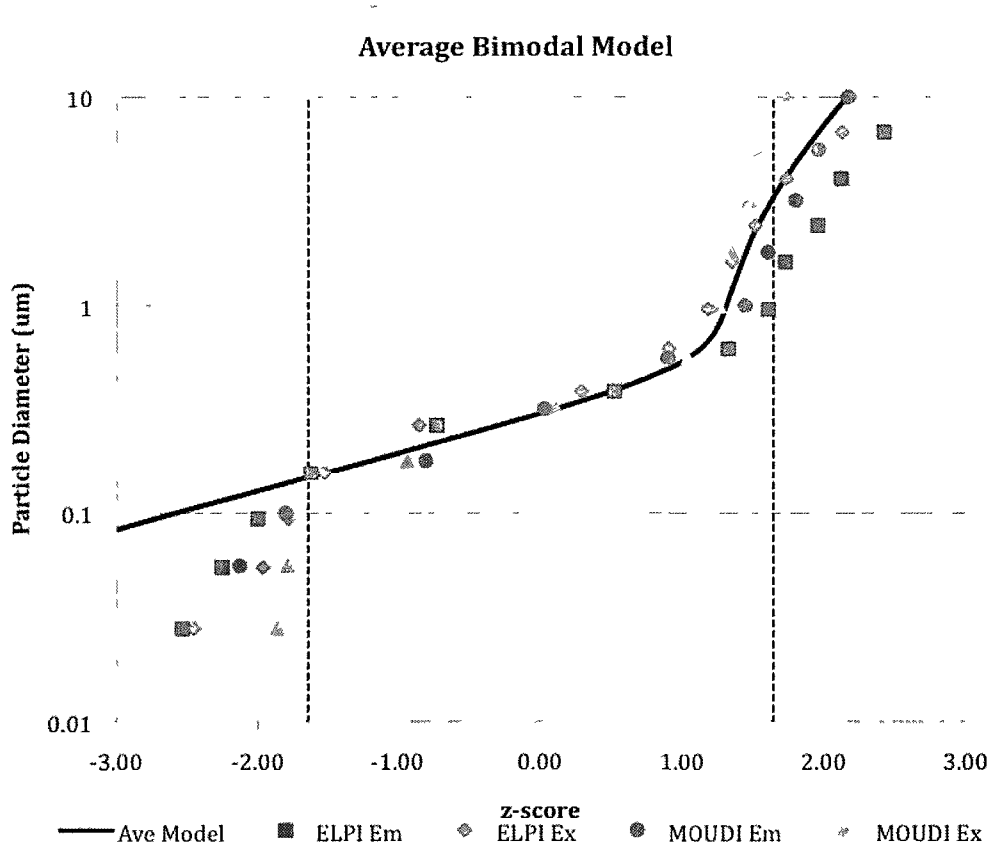

Note: Dashed lines represent lower and upper 5% of mass-based concentration distribution.

Figure 11: Log-probability plot average model.

Using the aggregate bimodal distribution parameters and the probability density function given in Eq 4, the percent contribution of a given particle size fraction to the overall mass-based concentration distribution is calculated. It is found that particles less than 3.35 μm in aerodynamic diameter account for 95% of the total mass, particles less than 1.0 μm in aerodynamic diameter account for 90.4% of the total mass and particles less than 0.15 μm in aerodynamic diameter

account for 5% of the total mass of the distribution. The model predicts that only 0.5% of the total mass would be contributed by particles less than 0.1 μm in aerodynamic diameter. However, cumulative fraction contributed by the same size particles account for approximately 3.5% of the total mass-based concentration based on measured data.

Data gathered from the PCIS sampler were not grouped along with the data from the ELPI and the MOUDI because the number of impaction stages in this instrument is substantially less than that of the ELPI and the MOUDI. The PCIS only has five stages and subsequently only four points available for construction of the log-probability plot of the mass-based concentration distribution (

). Despite the lack of particle size-fraction resolution associated with the PCIS, a similar methodology followed since this instrument cost significantly less than other cascade impactors utilized in this research and, thus, may capture greater market place and practical application for exposure assessment of welders. A bimodal lognormal fit was found to be the most representative of the PCIS data. The parameters of this bimodal lognormal distribution were again estimated using the computer software of Phillips, Esmen et al. 2004 and results are presented in **TABLE** V. Parameter estimates are similar to those obtained using the MOUDI and the ELPI, except for the d_{g1} (0.25 μm), which is slightly lower than that estimated by the ELPI and the MOUDI. Using the estimated parameters, we calculated that particles less than 0.55 μm in diameter account for 95% of the mass of the distribution, particles less than 1.0 μm in aerodynamic diameter account for 97.06% of the total mass and particles less than 0.14 μm in aerodynamic diameter account for 5% of the total mass of the distribution. The model predicts that only 0.0001% of the total mass would be contributed by particles less than 0.1 μm in aerodynamic diameter.

TABLE V: PCIS AVERAGE PSD PARAMETERS

d_{g1} (μm)	σ_{g1}	d_{g2} (μm)	σ_{g2}	γ_1	γ_2
0.25	1.42	1.3	3.3	0.95	0.05

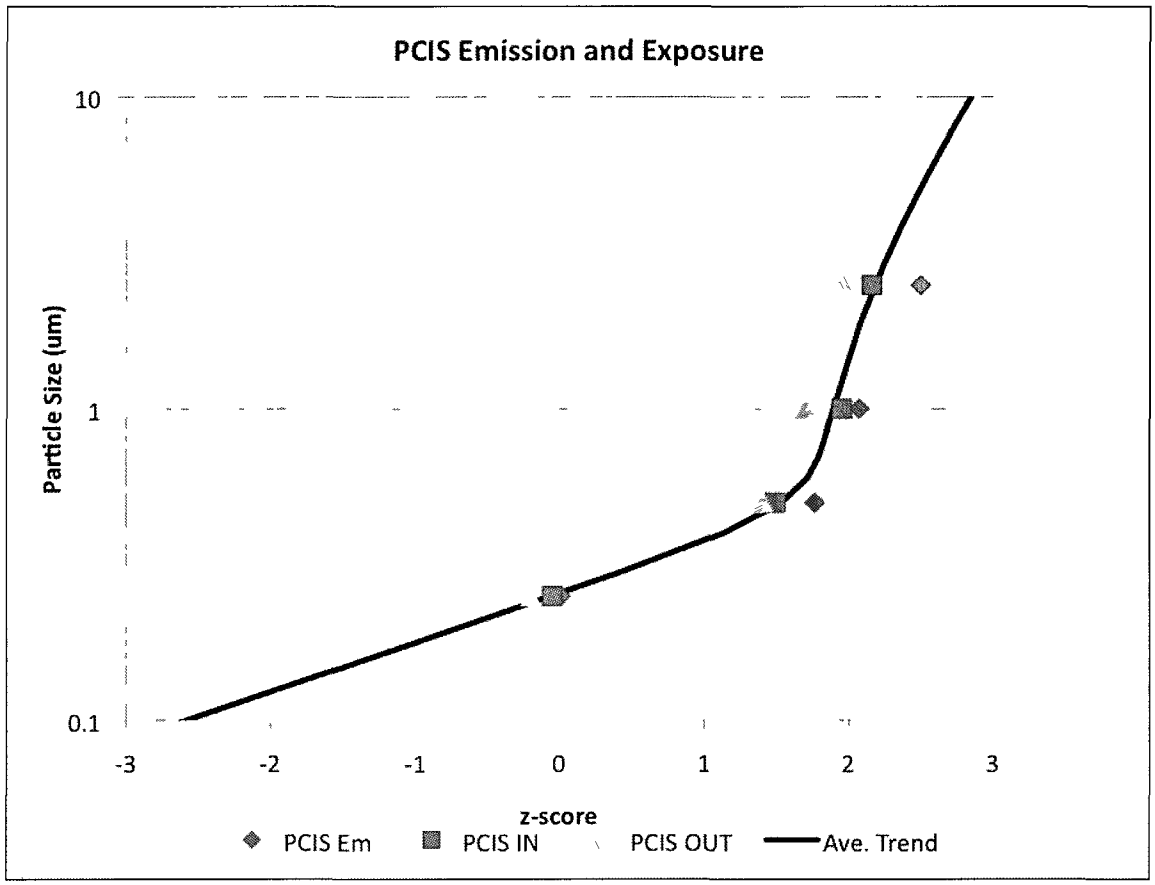

Figure 12: PCIS log-probability plot.

2.4.2 Real-time Number Concentrations

The ELPI was used to measure real-time number concentrations and count distributions of welding fume within the breathing-zone of the manikin. Nine experiments were conducted to explore the relationship between particle number concentration and electrode diameter 2.4 mm, 3.2 mm, 4.0 mm along with amperage setting (low [60, 90, 110], medium [70, 100, 120], high [80, 110, 130]). Summary statistics of total number concentrations measurements are presented in **TABLE** VI and Figure 13.

TABLE VI: TOTAL NUMBER CONCENTRATION BY ELECTRODE SIZE AND AMPERAGE

Electrode Size (mm)	Amperage (A)	Sample Size	Average Number Conc. (#/cm3)	Standard Error (#/cm3)	Maximum Conc. (#/cm3)	Minimum Conc. (#/cm3)
2.4	60	18	4.64E+04	6.00E+03	8.26E+04	1.81E+04
2.4	70	36	5.91E+04	7.06E+03	1.77E+05	2.50E+04
2.4	80	27	1.67E+05	1.87E+04	3.79E+05	4.82E+04
3.2	85	17	1.02E+05	1.11E+04	3.67E+05	2.69E+04
3.2	95	13	1.09E+05	1.11E+04	2.50E+05	4.32E+04
3.2	105	13	1.80E+05	1.76E+04	8.00E+05	5.55E+04
4	110	7	2.12E+05	2.02E+04	3.93E+05	9.98E+04
4	120	9	2.20E+05	2.01E+04	8.92E+05	7.54E+04
4	130	7	2.78E+05	2.44E+04	5.03E+05	9.38E+04

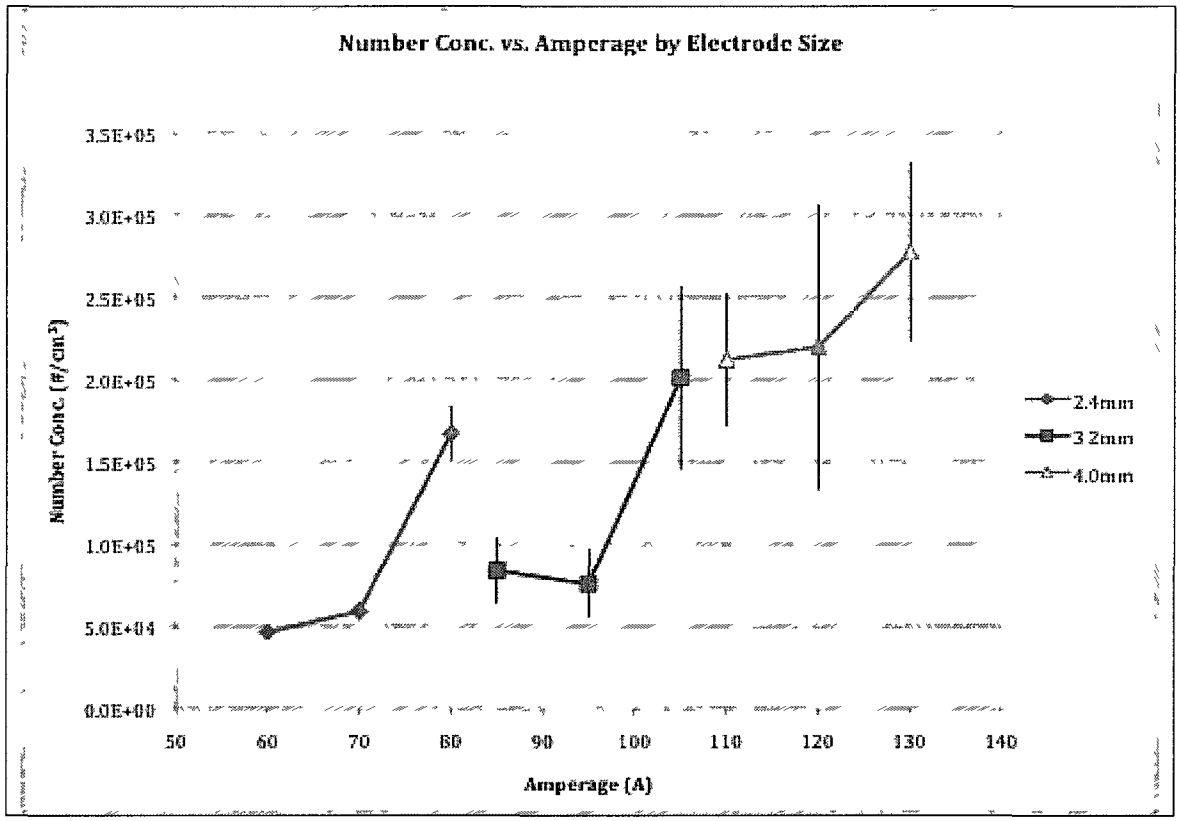

Note: Bars represent standard error around mean.

Figure 13: Number concentration by amperage and electrode size.

The average total number concentration ranged from 4.64E+04 particles per cm^3 (2.4 mm electrode, low amperage [60A]) to 2.78E+05 cm^{-3} (4.0 mm electrode, high amperage [130A]). When at low and medium amperage settings, the total number concentrations increased slightly for 2.4 mm and 4 mm electrodes, yet decreased slightly for 3.2 mm electrodes. The high amperage setting for all electrode sizes increased the measured number concentration substantially over the low and medium settings. Use of large diameter electrodes in welding results in the highest particles number concentrations in the breathing-zone as shown in Figure 8. The 2.4 mm and 3.2 mm electrodes when set to low and medium amperage generally experience similar average number

concentrations. Increasing the amperage to the high setting increases the number concentration despite electrode size. Thus, number concentration as a metric for exposure is more sensitive to amperage of welding current used than the electrode size.

With the data obtained by ELPI, real-time count-based particle size distribution can be constructed. The results of the count PSD measurements made with the ELPI are presented in **TABLE** VII. A log-probability plot (Figure 14) is constructed to determine the parameters of the size distribution. The visual inspection of the plot reveals a non-linear distribution and data are assumed bimodal. The bimodal parameters are estimated using computer software of Phillips, Esmen et al. 2004.

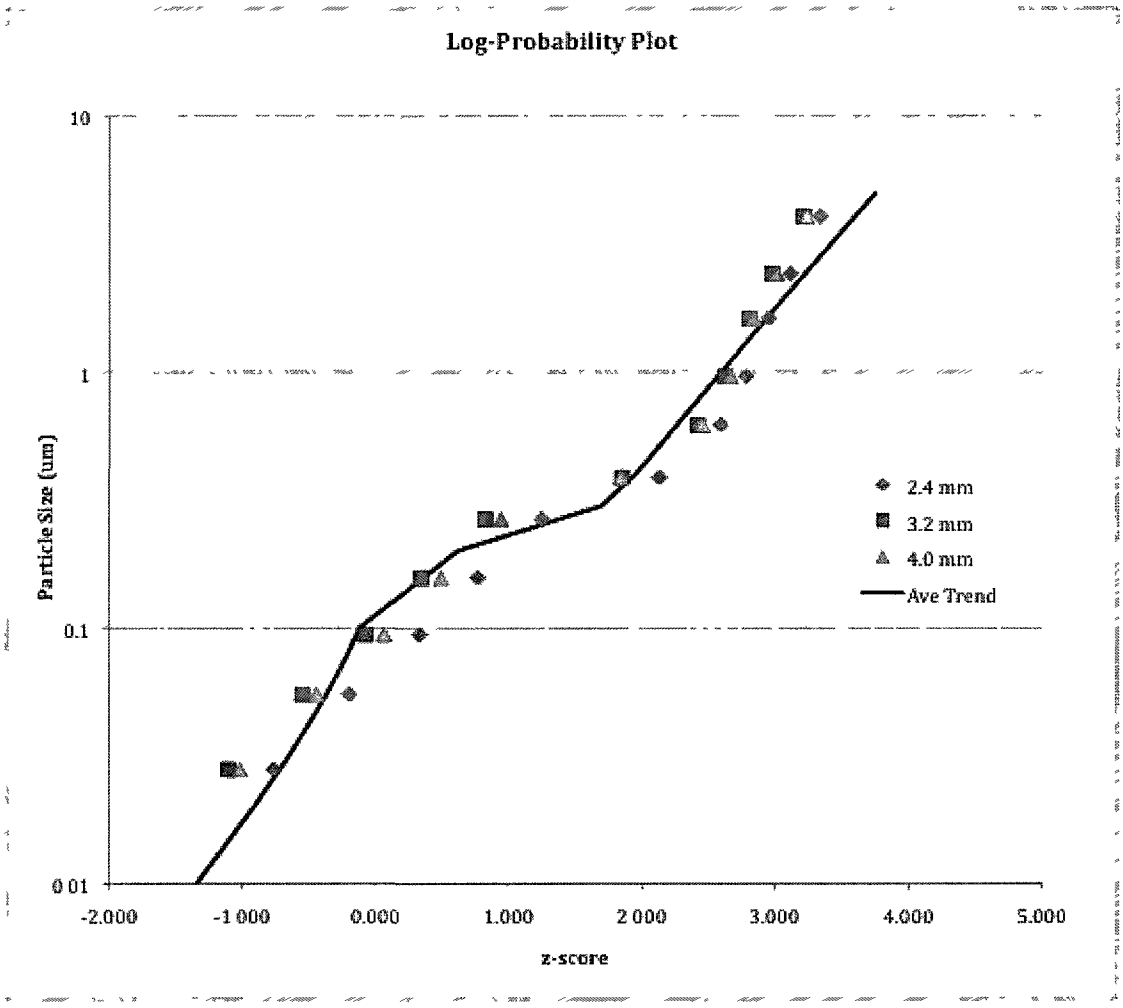

Figure 14: Log-probability plot count size distribution.

TABLE VII: NUMBER CONCENTRATIONS BY PARTICLE SIZE

Electrode Diameter (mm)	2.4	2.4	2.4	3.2	3.2	3.2	4.0	4.0	4.0
Amperage (A)	60	70	80	85	95	105	110	120	130
Particle Size (μm)									
0.028	8.80E+03	1.49E+04	3.83E+04	1.20E+04	1.79E+04	2.25E+04	3.61E+04	2.89E+04	4.55E+04
0.055	7.25E+03	1.25E+04	3.86E+04	1.56E+04	2.05E+04	2.34E+04	3.95E+04	3.72E+04	4.62E+04
0.094	8.84E+03	1.27E+04	3.56E+04	1.77E+04	2.19E+04	2.86E+04	4.64E+04	3.99E+04	5.27E+04
0.157	7.45E+03	8.15E+03	2.35E+04	1.63E+04	1.82E+04	2.89E+04	3.57E+04	3.50E+04	4.40E+04
0.266	6.92E+03	5.67E+03	1.70E+04	1.70E+04	1.38E+04	3.34E+04	2.63E+04	3.20E+04	3.97E+04
0.387	6.05E+03	4.38E+03	1.19E+04	1.96E+04	1.37E+04	3.71E+04	2.30E+04	3.75E+04	4.04E+04
0.622	8.02E+02	5.46E+02	1.64E+03	2.98E+03	1.97E+03	4.70E+03	3.85E+03	7.60E+03	7.26E+03
0.961	1.36E+02	1.04E+02	2.99E+02	3.80E+02	2.77E+02	8.34E+02	5.77E+02	8.35E+02	9.58E+02
1.62	7.09E+01	6.14E+01	1.50E+02	1.82E+02	1.49E+02	4.72E+02	2.94E+02	3.99E+02	4.67E+02
2.42	4.22E+01	3.57E+01	8.47E+01	1.02E+02	8.56E+01	2.78E+02	1.66E+02	2.45E+02	2.77E+02
4.05	3.25E+01	2.78E+01	5.98E+01	8.31E+01	6.02E+01	1.91E+02	1.16E+02	1.81E+02	2.08E+02
6.77	2.82E+01	2.41E+01	5.18E+01	7.88E+01	5.19E+01	1.42E+02	1.01E+02	1.53E+02	1.82E+02
Total	4.64E+04	5.91E+04	1.67E+05	1.02E+05	1.09E+05	1.80E+05	2.12E+05	2.20E+05	2.78E+05

Note: All values are in #/cm^3

Because the count distributions do not differ substantially as a function of electrode diameter or amperage setting, a single set of bimodal parameters (**TABLE** VIII) is used to describe all data generated. The particle count data reveal presence of two types of particle distributions (i.e., the two subdistributions) within the breathing-zone of the manikin. The first subdistribution is composed of very small particles, most likely the particles forming from the condensation of metal vapors. The second subdistribution is composed of still very small particles but about one order of magnitude larger, which may be an indication of agglomeration taking place in the breathing-zone.

TABLE VIII: BIMODAL COUNT DISTRIBUTION PARAMETERS

d_{g1} (μm)	σ_{g1}	d_{g2} (μm)	σ_{g2}	γ_1	γ_2
0.04	3.80	0.20	1.20	0.6	0.4

During these experiments, the ELPI is continuously measuring particle concentration over time during the actual process of welding. The particles sampled will include those generated at the beginning of the test (i.e., as soon as the arc is struck) and those having aged in the breathing zone/chamber before being sampled. Thus, the two observed underlying distributions here are most likely caused by simultaneously sampling of the condensation mode and coagulation mode of particle generation from welding.

2.4.3 Calculation of Particle Charge

The ELPI measures charge of particles that impact on a given stage with its electrometers. When the corona charger is turned on, a known charge is placed on the incoming particles and the electrometer signals detected are integrated and corrected to calculate a particle concentration metric. When the corona charger is turned off, the electrometers are still recording electric signals, however, without a point of reference that detected signal is difficult to interpret. If it is assumed that the number concentration of the aerosol remains relatively constant throughout a brief sampling period, then an experiment where the charger is turned on to measure number concentration and then turned off to measure inherent particle charge can be conducted and results used to calculate a given charge per particle.

During the number concentration experiments, a few of the electrodes burned were used to develop the charge per particle data. The ELPI corona charger was pulsed on and off for approximately 10 seconds and the measured number concentrations with charger on were used in conjunction with the inherent charge measured when the charger was off to calculate the charge per particle.

The particle charge calculations were made as follows:

$$q = \frac{E \cdot t_p}{60 \cdot C \cdot Q} \quad \textbf{Eq 6}$$

where:
q = median charge per particle (fC)
E = ELPI electrometer response (fA = fC/s)
t_p = pulse time (s)
C = number concentration (#/cm3)
Q = flow rate (cm3/min)

The median charge per particle was then divided by the elementary charge e (1.6 x 10-19 C) to obtain the median magnitude charge q/e. Results of the particle charge calculations as presented in TABLE IX. Results reveal that particle charge is close to neutral for the lower impactor stages corresponding to the particles less than 1 μm in aerodynamic diameter. Particles larger than this exhibit an increasing magnitude charge.

TABLE IX: MEDIAN MAGNITUDE PARTICLE CHARGE PER STAGE

Electrode Size (mm)	2.4	2.4	2.4	3.2	3.2	3.2	4.0
Amperage (A)	60	70	80	85	95	105	110
Particle Size (μm)							
0.028	0.01	0.01	0.02	0.01	0.01	0.01	0.01
0.055	0.04	0.03	0.05	0.03	0.04	0.04	0.03
0.094	0.12	0.09	0.16	0.08	0.10	0.10	0.08
0.157	0.28	0.23	0.35	0.17	0.17	0.22	0.16
0.266	0.93	0.81	0.70	0.30	0.21	0.46	0.38
0.387	2.39	1.92	1.34	0.48	0.27	1.00	1.15
0.622	1.71	2.04	0.87	0.55	0.10	1.15	2.23
0.961	10.85	6.70	4.44	0.96	1.37	0.94	1.25
1.620	29.91	8.43	12.09	2.73	2.82	3.59	3.33
2.420	68.19	23.84	24.80	6.81	4.83	7.98	6.46
4.050	213.18	25.14	46.38	6.88	9.29	14.27	10.78
6.770	1661.60	26.54	61.85	10.19	16.82	24.76	17.78

Values in # of elementary charges (electrons)

The relationship between median magnitude charge per particle and aerodynamic diameter can be described by a power function (Eq 3). The average magnitude charge per particle across all electrode size experiments was calculated and used to plot the particle charge to aerodynamic diameter relationship (see Figure 15). Using this plot, the parameters A and n are calculated as approximately 5 and 1.7, respectively. Very little variability on particle charge measurements is observed in particles les than 1 μm in aerodynamic diameter, while large variability is observed in larger size particles.

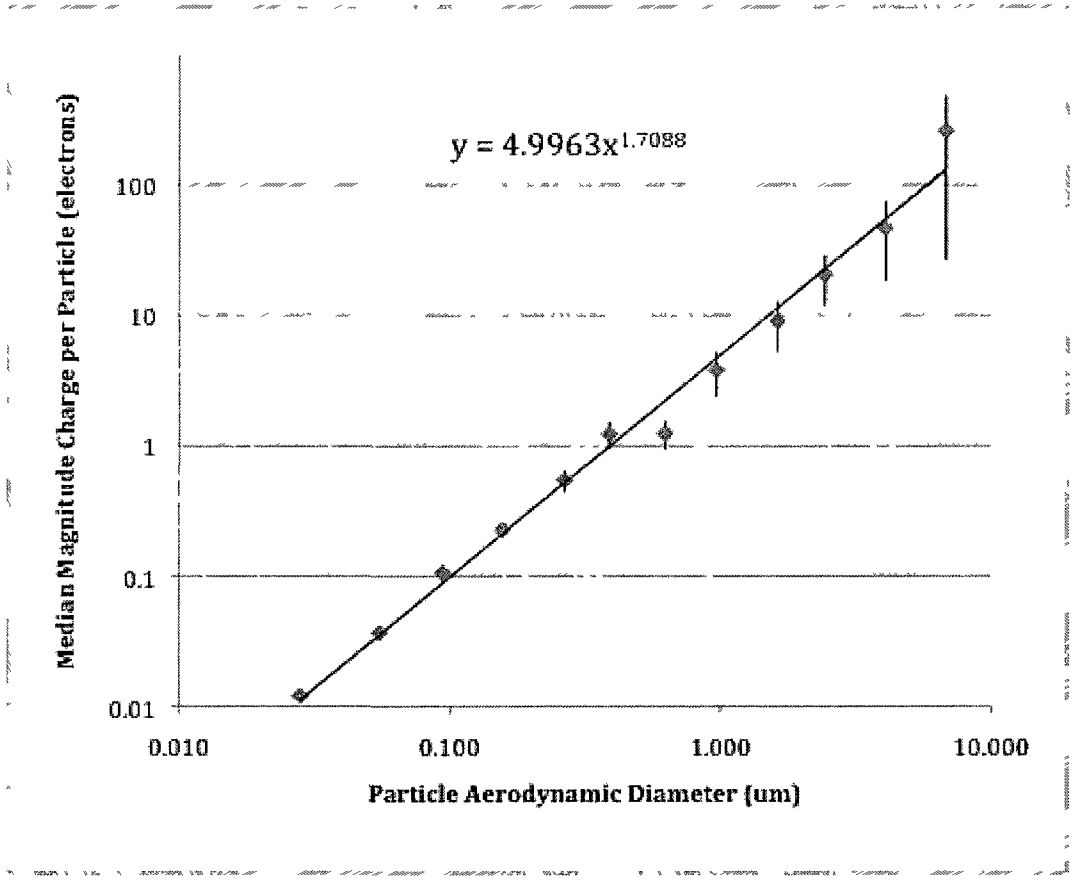

- Bars represent standard error around the mean.

Figure 15: Particle charge versus particle size.

2.5 Discussion

2.5.1 Mass Distributions

Measurements of the mass-based PSD of welding fume were performed in a laboratory-based emission chamber and exposure chamber. The most significant finding of these experiments is that the mass-based concentration distributions are bimodal in nature. Other researchers

reported the same finding in the literature (N. T. Jenkins, et al., 2005; Stephenson, et al., 2003; Surya Narayana, Sundararajan, Subramanian, Manjula, & Vijaya Kumari, 1995; A. T. Zimmer, et al., 2002; Zimmer & Biswas, 2001) and, possibly, trimodal distributions (Berner & Berner, 1982). Other reports of the mass-based PSD have only estimated parameters of unimodal lognormal distributions to date (Paul Hewett, 1995; Isaxon, et al., 2009b; Sowards, et al., 2008; Stephenson, et al., 2003). The reasons for the modal differences in reported PSD parameters are unclear but a few notable parameters may be influential. First, differences in methods used in PSD parameter estimation may explain the difference between unimodal and bimodal measurements observed in the literature. For instance, Hewett (1995) used a MOUDI and Sowards and Lippold (2008) used an ELPI, but instead of using log-probability plots both researchers estimated parameters from visual interpretation of distribution histograms. When investigating the distributions of the histograms, the coarse mode may be difficult to identify since it is small compared to the rest of the distribution. Relatively little mass is collected on the coarse stages of the cascade impactors and, therefore, this mode may be dismissed as non-significant. Other researchers like Stephenson (2003) and Jenkins (2005) used an Andersen impactor and plotted data on the log-probability graphs. Here, the inflection point of the curve is much more easily identifiable, resulting in a multi-modal distribution finding.

Although underlying particle formation mechanisms will be discussed in a greater detail below, the source of each mode is considered briefly in this discussion. In regards to the mass-based distribution, the smaller particle size mode (i.e., MMD = 0.29 μm) capture the condensation mode (i.e., the particles forming from the condensation of metal vapors) and the agglomeration of these primary particles; whereas the coarse particle size mode (i.e., MMD = 2.60 μm) capture the particles that have formed as microspatter (i.e., particles originating from the ejection of molten

droplets from the electrode tip). Previous research into microspatter has been conducted on the GMAW and FCAW processes and the general conclusion is that microspatter does not contribute substantially to the overall mass of the welding fume aerosol (Neil T. Jenkins & Thomas W. Eagar, 2005; Quimby & Ulrich, 1999; A. Zimmer, P. Baron, & P. Biswas, 2002). The microspatter arises from disruption and imperfections in the materials and the operation of the welding equipment and its formation is inconsistent and unpredictable (Zimmer & Biswas, 2001). Therefore, it is reasonable to consider the microspatter as a plausible explanation for the inconsistency in observing the coarse mode in welding PSD research as shown by our results. Its transient nature, extreme variability and small contribution to the overall mass (about 5%) of the distribution would explain why this mode is not often recognized in data collected during welding experiments. Further, the FCAW and SMAW processes are more likely to exhibit bimodal nature due to the flux, which creates more variability in the welding process and, thus, in the amount of microspatter formed. More in depth discussion of fume formation mechanisms and specific particle morphologies are presented in subsequent chapters of this dissertation.

2.5.2 Particle Number Concentrations

Measurements of the total particle number concentration within the breathing-zone of the manikin have been performed using the ELPI as a function of electrode size and amperage. The results indicate that low and medium amperage settings for 2.4 mm and 3,2 mm electrodes result in similar total number concentrations. On the other hand, the 4.0 mm electrode exhibits higher particle number concentrations regardless of amperage setting. These results are consistent with the effect that amperage and voltage play in welding emissions that have long been documented in welding fume formation studies (C. N. Gray & P. J. Hewitt, 1982; Gray, Hewitt, & Dare, 1982a; Heile

& Hill, 1975; Speight & Campbell, 1979; Stern, 1977; Voitkevich, 1995). Generally, increasing arc voltage has the impact of increasing the total amount of fume generated depending on the metal transfer mode of the welding process employed. Lower voltages correspond to short circuit transfer where fume forms only when the circuit is broken, thus, a lower fume formation rate. The fume formation, then, peaks with increasing voltage as the metal transfer mode approaches the transition between short circuit and globular transfer and decreases again slightly until spray transfer mode is established. The globular transfer region may be the most appropriate one for this research since SMAW primarily undergoes the globular metal transfer mode (Gray, Hewitt, & Dare, 1983)

Measurements of voltage were not recorded in this research and specific comparisons to metal transfer modes cannot be performed; however, it is probable that the dip in number concentration across the amperage settings shown here represents the transition from globular transfer to spray transfer mode. In this research, we have measured total particle number concentrations between 1.8×10^4 particles per cm^3 and 8.9×10^5 particles per cm^3. Previous studies have reported total number concentrations in the range of 6.8×10^6 particles per cm^3 for globular transfer and 5.4×10^6 particles per cm^3 for spray transfer modes in GMAW (A. Zimmer, et al., 2002).

2.5.3 Count-based Particle Size Distributions

Measurement of the count-based PSD parameters have been performed within the breathing-zone of a breathing thermal manikin intended to simulate the work of an actual welder. Count distributions constructed in this research are bimodal lognormal in nature. Both modes have

smaller diameters in the count-based PSD as compared to the mass-based PSD, as shown in **TABLE X.**

TABLE X: MASS- AND COUNT-BASED PSD PARAMETERS

PSD	d_{g1} (μm)	σ_{g1}	d_{g2} (μm)	σ_{g2}	γ_1	γ_2
Mass Based	0.29	1.50	2.60	3.29	0.88	0.12
Count Based	0.04	3.80	0.20	1.20	0.6	0.4

The only published study that estimated the count-based PSD parameters of SMAW process is the work of Sowards et al. (2010). This study evaluated SMAW electrode characteristics using the ELPI. The researchers found a unimodal lognormal count-based particle size distribution with an MMD of 0.21 μm (GSD = 1.18) for E308-16 electrodes, which agrees well with the second mode observed in our research. The first mode observed in our experiment may be representative of the nucleation mode. The relatively large GSD observed would be consistent with the numerous metal vapor species and numerous ways in which particles may form during this mode of fume formation. It is surprising to find a nucleation mode here under an exposure scenario since nucleation particles are scavenged quickly into agglomerates or grow larger through condensation, however, nucleation modes of the welding aerosol have been documented by Zimmer and Baron (2002) in welding experiments with GMAW in an emission chamber.

Observation of the smaller particle size mode may be a product of the sampling system utilized. For instance, it has been shown that the ELPI performs better with silicon oil treated

impaction plates, which reduces the tendency of particle bounce within the sampler (Yamada, Miyamoto, Tokonami, Shimo, & Yamasaki, 2000). Without treatment, count distributions bias towards smaller particles whereas treatment of impaction foils with silicon gel or oil results in a well-defined lognormal distribution. In our work, silicon treatment of impaction plates was not performed and a bias toward smaller particles, therefore, cannot be ruled out. Future studies of particle count distributions using the ELPI should incorporate greasing of impaction plates.

2.5.4 Particle Charge Measurements

Charge per particle measurements were conducted using the ELPI during a subset of electrodes burned during the count distribution experiments. Particle charge estimates show consistency across all electrode sizes and amperage settings for particles less than 1 μm in aerodynamic diameter. Particles less than 0.1 μm in aerodynamic diameter generally exhibit a near neutral charge. The lower the amperage, the greater the negative charge exhibited in larger particle sizes, however, this relationship is not consistent across electrode sizes. This inconsistency of particle charge measurements may be related to the response of the ELPI electrometers and the number concentration within each aerodynamic size fraction. For instance, stages that exhibit greater number concentrations (i.e., on the order of 10^4 or 10^5 per cm^3), the calculated average charge per particle is low and is in general agreement with previous results. However, when considering the number concentration of those stages greater than 1 μm in aerodynamic diameter (i.e., on the order of 10 or 10^2 per cm^3), the average charge per particle estimates may be suspect inasmuch as there are an insufficient number of particles in this distribution to make an accurate average. Further, as particles pass through the ELPI instrument, particle bounce may be playing a

role in drift of the electrometers response in the upper stages. As more particles impact on those stages and then bounce off, the electrometer records a charge when in fact there is none.

There is general agreement between our results and previous work on welding fume that estimated particle charge of two electrons for particles in 0.2 μm in diameter (J. H. Vincent, et al., 1983). In that work, researchers estimated the coefficient *A* as ~10 and were unable to determine the coefficient n due to the sampling instrumentation difficulties. Here, with the ELPI we have been able to calculate both parameters (A=5; n=1.7) and provided a better characterization of particle charge characteristics in welding. Previous charge per particle research has estimated similar coefficients of median magnitude of particle charge to aerodynamic diameter for rubber dusts and concluded that charging effects will not significantly affect exposure sampling or lung deposition (J. Vincent, 1986). However, since rubber particles differ greatly from welding fume in both size, chemistry and morphology, more detailed evaluation may be warranted in future research.

2.5.5 Experimental Considerations

This research was conducted within two different experimental chambers. First, the emission chamber used in this research is designed to sampling fume under isokinetic sampling conditions. This means that the airflow carrying the particles and traveling through the sampling duct has had sufficient time and distance to homogenize . Further, use of the isokinetic sampling probes ensures that further error is not introduced and samples pulled from the flow stream are representative of the particle concentrations in the incoming air stream. The exposure chamber used in this research is designed to represent a welder performing the welding task and sampling is conducted within the breathing-zone under laboratory-controlled conditions.

There is not a substantial difference in the obtained PSDs between the emission chamber and the exposure chamber. The results gathered here lead to the conclusion that the PSD obtained in the emission chamber is comparable to the PSD obtained in an exposure scenario. This finding is encouraging in terms of the consistency and integrity of the experimental system. In this research and in welding fume aerosol sampling in general, care must be paid to the amount of sampling time. This is even more important when conducting measurements with cascade impactors since samplers may easily become overloaded with too much fume impacting on one or more stages. If this were to occur, results would be much more variable and the consistency seen between chambers might not be observed.

We have used two large cascade impactor instruments (ELPI and MOUDI) to define the PSD of welding fume in two different experimental systems. Each instrument operates on the same fundamental principle of particle aerodynamics and impaction, however, the engineering and manufacturing of the instruments are different. Every air-sampling instrument has its own inherent variability and error associated measurements. These have an impact on the final PSD (Esmen, 2000). The experiments performed in this research offer an opportunity to compare the results of the two instruments. Here, we have not observed considerable differences between the distribution parameters as measured by each instrument. However, small sample size prevents definitive conclusions about our observations. We have also used the PCIS sampler but this instrument obtains a noticeably smaller MMD as compared to that obtained using the MOUDI and the ELPI instruments. The resolution (i.e. number of stages) may be the biggest reason for such a difference because the PCIS is unable to accurately resolve particles in sizes between 0.25 μm and 0.5 μm, the range where the MMD falls with the ELPI and MOUDI. We do, however, see the bimodal nature of the aerosol distribution. Direct comparison between cascade impactors cannot be readily

done because of the errors associated with each cut point of the instrument. Other complicated techniques such as data inversion (Ramachandran, Johnson, & Vincent, 1996) may be useful to determine the adequacy of the PCIS for measuring PSD within the breathing-zone, but the computational requirement for such modeling is beyond the scope of this study.

2.6 Summary

The count-based and mass-based particle size distribution parameters from the SMAW-SS process were obtained in a series of laboratory-controlled studies. Welding fume samples were collected in both an isokinetic emission chamber and an exposure chamber that incorporated a breathing thermal manikin in order to relate previous emission based PSD parameters to those obtained under an exposure scenario. Mass-based PSD parameters were obtained using two ambient-type particle cascade impactors (i.e., MOUDI and ELPI) and a personal cascade impactor (i.e., PCIS) to assess consistency of measurements between instruments. Number-based PSD parameters were obtained using the ELPI in a subset of experiments that explored the effect of welding electrode size and current setting.

The measured mass-based PSD parameters in this research define a bimodal lognormal distribution in both experimental systems. This well-defined bimodal distribution has been suggested previously in some welding characterization studies (N. T. Jenkins, et al., 2005; Stephenson, et al., 2003; Surya Narayana, et al., 1995; A. Zimmer, et al., 2002; Zimmer & Biswas, 2001) but not others (P Hewett, 1995; Isaxon, et al., 2009a; Sowards, et al., 2008). Defining the true distribution as bimodal is important for estimating actual dose if welding fume were inhaled by a worker performing task or animal in a toxicology study. Previous unimodal estimates of PSD

parameters may be insufficient to accurately characterize the complete exposure and dose in risk assessment and characterization studies for the health effects associated with welding fume.

Number-based particle size distribution parameters obtained also follow a lognormal bimodal distribution, which is consistent with mass findings and particle formation theory. The effect of increasing amperage to the highest recommended setting was to substantially increase the total particle number concentration within the breathing-zone of the manikin. Occupational hygienists and welding professionals may directly influence personal exposures of welding fume if they are to choose welding parameters that keep amperage settings below the mid-point of the recommended operation range.

3. INVESTIGATION OF ELEMENTAL COMPOSITION OF SIZE-FRACTIONATED WELDING FUME AEROSOL

3.1 Background

Information on toxicity of and human exposure to chemical agents are keys to any human health risk assessment for exposure scenarios in environmental and occupational settings. Potential adverse health effects associated with welding fume are dependent upon exposure to specific toxic agents found within the fume itself. Therefore, accurate characterization of the composition of welding fume in biologically significant aerosol fractions and exposures must be accomplished in order to develop the most relevant estimates of human health risk for welders.

3.1.1 Fume and Aerosol Formation Mechanisms in Welding

Although bulk chemical composition of welding fume is primarily dependent upon the composition of the electrode metal and coating in macro-scale, the ultimate chemical profile of an individual fume particle is determined by the formation mechanisms at work along with the molecular species supplying those formation reactions in micro-scale. A brief discussion of fume formation is prudent in understanding the final fume composition in both scales of importance.

3.1.1.1 Welding Fume Generation Mechanisms

In electric arc welding, solid fume aerosols are formed by the condensation of metal vapors and ejected solid particles emanating from multiple points within the arc-zone. Gray and Hewitt

(1982) describe key mechanisms responsible for the formation of welding fume particles. The size, shape and amount of fume generated from each mechanism are influenced by the underlying welding consumable- and process-related parameters.

A Droplet Evaporation

During the welding process, droplets of metal are formed at the tip of the electrode as it melts due to the electrical heat input. As the droplet forms at the tip of the electrode, metal vapors are emitted to the surrounding area at a rate, which can be explained by partial pressures of each metal oxide in the mixture (or molar fraction of each in the mixture) (Lucas, 2008). The droplet size, which can be determined by electrode size and heat input, can influence the amount of fume generated. Larger droplets generate more welding fume (Bosworth & Deam, 2000).

B Explosive Evaporation

As the droplet forms at the tip of the electrode, the neck region of the droplet detachment undergoes rapid heating due to the decreased cross-sectional area and increased temperature (Lucas, 2008). This results in the almost instantaneous evaporation of some of the remaining metal filament and the ejection of a spray of vary hot metal droplets (C. N. Gray & P. J. Hewitt, 1982). This mechanism of fume formation is particularly evident in low voltage short-circuiting metal transfer mode. Here, the filler wire contacts the base metal and creates a short circuit that breaks quickly due to the surface tension of the weld pool pulling the molten droplet away from the wire and into the weld. During droplet detachment, the resistance increases as the wire diameter decreases causing a rapid heating of the electrode wire. This heating is sufficient to rapidly vaporize metals in

the wire when the droplet detaches, as the short circuit is broken. The amount of fume generated from explosive evaporation is mainly dependent on the current used and the resistance of the electrode wire and base metal being welded (Lucas, 2008).

C Micro Spatter

Micro spatter is a portion of fume particles that are larger in size and are not formed by the condensation of metal vapors but rather by the ejection of molten particles from the electrode as the droplet detaches explosively (Lucas, 2008). These larger particles can also serve as a further source of metal vaporization; however, their overall contribution to fume mass is small (C. N. Gray & P. J. Hewitt, 1982; Neil T. Jenkins & Thomas W. Eagar, 2005).

3.1.1.2 Aerosol Formation Mechanisms

Arc welding operations generate metal vapors because the filler alloys and metal substrates reach temperatures that are sufficient to change their phase from a solid to a liquid (A. Zimmer, 2002). Fume formation during welding process stems from these metal vapors emanating from the weld area diffuse away from the molten metal surface to the gas phase. The high temperatures of the arc cause the high vapor pressure metallic species in the electrode consumable to enter the vapor phase. As the metal vapors chemically react and cool, particles are initially formed through nucleation and grow in size through condensation and nucleation (A. Zimmer, 2002). A short discussion of these primary aerosol formation mechanisms follows in regards to welding is prudent for this research.

A Nucleation

Homogeneous nucleation is the formation of particles from a supersaturated vapor without the assistance of condensation nuclei or ions (Hinds, 1999a). In welding, homogeneous nucleation is a major formation mechanism of particles. As the high temperature metal vapors present within the arc flux away from the arc plasma, the temperature decreases to the point where the metal vapors become super-saturated. Thermodynamically, super-saturated metal vapor species are no longer favored, resulting in a phase transformation that creates an initial welding aerosol (A. Zimmer, 2002).

B Condensation

Once stable nuclei form, condensation is an aerosol growth mechanism whereby small nuclei grow in diameter by condensation of vapors on the particle surface (Hinds, 1999a). In welding, transport of additional metal vapors onto the particle surface is the primary condensation mechanism. Additionally, particle growth through condensation becomes important for metal alloys composed of volatile species with multiple vapor pressures, as is often the case with welding with fluxes like the SMAW and FCAW processes (A. Zimmer, 2002).

The timing of condensation of metal vapors is determined by the physical properties (i.e., boiling point and, hence, the vapor pressure of the element or molecule in question. TABLE XI presents some of the physical properties of selected elements found in welding fume (Lide, 2004).

TABLE XI: MELTING POINTS AND BOILING POINTS OF SELECTED ELEMENTS IN WELDING FUME (LIDE, 2004)

Property	K	Na	Mn	Cr	Fe	Ni	Ti
Melting Point (K)	337	371	1518	2130	1808	1726	1933
Boiling Point (K)	1032	1156	2334	2944	3134	3186	3560

C Coagulation

Coagulation is a process where aerosols collide within one another due to the relative motion between them and adhere to form larger particles (Hinds, 1999a). These collisions can occur between single particles, between a single particle and an agglomerate, or between multiple agglomerates. In welding, collisions between liquid particles and solid particles can occur (A. Zimmer, 2002). Two liquid particles combining would result in one larger diameter spherical particle. If collisions occur between solid particles, an agglomerate forms that is held together by van der Waals and other attractive forces. And finally, collisions of welding particles that are slightly molten could result in partially sintered agglomerates (A. Zimmer, 2002). In all particle collision scenarios, the rates of coagulation are highly dependent on particle number concentration (Hinds, 1999a).

3.1.1.3 Fume Formation Chemistry

In GTAW, where filler material is not used, the vapor pressure of metal constituents in the base metal alloy can be used to estimate the final elemental composition of the generated fume with

good prediction (C. Gray & P. Hewitt, 1982). This is not the case, however, for GMAW and SMAW, where additional factors such as welding current, welding voltage and flux composition will account for the final composition of the fume

In general, a number of process -driven (thus, temperature-driven) competing formation mechanisms are in play in welding as time progresses. Zimmer (2002) has explained these phenomena in the following manner:

> In the time-temperature history for the formation of a welding aerosol, chemical species with relatively low vapor pressures will be the first species to form particles through nucleation. At the temperature that these species nucleate, the higher vapor pressure species will still exist as vapors. However, as the time increases and the temperature decreases, the higher vapor pressure species will condense upon the freshly nucleated particles resulting in particle growth. The interesting result of particles that grow through condensation is the tendency to form "shelled particles" (i.e., the chemical composition changes from the core to the surface of the particle). (A. Zimmer, 2002).

As a result, the welding fume consists of particles with different chemistry and morphology, which is governed by formation mechanisms and reaction kinetics responsible for particle generation, growth and chemistry.

3.1.2 Hazardous Metal Constituents of Welding Fume

Welding fume consists of solid particles, the composition of which is mainly oxides of various trace elements.. Metal toxicity is the most likely cause of adverse health effects associated with welding fume exposures and, therefore, detailed discussion on toxicity associated with hazardous elements within welding fume is provided below.

3.1.2.1 Chromium

Chromium is generally an abundant element occurring in oxidation states between +2 to +6, but trivalent chromium (CrIII) and hexavalent chromium (CrVI) are the two biologically-significant forms. CrIII is considered an essential nutrient and believed to be considerably less toxic, whereas the CrVI is related to the well known harmful effects in humans (Klaassen, 2001). Health effects of exposure to CrVI or CrIII in humans are documented mainly in occupational case reports and epidemiology studies, which investigate inhalation and dermal exposures. However, in occupational studies, it is often difficult to separate exposure to CrVI from CrIII. Occupational exposures to CrVI and/or CrIII are associated with respiratory and nasal, cardiovascular, gastrointestinal, hematological, hepatic, renal, and dermal effects (ATSDR, 2008). CrVI is corrosive and causes chronic ulceration and perforation of the nasal septum if inhaled. CrVI easily crosses cell membranes and its reduction within cells to CrIII and the formation of complexes with macromolecules are believed to be the primary mechanisms of cellular toxicity and carcinogenic potential (Zhitkovich, 2005). IARC classified CrVI as a Group 1 carcinogen (i.e., carcinogenic to humans) and categorized CrIII as a chemical that can not be classified as to its carcinogenicity to humans (i.e., Group C) (IARC, 1997).

Recently, CrVI has received heightened interest of the occupational health community due to the newly adopted CrVI Permissible Exposure Limit (PEL) of 5 $\mu g/m^3$ by the U.S. Occupational Safety and Health Administration (OSHA). While OSHA's PEL remains at 0.5 mg/m3 for CrII and CrIII compounds (as Cr) and 1 mg/m^3 for chromium metal and insoluble salt (as Cr), the potential to exceed this new lower PEL for CrVI in workplaces is high. . The American Conference of Governmental Industrial Hygienists (ACGIH) has set Threshold Limit Values (TLVs) for chromium

metal and CrIII compounds at 0.5 mg/m^3, water-soluble CrVI compounds at 0.05 mg/m^3 and insoluble CrVI compounds 0.01 mg/m^3 as a time-weighted average (TWA) over an eight-hour workday or 40 hour workweek in 1991.

3.1.2.2 Nickel

National Toxicology Program (NTP) carcinogenesis bioassay found that metallic nickel may reasonably be anticipated to be a carcinogen and that nickel compounds are known to be human carcinogens (NTP, 2000). While IARC classified metallic nickel in Group 2B (possibly carcinogenic to humans) and nickel compounds in Group 1 (carcinogenic to humans), EPA has classified nickel refinery dust and nickel subsulfide in Group A (human carcinogen) (IRIS 2005). EPA has not classified other nickel compounds. As gleaned from these classifications, not all nickel substances exhibit the same carcinogenic potential and a hierarchy of toxicity relates to the water solubility of compounds with nickel sulfate being the most toxic, followed by nickel subsulfide and nickel oxide (Klaassen, 2001). Specific cellular toxicity mechanisms have yet to be elucidated, however, theories of action are related to the ability of nickel compounds to enhance chromatin condensation, which is a preliminary event in apoptosis (Kass, Eriksson, Weis, Orrenius, & Chow, 1996; Sivulka, 2005). In addition, Nickel is a dermatological contact allergen.

The OSHA PEL for nickel as metal, insoluble or soluble compounds is 1 mg/m^3 as an eight hour TWA. The most recent ACGIH TLVs are set at 1.5 mg/m^3 for elemental nickel based on dermatitis and pneumoconiosis health effects, 0.1 mg/m^3 for soluble inorganic compounds based on lung damage and nasal cancer health effects, 0.2 mg/m^3 for insoluble inorganic compounds and

0.1 mg/m^3 for nickel subsulfide based on lung cancer. All TLVs are based on inhalable aerosol fractions and designated as TWA of eight-hour workday or 40-hour workweek..

3.1.2.3 Manganese

Manganese is an essential element and a cofactor for numerous biological enzymatic reactions. Toxicity related to the chronic inhalation of manganese compounds is associated with manganism, a neuropsychiatric disorder similar to Parkinson's disease (Klaassen, 2001). Manganese toxicity is related to its ability to accumulate in the cells of the basal ganglia, a section of the brain important for controlling motor functions and learning (Roth, 2009).

The OSHA PEL for manganese is 5 mg/m^3 ceiling concentration (i.e., an exposure level which should never be exceeded for any length of time). The ACGIH TLV for manganese is a TWA limit of 0.2 mg/m3. In 2010, the ACGIH has proposed an intended change of the TLV (eight-hour workday or 40 hour workweek TWA) for elemental and inorganic manganese compounds to 0.2 mg/m^3 in the inhalable aerosol fraction and 0.02 mg/m^3 in the respirable aerosol fraction based on the review of the literature pertaining to effects of manganese exposure on CNS impairment as the critical health effect.

3.1.3 Shielded Metal Arc Welding Electrode Chemistry

The hazardous metal components of welding fume originate mostly from the consumable electrode employed in the welding process. The composition of the welding electrode is highly

complex since electrodes are engineered to be employed in specific welding applications and to attain specific metallurgical properties.

3.1.3.1 Compositional Characteristics of Electrode

Composition of the welding electrode can be delineated in terms of the metal alloy filler wire and the flux, if any is provided, either coating (SMAW) or within (FCAW) the wire itself. The purpose of the consumable electrode is to provide additional metal to fill the gap of the joint being welded (J. F. Lancaster, 1987). Filler wire is chosen to best match the base materials being joined and, therefore, the composition is mainly alloyed metallic elements, whereas the flux composition is much more complicated.

Electrode flux is composed of a mixture of minerals, organic material, ferro-alloys and iron powder bonded with sodium or potassium silicate. The complex nature of flux composition is related to the following four distinct functions that it provides to the welding process (Kou, 1987):

i) flux provides a gaseous shield to protect the molten metal from air. In the case of a limestone ($CaCO_3$)-type electrode, CO_2 gas and CaO slag form when the limestone decomposes. The volume of gas generated during burning is low and requires a shorter arc length to properly shield the welding zone (J. F. Lancaster, 1987);

ii) it provides deoxidizers and fluxing agents to deoxidize and cleanse the weld metal. The solid slag formed also protects the already solidified, but still hot, weld metal from oxidation;

iii), it provides arc stabilizers and helps maintain a stable arc during welding. Arc stabilizers are readily ionizable compounds (such as potassium oxalate and lithium carbonate) and, thus, help the arc conduct the electric current; and

iv) it provides alloying elements and/or metal powders to the weld. The former helps control the composition of the weld, and the latter helps increase the deposition rate,

In SMAW, the drops that transfer from the electrode to the weld pool are coated with slag and the weld pool itself has a slag coating. The self-generated gas is the main protective agent during metal transfer, whereas the slag protects the solidifying and cooling welded metal. In SMAW, the gases generated by vaporization and chemical reaction at the electrode tip are protective (J. F. Lancaster, 1987) of weld from oxidation. Basic electrodes, like E308H-16, have a coating consisting primarily of calcium carbonate, which breaks down during welding to provide a $CO\text{-}CO_2$ shield.

3.1.3.2 Material Safety Data Sheet Data on Electrode Composition

Chemical composition of welding electrodes is highly complex and is often deemed proprietary by the manufacturer. Therefore, it is not readily publicly available. However, the OSHA Hazard Communication Standard (29 CFR 1910.1200) requires disclosure of hazardous agents associated with potential workplace exposures. As such, manufacturers of electrodes do provide some composition data within the Material Safety Data Sheet (MSDS). Compositional data as reported on the MSDS for the electrodes used in this research (E308H-16, Midalloy Mfg., St. Louis, MO) is provided in **TABLE** XII below.

TABLE XII: COMPOSITION OF SMAW E308H-16 ELECTRODES (MIDALLOY, 2005)

Ingredient	Lower %	Upper %
Iron	30	50
Chromium	15	25
Nickel	6	20
Manganese	1	3
Silicon	0.1	1
Molybdenum	0	4
Columbium	0	3
Calcium Carbonate	5	15
Calcium fluoride	2	10
Cryolite	0	5
Potassium Titanate	0	3
Titanium dioxide	1	15
Potassium silicate	0	2
Sodium silicate	1	5
Potassium hydroxide	0	0.5
Chromium oxide	0	0.5
Feldspar	0	3

It must be emphasized that the compositional data provided is for the electrode itself and not for the generated fumes. Further, the accuracy and consistency of the reported data from one batch of electrode to another batch in regards to ultimate fume composition have not been thoroughly researched. In a project aimed at re-evaluating a procedure of calculating exposure limits of welding fume, Howe (2000) collected compositional data on welding fume produced from SMAW, FCAW and GTAW to assess the reliability of data given on MSDSs. These researchers found that MSDSs that reported potential fume composition information may over- or under-estimate the analytically measured fume composition by as much as 50% (Howe, 2000). Clearly, the final composition of welding fume is not easily predictable since the ingredients of the electrode and exposure dynamics of the welding process are extremely complex.

3.1.4 Literature Review: Elemental Compositional Studies of Welding Fume

Elemental composition data for welding fume have long been documented in the literature and a review of available data is presented below. Here, focus is paid to those studies describing composition of fume generated from the SMAW on stainless steel (SS) (i.e., SMAW-SS). Due to a lack of publicly available published data on the SMAW process, data for FCAW of stainless steel are also described due to the similarity of flux materials between the two processes. All data are classified on whether or not they were collected under laboratory or field conditions. Also, when available, the analytical method employed to generate the compositional data as well as the electrode classification is highlighted.

3.1.4.1 Laboratory Based Studies

One of the first studies aimed at characterizing welding fume was commissioned by the American Welding Society (AWS) (Speight & Campbell, 1979). This comprehensive laboratory based study collected total fume samples from an emission chamber designed to capture all generated fume on a glass fiber filter. Researchers measured fume components from SMAW-SS E316-16 electrodes using Atomic Absorption Spectroscopy (AAS) and found 10.0% Fe, 8.8% Mn, 1.5% Ni and 6.5% Cr contained in fume. Also in this study, fume generated from E410-16 (SMAW-SS electrodes with higher chromium content) was analyzed with optical emission spectroscopy (OES) and found to contain 10-20% Fe, 2-3% Si, 10-20% K, 4-8% Na, 1-2% Mn, <0.1% Ni and 5-10% Cr.

One study analyzed fumes generated from SMAW-SS using OES and instrumental neutron activation analysis (INAA) (Minni, Gustafsson, Koponen, & Kalliomaki, 1984). Here, airborne samples of welding fume from E316L-16 (amperage setting 110±10 A; voltage setting 25±5 V) electrodes were collected on membrane filters. Authors measured elemental composition as 3.5% Fe, 1.4% Mn, 2.7% Cr and 0.3% Ni with OES, and 4.0% Fe, 2.2% Mn, 3.0% Cr and 0.4% Ni with INAA. Sodium and potassium were estimated at greater than 10% final weight of fume. Researchers also performed X-ray photoelectron spectroscopy (XPS) combined with ion bombardment to study the changes in concentrations and in the oxidation states of the elements present in the particles at different depths. During this analysis, iron and manganese valance states remained constant throughout particle depth while chromium was found exclusively in the hexavalent state on the surface of the particles and in mixed trivalent and hexavalent states after ion bombardment.

In an emission chamber experiment of SMAW-SS using E316L-16 electrodes (4.0 mm diameter), the elemental composition of total fume collected was performed using X-ray Fluorescence Spectroscopy (XRF) (Moreton & Smars, 1985).. Elemental composition it was documented as 5.1% Fe, 5.0% Mn, 0.4% Ni, 5.0% Cr (4.1% CrVI), 10.1% Na and 19.9% K. Authors note that analytical accuracy may have been reduced due to the small amount (0.3 g) of welding fume analyzed (Moreton & Smars, 1985).

Another study used multitude of methods, infra-red (IR) spectrophotometry, thermogravimetry and differential thermal analysis (TG/DTA), X-ray fluorescence (XRF), X-ray diffraction (XRD), atomic absorption spectroscopy (AAS) and electron microprobe analysis, to characterize fume generated from SMAW-SS using E316L-16, 3.15 mm electrodes (amperage 100 A,

voltage 24 V) (R. Tandon, et al., 1985). Fume samples were analyzed as collected and after washing with water to determine the water-soluble fractions. XRF revealed an elemental fume composition of 4.3% Na, 20.2% Si, 19.4% K, 4.2% Cr, 5.3% Mn and 1.0% Ni (Fe concentration not reported). Thirty percent of the fume was water-soluble and that fraction composed of 2.5% Na, 6.7% K, 5.1% Cr (>90 of this amount present as CrVI), 0.7% Mn, 0.15% Fe, and 0.08% Ni. Authors report that a mass balance on the fume concentration measurements recorded is completed when accounting for oxygen that associates with transition metal elements. IR spectrophotometry revealed the presence of chromate ions in the water-soluble fraction of fume. TG/DTA revealed the presence of Fe_3O_4, K_2CrO_4 and possibly Na_2CrO_4. XRD analysis of fume also revealed presence of K_2CrO_4, FeO_4 and $FeCrO_4$ species, but not the Na_2CrO_4. The inconsistent identification of Na2CrO4 was hypothesized to occur because of either crystallinity defects or because of the formation of mixed Na/K chromates or because CrO_4^{2-} ions may condense from the gas phase preferentially with K^+ ions due to their larger atomic size leading to a more stable ion-packing arrangement. XPS analysis was used in this study to reveal composition of fume particles at different surface depths. The concentrations of Na, K, Cr and F on the surface of particles suggested a mixture of NaF, Na2CrO4 and K2CrO4. Chromium was hypothesized to be present on the surface mainly as alkali metal chromates since it was removed by washing with water (R. Tandon, et al., 1985).

The same researchers also performed a study to characterize hard-facing and high-strength low-alloy (HSLA) electrodes using many of the same analytical techniques (R. Tandon, Ellis, Crisp, Baker, & Chenhall, 1986). The elemental composition for select metals included 1.9 – 4.1% Na, 1.1 – 4.5% Si, 0.1 – 17.3% K, 0.03 – 2.6% total Cr, 0.03 – 1.9% CrVI, 3.6 – 31.0% Mn, 11.5 – 32.3% Fe and 0.01 – 2.0% Ni in the total fume analysis. In the water-soluble fraction, element concentrations were 0.4 – 1.9 % Na, 0.1 – 15.1% K, 0.02 – 1.5% CrVI, 0.003 – 0.05% Mn and 0.03 – 0.09% Fe. The

elements Si, and Ni were not detected in soluble fraction. XRD analyses revealed crystalline compounds of FeO_4, CaF_2, and K_2CrO_4. No crystalline silica (SiO_2) was observed and it was concluded that all SiO_2 is in amorphous form. A specific comparison of the amount chromium (both CrIII and CrVI) found in fume to the chromium and alkali metals found in the flux was conducted. This analytical work observed a high correlation between the Na and K content of the flux composition and the water-soluble CrVI composition of the resulting fume. Authors concluded that reduction of the Na + K content of electrode fluxes may be a useful means of reducing the proportion of CrVI in fume (R. Tandon, et al., 1986).

In an emission chamber study in which SMAW-SS was performed using E308-16 electrodes, fume composition was analyzed using AAS (McIlwain & Neumeier, 1987). A small amount of fume (0.3 g) was scraped from air sampling filters to perform the elemental analysis. The reported metal fractions of the fume were: 18.2% Fe, 10.2% K, 9.3% total Cr, 5.1% CrVI, 6.9% Mn, and 1.9% Ni.

Matczak and Chmielnicka (1989) focused on development of analytical methods for determining the soluble and insoluble chromium compounds in welding fume. These researchers collected personal breathing-zone samples from workers in a welding shop and total welding fume samples from an emission chamber. Emission chamber samples were analyzed with AAS and found to contain 9.8 – 11.1 % Fe, 3.0 – 4.8% Mn, 5.9 – 7.7% CrTot and 0.74 – 3.1% Ni. Personal breathing-zone samples were found to contain 14.2% Fe, 4% Mn, 4% TotCr and 0.7% Ni. Of the TotCr measured, 70.3 – 80% was CrVI (20 – 24.3% insoluble, 46 – 59% soluble) while 20 – 29.7% was CrIII (10.8 – 14.3% insoluble, 5.7 – 18.9% soluble) (W Matczak & J Chmielnicka, 1989).

A study published by Hewett (1995) was the first that attempted to understand the elemental composition of welding fume in different aerosol fractions. In this study, composition of different particle size fractions of welding fume generated from E308-16 electrodes was determined using inductively coupled plasma-mass spectroscopy (ICP-MS) performed on a single set of filters placed on the stages of a MOUDI (no replicates were generated). The metal fractions in each aerosol size fraction were calculated as percent of total specific metal mass measured across all size fractions. These data are presented in **TABLE** XIII below and show that most of the fume mass was collected on stage 5 and 6, corresponding to stage cut-point of 0.57 and 0.31μm, respectively. The author concluded that the elemental distribution was similar to the mass distribution and therefore a specific chemical component would not likely fractionated to specific size ranges (Paul Hewett, 1995).

TABLE XIII: ELEMENTAL MASS-BASED COMPOSITION OF WELDING FUME MEASURED WITH A 8-STAGE CASCADE IMPACTOR HEWETT (1995)

Stage	Cut Point (μm)	Fe (wt. %)	Mn (wt. %)	Ni (wt. %)	Cr (wt. %)
0	15	1.6%	0.0%	0.0%	0.8%
1	5.6	2.2%	0.0%	0.0%	1.1%
2	3.2	0.0%	0.0%	0.0%	0.0%
3	1.8	1.4%	1.3%	0.0%	1.0%
4	1.0	13.2%	16.2%	0.0%	13.4%
5	***0.57***	***29.4%***	***37.2%***	***27.3%***	***31.7%***
6	***0.31***	***33.2%***	***35.0%***	***39.0%***	***34.8%***
7	0.155	15.9%	10.3%	33.8%	15.2%
8	0.071	1.9%	0.0%	0.0%	1.8%
Filter	<0.071	1.9%	0.0%	0.0%	0.0%

In another emission chamber study, welding fume generated during FCAW-SS with CO_2 shielding gas was studied (Yoon, Paik, Kim, & Chae, 2009). Fume samples were analyzed for soluble and insoluble elemental composition using ICP-AES. Total elemental content of fume was measured as 8.2%±3.5% Fe, 4.7%±1.5% total Cr, 1.1%±0.3% Ni, 8.2%±1.8% Mn and 11.7%±4.7% K. The insoluble elemental content was measured as 0.03%±0.02% Fe, 0.8%±0.3% total Cr, 0.04%±0.02% Ni, 0.15%±0.22% Mn and 9.74%±4.59% K.

The studies already described reveal bulk analysis of welding fume particles, but other studies have investigated individual particle composition as it varies through the internal depths of the particle. A group of studies explored the chemistry of the core-shell nature of welding fume particles generated from GTAW-SS and SMAW-MS (rutile electrodes) using secondary ion mass spectrometry (SIMS) (Konarski & Iwanejko, 2003; Konarski, Iwanejko, & Mierzejewska, 2003). Specific electrode types or welding conditions were not documented. Samples were collected using a 9-stage cascade impactor and the 300-400 nm size fraction was taken for SIMS depth profiling analysis. The analysis revealed that oxygen and potassium were detected at constant concentrations throughout the entire depth of the particle. Iron, manganese and chromium signals are detected mainly below the shell (>50nm depth). The shell is found to be composed of mainly K, F and Cl and t is observed that SMAW particles are much more oxidized than the GTAW particles. The difference in oxidation of the particles from the two welding processes is attributed to the use of the shielding gas in GTAW and not in SMAW (Konarski & Iwanejko, 2003; Konarski, et al., 2003).

3.1.4.2 Field Based Studies

In a large welding shop, personal exposure to fumes generated during SMAW-SS using E316L electrodes was measured using closed face sampling cassettes in the breathing-zone of workers (Karlsen, Farrants, Torgrimsen, & Reith, 1992). Authors reported 2.7 hour TWA concentrations of 6.4 mg/m^3 for total fume, 52 μg/m^3 for Ni, 450 μg/m^3 for Fe, 480 μg/m^3 for total Cr, 300 μg/m^3 for CrVI (soluble), and 120 μg/m^3 for Mn (Karlsen, et al., 1992). Metal fractions of total fume were measured as 0.96% Ni, 8.3% Fe, 8.8% TotCr, 4.1% CrVI (soluble) and 2.3% Mn.

A field study in a shipyard reported total fume personal exposure concentrations during SMAW-SS (E309CB, 3.175 mm electrodes) as 0.18 to 1.0 mg/m^3 (Castner & Null, 1998). The measurements were obtained using closed-face personal air samplers. Individual metal components (NIOSH Method 7300) of fume were reported as 0.7 to 5.5 μg/m^3 for Ni, 3.9 to 47 μg/m^3 for Mn, 0.2 to 34 μg/m^3 for total Cr and 0.4 to 54 μg/m^3 for CrVI as 8-hour TWAs.

Another field study measured personal exposure of total fume, CrVI, CrIII and Ni in a welding shop during normal FCAW-SS operations (Niemela, Koskela, & Engstrom, 2001). Total particulate exposure concentrations measured using unspecified personal samplers ranged from 2.2 to 16.1 mg/m^3. Metal fractions of total fume ranged from 0.2 to 4.9% for CrVI, 0.4 to 2.5 for CrIII and 0.4 to 1.7% for Ni. The workers in this welding shop were sampled during the fabrication of large cylindrical vessels, thus the exposure measurements obtained might represent confined space exposure (Niemela, et al., 2001).

In the Netherlands, personal exposure concentrations of respirable fume along with the associated total Cr and CrVI concentration during GMAW-SS and SMAW-SS operations were measured using Ravebo personal respirable cyclone samplers within the welding helmet (Scheepers, et al., 2008). While average respirable fume concentrations were reported as 0.30 mg/m^3 (0.04 – 6.30 mg/m3), average total Cr and CrVI concentrations were measured as 5.4 $\mu g/m^3$ (range: 2.3 – 387 $\mu g/m^3$) and 0.084 $\mu g/m^3$ (range: <0.02 – 19.0), respectively (Scheepers, et al., 2008).

TABLE XIV: SUMMARY OF LITERATURE REPORT CHEMICAL COMPOSITION OF WELDING FUME

Author	Process	Electrode Type	Analytical Technique	Na	K	Fe	Mn	Cr	CrVI	Ni
Speight and		E316-16	AAS	-	-	10	8.8	6.5	-	1.5
Campbell, 1979	SMAW-SS	E410-16	OES	4 - 8	10 - 20	10-20	1-2	5-10	-	<0.1
			OES	-	-	3.5	1.4	2.7	-	0.3
Minni et al. 1984	SMAW-SS	E316L-16	INAA	-	-	4	2.2	3	-	0.4
Moreton and Smars 1985	SMAW-SS	E316L-16	XRF	10.1	19.9	5.1	5	5	4.1	0.4
Tandon et al.1985	SMAW-SS	E316L-16	XRF	4.3	19.4	-	5.3	4.2	-	1
Tandon et al. 1986	SMAW-HSLA	N/R	XRF	1.9 - 4.1	0.1 - 17.3	11.5 - 32.3	3.6 - 31.0	0.03 - 2.6	0.03 - 1.9	0.01 - 2.0
McIlwain and Neumeier 1987	SMAW-SS	E308-16	AAS	-	10.2	18.2	6.9	9.3	5.1	1.9
Matczak and Chmielnicka 1989	SMAW-SS	N/R	AAS	-	-	9.8 - 11.1	3.0 - 4.8	5.9 - 7.7	4.4 - 5.7	0.7
Yoon et al. 2009	FCAW-SS	N/R	ICP-AES	-	11.7	8.2	8.2	4.7	-	1.1
Karlesen et al. 1992	SMAW-SS	E316L	AAS	-	-	8.3	2.3	8.8	4.1 (soluble)	0.96
Castner and Null 1998	SMAW-SS	E309CB	ICP-AES	-	-	-	2.2 - 4.7	0.1 - 3.4	0.2 - 5.4	0.4 - 0.5
Niemela et al. 2001	FCAW-SS	N/R	AAS	-	-	-	-	-	0.2 - 4.9	0.4 - 1.7
Scheepers et al. 2008	GMAW-SS, FCAW-SS, SMAW-SS	N/R	AAS	-	-	-	-	1.8	0.03	-

3.1.5 Summary of Literature

Welding fume consists of particles originating from the nucleation and condensation of metal vapors, including the known toxic metals chromium, nickel and manganese, directly outside of the intense heat of the electric arc. The ultimate composition of fume particles is dependent on the composition of the electrode being burned and welding-processing parameters, which is highly complex and related to the metallurgical properties desired in the finished weld. Compositional studies of welding fume have mostly focused on total fume measurements and have not thoroughly related elemental composition data to particle size fractions that are more biologically-relevant relevant in estimating human health risk. The research presented in this chapter aims to fulfill this data gap in the literature.

3.2 Study Objective

The general goal of this research is to determine the elemental composition of size-segregated welding fume samples to aid in the design of toxicity studies aimed at understanding health effects of welding fume exposures in the workplace and to steer the future direction on proper exposure assessment methodology for welders and for proper exposure standard development. For this purpose, two separate but complimentary experimental systems are used: i) an isokinetic emission chamber and ii) an exposure chamber containing a thermal manikin mimicking a welder. Employment of a number of aerosol measurement tools also allowed methodological research into exposure assessment for welding fume. Specifically, this research aims to:

1) To uncover whether there are compositional differences across aerodynamic size-fractions of the welding fume, particularly between those ultra-fine fractions expected to deposit within alveoli and those in the nano-size range, which can circulate within the blood stream throughout body, that can have significant biological implications;

2) To determine whether elemental composition findings along with particle size and shape information allow hypothesis development in mechanisms responsible for formation of welding fume particles, that can steer future research into green welding consumable manufacturing and materials processing to control toxic constituents of the fume; and

3) To provide preliminary understanding of consistency of exposure concentration and mass fraction data obtained via different aerosol measurement tools (i.e., MOUDI, ELPI and PCIS) and utility and reliability of these tools in measuring welding fume personal or area exposures in the workplace.

3.3 Methods

3.3.1 Experimental systems

This research is performed within the exposure and emission chambers as described in Chapter 2. Two sets of four experiments (two in the emission chamber and two in the exposure chamber) were performed. This first set of experiments was conducted to obtain full elemental composition of the fume collected, while the second set of experiments was conducted to measure the CrVI content. Welding process parameters (3.175 mm electrode, 100A), manikin physiological

conditions (16 bpm, 0.85 lpb) and chamber environmental parameters (0.2 m/sec) were held constant for all experiments. The ELPI, MOUDI, PCIS (inside and outside the welding helmet) and the manikin filter assembly were used in sampling the welding fume.

3.3.2 Sample Collection and Analysis

Sampling procedures and filter handling were performed as described in Chapter 2.

3.3.3 Analytical Chemistry

3.3.3.1 Full Elemental Composition

The Wisconsin State Laboratory of Hygiene (WSLH) analyzed all filters for elemental composition using High Resolution-Inductively Coupled Plasma-Mass Spectroscopy (HR-ICP-MS). Acid-washed pre-cleaned PTFE filters were used in these experiments. Filters were placed into individual digestion vials. Next, 1.0 mL 16N nitric acid, 0.25 mL 12N hydrochloric acid and 0.1 mL 28N hydrofluoric acid were added to each vial. Digestion vials were placed into an automated, temperature (and pressure)-regulated, trace analysis microwave system (Milestone Ethos+) to complete the digestion procedure. The microwave program included a 15 minute temperature ramp to 200 ºC followed by a 30 minute hold at 200 ºC. Once digestion was complete, extract solutions were transferred to 60 mL analytical vials and diluted to a 15 mL final volume with deionized water.

Elements were quantified with a magnetic sector High Resolution Inductively-Coupled Plasma Mass Spectrometer (HR-ICP-MS; Finnigan Element 2). Individual sample analysis was completed three times on the instrument and metal concentrations were reported as an average with the associated standard deviation. With this method, concentrations ranging from low pg/L to tens of mg/L can be quantified. The instrumental Limit of Detection (LOD) (3-sigma) is in the range of 0.01 to 100 ng/L.

In contrast to the HR-ICP-MS method LOD, we also calculated sampling method LODs based on a 3-sigma method (Armbruster, Tillman, & Hubbs, 1994; Thomsen, Schatzlein, & Mercuro, 2003). In this research LODs are sampler-, metal- and filter type-specific. The sampling method LODs are calculated as the average of the metal concentration obtained for all field blanks of that filter type plus three times the pooled standard deviation. The Limit of Quantification (LOQ) was defined as the average of the metal concentration obtained for all field blanks plus ten times the pooled standard deviation. All filter media used in this research were polytetrafluoroethylene (PTFE) in 25 mm, 37 mm and 47 mm diameter, dependent upon the sampler employed to collect the samples.

We must make a special note on instances of negative concentrations reported from analytical laboratory HR-ICP-MS analysis. A reported negative concentration occurs when instrument response to regent blanks is greater than the response of the filter sample. To calculate the final concentration, the instrument response of the reagent blank is subtracted from the instrument response of the sample. When the reagent blank value is larger than the sample value, the final concentration is negative. In terms of measures of concentration, a negative value means the final concentration is below the LOD.

This analytical method is optimized for at least a 50 μg mass gain on the analyzed filter. Due to the operational nature of sampling instruments (i.e., cascade impactors) used and sampling time, not all exposed sample filters had a 50 μg mass gain. Budgetary constraints also limited the number of samples that could be sent to the laboratory for HR-ICP-MS analysis. Therefore, in some instances, replicate samples were not analyzed by HR-ICP-MS.

3.3.3.2 Total Hexavalent Chromium Concentration

Total hexavalent chromium (Cr-VI) analysis of each filter was performed using NIOSH method 7605 (NMAM, 2003). This method uses an acid extraction of the filter followed by chromatography analysis. All beakers and watch glasses used in the analysis were rinsed with 10% nitric acid, then rinsed with deionized water and dried prior to sample analysis. Each of the filters was placed in a 50-mL beaker. Then, 5.0 mL of filter extraction solution (2% NaOH/3% Na2CO3) was added to each beaker containing a sample. The beakers containing the samples were covered with watch glasses and heated in a water bath at approximately 100 °C. The beakers were heated for 45 minutes with occasional swirling. The beakers were removed from the water bath and allowed to cool. The solution in each was transferred quantitatively with distilled water rinses to a 50-mL Falcon tube and brought to a 25 mL final volume. Next, 1.5 mL of each sample was transferred to an auto-sampler vial, capped, and analyzed by ion chromatography with UV/VIS detection.

All filter media used in this research were PTFE. The 47 mm and 37 mm PTFE filters had a limit of detection (LOD) and limit of quantification (LOQ) of 0.001 μg and 0.013 μg, respectively. For 25 mm PTFE filters the LOD and LOQ were 0.006 and 0.019 μg, respectively. Sampling method

LODs for the ELPI, MOUDI and PCIS were 0.04 $\mu g/m^3$, 0.002 $\mu g/m^3$ and 0.04 $\mu g/m^3$, respectively. Sampling method LOQs for the ELPI, MOUDI and PCIS were 0.12 $\mu g/m^3$, 0.03 $\mu g/m^3$ and 0.14 $\mu g/m^3$.

3.4 Results

3.4.1 Analysis of Recovered Metals

The HR-ICP-MS analysis provides mass data (ng) for 48 metal species per filter. Although many metal elements are present within the welding fume, it is necessary to determine which elements are present in significant quantities above the background levels. Figures 1-3 below provide a schematic presentation of the metal masses recovered in the HR-ICP-MS analysis of different filters (i.e., 25 mm, 37 mm and 47 mm in diameter) used in the study for 48 elements. Here, a 3-sigma range around the average metal mass is displayed (red and green lines) in contrast to the LOD of each metal (blue line) for the specific filter type. This enables a simplified way of judging whether the level of each metal found in the samples most likely emanated from fume as the source of exposure or associated with background levels detected in field blanks.

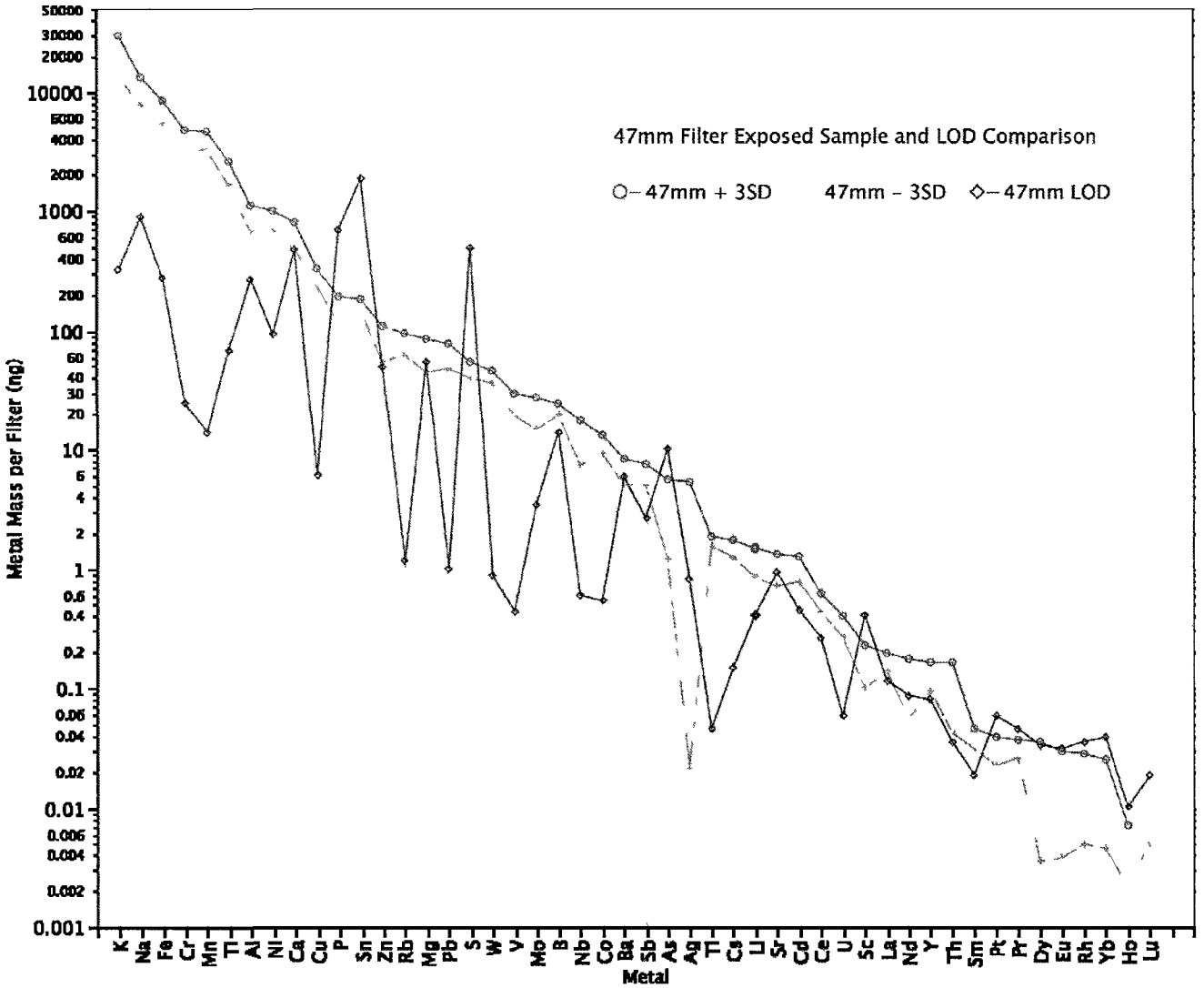

Figure 16: Recovered metal masses from 47mm filters.

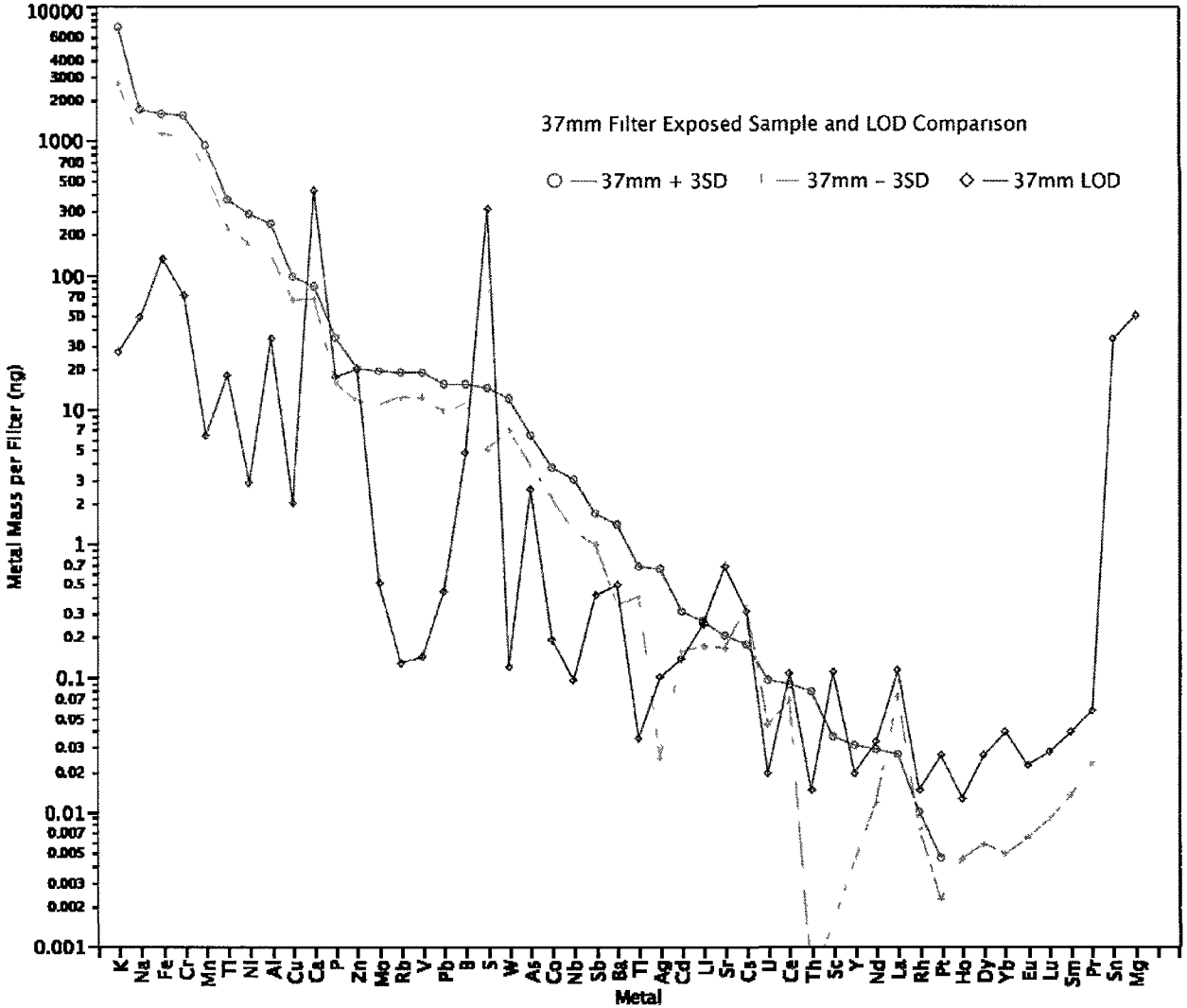

Figure 17: Recovered metal masses from 37mm filters.

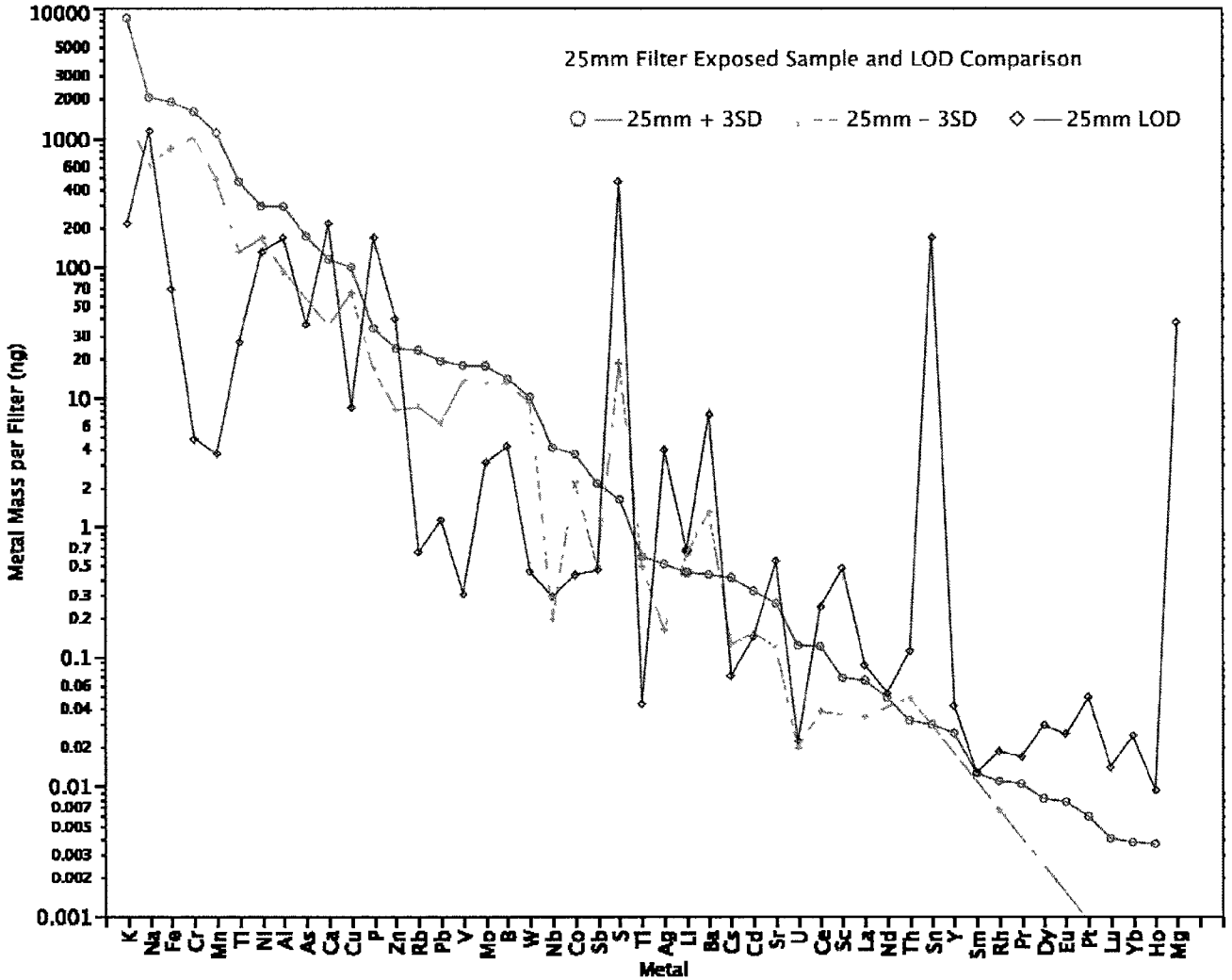

Figure 18 Recovered metal masses from 25mm filters.

Using the visual interpretation graphs as a guide, it is revealed that few elements are present above 1 μg (1,000 ng) and 0.1 μg (100 ng) within exposed samples. We should note that there is a 1 μg LOD of the analytical balance used to measure overall filter weight gain and therefore, 0.1 μg of recovered metal is one order of magnitude lower than can be detected with our analytical balance. In 47 mm filters, K, Na, Fe, Cr, Mn, and Ti have 95% confidence levels around the mean that are greater than 1 μg, and there is no overlap of these and their respected LOD all of these spread nicely from the LOD. Additionally, Al, Ni, Ca, Cu, P and Sn have 95%-CI around the mean that are greater than 0.1 μg, but, Ca, P and Sn mass on exposed filters overlap with their respective intervals with the LODs. In 37 mm filters, K, Na, Fe and Cr have 95%-CI around the mean greater than 1 μg and Mn, Ti, Ni and Al have 95%-CI around the mean greater than 0.1 μg. In 25 mm filters, only K has a 95%-CI around the mean greater than 1 μg, while Na, Fe, Cr, Mn, Ti, Ni and Al have 95%-CI around the mean greater than 0.1 μg. Of these, Na and Al intervals overlap their respective LODs.

The relatively low mass gain measurements obtained in this research is a function of the operational nature of the cascade impactor instruments used and the sampling time of experiments. Optimization of collected mass on all stages of the cascade impactor is often a difficult task because there may be collection of negligible mass on the upper and lower stages of the impactor, while the center stages begin to overload. The sampling time in this work was carefully chosen to strike a balance of obtaining sufficient mass gain at lower stages (smaller particles) to enable post-analysis of samples via HR_ICP-MS without overloading middle stages where majority of the fume mass is collected. Thus, mass gain is disproportionate across the impactor stages and some filters did not gain enough mass to be distinguishable from field blank filters. Five 47 mm (10% of total number

of samples), four 37 mm (50% of total number of samples) and seven 25mm (10% of total number of samples) field blanks were subjected to HR-ICP-MS in this study due to budgetary constraints.

Taking into account the amount of recovered metal mass across filter types and the LODs of the metals within each filter type, K, Fe, Cr, Mn, Ti and Ni are consistently present at the samples at levels above their respective LODs and, thus, can be considered with good confidence that they emanated from welding. Conveniently, these metals are often reported in welding fume compositional analysis literature and may be compared to previous research. Sodium is recovered in larger quantities for all filter types. However, in 25 mm filters, the 95%-CI around the mean overlaps the LOD. Regardless, Na will be included as one of the primary six elements of SS welding fume for in-depth evaluation in the remainder of this chapter because of its relationship with hexavalent chromium content of welding fume.

3.4.2 Elemental Composition of Size-Fractionated Stainless Steel Welding Fume

Mass fractions of each element in total fume are estimated from HR-ICP-MS mass gain data for each impactor stage or each aerosol fraction. . Here, fractionated concentrations of total fume mass collected on each stage are also presented. These analyses were performed for each sampling instrument utilized in each experimental system (i.e., emission chamber and exposure chamber).

3.4.2.1 Emission Chamber Results

A Electronic Low Pressure Impactor

Results of the ELPI emission chamber experiments are presented in Figure 19 and **TABLE** XV below. The fractionated fume mass concentrations range from 0.04 mg/m^3 (Stage 1 and 2; 0.028 μm and 0.055 μm) to 3.51 mg/m^3 (Stage 6; 0.387 μm) with higher concentrations observed in stages 5-7. The amount of metal mass recovered per stage ranges from 23% (stage 2; 0.055 μm) to 50% (Stage 6; 0.387 μm) of total fume mass. Elemental composition analysis could not be replicated for Stages 10 through 13 (2.42μm – 10.04 μm) since only one filter had enough mass to enable post-analysis.

Potassium is present above the LOQ on stages 3 – 12 and concentrations ranged from 834 μg/m^3 in stage 6 (0.387 μm) to 6 μg/m3 in stages 10 -12 (2.42 – 6.77 μm). The fraction of total mass contribution for potassium varies from 3.7% (Stage 13; 10.04 μm) to 23.9% (Stage 6; 0.387 μm) of total fume mass, with larger fractions observed between particle size cut-points of 0.157 and 0.961 μm (i.e., stages 4 – 8). Sodium is only present above the LOQ in stages 5 – 7 and concentrations rage from 81 μg/m^3 in stage 5 to 252 μg/m^3 in stage 6. The sodium concentration of stage 8 (17 μg/m3) is below the LOQ but above the LOD. Majority of sodium mass fraction in total fume resides in stages 5-8 (i.e., 0.266 μm – 0.961 μm) and accounts for 5.7 – 7.2% total mass of the size-fraction.

As would be expected, iron is present above the LOQ in all stages of the ELPI in concentrations ranging from 1.6 μg/m3 in stage 1 (0.028 μm) and 199.8 μg/m3 in stage 6 (0.387

μm). The fraction of total mass contribution per size fraction varies between 4.6% (stage 1; 0.028 μm) and 13.1% (stage 13; 10.04 μm) of total fume mass. Chromium is also present on all stages and is measured in concentrations between 0.6 $\mu g/m^3$ in stage 1 and 131.7 $\mu g/m^3$ in stage 6. Percent contribution to total fume mass per size fraction ranged from 1.6% (stage 10; 2.42 μm) and 18.4% (stage 13; 10.04 μm); however, besides stage 13, the maximum observed fraction is 5.5% (stage 4; 0.157 μm). Manganese is present in all stages in concentrations from 0.3 $\mu g/m^3$ in stage 1 to 147.4 $\mu g/m^3$ in stage 6, and ranged from 0.9% (stage 1; 0.028 μm) to 4.2% (stage 6; 0.387 μm) of total fume mass per size fraction. Titanium is present above the LOQ in stages 4 to 13 in concentrations ranging from 1.3 $\mu g/m^3$ in stage 10 (2.42 μm) to 55.6 $\mu g/m^3$ in stage 6 and is present above the LOD in stage 3. The percent contribution to total size fraction mass for titanium ranges from 0.05 (stage 2; 0.055 μm) to 7.9% (stage 12; 6.77 μm), with the stages with cut-points greater than 4.05 μm (stage 11) exhibiting larger mass fractions. Nickel is present above the LOQ in stages 5 – 7 in concentrations from 6.2 $\mu g/m^3$ (stage 7; 0.622 μm) to 16.7 $\mu g/m^3$ (stage 6) and above the LOD in stages 3, 4 and 8. Nickel percent of total fume mass per size fraction ranges from 0.4% (stage 7; 0.622 μm) to 1.9% and 2.0% (stage 2,3, 13 and 11) of total fume mass. Other metals constituted the remaining metal mass at fractions ranging from 1.9% (stage 7; 0.622 μm) to 14.7% (stage 1; 0.028 μm) of total fume mass. In addition, other metals accounted for 10.4% of total fume mass in stage 3 (i.e., 0.094 μm).

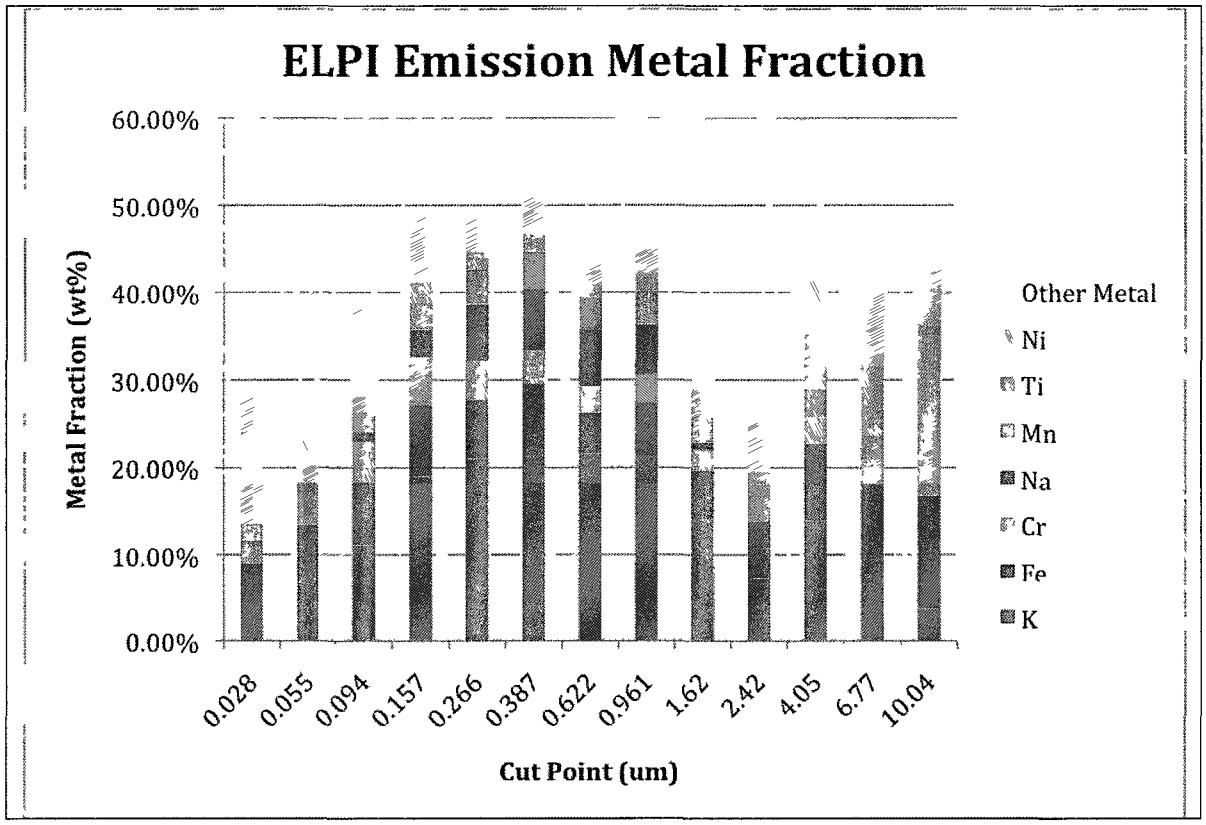

Figure 19: Metal fraction distribution of size-fractionated SS welding fume: emission chamber ELPI data.

TABLE XV: METAL MASS CONCENTRATIONS (μG/M3) IN SIZE-FRACTIONATED SS WELDING FUME: EMISSION CHAMBER ELPI DATA

Stage ID	Particle Size (μm)	Mass Concentration (mg/m^3)	Na ($\mu g/m^3$)	K ($\mu g/m^3$)	Ni ($\mu g/m^3$)	Ti ($\mu g/m^3$)	Fe ($\mu g/m^3$)	Mn ($\mu g/m^3$)	Cr ($\mu g/m^3$)
1	0.028	0.04	-1.61*	1.61	0.58	0.08	1.61	0.32	0.60
2	0.055	0.04	-1.99*	1.26	0.63	-0.02*	3.30	0.40	1.29
3	0.094	0.08	0.46	9.08	1.57	0.31	5.95	1.48	3.71
4	0.157	0.21	6.66	40.30	3.36	1.65	17.32	6.34	11.60
5	0.266	1.26	80.91	262.68	9.48	16.53	82.56	48.60	56.29
6	0.387	3.51	252.01	834.30	16.66	55.64	199.79	147.35	131.71
7	0.622	1.62	108.77	359.32	6.24	22.68	77.09	59.84	49.42
8	0.961	0.31	17.84	67.06	2.00	4.96	18.44	11.80	9.62
9	1.62	0.09	0.44	12.46	0.81	1.89	4.79	2.52	2.06
10	2.42	0.07	0.11	6.74	1.27	1.28	6.14	1.03	1.52
11	4.05	0.06	-1.91*	6.21	0.91	2.41	3.97	1.43	1.33
12	6.77	0.07	-1.58*	6.88	1.02	5.44	5.61	1.82	1.91
13	10.04	0.05	-2.99*	1.26	0.65	1.52	4.50	0.40	6.32
	LOD	0.01	11.55	2.21	1.34	0.27	0.70	0.04	0.05
	LOQ	0.03	29.27	5.35	3.79	0.54	1.48	0.08	0.09

* - The laboratory method for HR-ICP-MS may report negative values (see Section 3.3.3.1).

TABLE XVI: METAL FRACTIONS (WT. %) IN SIZE-FRACTIONATED SS WELDING FUME: EMISSION CHAMBER ELPI DATA

Stage ID	Particle Size (μm)	K	Fe	Cr	Na	Mn	Ti	Ni	Other Metal	Total Metal Mass	Other Mass
1	0.028	4.44%	4.62%	1.69%	<0.01%	0.88%	0.21%	1.71%	14.66%	28.21%	71.79%
2	0.055	4.32%	9.12%	3.59%	<0.01%	1.20%	0.05%	1.94%	3.27%	23.50%	76.50%
3	0.094	11.11%	7.28%	4.52%	1.13%	1.80%	0.38%	1.93%	10.39%	38.53%	61.47%
4	0.157	18.95%	8.20%	5.48%	3.15%	2.99%	0.78%	1.58%	7.48%	48.61%	51.39%
5	0.266	21.05%	6.62%	4.50%	6.51%	3.89%	1.32%	0.76%	3.90%	48.55%	51.45%
6	0.387	23.87%	5.69%	3.75%	7.19%	4.20%	1.58%	0.48%	4.23%	50.98%	49.02%
7	0.622	21.61%	4.68%	2.99%	6.56%	3.61%	1.37%	0.38%	1.93%	43.12%	56.88%
8	0.961	21.54%	5.96%	3.10%	5.72%	3.80%	1.61%	0.64%	2.56%	44.93%	55.07%
9	1.62	14.08%	5.57%	2.35%	0.91%	2.86%	2.15%	0.94%	2.01%	30.88%	69.12%
10*	2.42	7.26%	6.61%	1.64%	0.12%	1.10%	1.38%	1.37%	6.12%	25.60%	74.40%
11*	4.05	13.89%	8.88%	2.97%	<0.01%	3.20%	5.39%	2.04%	5.68%	42.04%	57.96%
12*	6.77	10.00%	8.15%	2.77%	<0.01%	2.65%	7.90%	1.48%	7.36%	40.30%	59.70%
13*	10.04	3.66%	13.09%	18.36%	<0.01%	1.16%	4.41%	1.88%	5.02%	47.57%	52.43%

* - Data presented reflect only one filter analyzed by HR-ICP-MS.

B Micro-Orifice Uniform Deposit Impactor

The results of the MOUDI Emission chamber experiments are presented in TABLE XVII and Figure 20 below. Fractionated mass concentrations ranged from 0.03 mg/m^3 (Back-up filter; <0.056 μm) and 1.45 mg/m^3 (Stage 7; 0.56 μm) with higher concentrations observed in stages 6-8. The amount of metal mass recovered per stage ranges from 3% (Back-up Filter; <0.056 μm) to 51% (stage 1; 18 μm) of total fume mass.

Potassium is present above the LOQ on all stages and concentrations ranged from 0.17 μg/m3 in the back-up filter (<0.056 μm) to 272 μg/m3 in stage 7 (0.56 μm). The fraction of total mass contribution for potassium varies from 0.5% (back-up filter; <0.056 μm) to 19.2% (stage 6; 1.0 μm), with larger fractions observed between stages 10 and 4 corresponding to particle cut-off points of 0.1 – 3.2 μm, respectively. Sodium is only present above the LOQ in stages 9 - 6 in concentrations from 289 μg/m3 in stage 7 to 39 μg/m3 in stage 6. The sodium concentrations of stages 10 and 5 are below the LOQ but above the LOD. Sodium mass fractions range from 0.1% (stage 11; 0.056 μm) to 20.5% (stage 7; 0.56 μm) of total fume mass with larger fractions observed between particle size cut-off points of 0.1 to 1.8 μm (i.e., stages 10 through 5).

Iron is present above the LOQ in all stages but the back-up filter and concentrations range from 2 μg/m3 in stage 11 (0.056 μm) to 66 μg/m3 in stage 8 (0.32 μm). The fraction of total mass contribution per size fraction is measured between 0.9% (back-up filter; <0.056 μm) and 10.4% (stage 3; 5.6 μm). Chromium is present above the LOQ on all stages except the back-up filter in concentrations ranging from 0.58 μg/m3 in stage 11 to 43 μg/m3 in stage 7 (0.56 μm). The fraction

of total mass contribution from chromium is measured between 0.4% (back-up filter; <0.056 μm) and 4.2%/4.4% (i.e., stage 10 (0.1 μm)/stage 1 (18 μm)). Manganese is present above the LOQ in all stages except the back-up filter and ranges in concentration from 0.3 μg/m3 in stage 11 to 49 μg/m3 in stage 7. The fraction of total fume mass contribution from manganese ranges from 0.1% (back-up filter; <0.056 μm) to 3.5% (stage 6 (1 μm)/stage 5 (1.8 μm)). Titanium is also present in all stages, ranging from 0.03% (back-up filter; <0.056 μm) to 15.2% (stage 1; 18 μm), with the stages with cut-off points greater than 3.2 μm (i.e., stage 4) exhibiting larger mass fractions (>6.5%). Nickel is present above the LOQ in stages 10 – 6 and stage 2 and above the LDD in the back-up filter and stages 5 -3 and 1. Nickel concentrations range from 0.01 μg/m3 in back-up filter to 6 μg/m3 in stage 9 and 8. The fraction of total fume mass contributed by nickel ranges from 0.02%% (back-up filter) to 1.6% (stage 10; 0.1 μm) of total fume mass. Other metals constituted the remaining metal mass at fractions ranging from 0.25% (back-up filter; <0.056 μm) to 13% (stage 1; 18 μm) of total fume mass. In addition, other metals accounted for 12% of total fume mass in stage 3 (i.e., 5.6 μm).

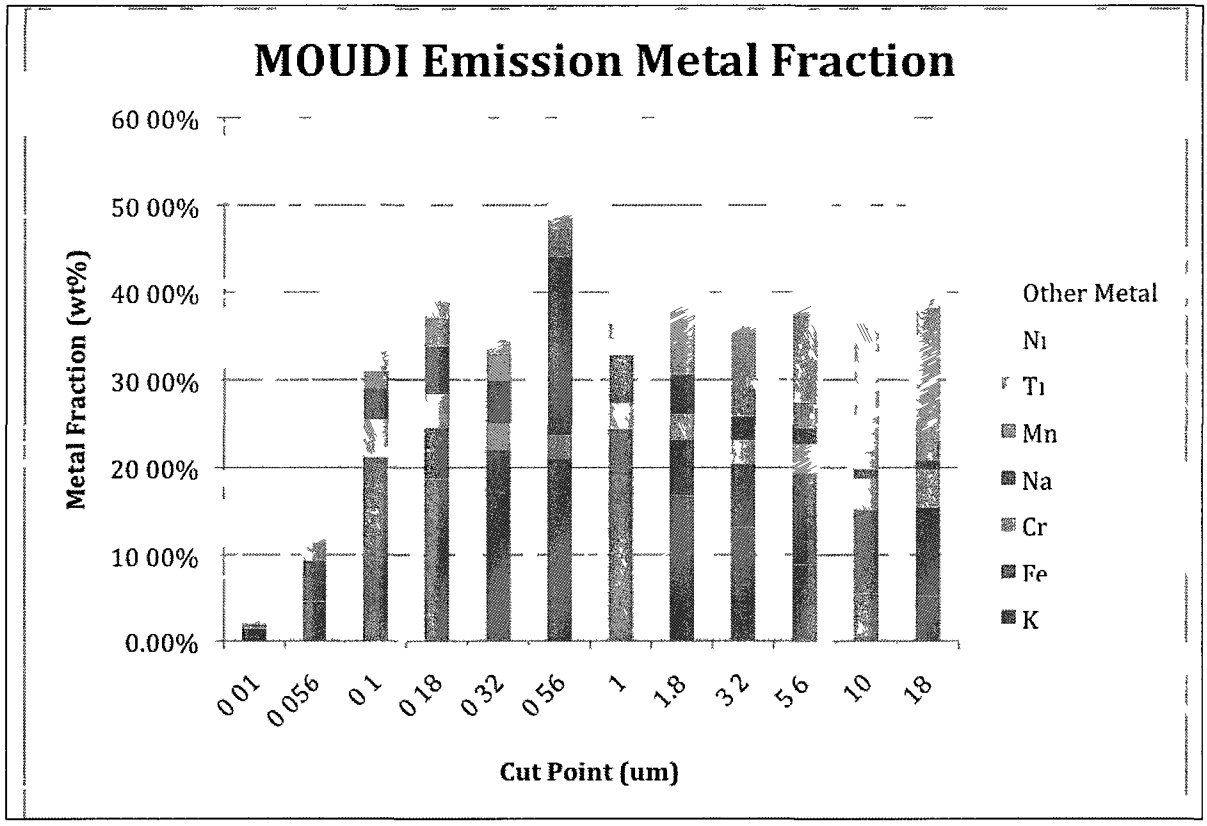

Figure 20: Metal fraction distribution of size-fractionated SS welding fume: emission chamber MOUDI data.

TABLE XVII: METAL MASS CONCENTRATIONS (μG/M³) IN SIZE-FRACTIONATED SS WELDING FUME: EMISSION CHAMBER MOUDI DATA

Stage ID	Particle Size (um)	Mass Conc. (mg/m3)	Na (μg/m³)	K (μg/m³)	Ni (μg/m³)	Ti (μg/m³)	Fe (μg/m³)	Mn (μg/m³)	Cr (μg/m³)
Backup	0.028	0.03	0.03	0.17	0.01	0.00	0.21	0.03	0.12
11	0.056	0.04	0.00	2.01	0.18	0.03	1.89	0.27	0.58
10	0.1	0.08	3.97	17.51	1.80	0.60	6.79	2.46	4.82
9	0.18	0.48	42.63	143.24	6.18	8.55	44.06	24.57	29.68
8	0.32	0.93	69.85	243.85	6.11	15.98	66.36	43.40	41.52
7	0.56	1.45	289.18	271.81	5.40	20.22	53.56	48.50	42.72
6	1	1.15	38.50	132.98	3.03	10.93	36.37	24.11	20.26
5	1.8	0.44	4.98	17.86	0.59	3.82	6.92	3.75	3.14
4	3.2	0.08	2.06	8.26	0.43	4.51	5.22	2.04	1.90
3	5.6	0.08	0.68	3.26	0.41	3.59	3.80	1.07	1.22
2	10	0.05	0.81	3.80	0.72	9.53	7.02	1.46	2.60
1	18	0.09	0.44	2.50	0.57	7.41	5.18	1.15	2.26
Back-up Filter	**LOD**	0.01	0.11	0.06	0.01	0.04	0.32	0.02	0.17
	LOQ	0.03	0.27	0.16	0.02	0.09	0.92	0.05	0.24
Stage Filters	**LOD**	0.01	2.10	0.77	0.22	0.16	0.64	0.03	0.06
	LOQ	0.03	5.37	1.47	0.60	0.27	1.03	0.06	0.09

TABLE XVIII METAL FRACTIONS (WT. %) IN SIZE-FRACTIONATED SS WELDING FUME: EMISSION CHAMBER MOUDI DATA

Stage ID	Particle Size (μm)	K	Fe	Cr	Na	Mn	Ti	Ni	Other Metal	Total Metal Mass	Other Mass
Backup	<0.056	0.48%	0.92%	0.41%	0.10%	0.08%	0.03%	0.02%	0.25%	2.28%	97.72%
11	0.056	4.54%	4.72%	1.35%	0.09%	0.65%	0.06%	0.42%	2.62%	14.44%	85.56%
10	0.1	15.25%	5.93%	4.20%	3.44%	2.15%	0.52%	1.57%	1.60%	34.68%	65.32%
9	0.18	18.72%	5.75%	3.86%	5.53%	3.19%	1.11%	0.80%	1.87%	40.81%	59.19%
8	0.32	17.30%	4.70%	2.96%	4.96%	3.09%	1.14%	0.44%	1.59%	36.19%	63.81%
7	0.56	17.46%	3.49%	2.74%	20.45%	3.13%	1.30%	0.35%	1.75%	50.67%	49.33%
6	1	19.19%	5.16%	2.93%	5.54%	3.47%	1.60%	0.45%	2.28%	40.61%	59.39%
5	1.8	16.75%	6.37%	2.89%	4.61%	3.49%	3.66%	0.57%	3.38%	41.71%	58.29%
4	3.2	13.13%	7.33%	2.66%	2.68%	3.03%	6.48%	0.69%	3.95%	39.95%	60.05%
3	5.6	8.90%	10.43%	3.36%	1.81%	2.94%	9.94%	1.15%	11.91%	50.45%	49.55%
2	10	5.36%	9.75%	3.67%	1.05%	2.08%	13.50%	1.05%	8.68%	45.14%	54.86%
1	18	5.13%	10.28%	4.35%	1.07%	2.24%	15.15%	1.07%	12.95%	52.24%	47.76%

C Personal Cascade Impactor Sampler

The results of the PCIS emission chamber experiments are presented in Figure 21 and below. Fractionated mass concentrations ranged from 0.07 mg/m^3 (Stage A; 2.5 μm) and 5.06 mg/m^3 (Back-up filter; <0.25 μm) with much higher concentrations observed in stage D (i.e., 4.6 mg/m^3) and back-up filter. The amount of metal mass collected per stage ranged from 10% (back-up filter) to 49% (stage A) of total fume mass. Elemental compositional analysis could not be replicated on stages A and B due to insufficient amount of fume collected on these filters, preventing post-treatment of samples by HR-ICP-MS.

Potassium is present above the LOQ on all stages except stage A where it is present above the LOD. Concentrations of potassium range from 5 μg/m3 on stage A (2.5 μm) to 992 μg/m3 on stage D (0.25 μm). Total mass fraction contribution from potassium per size fraction varies from 4.6% (back-up filter; <0.25 μm) to 21.6% (stage D) of total fume mass, with larger mass fractions observed between particle size cut-points of 0.25 – 0.5 μm corresponding to stages D–C. Sodium is only present above the LOQ in stages D (298 μg/m3) and back-up filter (52 μg/m2). Total mass fraction contribution from sodium is 1.2% (back-up filter; <0.25 μm) and 6.8% (stage D) of total fume mass.

Iron is present in all stages of the PCIS in concentrations ranging from 5 μg/m3 in stage B (1 μm) to 231 μg/m3 in stage D and total mass fractions are measured between 1.0% (back-up filter; <0.25 μm) and 7.8% (stage A; 2.5 μm) of total fume mass, while having about 5% mass fraction in each of stage C (0.5 μm) and D (0.25 μm). Chromium is also present on all stages in concentrations

ranging from 2 μg/m3 in stages A and B to 157 μg/m3 in sage D. Total mass fraction contributions from chromium are measured between 1.1% (stage B) and 3.4% (stage D) of total fume mass. Chromium is also present at 3.1% of total fume mass in stage A (2.5 μm). Manganese is present in all stages in concentrations ranging from 2 μg/m3 in stage A to 177 μg/m3 in stage D. Total mass fractions contribution from manganese range from 0.7% (back-up filter; <0.25 μm) to 3.8% (stage D; 0.25 μm) of total fume mass. Titanium is present in all stages in concentrations ranging from 3 μg/m3 to 76 μg/m3 in stage D. Total mass fraction contribution from titanium ranges from 0.3% (back-up filter; 0.1 μm) to 7.6% (stage A; 2.5 μm) of total fume mass, while highest mass fraction of total fume observed on stage A. Nickel is present only in stages D and back-up filter in concentrations of 18 μg/m3 and 12 ug/m3, respectively. Total mass fraction contribution from nickel ranges from 0.1% (back-up filter; <0.25 μm) to 0.4% (stage C/D; 0.5 μm/0.25 μm) of total fume mass. Other metals constituted the remaining metal mass at fractions ranging from 0.3% (back-up filter; <0.25 μm) to 19% (stage A; 2.5 μm) of total fume mass with stage A having significantly higher mass fraction as compared to other stages (<4.2%).

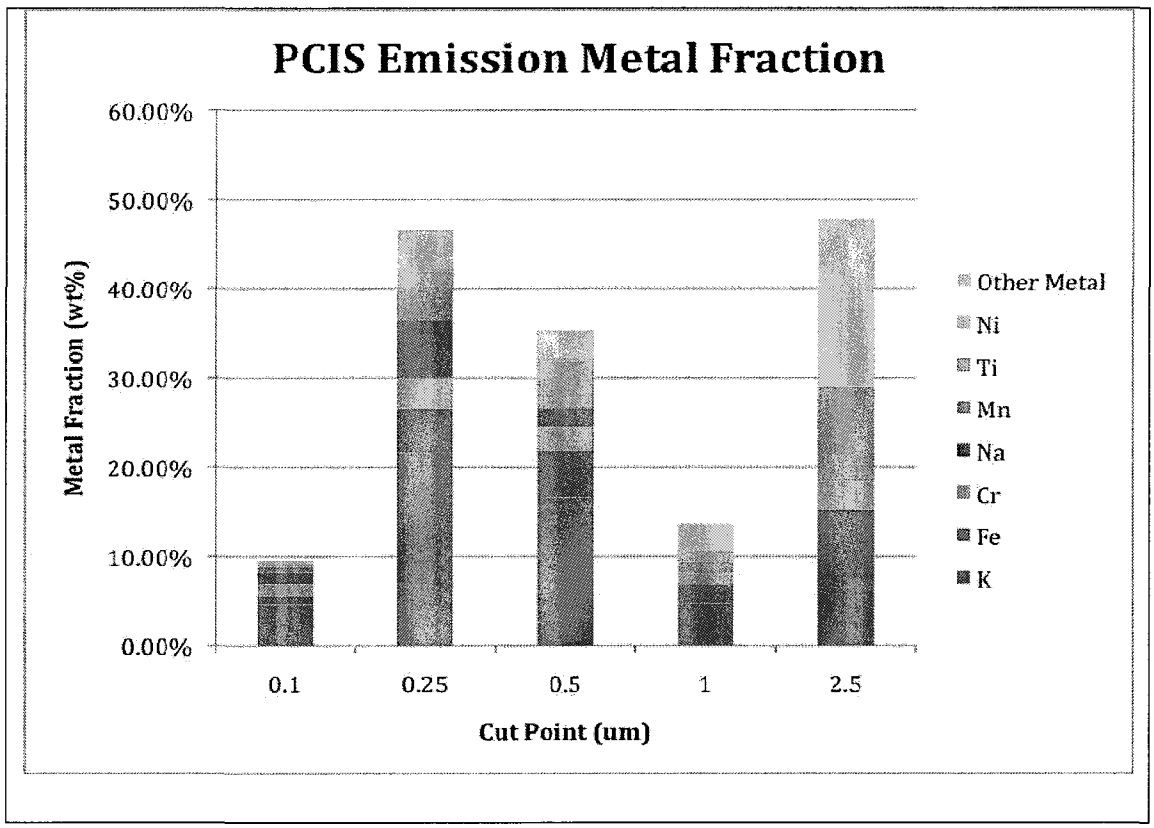

Figure 21: Metal fraction distribution of size-fractionated SS welding fume: emission chamber PCIS data.

TABLE XIX: METAL MASS CONCENTRATIONS (μG/M3) IN SIZE-FRACTIONATED SS WELDING FUME: EMISSION CHAMBER PCIS DATA

Stage ID	Particle Size (μm)	Mass Conc. (mg/m3)	Na (μg/m^3)	K (μg/m^3)	Ni (μg/m^3)	Ti (μg/m^3)	Fe (μg/m^3)	Mn (μg/m^3)	Cr (μg/m^3)
Backup	<0.25	5.06	52.41	191.00	5.48	11.85	42.88	29.62	59.94
D	0.25	4.60	297.86	992.13	17.52	75.91	230.59	176.60	156.80
C	0.5	0.19	3.63	31.11	0.78	3.49	9.69	6.40	5.30
B	1	0.17	-3.23*	10.18	-0.17*	2.88	4.91	2.94	2.37
A	2.5	0.07	-4.59*	5.34	-0.06*	5.51	5.68	2.22	2.28
Back-up	LOD	0.01	0.87	0.48	0.05	0.31	2.42	0.12	1.26
Filter	LOQ	0.03	2.03	1.21	0.14	0.69	6.98	0.36	1.81
Stage	LOD	0.01	20.31	3.89	2.36	0.47	1.23	0.07	0.09
Filters	LOQ	0.03	51.49	9.41	6.67	0.94	2.61	0.14	0.17

* - The laboratory method for HR-ICP-MS may report negative values (see Section 3.3.3.1).

TABLE XX: METAL FRACTIONS (WT. %) IN SIZE-FRACTIONATED SS WELDING FUME: EMISSION CHAMBER PCIS DATA

Stage ID	Particle Size (μm)	K	Fe	Cr	Na	Mn	Ti	Ni	Other Metal	Total Metal Mass	Other Mass
Backup	<0.25	4.56%	1.02%	1.33%	1.24%	0.70%	0.28%	0.13%	0.32%	9.57%	90.43%
D	0.25	21.62%	4.99%	3.40%	6.48%	3.82%	1.65%	0.38%	4.22%	46.56%	53.44%
C	0.5	16.60%	5.18%	2.83%	1.95%	3.41%	1.85%	0.43%	2.99%	35.25%	64.75%
B*	1	4.67%	2.25%	1.09%	<0.01%	1.35%	1.32%	<0.01%	2.95%	13.63%	86.37%
A*	2.5	7.35%	7.82%	3.14%	<0.01%	3.05%	7.59%	<0.01%	18.83%	47.79%	52.21%

* - Data presented reflect only one filter analyzed by HR-ICP-MS.

3.4.2.2 Exposure Chamber Results

A Electronic Low Pressure Impactor

Results of the ELPI Exposure chamber experiments are presented in Figure 22 and **TABLE** XXI below. Fractionated fume mass-based concentrations ranged from 0.03 mg/m^3 (Stage 13; 10.04 μm) to 0.92 mg/m^3 (stage 6; 0.387 μm) in the breathing-zone of the manikin with higher concentrations observed in stages 5-7 (i.e., 0.266μm - 0.622μm). The amount of recovered metal mass per stage ranged from 4% (stage 2; 0.055 μm) to 45% (stage 6; 0.387 μm) of total fume mass. Elemental compositional analysis could not be replicated for filters on stages 1 (0.028 μm), 2 (0.055 μm) or 10 (2.42 μm) due to insufficient amount of fume collected on these filters, preventing post-treatment of samples by HR-ICP-MS.

Potassium was present above the LOQ on stages 4 – 8 and above the LOD on stages 3 and 9 – 11. Concentrations of potassium range from 2 μg/m3 on stages 9 – 11 and 184 μg/m3 on stage 6. Total mass fraction contribution from potassium range from 0.3% (stage 2; 0.055 μm) to 19.4 %(stage 6; 0.387 μm) of total fume mass, with larger mass fractions observed in particle size cut-off points between 0.157 μm and 0.961 μm (stages 4 – 8). Sodium was present above the LOQ only in stages 6 and 7 in concentrations of 63 and 24 μg/m3, respectively. Total mass fraction contribution from sodium on stage 6 is 6.5% and on stage 7 is 5.9%.

Iron was present in all stages above the LOQ in concentrations ranging from 0.8 μg/m3 in stage 1 and 62 μg/m3 in stage 6. Total mass fraction contributions from iron range from 1.2%

(stage 1; 0.028 μm) to 14.4% (stage 4; 0.157 μm) of total fume mass. Chromium was present above the LOQ in all stages in concentrations from 0.3 μg/m3 in stage 13 to 34 μg/m3 in stage 6. Total mass fraction contribution from chromium ranges from 0.2% (stage 2; 0.055 μm) to 6.2 % (stage 4; 0.157 μm) of total fume mass. Manganese was also present above the LOQ in all stages in concentrations from 0.1 μg/m3 in stage 13 to 39 μg/m3 in stage 6. Total mass fraction contribution from manganese ranges from 0.03% (stage 2; 0.055 μm) to 4.2% (stage 6; 0.387 μm) of total fume mass. Nickel was present above the LOQ in stages 4 – 6 and above the LOD in stages 3, 7 and 8. Concentrations of nickel ranged from 1 μg/m3 in stage 8 to 7 μg/m3 in stage 6. Total mass fraction contribution from nickel ranges from 0.03% (stage 1; 0.028 μm) to 4.4%/3.9% (stage 4 (0.157 μm)/stage 3(0.094 μm)) of total fume mass. Titanium was present above the LOQ in stages 1 and 4 – 8 and above the LOD in stages 3 and 9 – 11. Titanium concentrations range from 0.2 μg/m3 in stages 3, 10 and 11 to 13 μg/m3 in stage 6. Total mass fraction contribution from titanium range from 0.04% (stage 2; 0.055 μm) to 2.7% (stage 1; 0.028 μm) of total fume mass. Other metals constituted the remaining metal mass at mass fractions ranging from 1.86% (stage 7; 0.622 μm) to 6.8% (stage 13; 10.04 μm) of total fume mass. Stage 3 (0.094 μm) also had other metal mass fraction totaling 6.2% of total fume mass.

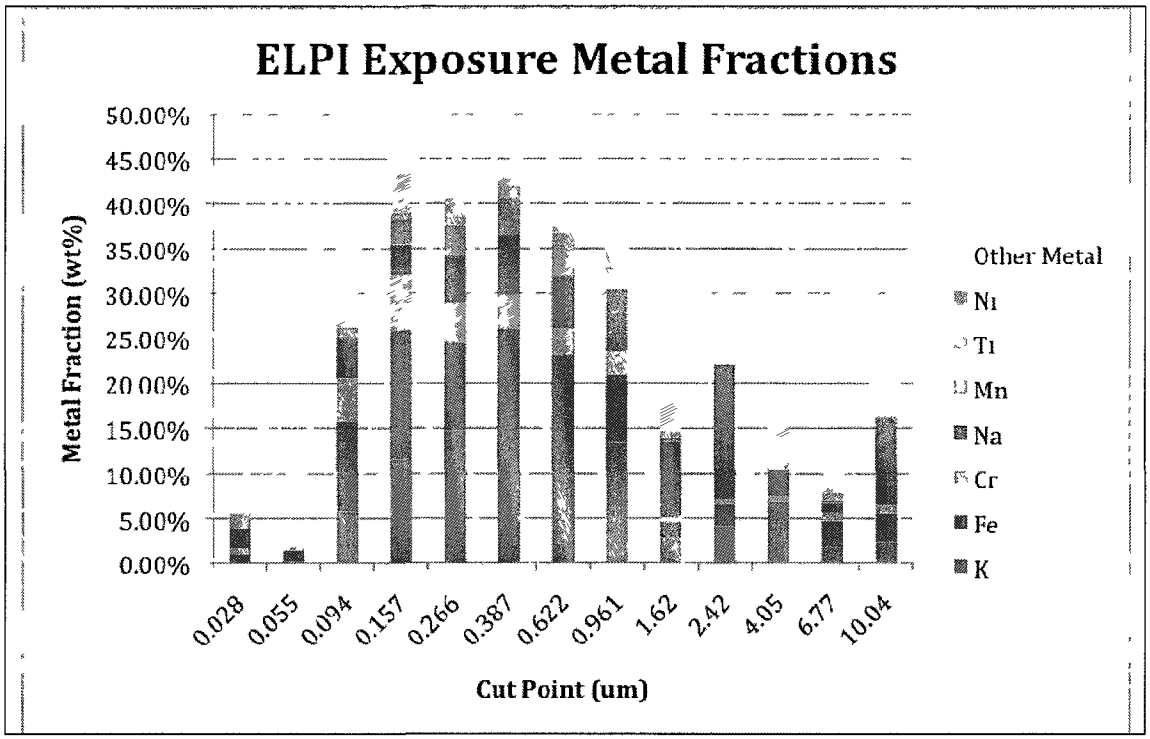

Figure 22: Metal fraction distribution of size-fractionated SS welding fume: exposure chamber ELPI data.

TABLE XXI: METAL MASS CONCENTRATIONS (μG/M3) IN SIZE-FRACTIONATED SS WELDING FUME: EXPOSURE CHAMBER ELPI DATA

Stage ID	Particle Size (μm)	Mass Conc. (mg/m3)	Na (μg/m³)	K (μg/m³)	Ni (μg/m³)	Ti (μg/m³)	Fe (μg/m³)	Mn (μg/m³)	Cr (μg/m³)
1	0.028	0.03	-0.61*	0.29	0.11	0.83	0.78	0.18	0.53
2	0.055	0.11	1.69	0.87	0.62	0.07	3.91	0.15	0.91
3	0.094	0.06	1.09	3.19	2.14	0.20	5.46	0.70	2.62
4	0.157	0.10	3.66	11.15	4.23	0.55	13.96	2.79	6.04
5	0.266	0.31	16.97	45.70	5.48	3.21	30.63	11.00	13.65
6	0.387	0.92	62.61	184.28	7.11	13.15	61.53	38.66	34.36
7	0.622	0.36	23.94	64.06	2.11	4.55	21.93	12.82	10.78
8	0.961	0.10	9.56	12.92	0.98	0.81	6.88	2.27	2.39
9	1.62	0.08	5.48	2.22	0.27	0.30	1.50	0.32	0.44
10	2.42	0.08	10.00	2.70	0.41	0.23	1.63	0.18	0.40
11	4.05	0.08	-0.39*	2.29	0.32	0.23	1.72	0.14	0.43
12	6.77	0.06	0.88	0.96	0.14	0.33	1.47	0.12	0.37
13	10.04	0.05	3.64	0.89	0.21	0.09	1.27	0.06	0.34
	LOD	0.01	7.70	1.47	0.90	0.18	0.76	0.03	0.03
	LOQ	0.03	19.51	3.57	2.53	0.36	0.99	0.06	0.06

* - The laboratory method for HR-ICP-MS may report negative values (see Section 3.3.3.1).

TABLE XXII: METAL FRACTIONS (WT. %) IN SIZE-FRACTIONATED SS WELDING FUME: EXPOSURE CHAMBER ELPI DATA

Stage ID	Particle Size (μm)	K	Fe	Cr	Na	Mn	Ti	Ni	Other Metal	Total Metal Mass	Other Mass
1*	0.028	0.86%	1.22%	1.32%	4.40%	0.48%	2.70%	0.03%	5.17%	16.19%	83.81%
2*	0.055	0.30%	2.68%	0.21%	<0.01%	0.03%	0.04%	0.13%	2.33%	8.47%	45.76%
3	0.094	5.70%	10.03%	4.83%	4.42%	1.28%	0.28%	3.94%	6.25%	36.73%	63.27%
4	0.157	11.53%	14.40%	6.22%	3.34%	2.89%	0.57%	4.39%	2.59%	45.93%	54.07%
5	0.266	14.68%	9.85%	4.42%	5.10%	3.57%	1.03%	1.78%	2.31%	42.76%	57.24%
6	0.387	19.40%	6.74%	3.71%	6.51%	4.21%	1.42%	0.79%	2.14%	44.92%	55.08%
7	0.622	17.18%	5.98%	2.93%	5.91%	3.50%	1.23%	0.59%	1.86%	39.18%	60.82%
8	0.961	13.48%	7.45%	2.57%	6.93%	2.48%	0.87%	1.08%	4.98%	39.84%	60.16%
9	1.62	2.70%	1.85%	0.54%	8.50%	0.40%	0.37%	0.33%	3.03%	17.72%	82.28%
10*	2.42	4.06%	2.45%	0.60%	15.03%	0.27%	0.35%	0.61%	2.38%	25.76%	74.24%
11	4.05	4.59%	2.34%	0.62%	2.72%	0.21%	0.39%	0.45%	5.15%	16.47%	83.53%
12	6.77	1.74%	3.04%	0.78%	1.26%	0.25%	0.78%	0.49%	2.12%	10.47%	89.53%
13	10.04	2.35%	3.20%	0.87%	9.94%	0.15%	0.22%	0.43%	6.79%	23.95%	76.05%

* - Data presented reflect only one filter analyzed by HR-ICP-MS.

B Micro-Orifice Uniform Deposit Impactor

Results from the MOUDI exposure chamber experiments are presented in Figure 23 and **TABLE** XXII below. Fractionated fume mass concentrations ranged from <0.01 mg/m^3 (stages 11 and 4/ 0.056 μm and 3.2 μm) to 0.19 mg/m^3 (stage 7; 0.56 μm) within the breathing zone of the manikin, with the higher concentrations observed in stages 9-7 (i.e., 0.18μm - 0.56μm). The amount of metal mass recovered per stage ranged from 3% (back-up filter; <0.056 μm) to 66% (stage 4: 3.2 μm) of total fume mass. Elemental compositional analysis could not be replicated for filters on stages 11 (0.056 μm), 5 (1.8 μm), 4 (3.2 μm) or 3 (5.6 μm) due to insufficient amount of fume collected on these filters, preventing post-treatment of samples by HR-ICP-MS.

Potassium was present above the LOQ on stages 10 – 4 in concentrations ranging from 1 μg/m3 in stages 10, 5 and 4 to 43 μg/m3 in stage 7. Total mass fraction contribution from potassium ranges from 0.3% (back-up filter; <0.056 μm) to 21.6% (stage 7; 0.56 μm) of total fume mass, with larger fractions observed in particle size cut-off points between 0.18 and 3.2 μm (i.e., stages 9 through 4). Sodium was present above the LOQ in stages 9 – 7 and above the LOD in stage 6. Sodium concentrations ranges from 3 μg/m3 in stages 9 and 6 to 12 μg/m3 in stage 7. Total mass fraction contribution from sodium ranges from 0.1% (stage 2; 10 μm) to 6.0% (stage 7; 0.56μm) of total fume mass, except in stages 3 (5.6μm) and 11 (0.056 μm) where negligible mass was collected (i.e., <0.01%). Furthermore, larger fractions of sodium in total fume mass (4.65%-6%) were found on stages with particle size cut-off points between 0.18 μm and 1.0 μm (i.e., stages 9 – 6).

Iron was present above the LOQ in stages 10 – 1 in concentrations ranging from 0.7 μg/m3 in stages 5 and 3 to 18 μg/m3 in stage 7. Total mass fraction contribution from iron ranges from 0.15% (back-up filter; <0.056 μm) to 19% (stage 4; 3.2 μm) of total fume mass. Chromium was present above the LOQ in all stages except the back-up filter in concentrations ranging from 0.2 μg/m3 in stage 11 to 8 μg/m3 in stage 7. Total mass fraction contribution from chromium ranges from 0.6% (back-up filter; <0.056 μm) to 8.4% (stage 10; 0.1 μm) of total fume mass. Manganese was present above the LOQ in all stages except the back-up filter in concentrations ranging from 0.04 μg/m3 in stage 11 to 8 μg/m3 in stage 7. Total mass fraction contributions from manganese range from 0.02% (back-up filter; <0.056 μm) to 4.3% (stage 7; 0.56 μm) of total fume mass. Titanium was present above the LOQ in stage 9 – 6 and 4 – 1 and above the LOD in stages 11 and 5. Concentrations of titanium range from 0.1 μg/m3 to 3 μg/m3 in stage 7. Total mass fraction contribution from titanium ranges from 0.01% (back-up filter; <0.056 μm) to 7.4% (stage 1; 18 μm) of total fume mass, with the majority of Ti metal accumulation occurring on stages with larger size cut-points (i.e., stage 1-4/18 μm-3.2 μm). Nickel was present above the LOQ in stages 10 – 6 and 2-1 in concentrations ranging from 0.4 μg/m3 in stage 2 and 1 to 2 ug/m3 in stages 9 and 8. Total mass fraction contribution from nickel ranges from 0.03% (back-up filter; <0.056 μm) to 5.8% (stage 10; 0.1 μm) of total fume mass. Other metals constituted the remaining metal mass at mass fractions ranging from 0.5% (stage 3; 5.6 μm) to 15.8%/15.3% (stage 1/10; 18 μm/0.1 μm, respectively) of total fume mass.

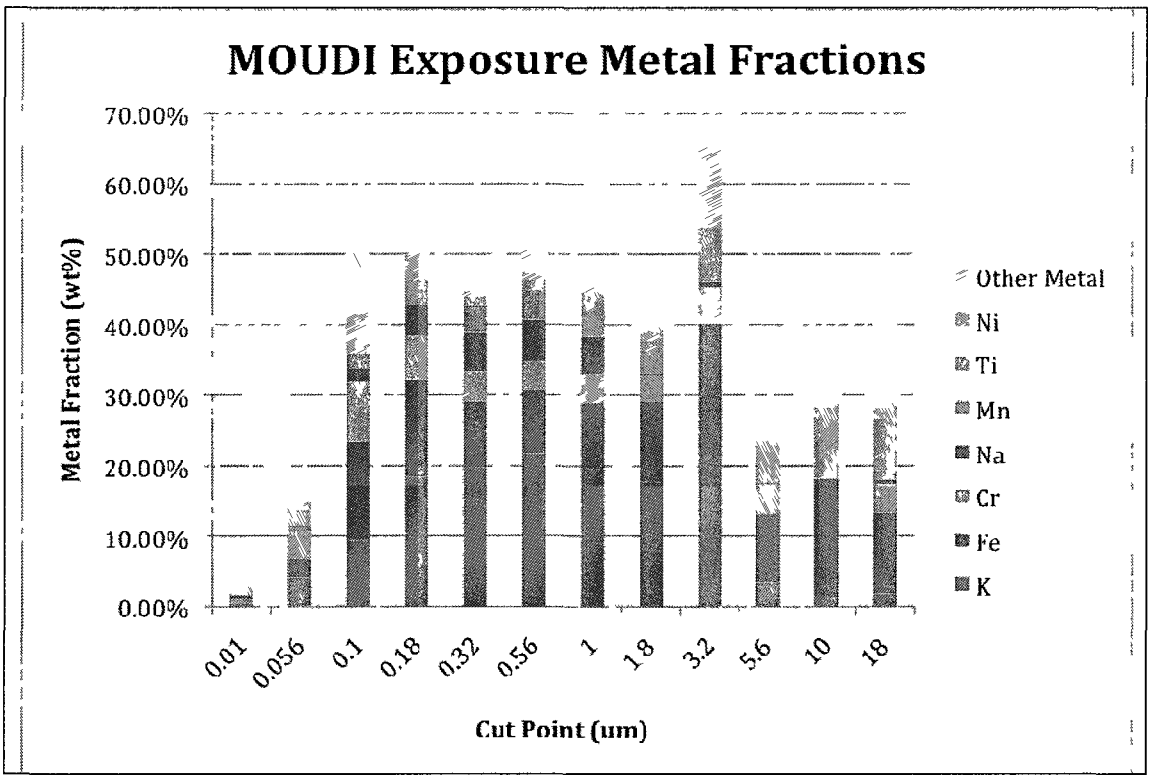

Figure 23: Metal fraction distribution of size-fractionated SS welding fume: exposure chamber MOUDI data.

TABLE XXIII: METAL MASS CONCENTRATIONS (μG/M3) IN SIZE-FRACTIONATED SS WELDING FUME: EXPOSURE CHAMBER MOUDI DATA

Stage ID	Particle Size (μm)	Mass Conc. (mg/m^3)	Na ($\mu g/m^3$)	K ($\mu g/m^3$)	Ni ($\mu g/m^3$)	Ti ($\mu g/m^3$)	Fe ($\mu g/m^3$)	Mn ($\mu g/m^3$)	Cr ($\mu g/m^3$)
Backup	<0.056	0.01	0.08	0.02	0.00	0.00	0.01	0.00	0.06
11	0.056	<0.01	-0.06*	0.19	0.05	0.10	0.13	0.04	0.18
10	0.1	0.01	0.24	1.25	0.77	0.03	1.87	0.25	1.13
9	0.18	0.07	3.48	13.88	2.18	0.63	10.36	2.54	4.55
8	0.32	0.15	8.23	30.29	2.09	1.87	14.56	6.07	6.67
7	0.56	0.19	11.78	43.10	1.90	2.64	18.31	8.44	7.85
6	1	0.05	2.58	9.16	0.55	0.58	4.39	1.94	1.92
5	1.8	0.01	0.01	1.14	0.08	0.14	0.74	0.17	0.24
4	3.2	<0.01	0.04	1.19	0.12	0.29	1.05	0.14	0.29
3	5.6	0.01	-0.08*	0.25	0.12	0.31	0.74	0.08	0.25
2	10	0.02	-0.04*	0.21	0.38	0.72	2.43	0.17	0.64
1	18	0.03	0.17	0.49	0.44	2.19	3.15	0.38	1.14
Back-up filter	LOD	0.01	0.07	0.04	0.01	0.03	0.19	0.01	0.10
	LOQ	0.03	0.16	0.09	0.02	0.05	0.53	0.03	0.14
Stage Filters	LOD	0.01	1.22	0.45	0.13	0.10	0.38	0.02	0.03
	LOQ	0.03	3.13	0.86	0.35	0.16	0.60	0.03	0.05

* - The laboratory method for HR-ICP-MS may report negative values (see Section 3.3.3.1).

TABLE XXIV: METAL FRACTIONS (WT. %) IN SIZE-FRACTIONATED SS WELDING FUME: EXPOSURE CHAMBER MOUDI DATA

Stage ID	Particle Size (μm)	K	Fe	Cr	Na	Mn	Ti	Ni	Other Metal	Total Metal Mass	Other Mass
Backup	0.01	0.29%	0.15%	0.63%	0.65%	0.02%	0.01%	0.03%	1.82%	3.60%	96.40%
11*	0.056	4.06%	2.76%	3.86%	<0.01%	0.82%	2.25%	1.06%	1.10%	15.91%	84.09%
10	0.10	9.41%	14.11%	8.44%	1.87%	1.90%	0.25%	5.76%	15.32%	57.05%	42.95%
9	0.18	18.45%	13.72%	6.16%	4.65%	3.40%	0.83%	3.00%	7.01%	57.22%	42.78%
8	0.32	19.69%	9.43%	4.35%	5.35%	3.94%	1.22%	1.37%	3.46%	48.82%	51.18%
7	0.56	21.64%	9.11%	3.98%	5.99%	4.30%	1.33%	0.98%	3.91%	51.24%	48.76%
6	1.0	19.65%	9.31%	3.94%	5.40%	4.02%	1.19%	1.12%	2.04%	46.67%	53.33%
5*	1.8	17.66%	11.42%	3.71%	0.21%	2.55%	2.14%	1.29%	1.34%	40.31%	59.69%
4*	3.2	21.37%	18.85%	5.16%	0.81%	2.45%	5.17%	2.09%	9.53%	65.42%	34.58%
3*	5.6	3.39%	9.92%	3.34%	<0.01%	1.07%	4.13%	1.61%	0.51%	23.97%	76.03%
2	10	1.54%	16.69%	4.15%	0.11%	1.11%	4.68%	2.39%	3.85%	34.51%	65.49%
1	18	1.84%	11.57%	3.95%	0.74%	1.28%	7.38%	1.56%	15.84%	44.15%	55.85%

* - Data presented reflect only one filter analyzed by HR-ICP-MS.

C Personal Cascade Impactor Sampler-Inside the Welding Helmet

The results of PCIS inside the manikin's welding helmet during exposure chamber experiments are presented in Figure 24 and TABLE XXV below. Fractionated fume mass concentrations ranged from 0.05 mg/m3 (Stages A and B; 2.5 μm and 1.0 μm) to 2.6 mg/m^3 (back-up filter; <0.25 μm), with majority of mass collected in stages D (0.25 μm; 1.6 mg/m^3) and back-up stage. The amount of metal mass recovered per stage ranged from 6% (back-up filter) to 44% (stage D). Elemental composition analysis was not performed in replicate for stage A, B, and C due to budgetary constraints.

Potassium was present in aerodynamic particle size cut-off points less than 1.0 μm in diameter in concentrations from 39 μg/m3 in stage C and 322 μg/m3 in stage D. Total mass fraction contribution from potassium 1.0 % (stage B; 1 μm) to 21.0 % (stage D; 0.25 μm), with higher mass fractions limited to stages C (0.5 μm-13.9%) and D (0.25 μm). Sodium was found above the LOQ only in particle size cut-off points less than 0.5 μm in diameter in concentrations of 18 and 108 μg/m3 in the back-up filter and stage D, respectively. The total mass fraction contribution of sodium ranges from 0.9% (back-up filter; <0.25 μm) to 6.9% (stage D; 0.25 μm), with higher mass fractions being observed in stages C (2.9%) and D, as indicated above for potassium.

Iron was found above the LOQ in stages back-up through C and above the LOD in stage B. Concentrations of iron ranged from 1 μg/m3 to 79 μg/m3 in stage D. Total mass fraction contribution from iron ranges from 1.0% (back-up filter; <0.25 μm) to 5.0%/5.2% (stageC/stage D;

0.5 μm/0.25μm). Chromium is found above the LOQ in all stages ranging in concentration from 0.3 μg/m3 in stages B and A to 47 μg/m3 in stage D. Total mass fraction contribution from chromium ranges from 0.4% (stage B; 1 μm) to 3.1% (stage D). Manganese is also found above the LOQ in all stages and concentrations range from 0.2 μg.m3 in stage A to 61 μg/m3 in stage D. Total mass fraction contribution from manganese ranges from 0.4% (stage B; 1 μm) to 3.9 % (stage D; 0.25 μm). Titanium is found above the LOQ in stages back-up through C in concentrations of 3 μg/m3 to 24 ug/m3 in stage D. Total mass fraction contribution from titanium ranges from 0.2% (back-up filter; <0.25 μm) to 1.5% (stage D; 0.25 μm). Nickel is not found above the LOQ but and above the LOD only in back-up filter and stage D in concentrations of 3 and 5 μg/m3, respectively. Total mass fraction contribution from nickel ranges from 0.1% (stage C; 0.5 μm) to 0.4% (stage D; 0.25 μm). In all cases except Ti, stage D (0.25 μm) followed by stage C (0.5 μm) had the largest fraction of total fume mass. In the case of Ti, stage A (2.5 μm) followed by stage D (0.25 μm) had the largest mass fraction. Other metals constituted the remaining metal mass at mass fractions ranging from 0.2% (back-up filter; <0.25 μm) to 16.1% (stage A; 2.5 μm) of total fume mass.

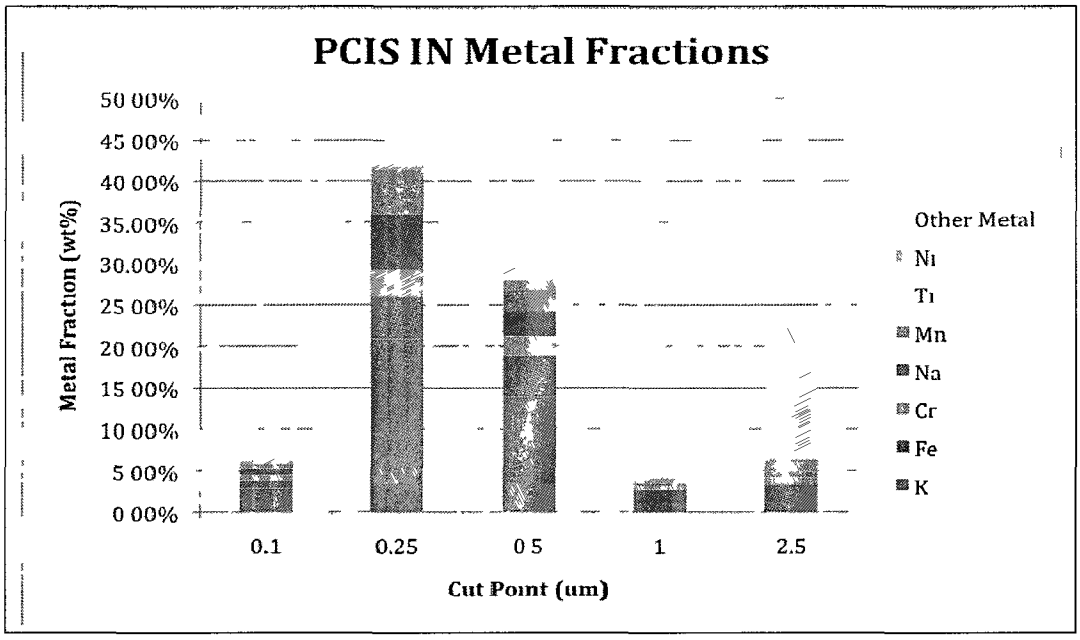

Figure 24: Metal fraction distribution of size-fractionated SS welding fume: exposure chamber PCIS-IN data.

TABLE XXV: METAL MASS CONCENTRATIONS (μG/M³) IN SIZE-FRACTIONATED SS WELDING FUME: EXPOSURE CHAMBER PCIS-IN DATA

Stage ID	Particle Size (μm)	Mass Conc. (mg/m3)	Na (μg/m³)	K (μg/m³)	Ni (μg/m³)	Ti (μg/m³)	Fe (μg/m³)	Mn (μg/m³)	Cr (μg/m³)
Backup	<0.25	2.60	18.41	60.03	3.16	3.98	19.36	10.36	13.29
D	0.25	1.58	107.72	322.17	5.37	24.01	78.54	60.50	47.02
C	0.5	0.20	8.21	38.75	0.28	3.29	13.98	7.47	6.55
B	1	0.05	-5.21*	0.69	-0.83*	0.34	1.23	0.30	0.30
A	2.5	0.05	-3.11*	-0.42*	-1.03*	0.54	1.19	0.22	0.31
	LOD	0.01	0.85	0.47	0.05	0.32	2.38	0.11	1.24
	LOQ	0.03	2.00	1.19	0.14	0.68	6.87	0.35	1.78
	LOD	0.01	19.97	3.82	2.33	0.47	1.21	0.07	0.08
	LOQ	0.03	50.63	9.25	6.55	0.94	2.57	0.14	0.17

* - The laboratory method for HR-ICP-MS may report negative values (see Section 3.3.3.1).

TABLE XXVI: METAL MASS CONCENTRATIONS (μG/M3) IN SIZE-FRACTIONATED SS WELDING FUME: EXPOSURE CHAMBER PCIS-OUT DATA

Stage ID	Particle Size (μm)	Mass Conc. (mg/m3)	Na (μg/m³)	K (μg/m³)	Ni (μg/m³)	Ti (μg/m³)	Fe (μg/m³)	Mn (μg/m³)	Cr (μg/m³)
Backup	<0.25	1.94	42.74	159.57	11.59	9.54	53.92	26.85	35.68
D	0.25	2.13	137.89	436.40	9.86	32.39	124.79	86.39	69.51
C	0.5	0.11	-4.61*	6.89	0.38	0.85	3.11	1.43	1.35
B	1	0.07	-6.07*	1.34	-0.13*	1.33	4.56	0.74	1.18
A	2.5	0.18	-4.91*	3.23	0.69	4.24	6.85	1.37	2.19
	LOD	0.01	0.87	0.48	0.05	0.33	2.43	0.12	1.27
	LOQ	0.03	2.04	1.21	0.14	0.70	7.01	0.36	1.82
	LOD	0.01	20.39	3.90	2.37	0.48	1.24	0.07	0.09
	LOQ	0.03	51.69	9.44	6.69	0.96	2.62	0.15	0.17

* - The laboratory method for HR-ICP-MS may report negative values (see Section 3.3.3.1).

TABLE XXVII: METAL FRACTIONS (WT. %) IN SIZE-FRACTIONATED SS WELDING FUME: EXPOSURE CHAMBER PCIS-IN DATA

Stage ID	d_{ae} (μm)	K	Fe	Cr	Na	Mn	Ti	Ni	Other Metal	Total Metal Mass	Other Mass
Backup	<0.25	2.82%	0.98%	0.66%	0.86%	0.49%	0.18%	0.16%	0.21%	6.36%	93.64%
D	0.25	20.95%	5.19%	3.06%	6.87%	3.88%	1.53%	0.36%	2.01%	43.85%	56.15%
C*	0.5	13.85%	5.00%	2.34%	2.94%	2.67%	1.18%	0.10%	1.41%	29.49%	70.51%
B*	1	0.97%	1.72%	0.42%	<0.01%	0.42%	0.47%	<0.01%	4.49%	8.50%	91.50%
A*	2.5	<0.01%	3.35%	0.87%	<0.01%	0.62%	1.51%	<0.01%	16.12%	22.47%	77.53%

- Data presented reflect only one filter analyzed by HR-ICP-MS.

TABLE XXVIII: METAL FRACTIONS (WT. %) IN SIZE-FRACTIONATED SS WELDING FUME: EXPOSURE CHAMBER PCIS-OUT DATA

Stage ID	d_{ae} (μm)	K	Fe	Cr	Na	Mn	Ti	Ni	Other Metal	Total Metal Mass	Other Mass
Backup	<0.25	8.02%	2.71%	1.79%	2.15%	1.35%	0.48%	0.58%	2.07%	19.16%	80.84%
D	0.25	20.60%	5.88%	3.27%	6.50%	4.07%	1.52%	0.47%	2.76%	45.07%	54.93%
C*	0.50	7.56%	3.41%	1.48%	<0.01%	1.57%	0.93%	0.42%	1.60%	16.97%	83.03%
B*	1.00	1.47%	5.01%	1.30%	<0.01%	0.82%	1.45%	<0.01%	1.85%	11.89%	88.11%
A*	2.50	2.42%	5.12%	1.64%	<0.01%	1.02%	3.17%	0.51%	2.50%	16.40%	83.60%

*- Data presented reflect only one filter analyzed by HR-ICP-MS.

D Personal Cascade Impactor Sampler Outside the Welding Helmet

The results of the PCIS outside the welding helmet of the manikin during exposure chamber experiments are presented in **TABLE** XXVIII above and Figure 25 below. Fractionated fume mass concentrations ranged from 0.07 mg/m^3 (stage B; 1.0 μm) to 2.13 mg/m^3 (stage D; 0.25 μm), with the higher concentrations observed for stages D and back-up (i.e., 1.9 mg/m^3). The amount of recovered metal mass per stage ranged from 12% (stage B) to 45% (stage D). The elemental composition analysis was not performed in replicate for stages A (2.5 μm), B (1 μm) and C (0.5 μm) due to budgetary constraints.

Potassium is present above the LOQ in stage D and back-up filter and above the LOD in stage C. Concentrations of potassium range from 7 μg/m3 to 436 μg/m3. Total mass fraction contribution from potassium ranges from 1.5% (stage B; 1 μm) to 20.6% (stage D; 0.25 μm), with back-up stage and stage C each accounting for 8% of total fume mass. Sodium is present only in stages with aerodynamic particle size cut-off points less than or equal to 0.25 μm in diameter in concentrations of 43 and 138 μg/m3 and total mass fraction contributions of 2.2% (back-up filter; <0.25 μm) and 6.5% (stage D).

Iron is present above the LOQ in all stages in concentrations ranging from 3 μg/m3 in stage C to 124 μg/m3 in stage D. Total mass fraction contribution of iron ranges from 2.7% (back-up filter; <0.25 μm) to 5.9 % (stage D; 0.25 μm). Chromium is also present above the LOQ in all stages in concentrations ranging from 1 μg/m3 in stages C and B to 70 μg/m3 in stage D. Total mass fraction contribution from chromium ranges from 1.3% (stage B; 1.0 μm) to 3.3% (stage D; 0.25

μm). Manganese is also present above the LOQ in all stages in concentrations ranging from ,0.7 μg/m3 in stage B to 86 μg/m3 in stage D. Total mass fraction contribution from manganese ranges from 0.8% (stage B; 1.0 μm) to 4.1 % (stage D; μm). Titanium is present above the LOQ in stages back-up, D B and A and above the LOD in stage C. Titanium concentrations ranged from 0.9 μg/m3 in stage C to 32 μg/m3 in stage D. Total mass fraction contributions from titanium range from 0.5% (back-up filter; 0.1 μm) to 3.2 % (stage A; 2.5 μm). Nickel is present above the LOQ in stages back-up and D in concentrations of 12 and 10 μg/m3, respectively. Total mass fraction contribution from nickel ranges from 0.4% (stage C; 0.5 μm) to 0.6% (back-up filter; 0.1 μm), except stage B (1.0 μm) on which negligible mass was collected (<0.01%). In all metal species examined, except for Ti and Ni, significantly more mass fractions of total fume occurred in stages with cut-points less than or equal to 0.5 μm (stages C, D and back-up) with stage D (0.25 μm) containing the highest amount. In the case of titanium, stage A (2.5 μm) with largest cut-point contained the highest mass fraction (3.2%) followed by stage D (1.5%) and stage B (1.45%). For nickel, back-up stage and stage A received relatively equal mass fractions of total fume (back-up stage: 0.6%; stage A: 0.5%) followed by stage D and C.

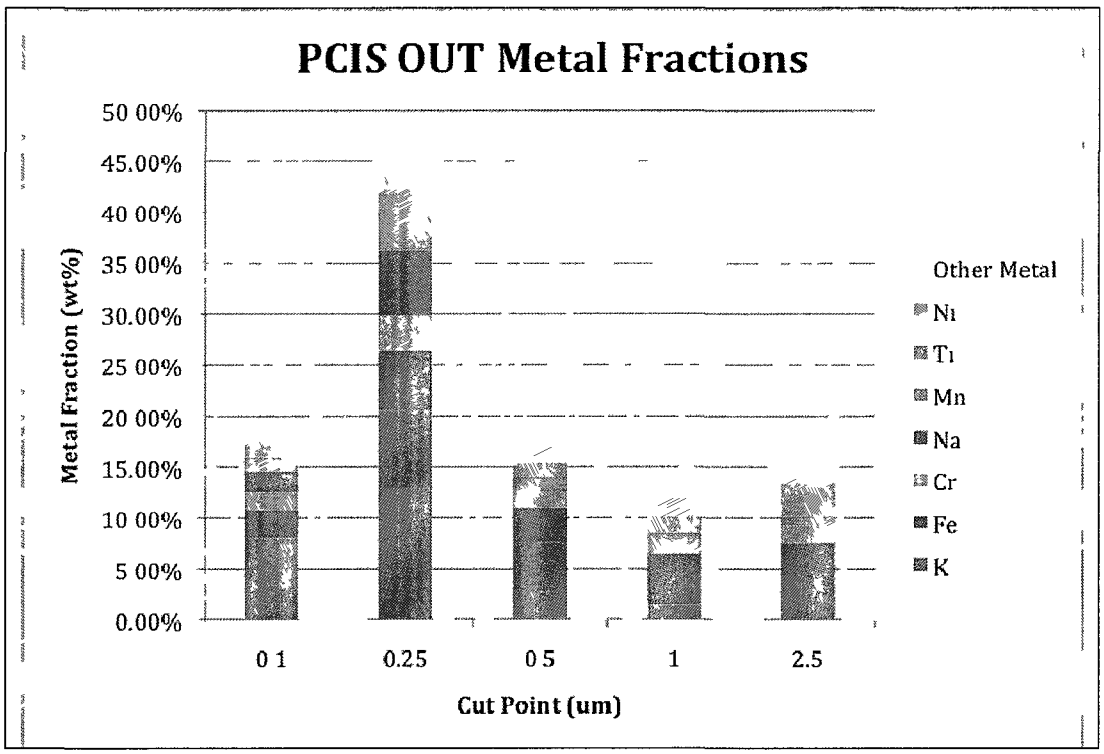

Figure 25: Metal fraction distribution of size-Fractionated SS welding fume: exposure chamber PCIS-OUT data

3.4.2.3 Comparison of Metal Fractions obtained in Emission and Exposure Chamber Experiments

In order to compare the metal distributions across particle sizes obtained in the two experimental systems, average metal mass fraction across the entire particle size range is plotted against particle size cut-point for each stage. To visualize trends better, the data are separated between alkali metals (i.e., K and Na) and transition metals (i.e., Fe, Cr, Mn, Ti and Ni).

The ELPI results obtained in the emission chamber and the exposure chamber are present in Figure 26 below. The alkali metal fraction distribution for potassium is very similar for both experimental systems with a bi-modal pattern, including a major peak at about 0.4μm (stage 6) and a minor peak at about 4 μm (stage 11). The plot of the sodium measurements with the ELPI are misleading, mainly due to high LOD experienced with the 25 mm PTFE filter used. During both emission and exposure chamber experiments, only stages 5 to 7 (0.266 – 0.622μm) consistently exhibited sodium concentrations above the LOD.

The transition metal distributions obtained using the ELPI are much flatter and less pronounced than the alkali metal distributions. Iron distribution in the emission chamber appears flat across stages, except stages with larger particle size cut-off points where there is an increase in the Fe fraction of total fume. In the exposure chamber, the iron mass fraction distribution is somewhat reversed with higher fractions at smaller particle sizes (stages 3 – 5; 0.094 μm – 0.266 μm). Chromium fraction distributions between the experimental systems are very similar with peaks at stage 4 (0.157 μm) and then a gradual decrease with increasing particle sizes. The exception is with stage 13 (10.04 μm) in the emission chamber experiment where a high Cr accumulation (18.4%) was obtained in the one and only sample for that size fraction, which is in the same order of potassium measurement in the middle stages of the ELPI. This finding could be categorized as an anomaly. Manganese mass fractions peak around stage 6 (0.387 μm) and decrease gradually on the upper and lower stages. Titanium mass fractions in the emission chamber are flat until stage 10 (2.42 μm) and then an increase was observed in larger particle size cut-off points (stages 11-13). In the exposure chamber experiments, titanium mass fraction remains consistently flat across the entire size range. Nickel mass fraction distribution in the emission chamber exhibits a slight U-shaped distribution. However, in the exposure chamber,

nickel mass fraction peaks at stage 4 (0.157 μm) and then gradually decreases across larger particle sizes.

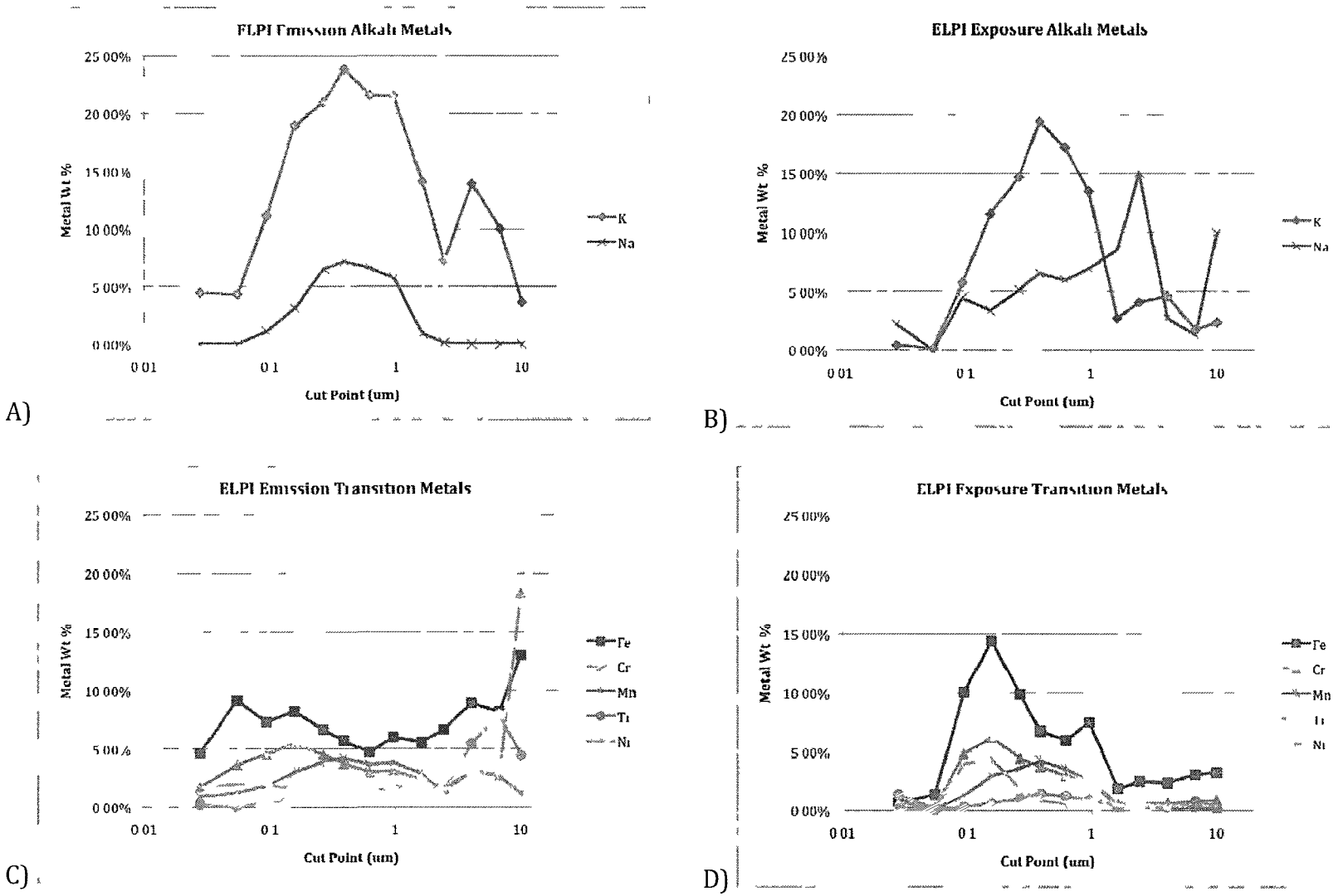

Figure 26: Measured metal fractions by stage—exposure and emission chamber ELPI data.

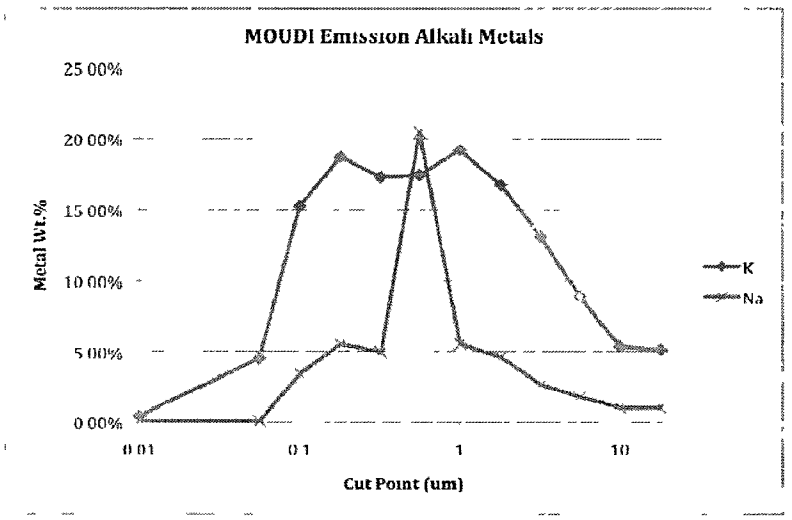

A)

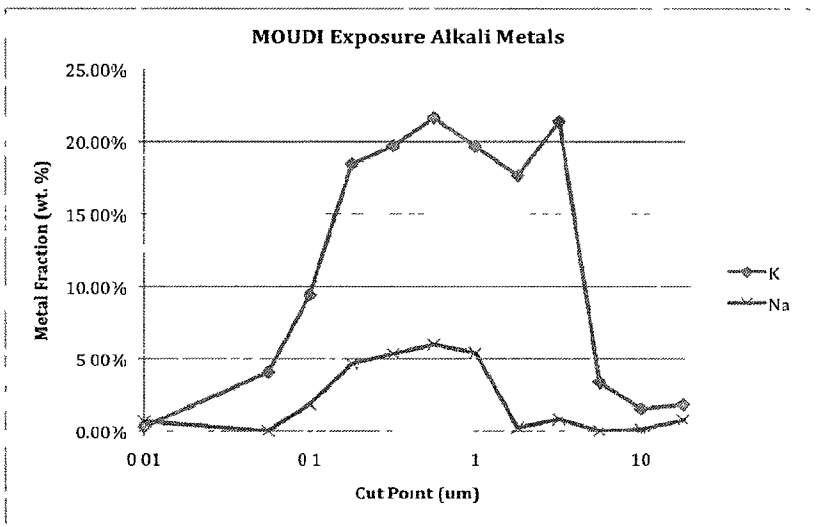

B)

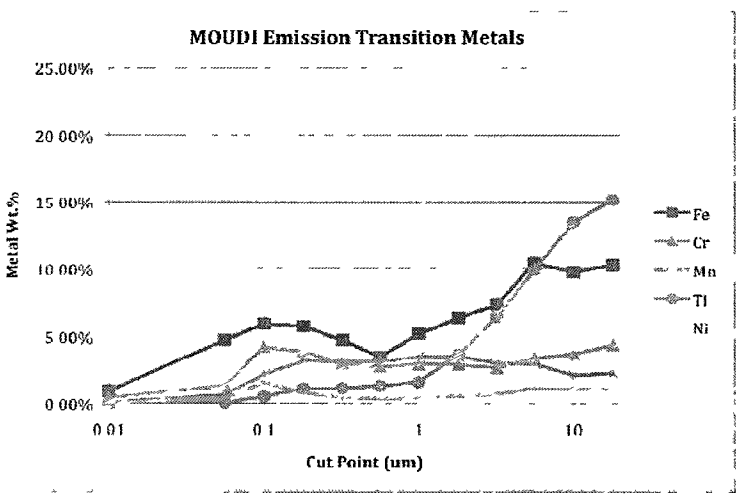

C)

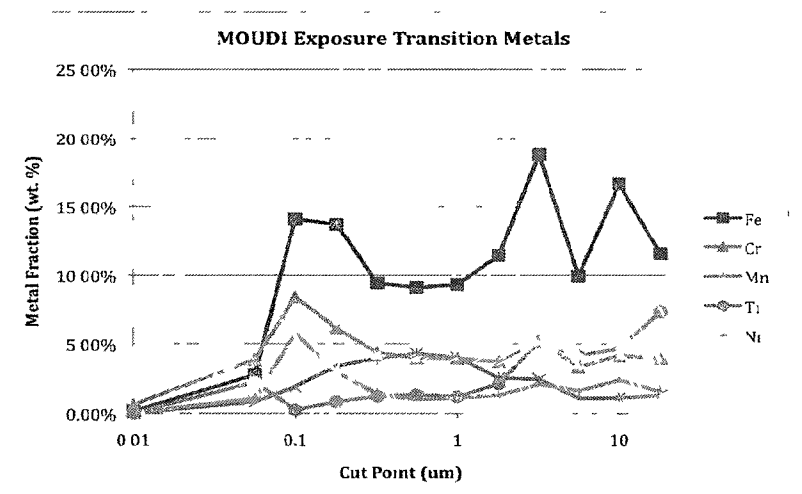

D)

Figure 27: Measured metal fractions by stage—exposure and emission chamber MOUDI data.

The alkali metal distributions are very similar to those obtained with the ELPI with a major but a wider peak observed in the middle stages of the instrument (stages 6-7; 1.0 μm-0.56 μm), with the exception of the minor peak observed in the ELPI experiments in larger cut-off points for potassium. Sodium mass fraction on stage 7 (0.56 μm) of the emission chamber experiment experienced an anomaly with a sudden spike in the mass fraction measured (20.5%), which is associated with one experimental run (Exp-3B). In this particular experiment, excess loose particles were observed on the sampler sidewall and, subsequently, brushed onto the filter media on the stage. Most likely, these loose particles represent accumulation of particle bounce from other parts of the instrument and do not represent particles of that size fraction, thus, should not have been accounted for stage 7. The iron mass fraction distribution is likely to have a multimodal distribution in both chambers with one mode occurring at stage 10 (0.10 μm) and another mode around a larger particle size (>10 μm) above the measurable particle size range with our instrument, although more variability is observed in the exposure chamber experiments. The chromium mass fractions in both chambers peak at stage 10 (0.1 μm) and, then, remain consistent for the rest of the particle sizes, with the exception of stage 1 (18 μm) in the emission chamber where an estimate in the same magnitude as stage 10 is obtained. Manganese mass fractions peak at around stages 5-7 (1.8 μm-0.56 μm) and, decrease at larger and smaller particle size cut-off points. Titanium mass fractions in both chambers, in general, gradually increase with increasing particles sizes with the emission chamber results showing higher observed fractions in the larger particle sizes (i.e., stages 1-4) and with higher variability in exposure chamber results. Nickel mass fractions in the emission chamber are flat, while a small peak is observed at stage 10 (0.1 μm) of the instrument when operated in both chambers.

The alkali metal distributions are very similar to those obtained with the ELPI with peaks observed in the mid-range (roughly stage 6; 1.0 μm) of the particle sizes. Sodium fraction on stage 6 of the emission chamber experiments experiences and anomaly with a sudden spike in the fraction measured. This spike is associated with one experimental run (Exp3B) where excess loose particles were observed on the sampler sidewall and subsequently brushed onto the filter media. Most likely, these particles were an accumulation of particle bounce from other parts of the instrument and do not represent particles of that size fraction.

The mass fraction distributions of the PCIS samplers are presented in Figure 28 below. Due to the low resolution of this sampler (i.e., fewer number of stages as compared to ELPI and MOUDI samplers), the distributions of all measured metals do not differ substantially. Also, duplicate analyses of the filters on the upper stages of the PCIS (i.e., stages A and B) were not performed by HR-ICP-MS, therefore, there is no measure of variance for the results pertaining to these stages. The alkali metal mass fraction distributions for all the alkali and transition metals are similar for both systems, with stage D (0.1 μm) containing the largest fraction, except for iron, nickel and titanium. In the case of iron, stage A (2.5 μm) with the largest particle size cut-off point had the largest fraction in the emission chamber experiments while the iron content was the second most prominent in stage A in exposure chamber experiments, which was followed by stage D. For titanium, there was a shift to stage A in both exposure and emission chamber experiments, with the largest mass fraction accumulating on the stage with the largest particle size cut-off point. Nickel results, on the other hand, showed more variability across stages in either chamber experimental runs.

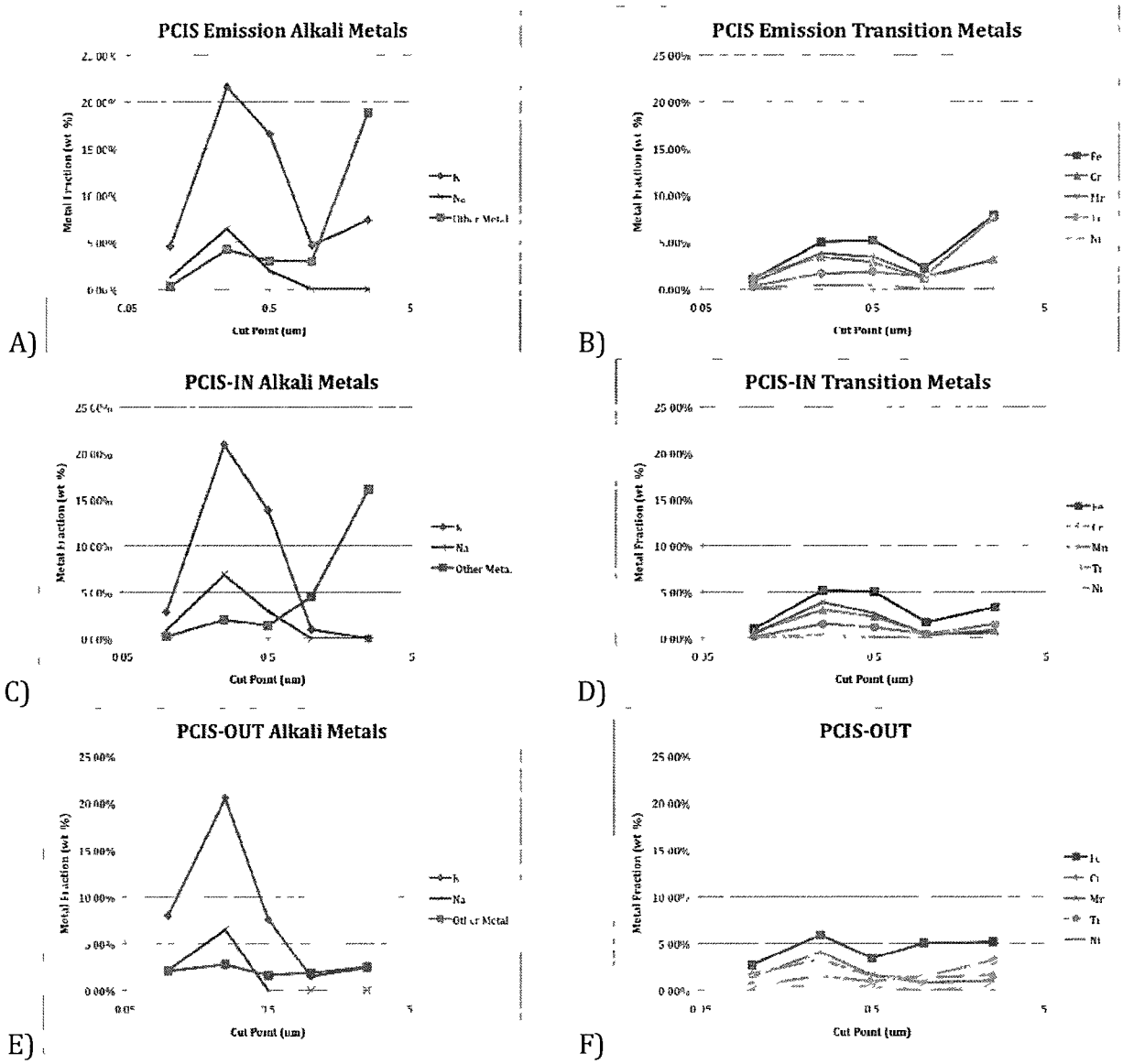

Figure 28: Measured metal fractions by stage—exposure and emission chamber PCIS data.

3.4.2.4 Total Chromium and Hexavalent Chromium Comparison

A Chromium Concentrations

Size-fractionated hexavalent chromium and total chromium concentrations measured in the emission and exposure chamber are presented in TABLE XXIX, **TABLE** XXX and **TABLE** XXXI below for the ELPI, the MOUDI and the PCIS, respectively. These data are average concentrations of two samples collected for each experimental system.

Hexavalent chromium concentrations are, in general, within the same order of magnitude (one-to-one relationship) across all stages of the ELPI in both experimental systems, except for stage 13 (10.04 μm) for which a five-fold higher estimate was obtained in the exposure chamber as compared to emission chamber. On the other hand, total chromium concentrations exhibited a different trend, with much higher measurements obtained in the emissions chamber with the ELPI as compared to those obtained in the exposure chamber.

With MOUDI, higher concentration measurements were made in the emission chamber for both total and hexavalent chromium, except stage 11 (0.056 μm) and stage 2 (10 μm) of the MOUDI in which measurements for hexavalent chromium were nearly equivalent in both chambers. Total chromium concentrations measured in the emission chamber exceeded those in the exposure chamber by two to thirteen times, depending on the stage of the instrument. With hexavalent chromium, emission chamber measurements were significantly higher as compared to those in the exposure chamber, except for those aforementioned stages (i.e., 2 and 11).

Similarly, emission chamber measurements made by PCIS was higher than those in the exposure chamber, albeit the difference is smaller as compared to those by MOUDI. When CrVI measured inside and outside of the helmet by the PCIS, nearly one-to-one relationship was obtained for back-up stage and stages A, B, and D. For stage C, hexavalent chromium concentration outside of the helmet is about 25% higher than that inside the helmet. A different relationship was obtained for total chromium concentration for which higher concentrations inside the helmet were obtained for stages A, B and C as compared to those outside the helmet but the opposite is found to be true for back-up stage and stage D. This finding, i.e., particle-size dependent safety factor observed for five-stages of the PCIS, is note-worthy since welding helmet does not appear to shield the welder from exposure to welding fume consistently throughout all particle size ranges.

TABLE XXIX: TOTAL AND HEXAVALENT CHROMIUM CONCENTRATIONS (μG /M³): ELPI DATA

Stage ID	Cut Point (um)	Emission		Exposure	
		CrVI Conc. (μg/m3)	TotCr Conc. (μg/m3)	CrVI Conc. (μg/m3)	TotCr Conc. (μg/m3)
1	0.028	0.042	0.60	0.046	0.53*
2	0.055	0.058	1.29	0.149	0.91*
3	0.094	0.617	3.71	0.620	2.62
4	0.157	5.244	11.60	3.788	6.04
5	0.266	35.303	56.29	37.027	13.65
6	0.387	60.495	131.71	59.084	34.36
7	0.622	25.333	49.42	35.071	10.78
8	0.961	2.517	9.62	3.527	2.39
9	1.62	0.106	2.06	0.131	0.44
10	2.42	0.069	1.52*	0.050	0.40*
11	4.05	0.048	1.33*	0.046	0.43
12	6.77	0.042	1.91*	0.046	0.37
13	10.04	0.042	6.32*	0.245	0.34

*- Data presented reflect only one filter analyzed by HR-ICP-MS.

- Each column represents averaged concentrations from different experimental designs. Total chromium and hexavalent chromium were not determined from samples collected within the same experiments.

TABLE XXX: MOUDI CHROMIUM CONCENTRATIONS (UG/M3)

Stage ID	Cut Point (um)	Emission		Exposure	
		CrVI Conc. (μg/m3)	TotCr Conc. (μg/m3)	CrVI Conc. (μg/m3)	TotCr Conc. (μg/m3)
Back-Up	0.01	0.057	0.121	0.002	0.06
11	0.056	0.022	0.585*	0.019	0.18
10	0.1	2.433	4.815	0.286	1.13
9	0.18	22.010	29.680	3.826	4.55
8	0.32	34.252	41.517	11.516	6.67
7	0.56	31.311	42.722	6.261	7.85
6	1	7.451	20.256	0.341	1.92
5	1.8	0.366	3.144*	0.002	0.24
4	3.2	0.156	1.902*	0.002	0.29
3	5.6	0.091	1.217*	0.001	0.25
2	10	0.004	2.604	0.004	0.64
1	18	0.266	2.263	0.002	1.14

*- Data presented reflect only one filter analyzed by HR-ICP-MS.

- Each column represents averaged concentrations from different experimental designs. Total chromium and hexavalent chromium were not determined from samples collected within the same experiments.

TABLE XXXI: TOTAL AND HEXAVALENT CHROMIUM CONCENTRATIONS: (μG /M3): PCIS DATA

Stage ID	Cut Point (μm)	Emission		PCIS-IN		PCIS-OUT	
		CrVI Conc. (μg/m3)	TotCr Conc. (μg/m3)	CrVI Conc. (μg/m3)	TotCr Conc. (μg/m3)	CrVI Conc. (μg/m3)	TotCr Conc. (μg/m3)
Back-Up	0.1	121.543	59.94	85.876	13.29	77.295	35.678
D	0.25	33.425	156.80	108.183	47.02	101.643	69.510
C	0.5	1.015	5.30	0.672	6.55*	0.846	1.346*
B	1	0.294	2.37*	0.166	0.30*	0.172	1.180*
A	2.5	0.084	2.28*	0.184	0.31*	0.172	2.189*

*- Data presented reflect only one filter analyzed by HR-ICP-MS.

- Each column represents averaged concentrations from different experimental designs. Total chromium and hexavalent chromium were not determined from samples collected within the same experiments.

B Total and Hexavalent Chromium Mass Fractions

The fractions of hexavalent chromium (CrVI) and total chromium (TotCr) in total fume mass measured in the emission and exposure chamber experiments along with the ratio of CrVI to TotCr fractions are presented in **TABLE** XXXII, TABLE XXXIII and TABLE XXXIV below for the ELPI, the MOUDI and the PCIS, respectively.

The TotCr mass fraction is greater than the CrVI mass fraction on every stage of the ELPI during emission and exposure chamber experiments. CrVI measured mainly in particles size cut-off points between 0.094 μm and 0.961 μm (i.e., stages 3-8). In these stages, CrVI fractions range from 25 to 69% of their respective TotCr fractions measured in the emission chamber and from 20% to 79% of their respective TotCr mass fraction measured in the exposure chamber. In all other stages, CrVI fraction does not exceed 0.22% of total fume mass in either chamber experiments.

The TotCr fraction was larger than the CrVI fraction for all stages except stage 10 (0.1 μm) for the MOUDI during the emission chamber experiment. (This result highlights the limitations of our experimental method since this finding is most likely due to not being able to carry out the speciation analyses for TotCr and CrVI on the same filter). CrVI is mostly found between particle size cut-off points of 0.1 and 1.0 μm in diameter (i.e., stages 10 and 6). Within these size ranges, CrVI mass fraction ranged from 73% to 108% and 28% to 72% that of the total chromium mass fraction in the emission and exposure chamber, respectively, depending on a given stage of the instrument. A comparison of the CrVI to TotCr mass fraction ratios is presented in Figure 29 below. This plot schematically demonstrates that distribution of CrVI to TotCr mass fraction peaks around 0.4 μm with a much smaller potential minor peak at a larger particle size, approximately, 10 μm.

With the PCIS, the TotCr mass fraction was consistently higher than the CrVI mass fraction for particle size cut-off points greater than or equal to 0.25 μm (i.e., stage D). However, the opposite was observed on the back up filter of the instrument where CrVI mass fraction was two to three times higher in the emission chamber experiments and exposure chamber experiments with the sampler outside the helmet, respectively. In the exposure chamber experiment with the sampler placed inside the helmet, nearly identical estimates were obtained for CrVI and TotCr mass fractions with CrVI mass fraction slightly higher than that of total chromium mass fraction. The CrVI was found mostly in the particle size cut-off points less than 0.25 μm (stage D) in diameter. In these stages, CrVI mass fractions ranged from 26% (stage D) to 208 % (back-up stage)of the TotCr fractions in the emission chamber, from 71% (stage D) to 315% (back-up stage) of the TotCr fractions for the exposure chamber with the PCIS sampler placed inside the helmet and from 66% (stage D) to 110% (back-up stage) for the exposure chamber with the PCIS placed outside of the helmet.

TABLE XXXII: TOTAL AND HEXAVALENT CHROMIUM FRACTIONS (WT. %): ELPI DATA

Stage ID	Cut Point (um)	Emission			Exposure		
		CrVI Wt. %	TotCr Wt. %	Ratio %	CrVI Wt. %	TotCr Wt. %	Ratio %
1	0.028	0.11%*	1.69%	6.75%	0.19%*	6.90%	2.70%
2	0.055	0.13%*	3.59%	3.71%	0.22%**	5.49%	3.98%
3	0.094	1.14%	4.52%	25.12%	0.96%	4.83%	19.82%
4	0.157	2.75%	5.48%	50.27%	2.20%	6.22%	35.29%
5	0.266	2.99%	4.50%	66.56%	3.49%	4.42%	78.92%
6	0.387	2.16%	3.75%	57.52%	2.09%	3.71%	56.33%
7	0.622	2.07%	2.99%	69.31%	2.15%	2.93%	73.43%
8	0.961	1.20%	3.10%	38.71%	0.77%	2.57%	29.97%
9	1.62	0.15%**	2.35%	6.34%	0.11%**	0.54%	19.57%
10	2.42	0.05%*	1.64%	2.91%	0.07%*	0.60%	11.89%
11	4.05	0.09%*	2.97%	3.06%	0.04%*	0.62%	7.28%
12	6.77	0.05%*	2.77%	1.89%	0.05%*	0.78%	6.11%
13	10.04	0.08%*	18.36%	0.42%	0.17%*	0.87%	19.93%

* - both samples below the LOD for CrVI

** - one sample below LOD for CrVI

TABLE XXXIII: MOUDI CHROMIUM FRACTIONS (WT. FRACTION)

Stage ID	Cut-Off Point (μm)	Emission Chamber			Exposure Chamber		
		CrVI Wt. %	TotCr Wt. %	Ratio %	CrVI Wt. %	TotCr Wt. %	Ratio %
Back-Up	0.01	0.29%	0.41%	70.55%	0.01%*	0.63%	1.33%
11	0.056	0.04%**	1.35%	3.17%	0.09%**	3.86%	2.22%
10	0.1	4.55%	4.20%	108.13%	2.35%**	8.44%	27.82%
9	0.18	2.80%	3.86%	72.67%	3.65%	6.16%	59.25%
8	0.32	2.64%	2.96%	89.03%	3.15%	4.35%	72.40%
7	0.56	2.69%	2.74%	98.23%	2.67%	3.98%	67.00%
6	1	2.46%	2.93%	83.94%	2.63%	3.94%	66.77%
5	1.8	0.47%	2.89%	16.21%	0.01%*	3.71%	0.30%
4	3.2	0.16%	2.66%	6.19%	0.01%*	5.16%	0.23%
3	5.6	0.15%	3.36%	4.37%	0.02%*	3.34%	0.64%
2	10	0.01%*	3.67%	0.20%	0.51%*	4.15%	12.35%
1	18	0.42%	4.35%	9.66%	0.01%*	3.95%	0.15%

* - both samples below the LOD for CrVI

** - one sample below LOD for CrVI

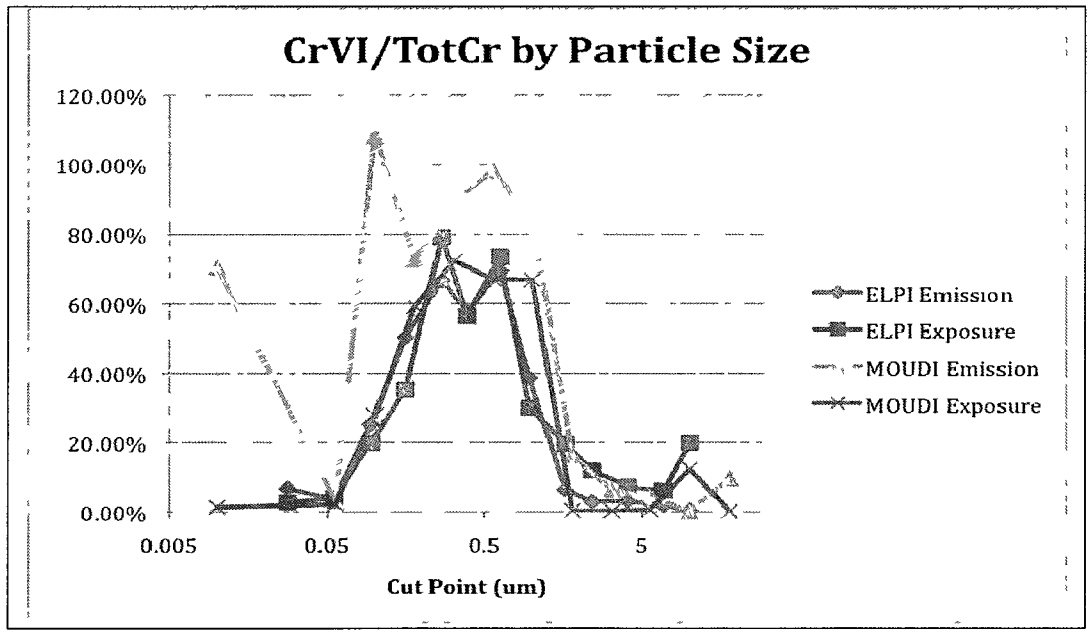

Figure 29: Distribution of ratios of CrVI/TotCr mass fractions across particle sizes.

TABLE XXXIV: PCIS CHROMIUM FRACTIONS (WT. FRACTION)

Stage ID	Cut Point (um)	CrVI wt. %	Emission TotCr wt. %	Ratio
Back-Up	0.1	2.77%	1.33%	208.19%
D	0.25	0.88%	3.40%	25.86%
C	0.5	0.65%	2.83%	23.15%
B	1	0.33%*	1.09%	30.44%
A	2.5	0.19%*	3.14%	6.01%
Stage ID	**Cut Point (um)**	**CrVI wt. %**	**PCIS-IN TotCr wt. %**	**Ratio**
Back-Up	0.1	2.08%	0.66%	315.43%
D	0.25	2.18%	3.06%	71.11%
C	0.5	0.22%*	2.34%	9.43%
B	1	0.29%*	0.42%	68.94%
A	2.5	0.16%*	0.87%	18.03%
Stage ID	**Cut Point (um)**	**CrVI wt. %**	**PCIS-OUT TotCr wt. %**	**Ratio**
Back-Up	0.1	1.97%	1.79%	109.91%
D	0.25	2.17%	3.27%	66.22%
C	0.5	0.25%*	1.48%	17.15%
B	1	0.17%*	1.30%	12.82%
A	2.5	0.28%*	1.64%	16.97%

* - both samples below the LOD for CrVI

** - one sample below LOD for CrVI

3.5 Discussion

3.5.1 Transition Metals

Iron mass fractions are present throughout all of the stages of the instruments utilized in emission chamber experiments. With the ELPI, the highest mass fraction was observed in stage 13 (10.4 μm). With MOUDI, stages 1-3 (18 μm-5.6 μm) received the highest mass fractions. The PCIS in the emission chamber yielded largest iron mass fraction in Stage 1 (2.5 μm). There is more variability seen in the exposure chamber experiments where larger iron mass fractions from stage 8 and below (≤ 0.961 μm) were obtained using the ELPI, whereas the MOUDI yielded larger mass fractions in larger particle size cut-off sizes corresponding to stages 3 (5.6 μm) and lower. In the case of PCIS in exposure chamber, stage D (0.25 μm) followed by stage A (2.5 μm) had the highest iron mass fractions. Iron is the primary component of stainless steel. The iron within the electrode is primarily the filler material that is used to bond the base metals together. In many experiments, preferential accumulation of iron in stages with the larger size cut-off points was found with the exception of ELPI in exposure chamber experiments.

Total chromium mass fractions are relatively consistent across all stages of the ELPI (except stage 13 with the highest mass fraction), MOUDI and PCIS in emission chamber experiments. In the exposure chamber experiments, total chromium mass fractions are similar in magnitude in stages 8 (0.961 μm) and below in the ELPI (with a peak at stage 4 (0.157 μm)), in all stages except the back-up filter in the MOUDI, and all stages of the PCIS (with a peak in stage D (0.25 μm). Chromium is a major component of stainless steel. The chromium present within the electrode comes from the filler wire and is used as an alloy in the bonding of the base metals.

Nickel mass fractions are greater on the high (stages 10-13) and low (stages 1-4) ends of the particle size distribution of the ELPI, greater on the high-end stages (stages 1-3) and stage 10 (0.1 μm) of the MOUDI, and found only in the lower stages (stages C to back-up filter) of the PCIS in the emission chamber experiments. In the exposure chamber experiments, the nickel mass fractions measured by the ELPI are greater at the lower cut-off point stages (stages 2-5), slightly greater at the high (stage 1-4) and low stages (8-11) of the MOUDI, found only in the lower stages of the PCIS IN (stage D>back-up filter>stage C) and also found in all stages of the PCIS OUT, except stage B (1.0 μm). Nickel is a primary constituent of stainless steel and would be present within the core wire of the electrode. The variability observed in Ni metal fractions across stages of the cascade impactors utilized is an unexpected finding. The small total mass gain on the exposed filters may be one reason for this observation. As other metal constituents are not detected on these stages due to small mass gained, the ones that are detected will reveal themselves at greater mass fractions. Furthermore, slight changes in composition of electrodes from one batch to the next and changes in semi-automated welding environment from one experiment to another may account for small differences observed in the results.

Manganese is found in relatively consistent mass fractions in all but the last stages of the ELPI (with a peak at stage 6), MOUDI (with a peak at stage 5-6) and PCIS (with a peak in stage D) in the emission chamber experiments. In the exposure chamber experiments, manganese is found in similar mass fractions in all stages, except stage 2 of the ELPI, stages 11 and back-up filter of the MOUDI, and stage B of the PCIS. Manganese is contained within stainless steel as a similar alloying metal to nickel although at lower concentrations.

An important finding is that iron and the titanium mass fractions are found in increased amounts in the large particle size cut-off points during the emission and exposure chamber experiments (except the ELPI in exposure chamber). This behavior was uniquely different than mass fraction distribution found for other transition metals in which metal species were observed in mass fractions in all size fractions with a peak at a middle-stage followed by lower amounts in upper and lower stages.

3.5.2 Potassium and Hexavalent Chromium Relationship

Potassium mass fractions peak at stage 6 (0.387 μm) of the ELPI, stage 6 (1 μm) of the MOUDI, and stage D (0.25 μm) of the PCIS in the emission chamber experiments. The same is true for the exposure chamber experiments except for the MOUDI, which has a peak at stage 7 (0.56 μm) for potassium mass fraction. In general, potassium is present at higher amounts in middle stages of the ELPI (stages 4-9) and the MOUDI (4-10), trailing off in the lower and the upper stages.

Potassium is added to the welding electrode coating primarily as an arc stabilizer. The arc is an ionic gas (plasma) and the potassium compounds are readily broken down within the intense heat allowing the resultant ions to aid in the electrical conductivity of the gas. Therefore, presence of potassium in all fractionated welding fume samples is reasonable because potassium is meant to decompose and ionize in the gases surrounding the arc as opposed to aiding in the metallurgical properties of the resulting welded metal. In general, higher fractions of potassium are found in the upper stages of the instruments with the larger particle size cut-off points as compared to lower stages. The structure of these larger particles are agglomerates of primary particles on the order of tens of nanometers in diameter, which are expected to contain larger percentages of potassium in

the shell. A more definitive conclusion can be reached by microscopic analysis of individual particles for which we have limited data. (see section 0)

Sodium is also present at higher amounts in the middle stages of the ELPI (stages 5-8) and of the MOUDI (stages 5-9) and in the lower stages of the PCIS (stages D, C, back-up filter) in the emission chamber experiments. In the exposure chamber experiments, sodium content showed more variability. While sodium was present in all stages of ELPI with a peak at stage 10 (2.42 μm), it was higher in the middle stages of MOUDI (stage 6-9) with lower amounts in upper and lower stages. Sodium presence was limited to stages C, D and back-up filter in PCIS measurements in the exposure chamber, with the highest amount observed in stage D, followed by back-up filter. The sodium present within the electrode comes from the sodium silicate binder or the other minerals (feldspar and cryolite) that are added to create the slag that protects the weld pool. Sodium follows the general mass distribution of welding fume with abundance in middle stages and lower amounts in both ends of the particle size distribution.

The chromium fraction analysis reveals more about the nature of total chromium and hexavalent chromium contained within the welding fume samples. In the ELPI, the total chromium is detected throughout the entire instrument while the hexavalent chromium is, found, primarily in stages 3 (0.094 μm) to 9 (1.62 μm). In the MOUDI, total chromium is again found in all stages while the hexavalent chromium is, primarily, found in stages 10 (0.1 μm) through 5 (1.8 μm). Hexavalent chromium concentration exceeded the concentration of total chromium in stage 8 (0.32 μm) of the MOUDI and in stages of 5-8 of the ELPI in the exposure chamber experiments. In all other cases, total chromium concentration exceeds the hexavalent chromium concentration measured by either MOUDI or the ELPI. Variability considerations aside, this would lead to the conclusion that all

chromium in these size range stated are in the hexavalent state. With the PCIS exposure and emission chamber experiments, the backup filter yielded greater hexavalent chromium concentrations consistently than total chromium concentrations. This finding was not expected and could not be verified using the MOUDI and the ELPI data. Although the sample size was small (n=2 max), the consistent nature of this finding gives credence to analytical results.

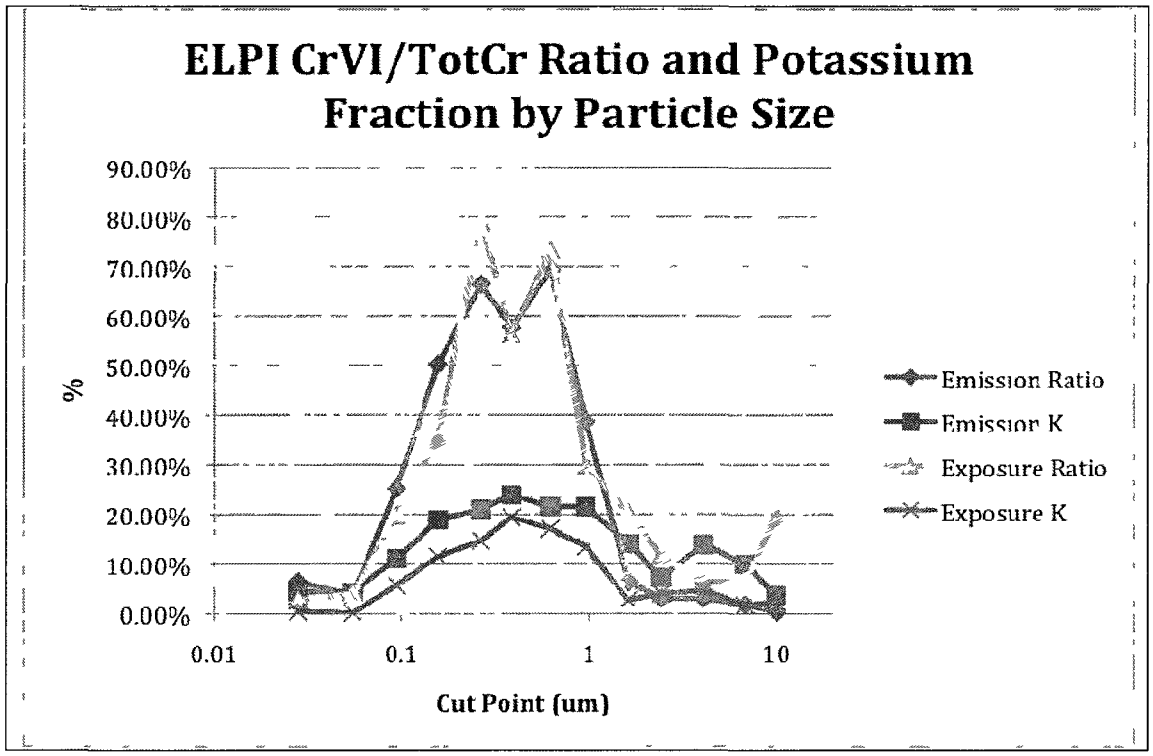

Figure 30 ELPI CrVI/TotCr ratio and potassium mass fractions by particle size: ELPI data.

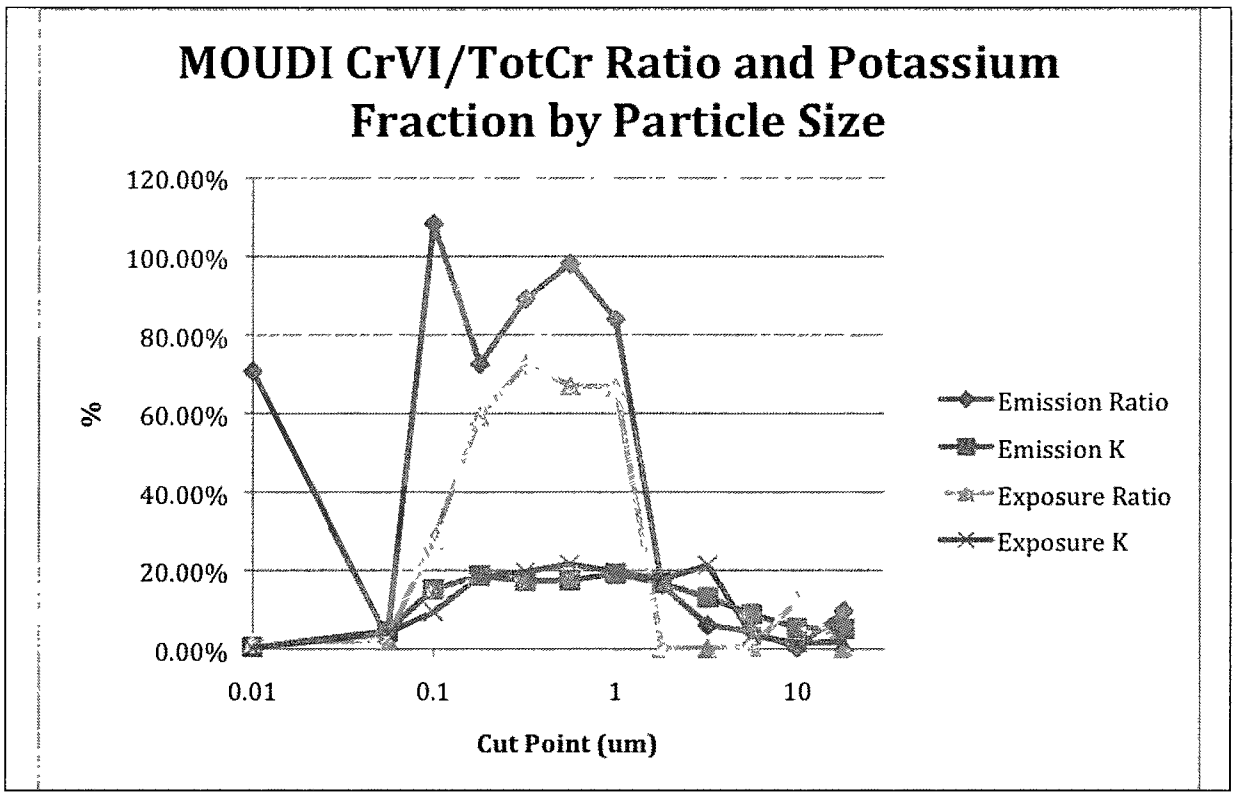

Figure 31 CrVI/TotCr and potassium fractions by particle size: MOUDI data.

The CrVI/TotCr ratio is a estimate of how much of the chromium in the fume is expected to be in the hexavalent state. (Since determination TotCr and CrVI were performed in different experiments, this metric can only be suggestive and is of limited interpretive value.) When the ratio is plotted against particle size, there is a strong spike in particles between 0.1 and 1 μm in aerodynamic diameter. A similar type of spike was also observed with the potassium fraction of total fume mass across particle sizes. Potassium mass fractions of particles in the 0.1 to 1 μm aerodynamic size ranges is larger than of those for CrVI or total chromium in this size range as expected since potassium is in the coating of electrodes in large amounts. However, the presence of

both species in the fume across particles size ranges measured follows the same pattern, as shown in Figure 16 and 17.

A relationship between the hexavalent chromium content and potassium has previously been documented in the literature (J. H. Dennis, M. J. French, P. J. Hewitt, S. B. Mortazavi, & C. A. J. Redding, 1996; Dennis, Mortazavi, French, Hewitt, & Redding, 1997; Gray, Hewitt, & Dare, 1982b; R. Tandon, et al., 1986; R. Tandon, et al., 1985; R. K. Tandon, Crisp, Ellis, & Baker, 1982; Yoon, Paik, & Kim, 2003). These studies, however, analyze only total fume samples as opposed to size-fractionated samples like those analyzed in this research. To this author's knowledge, the increase in mass fraction contribution of potassium in the mid-range of the PSD (i.e., particle size between 0.1 and 1 μm) has not been documented before.

The underlying chemical mechanisms of CrVI formation and its relationship to potassium are unclear. It has been suggested that, during welding, CrIII is initially formed by oxidation at high temperature as welding fume condenses, whereas, CrVI compounds are not formed in the initial stages due to their unstable nature at high temperatures (C. Gray & P. Hewitt, 1982). As the temperature of welding fume decreases to about 1500 °C or less, sodium or potassium chromate are formed due to further oxidation of CrIII (C. Gray & P. Hewitt, 1982). Therefore, a relationship is expected to be present between CrVI formation and alkali species (K or Na) in the fume. In addition, it has been shown that the addition of an "active" metal (namely Zn) to the welding wire can decrease the final CrVI composition of the fume (J. Dennis, M. French, P. Hewitt, S. Mortazavi, & A. Redding, 1996). Future research into the mechanisms of CrVI formation in welding fume and it's dependence on potassium in specific particle size fractions may be beneficial in creating new formulations of electrode that reduce CrVI in welding fume.

3.5.3 Data Limitations

The overall mass gain (total mass) must be considered when analyzing analytical results of our welding fume samples. In our experiments, a very small amount of mass was often collected on cascade impactor stages, especially, on the upper stages of instruments with larger particle size cut-off points. (On the last stage of the ELPI and the back-up filter of the MOUDI, much less mass relative to the middle stages of each instrument was also collected.) During the experiments, we aimed to not to overload the middle stages where collection of higher amounts of fume is expected while obtaining enough mass to enable elemental speciation of samples collected on higher and upper stages. This resulted in an iterative exercise in sampling duration from one experiment to another in order to meet these competing aims.

Further, when considering the tail ends of the distribution, i.e., high and low stages, the upper stages are found to have a higher total metal fraction than the lower stages. This holds true for all samplers in the emission chamber. However, in the exposure chamber, this only holds true for the MOUDI and the PCIS-IN. The non-metal fraction, not accounted for by the HR-ICP-MS analysis, would primarily consist of lower atomic mass elements like carbon. If the carbon in welding fume is in the form of soot, it would be consistent that more carbon be found on lower stages since soot particles are very small. Further, microspatter from welding may account for the larger particles found on the upper stages. These larger particles would primarily be composed of metal and, therefore, account for a greater proportion of the total metal mass of those stages.

The total chromium and hexavalent chromium concentrations were measured in two separate sets of experiments because of the different analytical methods used for the post-analysis

of the filters. Therefore, total mass collected is variable due to the inherent variability of the experiments.

Major limitation of the study is the sample size for each measurement, which is n=2 at maximum. The experiments were replicated in each case. However, not all the samples were subjected to HR-ICP-MS analyses due to technical (not enough mass collected) and/or budgetary limitations. Thus, the study should be considered preliminary and hypothesis generating. Variability in measurements (i.e., concentrations and mass fractions) has not been fully characterized.

3.6 Summary

A study of the chemical composition of size fractionated welding fumes samples collected under laboratory-controlled conditions was performed. Total transition metal composition and hexavalent chromium content of size-fractionated welding fume samples collected in both an emission chamber and an exposure chamber, were determined using ICP-MS and AAS. Transition metal content was found to not vary substantially across size fractionated welding fume samples and sample size limited ability to distinguish small differences in concentrations as statistically significant. A spike in the content of alkali metals was found in particles sizes between 0.1 μm and 1.0 μm. Hexavalent chromium analysis also revealed a spike in particles sizes between 0.1 and 1.0 μm diameter suggesting a chemical dependence of hexavalent content with alkali metal content of welding fume samples, however, specific correlation between species could not be verified because composition of the two species was not conducted on the same sample. Further exploration on the

size dependence of alkali metal and hexavalent chromium content of welding fume should be completed.

4. MORPHOLOGICAL AND COMPOSITIONAL ANALYSIS OF SIZE-FRACTIONATED WELDING FUME USING ELECTRON MICROSCOPY TECHNIQUES

The aerodynamic diameter of a particle is a useful metric when comparing different types of particles that originate from different processes. The aerodynamic diameter describes a spherical particle of unit density, which settles at the same rate as the actual particle in question. Although characterization of the aerodynamic diameter is essential for understanding the biological deposition potential of a given aerosol, the physical dimensions (i.e., size and shape) are also important for understanding the surface area and potential for the particle to adversely affect human tissues. This chapter describes welding aerosols beyond just aerodynamic size properties described in previous chapters and provides information in physical size and shape of the size-fractionated welding fume particles found in the breathing-zone of a manikin simulating a welder on the microscopic level using Scanning Electron Microscopy and Transmission Electron Microscopy techniques.

4.1 Background

Microscopic analysis of airborne particles has long been described in occupational exposure studies (Hinds, 1999b). Optical microscopy is useful in instances where particles are relatively large (greater than 0.5 μm particle diameter), however, electron microscopy (EM) is better suited for situations where particle size is small (less than 0.5 μm particle diameter) as is the case for welding fume. This background section outlines specific methods of EM available for ultrafine particle analysis and previous studies that have used EM for welding fume particle analysis.

4.1.1 Electron Microscopy Methods

As a general analytical technique, EM uses a beam of high-energy electrons to illuminate a sample substrate, a set of electromagnetic lenses to focus the electron beam, and a series of detectors capable of detecting electrons that have interacted with or been displaced by the sample.

4.1.1.1 Scanning Electron Microscopy

A scanning electron microscope (SEM) permits the observation and characterization of materials on the nanometer and micrometer scale. In the SEM, the area to be examined is irradiated with a finely focused beam of electrons (usually between 1 – 30 keV), which is swept in a raster across the surface of the specimen to form images. The SEM primarily detects secondary and back-scattered electrons that have resulted from the interaction with the beam and the sample's surface. Because of this, images obtained with the SEM often appear three-dimensional. Resolution of the SEM is at best in the single nanometer range.

4.1.1.2 Transmission Electron Microscopy

A transmission electron microscope (TEM) uses a higher-energy electron beam (60-350 keV) and detects electrons that have been transmitted through a sample. The images obtained with a TEM do not have the three-dimensional character but better represent the internal structures of the sample. The TEM provides a much higher spatial resolution than the SEM and is commonly used for nano-size particle characterization by facilitating analysis of features at atomic scale (in the range of a few nanometers).

4.1.1.3 Energy Dispersive X-ray Spectroscopy

In both types of EM, the interaction of the electron beam with the specimen produces X-rays, which are characteristic of the specimen composition. These x-rays may be collected using an Energy Dispersive X-ray (EDX) detector to elicit compositional information on the sample.

4.1.2 Electron Microscopy of Welding Fume

In regards to EM studies of welding fumes, early work in this area was performed mainly for illustrative purposes and at resolutions that explored larger diameter particles (Hewitt & Gray, 1983; Koponen, Gustafsson, Kalliomäki, & Pyy, 1981; Wemmert, 1994). More recently, electron microscopy with higher resolutions capable of examining smaller particles have been performed with the intention of characterizing welding fume particles. One of the earliest EM studies of welding fume identified four principle types of particles: 1) clusters of globules; 2) granular networks; 3) chains; and 4) large spheres (Kalliomaki, Grekula, Hagberg, & Sivonen, 1987). Authors devised a rating system (1 = rare, ..., 5 = predominant) for describing the frequency of particle types when analyzing TEM micrographs. When analyzing the micrographs of SMAW process on both MS and SS, researchers found granular networks (rating scale # 2), clusters of globules (rating scale # 5) and large spheres (rating scale #3). The reported physical dimensions of the granular networks were an agglomerate diameter of 10 μm and a primary particle size of 0.03 μm. The physical dimensions of the clusters of globules were an overall agglomerate diameter of 1 μm and a primary particle diameter of 0.2 μm. The large sphere diameter was reported as 0.5 μm. If one examines the images presented in this paper, globules can be seen as actually spherical in nature.

A field study presented morphology data on SMAW of Iconel (high nickel alloy similar to SS) fume that had been collected by personal sampling in a shipyard welding shop (Farrants, Schuler, Karlsen, Reith, & Langard, 1989). From EM image analysis, these researchers classified particles into three main types called small, medium and large. There is no primary particle size associated with the small particles but it is observed that they form chainlike agglomerates up to 45 μm large in their greatest dimension. The medium particles are classified as having a mean diameter of 70 nm (mean projected area of 370 nm^2) and large particles 145 nm mean diameter (22,000 nm^2).

Development of better instrumentation over time enabled the study of welding fume collected in laboratory experiments at better imaging resolutions. During a toxicological study, one research group used TEM and SEM to image SS welding fume generated during GMAW (Antonini, et al., 2006). Authors recorded homogeneous, chain-like agglomerates of primary particles. Larger, more spherical particles, referred to as microspatter, were sometimes observed among the agglomerates. Similar morphological characteristics were seen in an emission chamber study of SMAW on carbon steel (N. T. Jenkins & T. W. Eagar, 2005b). Another study aimed at exploring the surface chemistry of ultrafine particles generated from GMAW on MS using TEM/STEM with EDS and Electron Energy Loss Spectroscopy (EELS) (Maynard, et al., 2004). Authors identified chainlike agglomerates and classified primary particles into two predominant categories of fume particles, namely particles approximately 5-10 nm in diameter and spherical particles around 50-150 nm in diameter.

Another study performed a compositional analysis of SMAW-MS fume using x-ray and Ramen spectroscopy along with SEM imaging (Worobiec, et al., 2007). Researchers did not categorize primary particles quantitatively but did describe certain morphologies observed across

stages of a cascade impactor. Authors found that fine particle fractions (stages of impactor collecting <0.5 μm in aerodynamic diameter) contained mostly irregular shaped particles representing highly agglomerated formations having typical spongy and fibrous structures formed by accumulation of primary nanometer-sized particles appearing due to condensation mechanisms. It is also noted that overall agglomerate dimensions were often larger than would be expected from impactor stage cut-off size owing to the fact that the agglomerates were non-compact and with physical dimensions larger than aerodynamic ones. At the midsize fractions (stage with 1 μm diameter cut-off point), spherical particles contained in webs of fine particle chains were observed. No measure of primary particle diameter is presented in this article. On the stages with coarse fractions of particles (stages with >2 μm cutoff), larger spherical particles were observed, often with irregular chain structures connecting them together. Authors suggested magnetic and adhesive properties of the particles as an explanation of this binding behavior.

Most recently, welding fume generated from the SMAW process on MS and SS were studied using electron microscopy techniques (Sowards, et al., 2008; Sowards, et al., 2010). Authors sampled welding fume with an ELPI and characterized the size-fractionated samples with SEM and TEM. Three major types of particles described in this work were spherical, irregular and agglomerated. Spherical particles were reported to be the most abundant type of individual particle. On the other hand, irregular particles were not very abundant and were generally rod-shape in dimension. Agglomerates were consisted of tens to hundreds of spherical and irregular particles bound together. Researchers reported that single spherical particles were found in upper stages, large "well-packed" agglomerates were found in lower stages (i.e., cut-off points between 0.09 – 0.39 μm), and "loosely-packed" agglomerates were found on the middle stages (i.e., cut points of 0.62 – 4.01 μm).

The more recent studies with instrumentation with better resolution have analyzed samples collected in laboratory conditions and did not provide data on welding fume characteristics under exposure circumstances. One study examined welding fume collected both in laboratory and in the field using SEM and noted that particles consisted of clusters and chain aggregates formed from smaller primary particles (Stephenson, et al., 2003). These researchers noted that the size of primary particles within an aggregate was uniform, however, between aggregates, primary particle size varied greatly. No data on physical particle size measurements was reported in this work. Another study explored welding fume generated during resistance spot welding of galvanized steel in an automotive plant (Dasch, 2008). These researchers not only observed similar morphologies but also an additional fluffy type of material in size-fractionated samples that was less than 1μm in aerodynamic diameter.

4.1.3 Summary of Literature

EM is a useful analytical technique capable of resolving the small particles generated during welding. Previous studies of welding fume have identified spherical primary particles of different sizes that tend to agglomerate into chainlike structures. Detailed EM analysis of welding fume performed thus far has mostly been conducted in laboratory studies employing controlled emission chambers. Although this approach is useful and informative, the measured particle size distribution and its ultimate relevance to actual exposure scenarios are largely unknown. We advocate that a laboratory-based study that simulates welder exposure under controlled conditions would prove a better approach as it mimics the types of exposure an actual welder might experience in the work place. The ability to conduct experiments in a controlled environment equipped with a thermal breathing manikin simulating a welder uniquely allows the study of the

variability of process parameters on fume morphology, kinetics, particle size and surface chemistry. Furthermore, this experimental system distinctively allows the use of sampling instrumentation for PSD analysis that would not be practical to use in actual working environment because of size and/or impedance to the work practices.

4.2 Study Objectives

To assess morphology of size-segregated welding fume under laboratory-controlled conditions employing EM techniques on samples collected using a number of exposure monitoring tools (i.e., cascade impactors) in two different experimental systems (i.e., exposure and isokinetic emission chambers).

The specific goals of this research are to:

1) describe and categorize the primary particles generated during the SMAW-SS process.
2) describe the specific morphologies that welding fume particles exhibit.
3) determine if welding fume aerosol may be classified into a certain categories of particle shapes and structures.
4) describe how morphologies of particles change as a function of stage of impactor.

5) to develop hypotheses in regards to source and formation mechanism of particles with different size, shape and structures found in welding fume;

6) to gain insight into microscopic structure of the particles in specific size fractions and relevance of the observed microscopic structures for health effects reported in the literature for welders

4.3 Methods

Experiments described in this research are consistent with those described in Chapter 2.

4.3.1 Experimental Design

A set of four experiments, two in the emission chamber and two in the exposure chamber, were performed. The welding parameters were held constant during all experiments. The 308H-16 electrode size was 3.2 mm and welding current was set at 100 A. During the emission chamber experiments, isokinetic sampling probes were attached to the cascade impactor instruments and positioned within the sampling plane of the chamber. In the exposure chamber, the manikin was positioned within the center of the chamber at a distance 28 cm from the base metal piece. Physiological conditions (16 breaths per minute, 0.85 liters per breath) and posturing (20 degree torso tilt, 20 degree head tilt) were held constant during all experiments performed in the exposure chamber. The ELPI, MOUDI, PCIS (inside and outside the welding helmet) and the manikin filter assembly were used in sampling the welding fume.

4.3.2 Electron Microscope

The scanning electron microscope (SEM) used to analyze welding fume particles is a JEOL JSM7500F located at the Argonne National Laboratory Center for Nano-Materials (CNM). The SEM has a unique transmission detector (TED) that allows imaging and analysis similar to that of a TEM. The SEM with the TED can be used for high magnification imaging in determining particle size and particle morphology. Additionally, the SEM has a Noran EDX detector that can be used to identify the elemental composition of welding fume particles. Imaging of welding fume samples was performed with a beam energy of 30 keV and a probe current of 10 μA.

4.3.3 Sampling Media

We employed the method the method developed by Farrants et al. (1989) in collecting welding fume for microscopic analysis. Specialty TEM grids were ordered from Electron Microscopy Sciences (Hatfield, PA) (model #:HD-300-Cu). These grids were 300 mesh copper with single handle and holey carbon film. The handle was used as an attachment point to the 0.4 μm pore-size polycarbonate (PC) filter that was placed on the stages of the impaction devices during the experiments. Carbon adhesive was used to attach the grid to the PC filter. The grid was handled with tweezers and carefully placed on the filter. A paintbrush was used to gather a small drop of carbon adhesive and adhere the grid to the PC filter. The adhesive was allowed to dry before placing the filter with attached grid into an individual Petri dish and stored prior to experiments.

The grids affixed to filter surface for electron microscope analysis remained attached to the filter and stored in individual Petri dishes before and after experiments. The grid was not disturbed from the filter until just prior to insertion into the microscope. This precaution is intended to eliminate contamination or sample degradation from over handling of the PC filter over time.

4.3.4 Fume Collection Method

Just before the experiments, filters with attached grids were loaded into the cascade impactor instruments (ELPI and MOUDI). All the stages of the instruments were assembled and calibrated to their design flow rates as explained in detail in Chapter 2. Welding was performed for roughly 10 seconds as to not overload the impaction plates and overlap particles on the TEM Grid.

4.3.5 Image Collection Method

Once the sample is placed in the microscope, adjustments to the instrument are performed within the first visible grid square. After microscope adjustments are complete, a wide angle (lower magnification) survey of the sample is performed to determine the extent of particle loading on the grid. A few images of the sample at this low magnification are captured for further analysis. Next, higher magnification images of individual particles within a grid square are captured. The final magnification depended on the size of the particle present and the morphologies observed in the sample.

Images are stored on the computer running the microscope software during the microscope session in UIC Electron Microscopy or Argonne CNM Electron Microscopy facilities. Images are recorded by an identification number, which incorporated the date and the count of images taken during that day. An excel spreadsheet identifying the sample, the date of the session and observational notes for each view of each filter is created and maintained for good record keeping purposes. At the end of the microscope session, all images are transferred via jump drive to another computer. Notes taken during imaging include the relative location of the image in question within the sample, the magnification and the morphology observations.

4.4 Results

The manner in which experimental data were collected for this research resulted in a 130 (including replicates) individual TEM grids exposed to welding fume particles and available for microscopic analysis. Due to time constraints, only one replicate of each experiment was subjected to electron microscopy. Further, no notable differences in samples collected in exposure and emission chamber experiments were observed in terms of particle size or morphology.

4.4.1 Primary Particle Size

As has been observed in previous research, welding particles collected in our experiments are primarily spherical in shape. This is a trait of condensation formed particles. Across all size-fractionated samples collected during this research, three main primary particle sizes were observed, which we classify into three groups as follows:

Group 1: Particles less than 10 nm in diameter

Group 2: Particles greater than 10 nm but less than 100 nm in diameter

Group 3: Particles greater than 100 nm in diameter

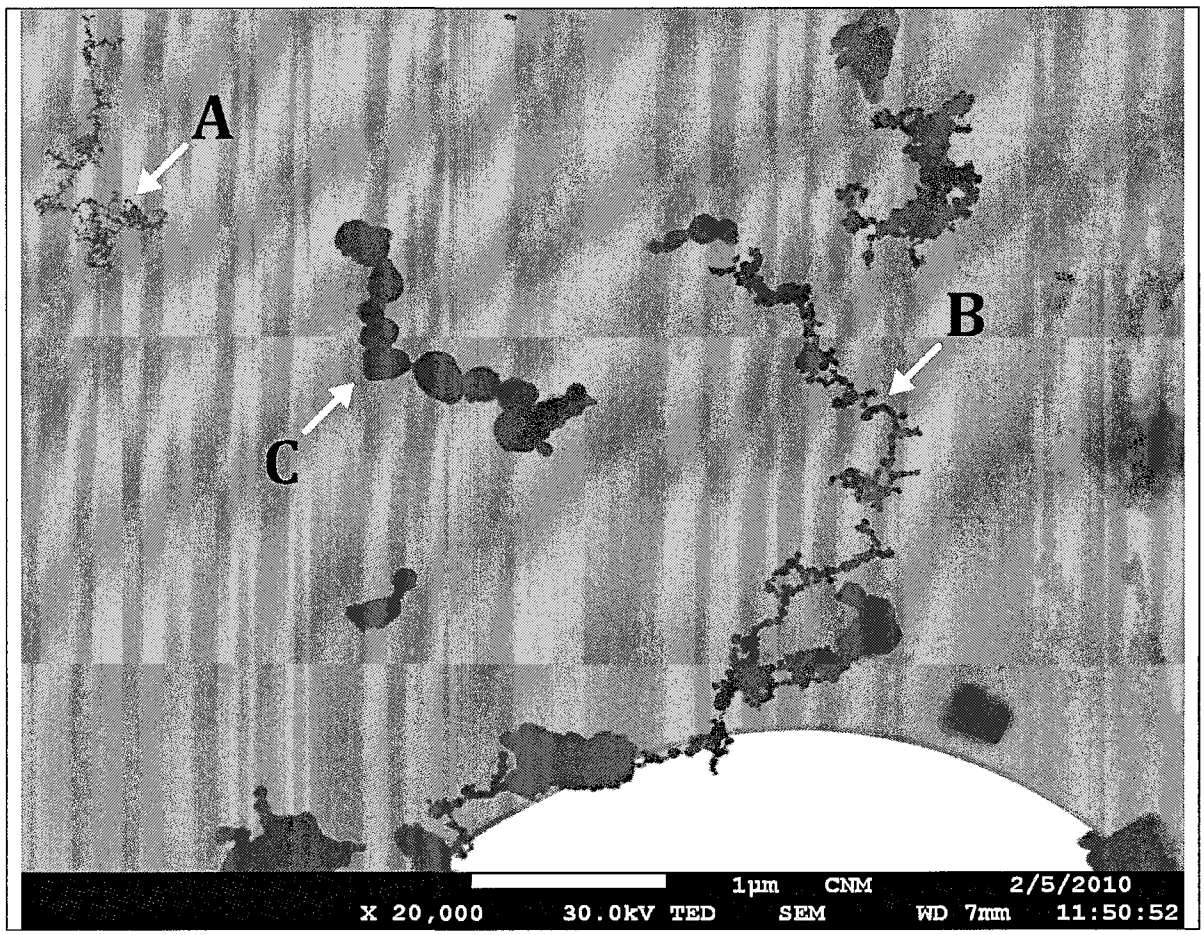

Exposure Chamber, Stage 8 ELPI (0.961 µm cut-point)

Figure 32: Primary particle sizes observed in the exposure chamber experiments.

These different groups of primary particles are displayed in Figure 32. Here, particles highlighted at point A are <10 nm in diameter (Group 1), particles highlighted at point B are approximately 40nm in diameter (Group 2), and particles highlighted at point C are approximately 230 nm in diameter (Group 3). No single primary particle greater than 390 nm was observed (Figure 33). This is consistent with nucleation and condensation formation theory for welding fume, which dictates that fume particles would not grow larger than 0.5 μm in diameter (Voitkevich, 1995; Worobiec, et al., 2007).

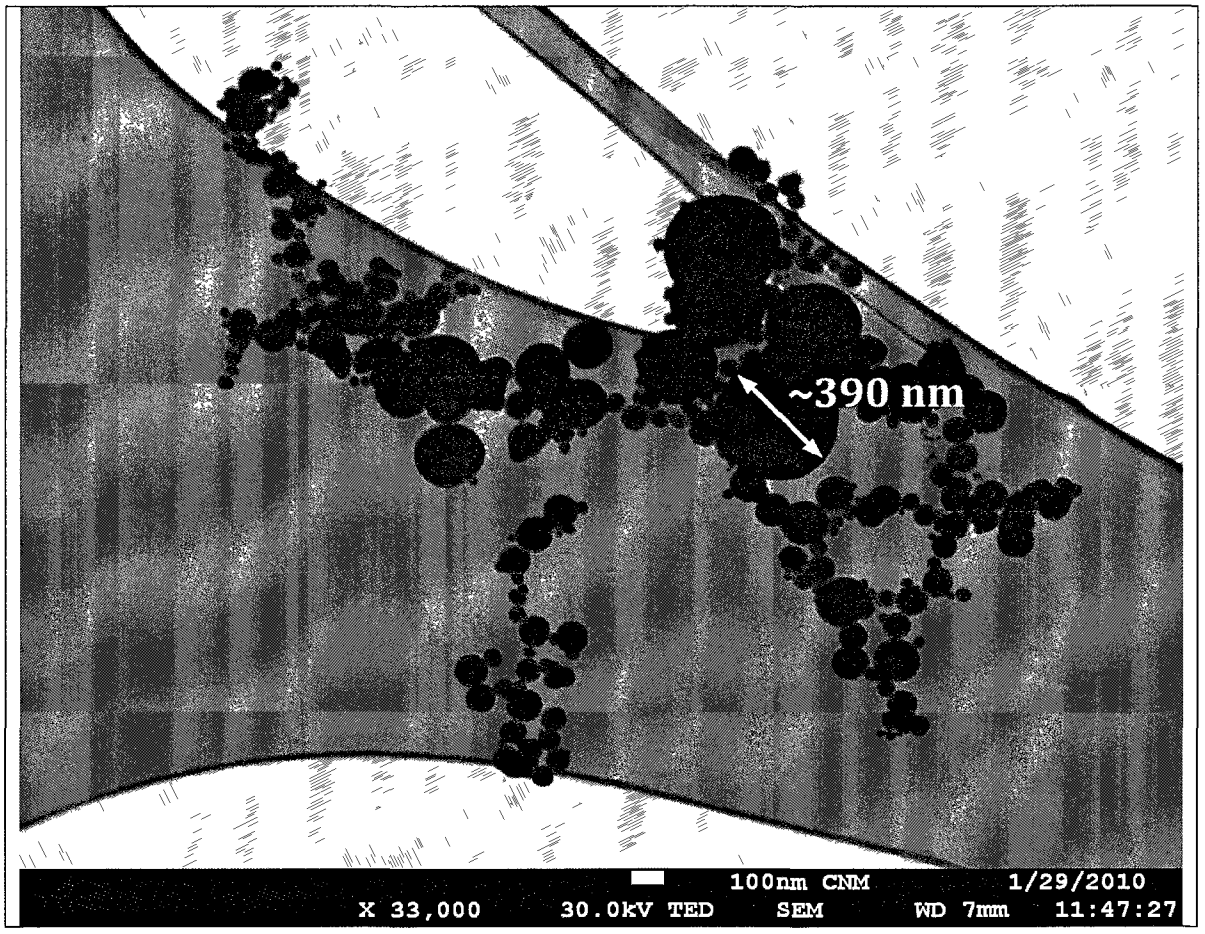

Note: Image was taken from a sample on Stage 1 (18.0 μm cut-off point) of MOUDI operated in the exposure chamber.

Figure 33: Largest primary particle observed exposure and emission chamber experiments.

4.4.2 Particle Morphologies

Consistent with previous welding fume studies, the most common form of morphology observed was agglomerated spherical primary particles in samples across all stages of impactors.

There were, however, different types of agglomerates found within the collected samples across all stages and two major categories shown in Figure 34 were identified. Point A in this figure shows the first types that are chainlike agglomerates consisting of primary particles <10 nm. These agglomerates almost always consisted of hundreds of primary particles. Point B highlights the second type that are densely packed agglomerates consisting of primary particles >100 nm. The densely packed agglomerates often contained tens of primary particles. The chainlike agglomerates of small primary particles described in point A could be many microns long (often >10 μm) in their greatest diameter. The densely packed agglomerates of larger primary particles described in point B were much smaller in greatest diameter, often not exceeding 1-2 μm in overall agglomerate size.

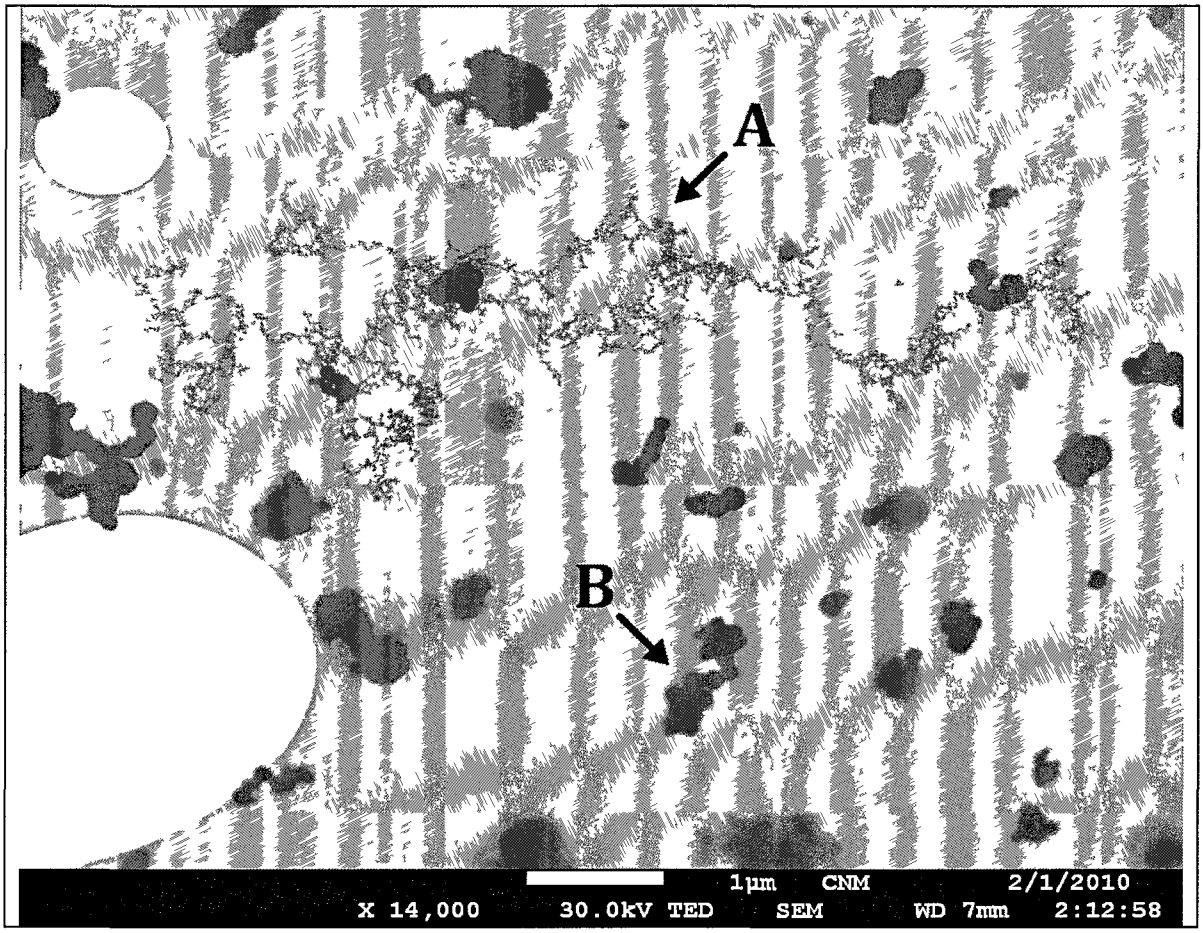

Note: Image was taken from a sample on Stage 12 (6.77 µm cut-off point) of ELPI operated in the exposure chamber

Figure 34: Major agglomerate types observed in the exposure chamber experiments.

In addition to these two major morphologies frequently observed, other agglomerate shapes were also identified. One such morphology found in stages 4 through 10 (cut-off points 0.157 µm to 2.42 µm), was a densely packed agglomerate consisting of smaller primary particles, as shown in Point A in Figure 35. This type of agglomerate seems to be a collection of chainlike agglomerates observed in Point B in the same figure, where the chainlike structure is extending from the overall mass. It cannot be determined whether this agglomerate was formed between the

time of welding fume generation and entry into the instrument, during the residence time within the instrument, or from many chainlike agglomerates impacting on top of one another.

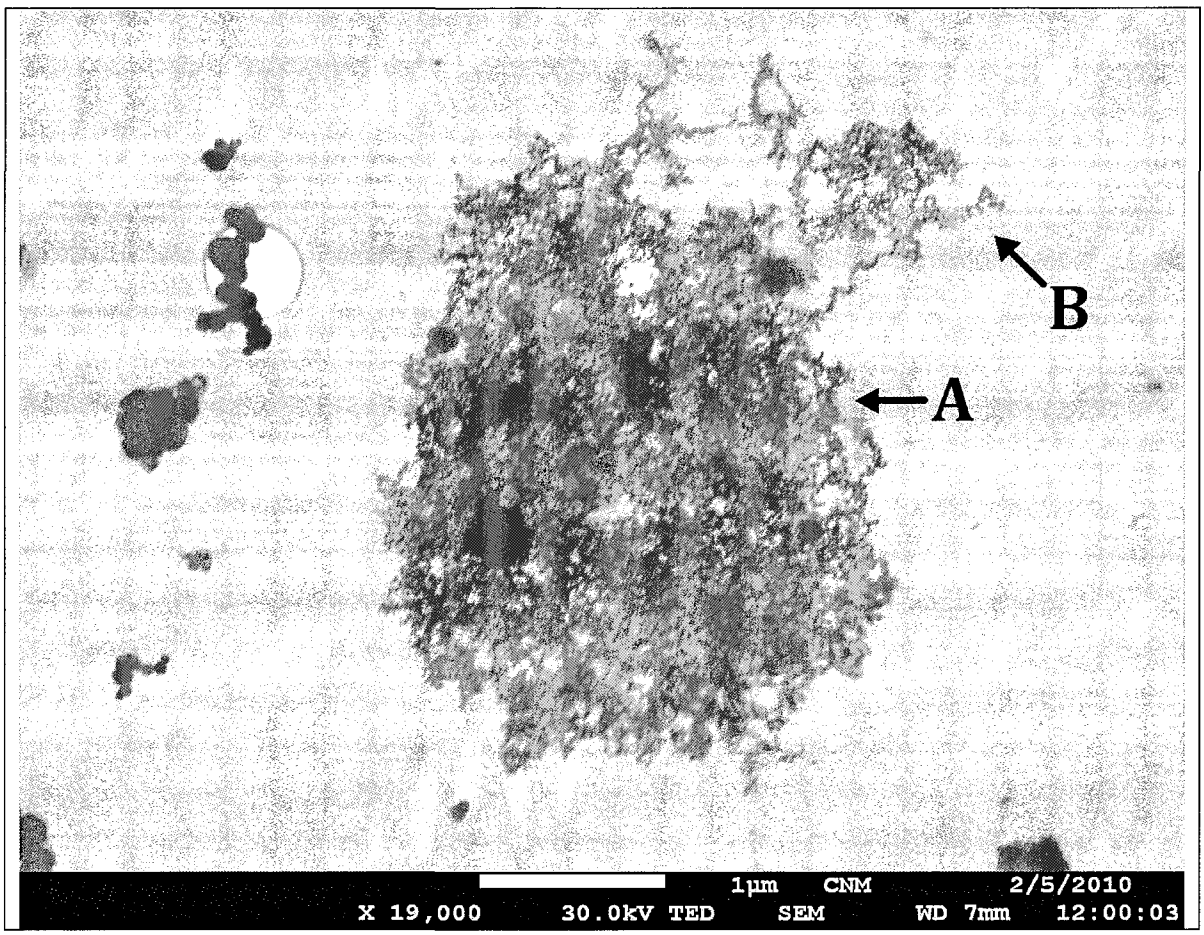

Note: Image was taken from a sample on Stage 8 (0.961 µm cut-off point) of ELPI operated in the exposure chamber.

Figure 35: Densely packed agglomerate of small primary particles observed in the exposure chamber experiments.

Another morphology often observed in the samples across all stages is irregularly shaped agglomerate, which seems to be a form of the densely packed larger particle agglomerate. An example of this type of morphology is highlighted in Point A in Figure 36. Here, we see nearly spherical particles on the edges of these agglomerates, however, the inner portion of the agglomerate is so dense that no discernable features can be clearly identified. Therefore, the agglomerate takes on an irregular pattern. A possible explanation for such observed agglomerates is that the thickness of the agglomerate is great enough to not permit the electron beam to pass through the specimen. A higher energy beam, like those used with a TEM, would be required to recognize whether individual spherical particles are present in this structure.

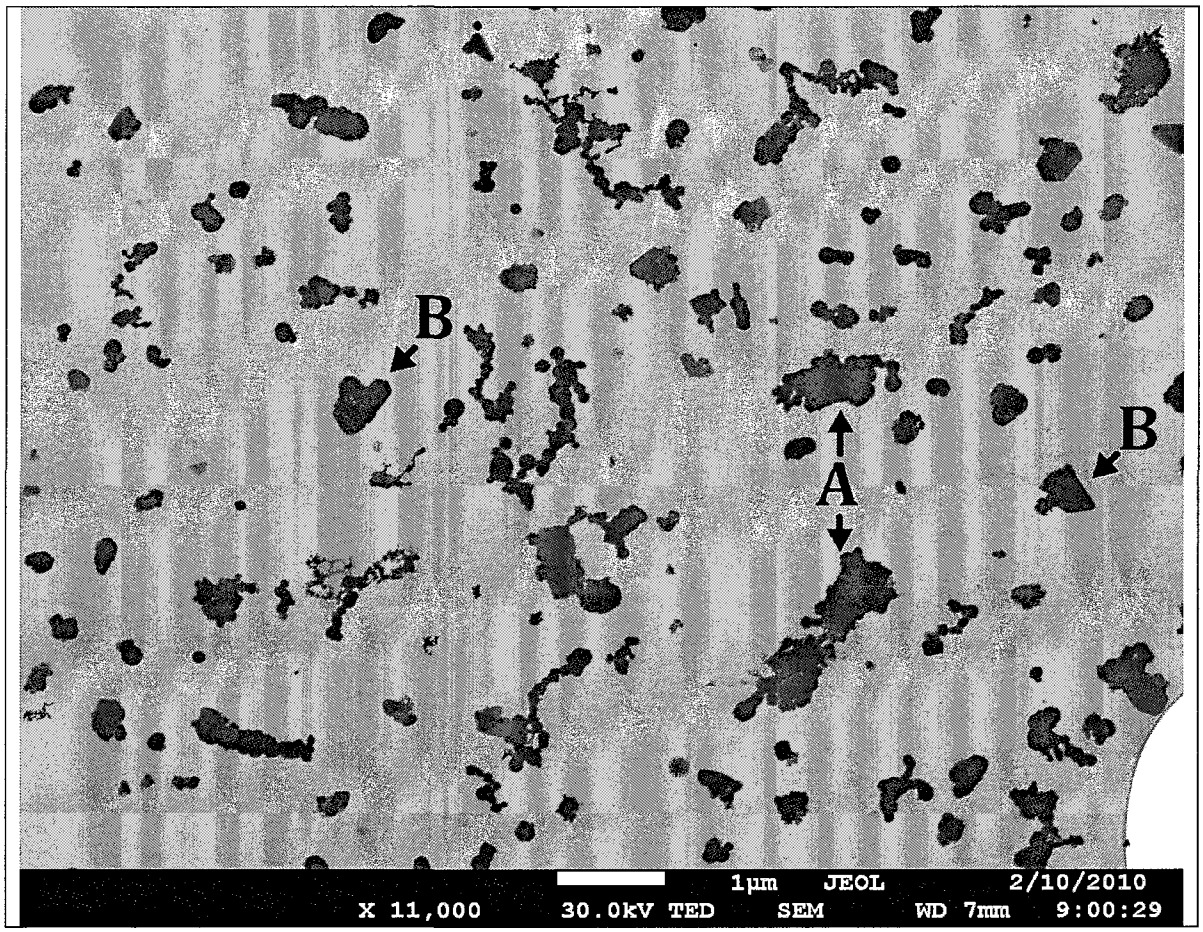

Note: Image was taken from a sample on Stage 6 (0.387 μm cut-off point) of ELPI operated in the exposure chamber

Figure 36: Other observed morphologies observed in the exposure chamber experiments.

Although observed across all size fractions, the irregular morphology is definitely prominent in the mid range size fractions. The SEM with TED detector did not have enough energy to distinguish the internal structure of these types of agglomerates. We did have a limited number of samples analyzed with the TEM. These images obtained using the TEM aid in identification of the underlying structure of the irregularly shaped morphologies. One example of this is presented in Figure 37. At Point A of this figure, a spherical particle within the irregular structure is highlighted.

From the image, we cannot be certain whether this spherical particle is within the agglomerate or resting above or below it. Determination of spatial arrangement of individual particles would require additional microscope analysis with stage tilting capabilities. By tilting the stage, and thus the angle of beam interaction with the sample, we may identify whether the larger spherical particles is surrounded by the irregular structure. Only then can we begin to understand the spatial orientation of particles like the one shown in Point A. But, if we are to assume that this spherical particle is surrounded by the irregular structure shown around it, we have some unexplained formation mechanism that cannot be not fully described by the Jenkins theory (Neil T. Jenkins & Eagar, 2003). Obviously, detailed chemical composition data on individual particle level are needed to formulate potential mechanisms or to begin to form a new theory.

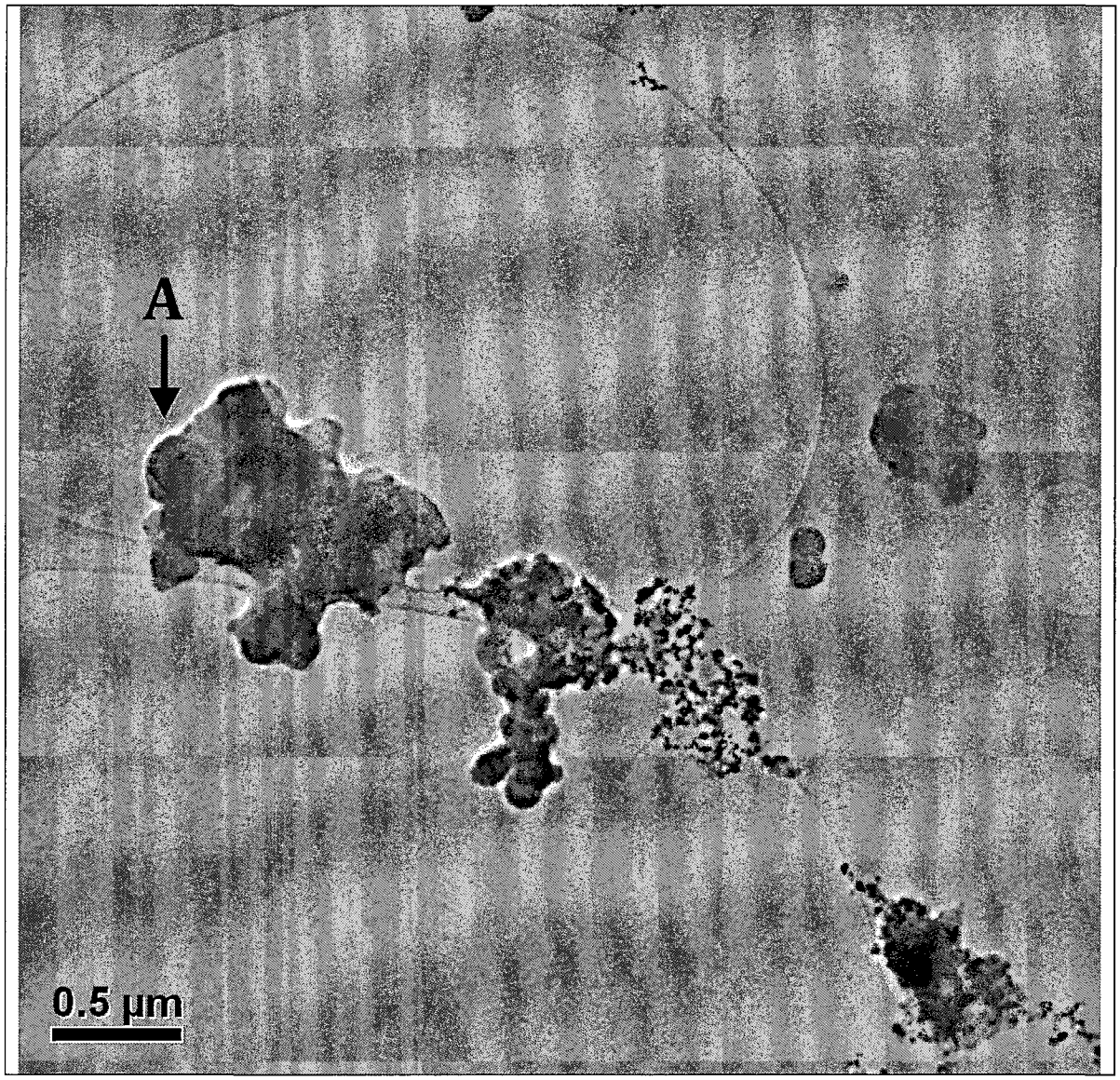

Note: Image was taken from a sample on Stage 5 (1.8 µm cut-off point) of MOUDI operated in the emission chamber.

Figure 37: TEM image of an irregular morphology observed in the exposure chamber experiments

Another morphology at times observed is what we refer to as a straightedge particle. Examples of these types of morphologies are presented in Point B in Figure 36. Here, particles

within an agglomerate seem to have a definitive crystal like edge. These particles were observed in multiple size fractions and no trend in their appearance was distinguished from one stage to the next. The origin of such particles is unknown, however, since they are often associated with particles in an agglomerate, it cannot be ruled out that their source is in fact welding fume.

4.4.3 Particle Morphology Across Size Fractions of Welding Fume

Since the specific definitions of observed morphologies are defined above a qualitative and descriptive analysis of differences in morphology observations across size fractions can be performed. Results of this descriptive process as applied to samples collected in the ELPI during the exposure chamber experiments are presented in **TABLE** XXXV. To aid in the process of characterizing morphologies, descriptions of morphologies with primary particles less than 100 nm and greater than 100 nm were grouped together. This distinction was made primarily on the basis of image resolution. Identification of primary particles less than 10 nm in diameter often requires magnification on the order of 25,000-50,000X. At that magnification, however, larger primary particle agglomerates are difficult to characterize because they often fill the field of view and a lower magnification level is required (i.e., 10,000 – 20,000X magnification). Therefore, it is much more convenient to split the particles into size ranges that are easily distinguishable at magnification levels that were used to observe the overall morphology of particle agglomerates. Some attempt at distinguishing particles between the size ranges of <10 nm and 10-100 nm was still performed in describing the size fractionated samples of ELPI.

TABLE XXXV: MORPHOLOGIES OBSERVED ACROSS SIZE-FRACTIONS

Stage	Loading	Particles Less than 100nm	Particles Greater than 100 nm	Other Observations
1 0.028	Low	• Chainlike agglomerate. - Hundreds of particles forming the single chainlike particle.	• Densely packed. - Few particles packed together in the agglomerate.	• Overall agglomerate structure smaller than observed on other stages. • Some irregular structure mass surrounding the >100nm agglomerates is observed.
2 0.055	Low	• Chainlike agglomerate. - Hundreds of particles forming the single chainlike particle.	• Densely packed. - Few particles packed together in the agglomerate.	• Irregular structure surrounding the >100 nm agglomerates observed.
3 0.094	Medium	• Chainlike agglomerate. - Hundreds of particles forming the single chainlike particle.	• Densely packed. - Tens to hundreds of primary particles together in agglomerate.	• Irregular structure surrounding the >100 nm agglomerates observed. • Some larger particles (>100 nm) have irregular shapes and do not seem associated with the spherical particle agglomerates. • One cubic structure particle observed.

TABLE XXXV: MORPHOLOGIES OBSERVED ACROSS SIZE-FRACTIONS (continued)

Stage	Loading	Particles Less than 100nm	Particles Greater than 100 nm	Other Observations
4 0.157	Medium	• Chainlike agglomerate. - Hundreds of particles forming the single chainlike particle. • Densely packed agglomerates associated with the larger particle sizes. - Irregular shape structures associated with densely packed agglomerates.	• Densely packed. - Tens to hundreds of primary particles together in agglomerate.	• Irregular structure surrounding the >100 nm agglomerates observed. • Some larger particles (>100 nm) have irregular shapes and do not seem associated with the spherical particle agglomerates. • One agglomerate observed to have few particles with straight edges.
5 0.266	Heavy	• Chainlike agglomerate. - Hundreds of particles forming the single chainlike particle. • Densely packed agglomerates associated with the larger particle sizes. - Irregular shape structures associated with densely packed agglomerates.	• Densely packed. - Tens to hundreds of primary particles together in agglomerate.	• Particle loading resulted in some broken carbon film of TEM grid. • Irregular structures associated with densely packed smaller particle agglomerates. • Irregular structures associated with larger particle densely packed agglomerates.

TABLE XXXV: MORPHOLOGIES OBSERVED ACROSS SIZE-FRACTIONS (continued)

Stage	Loading	Particles Less than 100nm	Particles Greater than 100 nm	Other Observations
6 0.387	Medium	• Chainlike agglomerate. - Hundreds of particles forming the single chainlike particle. • Densely packed agglomerates associated with the larger particle sizes. - Irregular shape structures associated with densely packed agglomerates.	• Densely packed. - Tens to hundreds of primary particles together in agglomerate. • Chainlike agglomerate. - Tens of primary particles together in agglomerate.	• Irregular structure surrounding the >100 nm agglomerates observed. • Some larger particles (>100 nm) have irregular shapes and do not seem associated with the spherical particle agglomerates. • One agglomerate observed to have straight edges.
7 0.622	Medium to Heavy	• Chainlike agglomerate. - Hundreds of particles forming the single chainlike particle. • Densely packed agglomerates associated with the larger particle sizes. - Irregular shape structures associated with densely packed agglomerates.	• Densely packed. - Tens to hundreds of primary particles together in agglomerate. • Chainlike agglomerate. - Tens of primary particles together in agglomerate.	• Very dense agglomerates containing large and small particles observed. - Distinguishing primary particles can only be performed on the edges of these agglomerates because the density is too great to see structure at the center of the particle.

TABLE XXXV: MORPHOLOGIES OBSERVED ACROSS SIZE-FRACTIONS (continued)

Stage	Loading	Particles Less than 100nm	Particles Greater than 100 nm	Other Observations
8 0.961	Heavy	• Chainlike agglomerate. - Hundreds of particles forming the single chainlike particle. • Densely packed agglomerates associated with the larger particle sizes. - Irregular shape structures associated with densely packed agglomerates.	• Densely packed. - Tens to hundreds of primary particles together in agglomerate. • Chainlike agglomerate. - Tens of primary particles together in agglomerate.	• Very dense agglomerates containing large and small particles observed. - Distinguishing primary particles can only be performed on the edges of these agglomerates because the density is too great to see structure at the center of the particle. • Few large (> 1um) cubic particles observed.
9 1.62	Medium to Heavy	• Chainlike agglomerate. - Hundreds of particles forming the single chainlike particle. • Densely packed agglomerates associated with the larger particle sizes. - Irregular shape structures associated with densely packed agglomerates.	• Densely packed. - Tens to hundreds of primary particles together in agglomerate.	• Irregular structure surrounding the >100 nm agglomerates observed.

TABLE XXXV: MORPHOLOGIES OBSERVED ACROSS SIZE-FRACTIONS (continued)

Stage	Loading	Particles Less than 100nm	Particles Greater than 100 nm	Other Observations
10 2.42	Heavy	• Chainlike agglomerate. - Hundreds of particles forming the single chainlike particle. • Densely packed agglomerates associated with the larger particle sizes. - Irregular shape structures associated with densely packed agglomerates.	• Densely packed. - Tens to hundreds of primary particles together in agglomerate.	• Chainlike agglomerates of smaller particles seem more abundant than larger particle agglomerates. • Irregular structures surrounding larger particle agglomerates.
11 4.05	Medium	• Chainlike agglomerate. - Tens to hundreds of primary particles forming the single chainlike agglomerate. - Thin chain and dense chain agglomerates observed.	• Densely packed. - Few particles packed together in the agglomerate.	• Few straight edge particles <100nm observed.
12 6.77	Low	• Chainlike agglomerate. - Tens to hundreds of primary particles forming the single chainlike agglomerate. - Thin chain and dense chain agglomerates observed.	Very few observed. Single particles or small agglomerates of few primary particles.	• Irregular structure surrounding the <100 nm observed. • Overall agglomerate structure smaller than observed on other stages.
13 10.04	Low	• Not observed in significant quantities.	Very few observed. Single particles or small agglomerates of few primary particles.	• Very large irregular particles observed with dense appearance and sharp crystal like edges.

The amount of loading per a given size-fractionated TEM grid was recorded. Consistent with mass-based distribution findings presented in Chapter 2, particle loading on grids was low at larger and smaller size fractions (upper and lower stages). The mid-range size fractions (middle stages) often experienced moderate to heavy loading, sometimes so great as to make primary particle resolution within the agglomerate difficult despite the ≤10 second sampling time.

Particles less than 100 nm in diameter were always observed to form chainlike agglomerates consisting of hundreds of primary particles. At the smaller size fractions (stages 1-3), this was the only morphology observed. As size fractions move to larger aerodynamic diameters (stages 4-10), an additional morphology of densely packed agglomerates of primary particles in the 10-100 nm range is also observed in addition to the chainlike agglomerates. Often these densely packed agglomerates are associated with irregular structures that surround the agglomerate. In the largest diameter size fractions (stage 11-13), the chainlike agglomerates were still observed, however to a lesser extent. In fact, no agglomerates with primary particles less than 100 nm were observed the upper most stage of the ELPI.

Particles greater than 100 nm were always observed to form densely packed agglomerates. The number of primary particles within the agglomerate varied from a few in the smaller diameter size fractions (stages 1-2) to tens and hundreds in the larger size fractions (3-10). The largest size fractions (stages 11-13) again experienced agglomerates of only a few primary particles. Some chainlike agglomerates of greater than 100 nm primary particles were observed within the mid-range size fractions (stages 6-8) and these consisted of tens of particles within the agglomerate. In all size fractions, irregular structures were often observed surrounding the greater than 100 nm primary particle agglomerates. No distinguishable trend in the frequency of these structures'

appearance across size fractions is noticeable, however, not all of the agglomerates were associated with the irregular shapes.

4.4.4 Chemical Analysis

Despite multiple attempts to perform a compositional analysis using the EDX detector on the on the Argonne CNM SEM microscope, the number of x-ray counts needed to accurately describe the compositional spectra of a sample were not adequate in any circumstance. The primary reason for this deficiency and limitation was that the probe size available on the SEM was on the order of 1μm in diameter. As we have demonstrated in the previous sections, primary particles were much smaller than this and individual particle analysis was not feasible with this microscope. In some instances we attempted to analyze a grouping of similar type particles but the adequate number of x-ray counts was still not achievable. This resulted in insufficient data to accurately describe composition on the particle level.

However, the probe size on the TEM at UIC is much finer than that of the SEM. Some elemental analysis was performed using the TEM, however, a sufficient count rate for the EDS detector was still rarely achievable. Some of the EDS spectra gathered in this research are presented in Figures 38 through 42, below. Although these count rates are not ideal for precise and accurate quantitative measurements, the analysis presented here may be suggestive in qualitative terms of hypotheses generation for future research. The metals analyzed with the EDS detector include those analyzed with HR-ICP-MS (Na, K, Fe, Ti, Ni, Mn, Cr) as well Si and Cu. The silicon analysis with HR-ICP-MS was not performed due to sample preparation difficulties of the WSLH. Copper is also reported in the EDS data. Although welding fume contains copper, the use of the

copper TEM grids for sample collection, produces a high background signal in most EDX spectra. Thus, copper results are not reliable since copper not only originated from welding fume but also was contributed by using copper grid on sampling media.

The EDS computer software for the TEM did not allow direct copying of images of spectra. Spectra presented in the figures below were created as a scatter plot using Microsoft Excel spreadsheet program and thus do not specifically identify peaks associated with each element. **TABLE** XXXVI lists the energies and associated spectral lines used in elemental identification.

TABLE XXXVI: ENERGIES FOR SPECIFIC SPECIES IN EDS CHEMICAL COMPOSITION ANALYSIS

Energy (keV)	Spectral Line	Energy (keV)	Spectral Line
1.05	Na Ka	0.63	Mn La1
1.75	Si Ka	5.9	Mn Ka
3.33	K Ka	0.7	Fe La1
3.64	K Kb1	6.42	Fe Ka
0.45	Ti La1	7.05	Fe Kb1
4.52	Ti Ka	7.47	Ni Ka1
4.95	Ti Kb1	0.92	Cu La1
0.57	Cr La1	8.04	Cu Ka1
5.91	Cr Kb1	8.91	Cu Kb1

In Figure 38, an EDS spectra is presented of a particle ~115 nm in diameter collected on stage 9 of the MOUDI (particle cut-off size=0.18 μm) operated in the emission chamber. This particle is situated within an agglomerate with many other smaller particles present and the EDS probe overlaps with some of these smaller particles. Spectra reveal larger amounts of Si (19.1%), K

(18.1%) and Mn (12.9%) as compared to Na (4.2%), Ti (7.9%), Cr (3.2%), Fe (8.6%) and Ni (2.9). Figure 39 also presents a particle collected on stage 9 of the MOUDI operated in the emission chamber, this time with a physical diameter >115 nm. This larger particle is situated within an agglomerate of larger particles but also has irregular structure linking the particles together. Here, the amount of Si (19.6%), K (24.5%) and Ni (19.4%) are larger compared to Na (11.0%), Mn (9.7%) and Fe (10.2%) and small amounts of Ti (1.1%) and Cr (4.6%) are also observed.

Figure 40 presents the EDS spectra of a 54 nm diameter particle captured on stage 8 of the MOUDI (particle cut-off size=0.32 μm cut point) operated in the emission chamber. This particle is situated in an agglomerate with other particles of roughly the same diameter but also adjacent to an agglomerate of particles in the single nanometer size range. Here Si (18.5%), K (20.5%) and Cr (15.7%) are detected in larger amounts than Na (3.5%), Ti (3.3%), Mn (6.9%) and Fe (9.2%) while Ni (0.7%) is barely detectable.

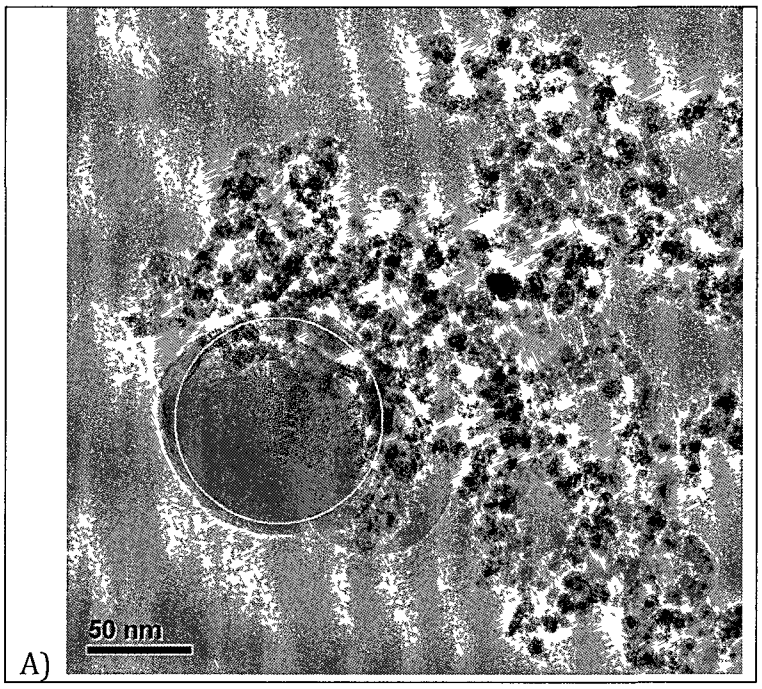

A)

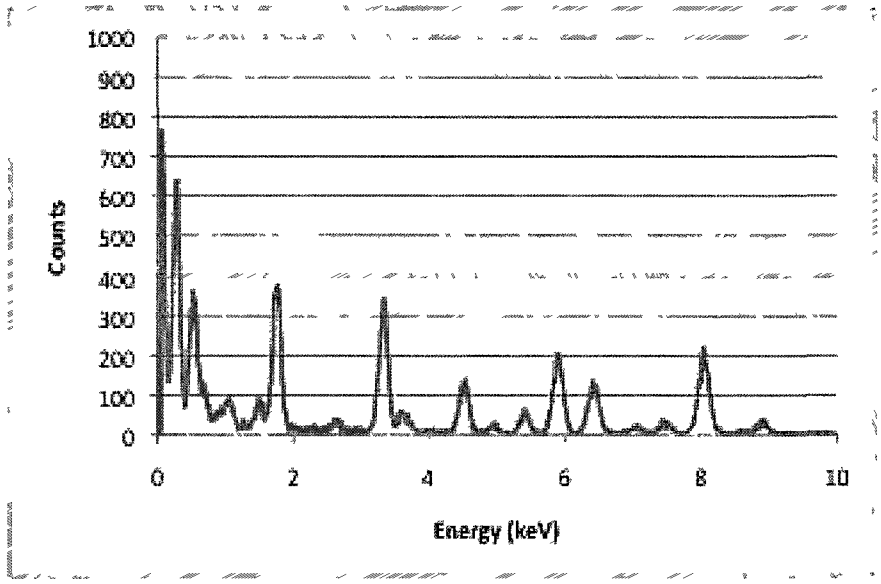

B)

Element	Wt%
Na	4.2%
Si	19.1%
K	18.1%
Ti	7.9%
Cr	3.2%
Mn	12.9%
Fe	8.6%
Ni	2.9%
Cu	17.4%

Note: Image was taken from a sample on Stage 9 (0.18 μm cut-off point) of MOUDI operated in the emission chamber; Measured Particle Diameter =115 nm

Figure 38: TEM image and EDS spectra 1 of a sample obtained in the emission chamber.

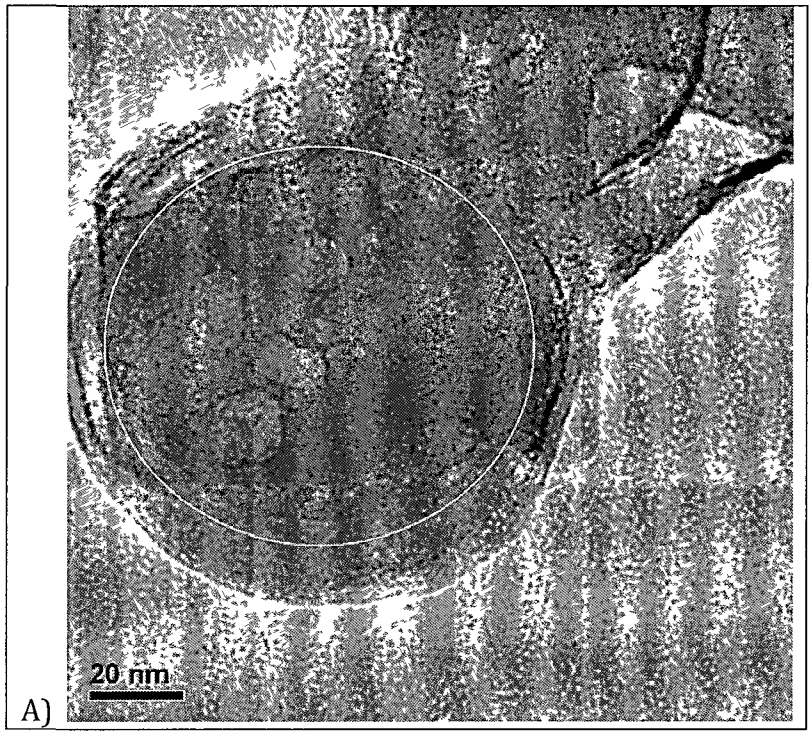

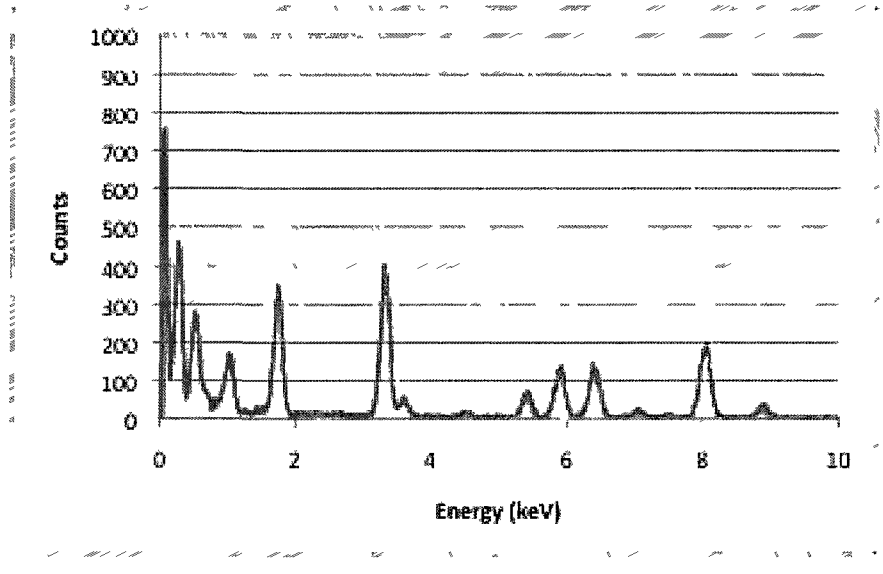

Element	Wt%
Na	11.0%
Si	19.6%
K	24.5%
Ti	1.1%
Cr	4.6%
Mn	9.7%
Fe	10.2%
Ni	19.4%
Cu	11.0%

MOUDI Stage 9 (0.18 μm cut-point); Measured Particle Diameter >115 nm

Figure 39: TEM image and EDS spectra 2 of a sample obtained in the emission chamber.

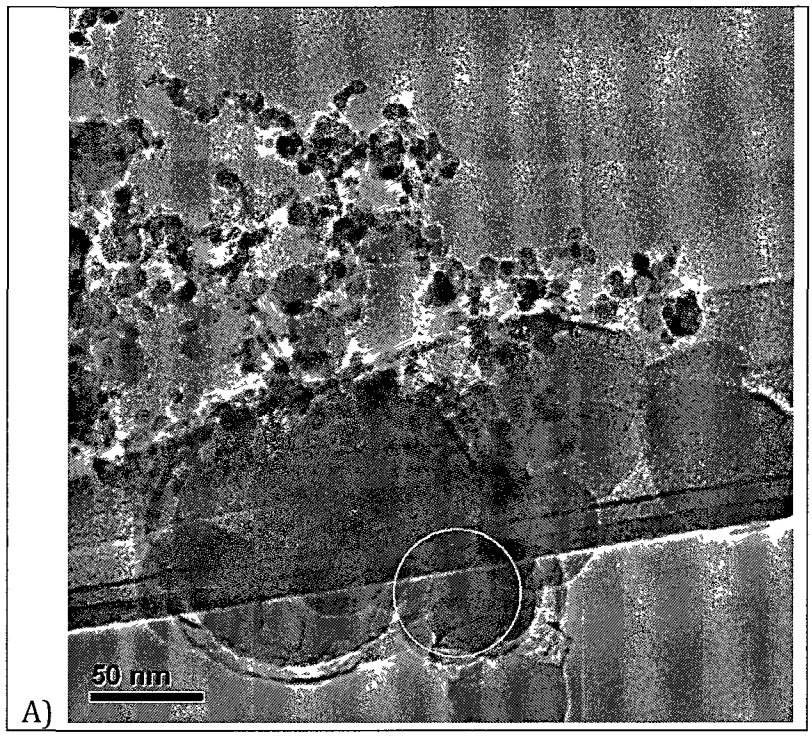

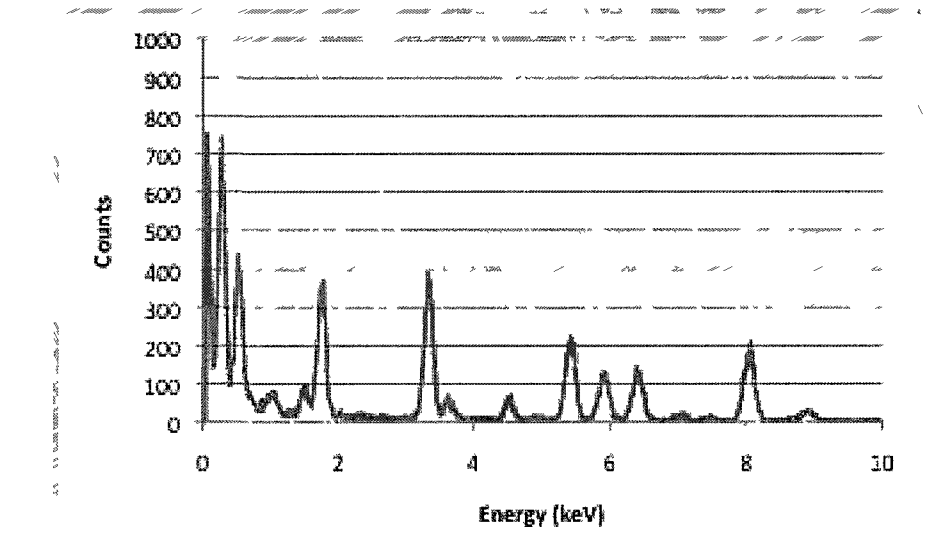

Element	Wt%
Na	3.5%
Si	18.5%
K	20.5%
Ti	3.3%
Cr	15.7%
Mn	6.9%
Fe	9.2%
Ni	0.7%
Cu	17.1%

Note: Image was taken from a sample on Stage 8 (0.32 μm cut-off point) of MOUDI operated in the emission chamber; Measured Particle Diameter=54 nm

Figure 40: TEM image and EDS spectra 3 of a sample obtained in the emission chamber.

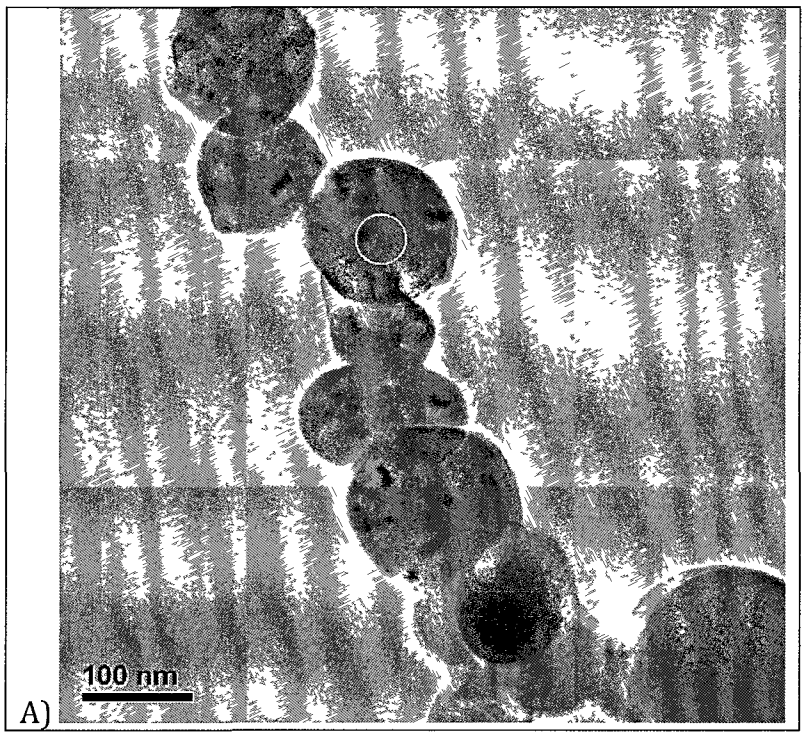

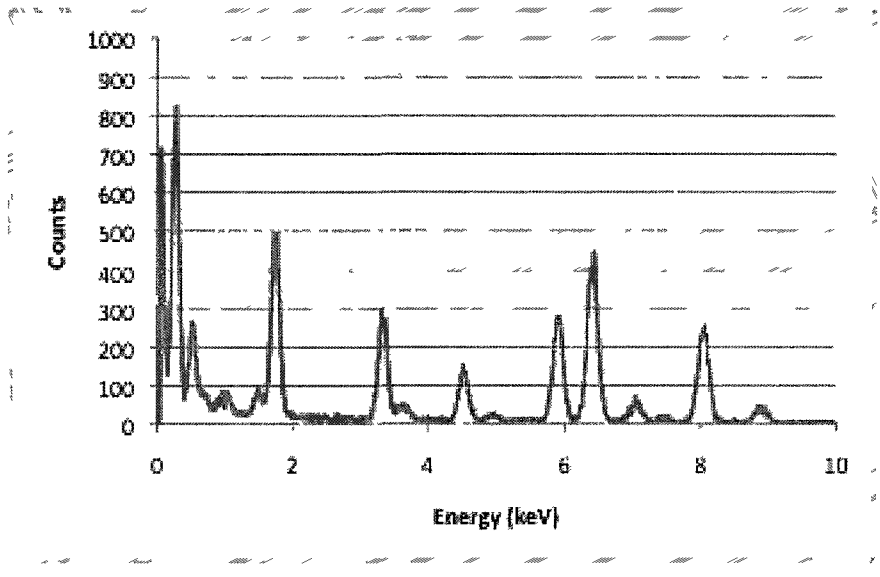

Element	Wt%
Na	n.d.
Si	20.6%
K	12.0%
Ti	6.6%
Cr	0.2%
Mn	15.5%
Fe	22.9%
Ni	n.d.
Cu	18.1%

Note: Image was taken from a sample on Stage 7 (0.56 μm cut-off point) of MOUDI operated in the emission chamber; Measured Particle Diameter=138 nm

Figure 41: TEM image and EDS spectra 4 of a sample obtained in the emission chamber.

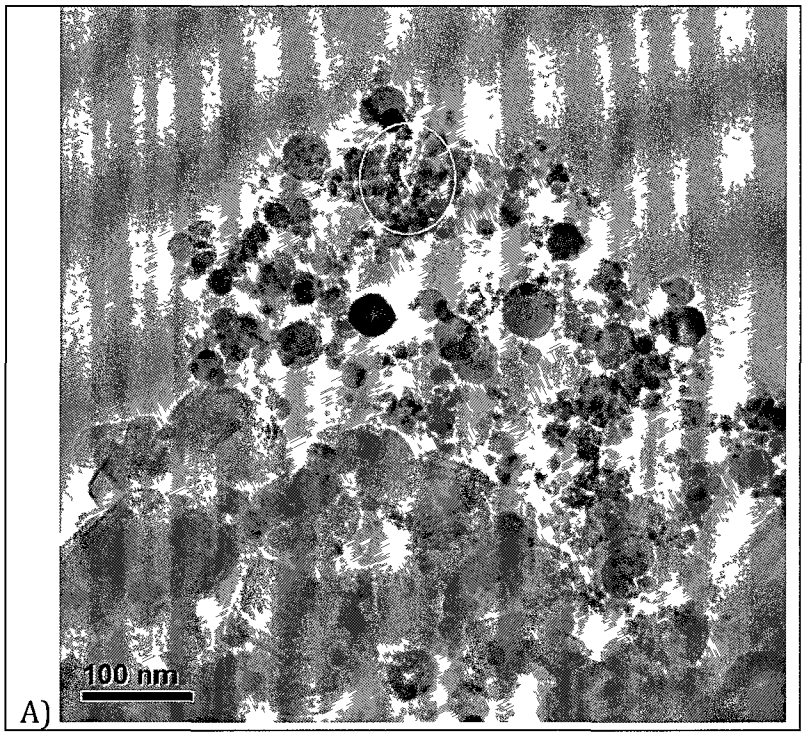

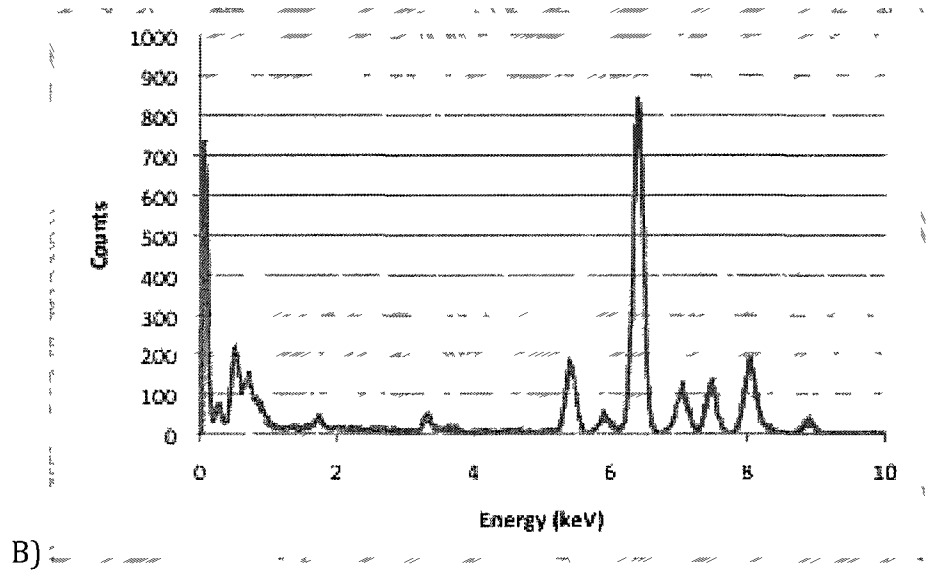

Element	Wt%
Na	n.d.
Si	12.3%
K	n.d.
Ti	n.d.
Cr	8.4%
Mn	1.2%
Fe	39.8%
Ni	17.5%
Cu	20.9%

MOUDI Stage 5 (1.8 μm cut-point); Average Measured Particle Diameter 31 nm

Figure 42: TEM image and EDS spectra 5 of a sample obtained in the emission chamber.

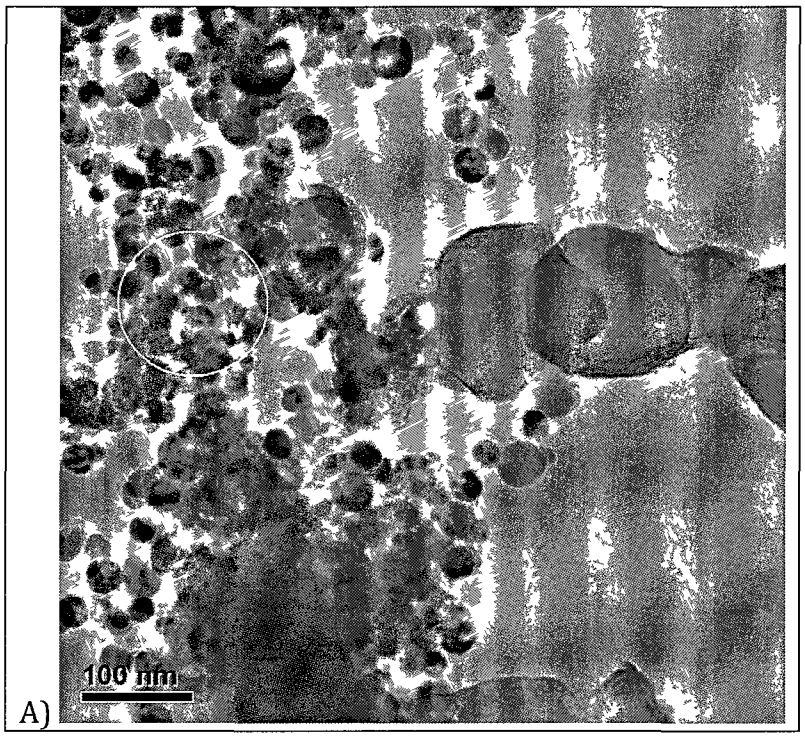

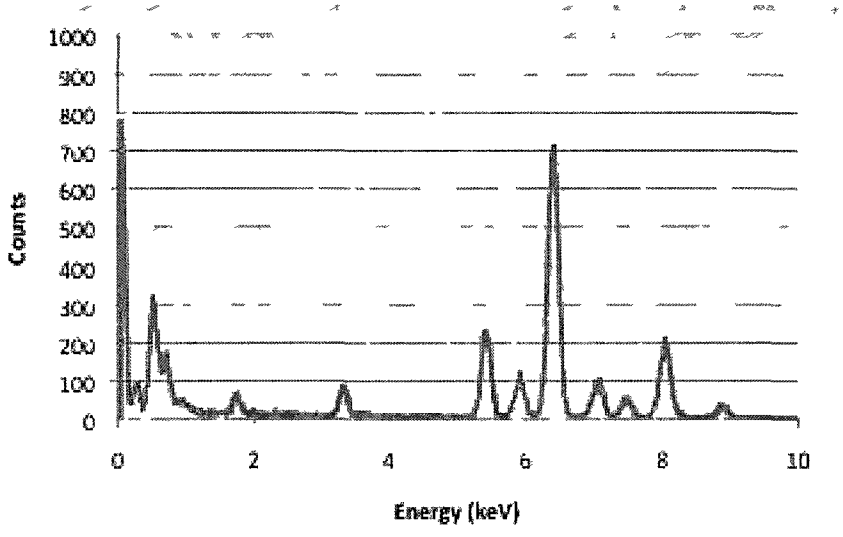

Element	Wt%
Na	n.d.
Si	14.8%
K	9.6%
Ti	n.d.
Cr	10.6%
Mn	3.4%
Fe	38.5%
Ni	5.4%
Cu	17.8%

B)

Note Image was taken from a sample on Stage 5 (1.8 μm cut-off point) of MOUDI operated in the emission chamber, Average Measured Particle Diameter=25 nm

Figure 43: TEM image and EDS spectra 6 of a sample obtained in the emission chamber.

Figure 40 presents the EDS spectra of a particle 138 nm in diameter that was captured on stage 7 of the MOUDI (particle size cut-off: 0.56 μm) operated in the emission chamber. The particle is situated within a chain-like agglomerate composed of particles similar in physical diameter. The spectra reveal larger amounts of Si (20.6%) and Fe 22.9%) as compared to K (12.0%), Mn (15.5%) and Ti (6.6%). Na and Ni are not detected and Cr (0.2%) is barely detected. Figure 41 presents the EDS spectrum of a cluster of particles with an average diameter of 31 nm that are situated in densely packed small particle agglomerate. These particles were captured on stage 5 of the MOUDI (particle size cut-off point=1.8 μm) operated in the emission chamber. Fe (39.8%) is detected in large amount with Si (12.3%), Cr (8.4%) and Ni (17.5%) in less abundant amounts. Na, K and Ti are not detected while Mn (1.2%) is hardly detectable. Figure 42 also presents the EDS spectra of a cluster of particles with an average diameter of 25 nm captured on stage 5 of the MOUDI operated in the emission chamber. Here, Fe (38.5%) is most abundant followed by lesser amounts of Si 14.8%), K (9.6%) and Cr (10.6%). Even less amounts of Mn (3.4%) and Ni (5.4%) are detected and Na and Ti are not detected at all.

A summary of the EDS compositional analysis is presented in TABLE XXXVII below where chemical composition of particles are grouped by the physical diameter measured from the specific particle analyzed on the sample. Sodium seems transient in nature as it is detected sometimes in small and large particles. Silicon is consistently present in all particles sizes, however, it is observed that smaller particles have less silicon than larger particles. Potassium is present in most particles analyzed and no consistent trend is readily observed. Titanium is not detectable in two of the smaller particles analyzed but present in all of the larger particle sizes. Chromium content is observed in larger amounts in smaller particle sizes as compared to larger. Manganese may have higher concentrations in larger particle sizes, however, a clear trend is not discernable. Iron is

present in much higher amounts of two of the small particles analyzed while iron amount in the larger particles analyzed do not approach these levels. Nickel is more abundant in the smaller particles sizes but not in the larger particle sizes where it was not detected in two of those particles. Copper is detected in relatively consistent amounts in all samples. Although there may be copper within the fume, the TEM grid used during these experiments was also made of copper and, in our results, we would not be able to distinguish the sources of copper from these two sources.

TABLE XXXVII: SUMMARY OF SEM-EDS COMPOSITIONAL (AT%) ANALYSIS FOR SAMPLES COLLECTED IN EMISSION CHAMBER OPERATING A MOUDI

Particle Diameter (nm)	Na	Si	K	Ti	Cr	Mn	Fe	Ni	Cu
25	n.d.	14.8	9.6	n.d.	10.6	3.4	38.5	5.4	17.8
31	n.d.	12.3	n.d.	n.d.	8.4	1.2	39.8	17.5	20.9
54	3.5	18.5	20.5	3.3	15.7	6.9	9.2	0.7	17.1
115	11.0	19.6	24.5	1.1	4.6	9.7	10.2	n.d.	19.4
115	4.2	19.1	18.1	7.9	3.2	12.9	8.6	2.9	17.4
138	n.d.	20.6	12.0	6.6	0.2	15.5	22.8	n.d.	18.1

4.5 Discussion

4.5.1 Particle Size

A microscopic characterization of welding fume within different size-segregated samples has been performed. We have identified three different groups of primary particles: particles <10 nm in diameter (Group 1); particles between 10 and 100 nm in diameter (Group 2); and particles >100 nm in diameter (Group 3). These classifications are very similar to those observed by Farrants and Schuler et al. (1989) where they classified particles into small, medium and large. These researchers calculated a mean diameter for medium particles at approximately 70 nm and for large particles at approximately 150 nm. Small particles diameters were not measured because image resolution was not adequate enough to define particle boundaries.

The differences in primary particle size has been attributed to the chemical compositions of different size welding particles and a time and temperature based theory of formation has been developed (Neil T. Jenkins & Eagar, 2003). In this model (Figure 44) the distance vapor has to travel from the arc point into the room atmosphere is estimated to roughly 10 mm. Within that distance, there is a temperature decrease from >4,000 K at the arc to roughly 300 K (room temperature). In this model the first particles to nucleate will be relatively large because the critical diameter of nucleation is inversely proportional to the super cooling (i.e., the temperature gradient). Nucleated particles then grow by vapor condensation and collision with other particles. As we move away from the arc, the temperature decreases and therefore newly nucleated particle diameters decrease as well. At some point all vapors have condensed and particle formation from temperature dependent mechanisms will cease. After that, agglomeration may continue through

means of some type of attractive forces like magnetic or Van der Waals forces. Jenkins and Eagar (2003) grouped particles into bins of 20, 40, 60 and 80 nm in diameter and described what they called "significant change" in the chemistry with particle size, which leads to the conclusion that particles nucleated at different points along the model path.

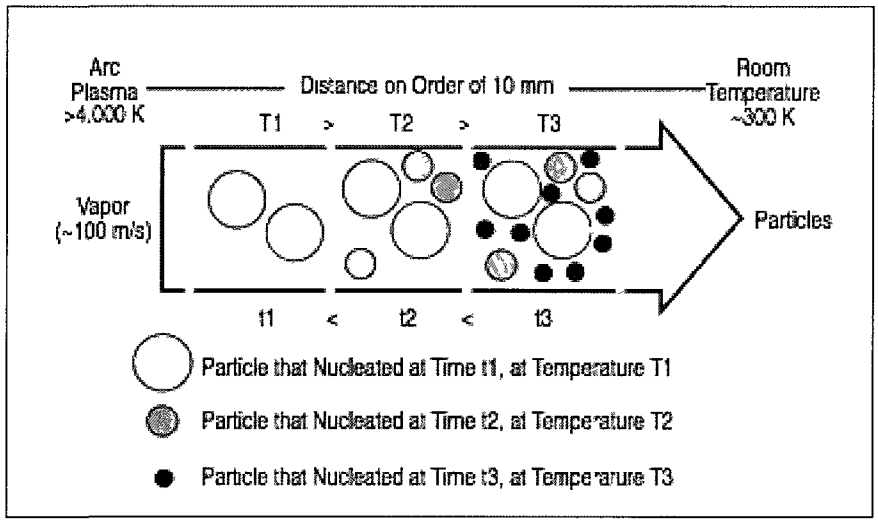

(reprinted with permission from Springer)

Figure 44: Formation of welding fume particles as a function of time and distance (Jenkins and Eager, 2003).

The theory presented by Jenkins and Eager (2003) is consistent with the findings of this research in which primary particles form distinct size classes. This theory does not however, take into account the formation of agglomerates or the specific particle morphology at the receptor (i.e. breathing-zone of the welder). Although we observe the distinct particle size classes and may be able to predict their formation mechanism dictated by temperature, ultimately, the health risk

posed by inhalation of the welding fume particles will be determined through their deposition within the respiratory tract. We have observed that all primary particle sizes are present within all size fractions of the welding aerosol studied mainly because the particles form agglomerates of varying size. A more comprehensive theory of welding fume formation that incorporates the mechanisms of agglomerate formation may be needed to predict the ultimate toxicological risk.

4.5.2 Particles Morphologies

The particle morphologies identified in this research include chainlike agglomerates of small particles, and densely packed agglomerates of larger particles. The significant observation from this data is that primary particles of the same size tend to group together within an agglomerate. This phenomenon has been described previously in a welding workshop (Stephenson, et al., 2003). This finding would suggest that primary particles of similar size are formed at the same time and then agglomerate quickly to form the final welding fume particle. If this were the case, we would expect all of the particles within an agglomerate to have a similar composition. This cannot be assumed with the collected samples, mainly because of positioning of sampling equipment and its relation to the fume generation point. Referring to Figure 45, nucleation and condensation of primary fume particles occurs practically right in the arc-zone. However, agglomeration and other particle interactions would begin to occur soon after and would continue into the breathing-zone, within the sampling probe and even within the cascade impactor. Therefore, the morphologies identified and compositionally analyzed within the breathing-zone may have formed in any of these locations of the welding environment.

One of the problems that we have when sampling welding fume in this fashion is that there are interactions between and among particles the entire time before entry into the sampler and impaction on the sampling grid. We therefore do not know whether the observed agglomeration occurred before or after sampling. One study did account for this and went so far as to explore the difference in observed morphologies between particles collected in the ELPI and those sampled thermoporetically (Sowards, et al., 2010). In this instance, the researchers passed carbon coated TEM grids through the weld plume at different distances from the welding point. They reported that there was agglomeration observed on these samples similar to that observed when sampling with the ELPI and concluded that agglomeration or deagglomeration during ELPI sample collection would be minimal. Other research that has employed thermoporetic sampling (Neil T. Jenkins & Eagar, 2003; N. T. Jenkins & T. W. Eagar, 2005a; N. T. Jenkins, et al., 2005) reported similar morphologies observed in our work. It is plausible that the agglomeration of welding particles occurs very quickly after condensation growth in the microenvironment around the arc that has very high number concentrations. A good indication of this is the sintered appearance of some agglomerates. In these instances the primary particles fused most likely when the particles were still in a semi fluid form. This would have occurred at a point just near the melting temperature where the particles began to combine but were frozen together when the temperature dropped sufficiently enough to solidify into fume.

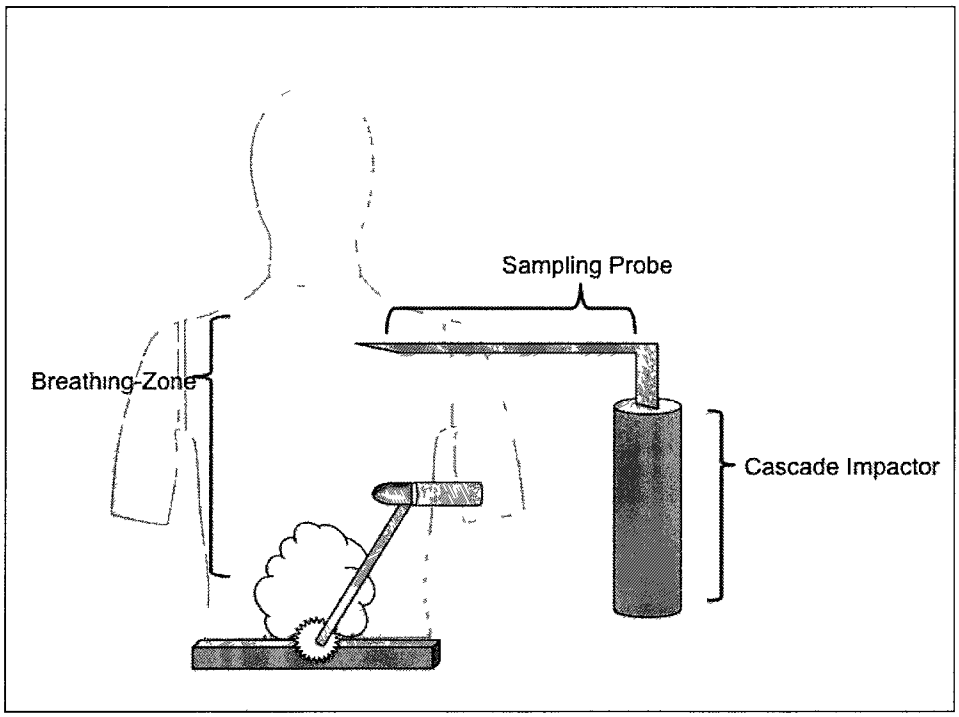

Figure 45: Pictorial representation of breathing-zone sampling within the exposure chamber.

4.5.3 Chemical Analysis

The EDS analysis performed with the TEM in this research provides marginally reliable qualitative compositional data for different particle sizes and morphologies observed in the samples. However, there are observations within these data that may be pertinent to future welding fume characterization research, particularly, for laboratory-based studies aimed at understanding etiology and mechanisms of health effects epidemiologically observed in welders.

Silicon is present across all particle sizes. Previous characterization research has indicated that Si is most likely present in the form of amorphous silicates (R. Tandon, et al., 1986). Without

the Si analysis in the HR-ICP-MS results, a full understanding of the Si distribution in welding fume cannot be gained. Further analytical work would be required.

The large spike in iron detection in the small particle sizes is consistent with Zimmer's (2002) observation that primary particles first form from the nucleation and condensation of iron. The small particles observed here have not yet grown much by condensation and therefore the iron rich core in the particles is present. Chromium and nickel appear slightly more abundant in particles of smaller diameter, which is in contrast to manganese, and titanium where the opposite is observed. The data generated here are too limited to draw any conclusions. Previous studies explored the chemistry of the core-shell nature of welding fume particles using secondary ion mass spectrometry (SIMS) revealed that potassium was detected at constant concentrations throughout the entire depth of the particle while iron, manganese and chromium signals were detected mainly below the shell (>50nm depth) (Konarski & Iwanejko, 2003; Konarski, et al., 2003).

There are other morphologies that need to be explored in gaining insight into compositional aspects of the welding fume. We speculate that welding fume particles are formed by the mechanisms described above but there is another type of condensation that is responsible for the formation of particles as described by Sowards (2008). The microenvironment within and just outside the arc must be extremely turbulent and the composition of vapors within that environment is changing constantly. This would be the reason for such variability seen between particle sizes and morphologies. The morphologies that have irregular structures surrounding spherical primary particles seem most abundant in size fractions through the middle 90% of the mass-based size distribution (i.e., stages 4, 5, 6, 7 and 8 of ELPI). We know from HR-ICP-MS analysis that potassium preferentially fractionates into the mid range of the size distribution.

Owing to the fact that potassium has the lowest vapor pressure, it is plausible that these structures are composed of the potassium condensing out quickly as the particle is super cooled. The EDS results reported here cannot confirm the validity of this hypothesis because potassium is observed in both small and large particles. It may be that past research primarily studied spherical particles and largely overlooked the irregular type particles. Further analysis of irregular structured particles would provide a more comprehensive characterization of welding fume.

4.6 Summary

A study to determine the primary particle size and agglomerate particle morphology of size-fractionated welding fume samples was conducted. Samples were collected using cascade impactor instruments fitted with electron microscope grids attached to sampling filters. Microscopic analysis was performed using SEM and TEM. Particle shape and morphology characterization with electron microscopy revealed three distinct size groups of primary particles classified as small medium and large which corresponded to physical diameter ranges of less than 10 nm, between 10 nm and 100 nm and larger than 100 nm, respectively. Analysis of the morphological characteristics of welding fume revealed that fume particles agglomerate into primarily chainlike structures or densely packed structures. The smallest primary particle size groups were more often associated with chain-like agglomerates while larger primary particle size groups were more often associated with densely packed agglomerates. Overall differences in the distribution of morphology types across particle size fractions were not observed. The classification of morphologies presented herein can provide a standardized system for future single particle chemical analysis studies. Chemical analysis did not have sufficient x-ray generation to reliably quantify elemental composition of specific particle morphologies.

REFERENCES

Antonini, J. (2003). Health effects of welding. *Critical reviews in toxicology, 33*(1), 61-103.

Antonini, J., Afshari, A., Stone, S., Chen, B., Schwegler-Berry, D., Fletcher, W., et al. (2006). Design, Construction, and Characterization of a Novel Robotic Welding Fume Generator and Inhalation Exposure System for Laboratory Animals. *Journal of Occupational and Environmental Hygiene, 3*(4), 194-203.

Antonini, J. M. (2003). Health effects of welding. *Crit Rev Toxicol, 33*(1), 61-103.

Armbruster, D., Tillman, M., & Hubbs, L. (1994). Limit of detection (LQD)/limit of quantitation (LOQ): comparison of the empirical and the statistical methods exemplified with GC-MS assays of abused drugs. *Clinical Chemistry, 40*(7), 1233.

ATSDR (2008). *Toxicological profile for Chromium*. Atlanta, GA: Agency for Toxic Substances and Disease Registry (ATSDR), U.S. Department of Health and Human Services, Public Health Service.

Beach, J., Dennis, J., Avery, A., Bromly, C., Ward, R., Walters, E., et al. (1996). An epidemiologic investigation of asthma in welders. *American Journal of Respiratory and Critical Care Medicine, 154*(5), 1394.

Berner, V., & Berner, A. (1982). Mass size distributions and elemental frequency distributions of arc welding fumes. *Journal of Aerosol Science, 13*(3), 191-193.

BLS (2008). *Occupational Outlook Handbook*. from http://www.bls.gov/oco/ocos226.htm

Borm, P., Robbins, D., Haubold, S., Kuhlbusch, T., Fissan, H., Donaldson, K., Schins, R., Stone, V., Kreyling, W., Lademann, J., Krutman, J., Warheit, D. and Orberdorster, E. (2006). The potential risks of nanomaterials: a review carried out for ECETOC. . *Part. Fibre Toxicol. , 3*(11), 1-35.

Bosworth, M., & Deam, R. (2000). Influence of GMAW droplet size on fume formation rate. *Journal of Physics D: Applied Physics, 33*, 2605.

Bracarense, A., & Liu, S. (1993). Chemical composition variations in shielded metal arc welds. *Welding journal, 72*(12), 529-536.

Breskey, J. D. (2008). *Assessment of Inhaled Dose and Personal Exposure to Welding Fumes Under Laboratory Controlled Conditions.* University of Illinois at Chicago, Chicago.

Castner, H., & Null, C. (1998). Chromium, nickel and manganese in shipyard welding fumes. *Welding journal, 77*(6), 223-231.

Dasch, J. (2008). Physical and Chemical Characterization of Airborne Particles from Welding Operations in Automotive Plants. *Journal of Occupational and Environmental Hygiene, 5*(7), 444-454.

Day, J. C., & Rosenthal, J. (2008). *Detailed Occupations and Median Earnings: 2008*: US Census Bureau.

de Ruiter, C., & Oeseburg, F. (1987). A comparison of parameter estimation procedures for experimental bimodal lognormal particle size distributions and grouped data. *Journal of Aerosol Science, 18*(4), 431-444.

Dennis, J., French, M., Hewitt, P., Mortazavi, S., & Redding, A. (1996). Reduction of hexavalent chromium concentration in fumes from metal cored arc welding by addition of reactive metals. *Annals of Occupational Hygiene, 40*(3), 339.

Dennis, J. H., French, M. J., Hewitt, P. J., Mortazavi, S. B., & Redding, C. A. J. (1996). Reduction of hexavalent chromium concentration in fumes from metal cored arc welding by addition of reactive metals. *Annals of Occupational Hygiene, 40*(3), 339-344.

Dennis, J. H., Mortazavi, S. B., French, M. J., Hewitt, P. J., & Redding, C. R. (1997). The effects of welding parameters on ultraviolet light emissions, ozone and Cr-VI formation in MIG welding. *Annals of Occupational Hygiene, 41*(1), 95-104.

Durgam, S. (2004). *Design, testing, and validation of an exposure chamber for welding fume emission characterization studies.* University of Illinois at Chicago, Chicago.

Erdal, S., Schauer, J., Breskey, J. D., & Indacochea, E. (2008). *Size-Fractionated Stainless Steel Fume Emissions in an Isokinetic Chamber and in the Breathing Zone*. Paper presented at the American Welding Society Meeting

Esmen, N. (2000). Multicomponent Error Model for Mass Measurement Based Size Fractionating Aerosol Samplers. *Appl Occup Environ Hyg, 15*(1), 72-79.

Farrants, G., Schuler, B., Karlsen, J., Reith, A., & Langard, S. (1989). Characterization of the morphological properties of welding fume particles by transmission electron microscopy and digital image analysis. *American Industrial Hygiene Association Journal, 50*(9), 473-479.

Glover, W., & Chan, H. (2004). Electrostatic charge characterization of pharmaceutical aerosols using electrical low-pressure impaction (ELPI). *Journal of Aerosol Science, 35*(6), 755-764.

Gray, C., & Hewitt, P. (1982). Control of particulate emissions from electric-arc welding by process modification. *Annals of Occupational Hygiene, 25*(4), 431.

Gray, C. N., & Hewitt, P. J. (1982). Control of particulate emissions from electric-arc welding by process modification. *Annals of Occupational Hygiene, 25*(4), 431-438.

Gray, C. N., Hewitt, P. J., & Dare, P. R. M. (1982a). New approach would help control weld fumes at source. Part two: MIG fumes. *Welding & Metal Fabrication, 50*(8), 393-397.

Gray, C. N., Hewitt, P. J., & Dare, P. R. M. (1982b). New approach would help control welding fumes at source. Part 1. Biomedical background. *Welding & Metal Fabrication, 50*(7), 318-320, 322-314.

Gray, C. N., Hewitt, P. J., & Dare, P. R. M. (1983). New approach would help control weld fumes at source. Part 3. MMA fumes. *Welding & Metal Fabrication, 51*(1), 52-55.

Heile, R. F., & Hill, D. C. (1975). Particulate fume generation in arc welding processes. *Welding Research (Miami, FL, United States)*(July), 201-210.

Hewett, P. (1995). The particle size distribution, density, and specific surface area of welding fumes from SMAW and GMAW mild and stainless steel consumables. *American Industrial Hygiene Association Journal, 56*(2), 128-135.

Hewett, P. (1995). The particle size distribution, density, and specific surface area of welding fumes from SMAW and GMAW mild and stainless steel consumables. *American Industrial Hygiene Association Journal (1958-1999), 56*(2), 128-135.

Hewitt, P. J., & Gray, C. N. (1983). Some difficulties in the assessment of electric arc welding fume. *American Industrial Hygiene Association Journal (1958-1999), 44*(10), 727-732.

Hinds, W. (1999a). Aerosol Technology: Properties. *Behavior, and Measurement of Airborne Particles. 2New York: Wiley-Interscience.*

Hinds, W. (1999b). Aerosol Technology: Properties, Behavior, and Measurement of Airborne Particles. *Behavior, and Measurement of Airborne Particles. 2New York: Wiley-Interscience.*

Howe, A. H. (2000). *Assessment of Exposure to Chemical Agents in Welding Fume: Final Report.* Sheffield, UK: Health and Safety Laboratory.

IARC. (1990a) Tilte. In & *IARC Monographs: Vol. 49*. Lyon, France: International Agency for Research on Cancer (IARC).

IARC (1990b). *Monographs on the evaluation of carcinogenic risk of chemicals to man: Welding.*

IARC (1997). Chromium, Nickel and Welding. *International Agency for Research on Cancer (IARC) Monographs on the Evaluation of Carcinogenic Risk of Chemicals to Humans, 49*, 447.

Ibald-Mulli A, W. H., Kreyling W, Peters A (2002). Epidemiological evidence on health effects of ultrafine particles. . [Review]. *Journal of Aerosol Medicine, 15* (2), 189-201.

Isaxon, C., Pagels, J., Gudmundsson, A., Asbach, C., John, A., Kuhlbusch, T., et al. (2009a). *Characteristics of welding fume aerosol investigated in three Swedish workshops.* Paper presented at the Inhaled Particles X, Manchester, UK.

Isaxon, C., Pagels, J., Gudmundsson, A., Asbach, C., John, A., Kuhlbusch, T., et al. (2009b). *Characteristics of welding fume aerosol investigated in three Swedish workshops.*

Jenkins, N. T., & Eagar, T. W. (2003). Submicron particle chemistry: vapor condensation analogous to liquid solidification. *Jom, 55*(6), 44-47.

Jenkins, N. T., & Eagar, T. W. (2005a). Chemical analysis of welding fume particles. *Welding Journal, 84*(6), 87S-93S.

Jenkins, N. T., & Eagar, T. W. (2005b). Chemical analysis of welding fume particles - Airborne particle size is the most important factor in determining the accuracy of a method for chemical analysis. *Welding Journal, 84*(6), 87S-93S.

Jenkins, N. T., & Eagar, T. W. (2005). Fume formation from spatter oxidation during arc welding. *Science and Technology of Welding and Joining, 10*(5), 537-543.

Jenkins, N. T., Pierce, W. M. G., & Eagar, T. W. (2005). Particle size distribution of gas metal and flux cored arc welding fumes. *Welding Journal, 84*(10), 156S-163S.

Johnston, A. (1983). A semi-automatic method for the assessment of electric charge carried by airborne dust. *Journal of Aerosol Science, 14*(5), 643-655.

Johnston, A., Vincent, J., & Jones, A. (1985). Measurements of electric charge for workplace aerosols. *Annals of Occupational Hygiene, 29*(2), 271.

Kalliomaki, P. L., Grekula, A., Hagberg, J., & Sivonen, S. (1987). Analytical electron microscopy of welding fumes. *Journal of Aerosol Science, 18*(6), 781-784.

Karlsen, J., Farrants, G., Torgrimsen, T., & Reith, A. (1992). Chemical composition and morphology of welding fume particles and grinding dusts. *American Industrial Hygiene Association Journal, 53*(5), 290-297.

Kass, G., Eriksson, J., Weis, M., Orrenius, S., & Chow, S. (1996). Chromatin condensation during apoptosis requires ATP. *Biochemical Journal, 318*(Pt 3), 749.

Keskinen, J., Pietarinen, K., & Lehtimaki, M. (1992). Electrical low pressure impactor. *Journal of Aerosol Science, 23*(4), 353-360.

Klaassen, C. D. (2001). *Casarett and Doull's Toxicology - The Basic Science of Poisons (6th Edition)*: McGraw-Hill.

Konarski, P., & Iwanejko, I. (2003). Core-shell morphology of welding fume micro-and nanoparticles. *Vacuum, 70*(2-3), 385-389.

Konarski, P., Iwanejko, I., & Mierzejewska, A. (2003). SIMS depth profiling of working environment nanoparticles. *Applied Surface Science, 203*, 757-761.

Koponen, M., Gustafsson, T., Kalliomäki, P. L., & Pyy, L. (1981). Chromium and nickel aerosols in stainless steel manufacturing, grinding and welding. *American Industrial Hygiene Association Journal, 42*(8), 596-601.

Kou, S. (1987). *Welding metallurgy*. New York: Wiley.

Lancaster, J. (1984). The physics of welding. *Physics in Technology, 15*, 73.

Lancaster, J. F. (1987). *Metallurgy of welding* (4th ed.). London ; Boston: Allen & Unwin.

Lide, D. (2004). *CRC handbook of chemistry and physics: a ready-reference book of chemical and physical data*: CRC Pr I Llc.

Lucas, O. (2008). *Investigation of Welding Fume Plumes Using Laser Diagnostics.* Unpublished Dissertation, The University of Adelaide, Adelaide, Australia.

Marjamaki, M., Keskinen, J., Chen, D., & Pui, D. (2000). Performance evaluation of the electrical low-pressure impactor (ELPI). *Journal of Aerosol Science, 31*(2), 249-261.

Marjamaki, M., Lemmetty, M., & Keskinen, J. (2005). ELPI response and data reduction I: Response functions. *Aerosol Science and Technology, 39*(7), 575-582.

Marjamaki, M., Niemela, V., Ntziachristos, L., Virtanen, A., Ristimaki, J., Keskinen, J., et al. (2002). Electrical filter stage for the ELPI.

Marple, V., Rubow, K., & Behm, S. (1991). A microorifice uniform deposit impactor (MOUDI): description, calibration, and use. *Aerosol Science and Technology, 14*(4), 434-446.

Matczak, W., & Chmielnicka, J. (1989). Methods for determining soluble and insoluble Cr III and Cr VI compounds in welding fumes. *Polish Journal of Occupational Medicine, 2*(4), 376-388.

Matczak, W., & Chmielnicka, J. (1989). Methods for determining soluble and insoluble Cr III and Cr VI compounds in welding fumes. *POL. J. OCCUP. MED., 2*(4), 376-388.

Maynard, A., Ito, Y., Arslan, I., Zimmer, A., Browning, N., & Nicholls, A. (2004). Examining elemental surface enrichment in ultrafine aerosol particles using analytical scanning transmission electron microscopy. *Aerosol Science and Technology, 38*(4), 365-381.

McIlwain, J. F., & Neumeier, L. A. (1987). *Fumes from Shielded Metal Arc Welding Electrodes*: United States Department of the Interior.

MidAlloy (2005). Material Safety Data Sheet: Stainless Coated electrodes Retrieved November 25, 2010, from www.midalloy.com/html/pdf/.../MSDS-Stainless%20Coated%20Electrodes.pdf

Minni, E., Gustafsson, T., Koponen, M., & Kalliomaki, P. (1984). A study of the chemical structure of particles in the welding fumes of mild and stainless steel. *Journal of Aerosol Science, 15*(1), 57-68.

Misra, C., Singh, M., Shen, S., Sioutas, C., & Hall, P. (2002). Development and evaluation of a personal cascade impactor sampler (PCIS). *Journal of Aerosol Science, 33*(7), 1027-1047.

Moreton, J., & Smars, E. (1985). Fume emission when welding stainless steel. *Metal Construction, 17*, 794-798.

Narayana, S. (1995). Chemical characteristics of stainless steel welding fumes. *Journal of Aerosol Science, 26*.

Niemela, R., Koskela, H., & Engstrom, K. (2001). Stratification of welding fumes and grinding particles in a large factory hall equipped with displacement ventilation. *Annals of Occupational Hygiene, 45*(6), 467.

NIOSH (1988a). Criteria for a Recommended Standard Welding, Brazing, and Thermal Cutting.

NIOSH (1988b). *Criteria for a Recommended Standard: Welding, Brazing, and Thermal Cutting.* Retrieved 07/17/2009. from http://www.cdc.gov/niosh/88-110.html.

NMAM (2003). *NIOSH Manual of Analytical Methods (NMAM), 4th edition, 3rd supplement.* Cincinnati, OH: National Institute of Occupational Safety and Health (NIOSH).

NTP (2000). *Report on Carcinogens, Eleventh Edition.*

Oberdorster, G., Sharp, Z., Atudorei, V., Elder, A., Gelein, R., Kreyling, W., et al. (2004). Translocation of inhaled ultrafine particles to the brain. *Inhalation Toxicology, 16*(6-7), 437-445.

Phillips, M., Esmen, N., Hall, T., & Lynch, R. (2004). Determinants of exposure to volatile organic compounds in four Oklahoma cities. *Journal of Exposure Science and Environmental Epidemiology, 15*(1), 35-46.

Quimby, B. J., & Ulrich, G. D. (1999). Fume formation rates in gas metal arc welding. *Welding Journal, 78*(4), 142S-149S.

Ramachandran, G., Johnson, E., & Vincent, J. (1996). Inversion techniques for personal cascade impactor data. *Journal of Aerosol Science, 27*(7), 1083-1097.

Roth, J. (2009). Are there common biochemical and molecular mechanisms controlling manganism and parkisonism. *NeuroMolecular Medicine, 11*(4), 281-296.

Sadak, A., Schulz, P., Racette, B., & Perlmutter, J. (2001). Welding-related parkinsonism: clinical features, treatment, and pathophysiology. *Neurology, 57*(9), 1738.

Scheepers, P., Heussen, G., Peer, P., Verbist, K., Anzion, R., & Willems, J. (2008). Characterisation of exposure to total and hexavalent chromium of welders using biological monitoring. *Toxicology letters, 178*(3), 185-190.

Sferlazza, S., & Beckett, W. (1991). The respiratory health of welders. *American Journal of Respiratory and Critical Care Medicine, 143*(5), 1134-1148.

Sivulka, D. (2005). Assessment of respiratory carcinogenicity associated with exposure to metallic nickel: a review. *Regulatory Toxicology and Pharmacology, 43*(2), 117-133.

Sobaszek, A., Boulenguez, C., Frimat, P., Robin, H., Haguenoer, J., & Edme, J. (2000). Acute respiratory effects of exposure to stainless steel and mild steel welding fumes. *Journal of occupational and environmental medicine, 42*(9), 923.

Sowards, J., Lippold, J., Dickinson, D., & Ramirez, A. (2008). Characterization of Welding Fume from SMAW Electrodes - Part I. *Welding Journal, 87*(4), 106s - 112s.

Sowards, J., Ramirez, A., Dickinson, D., & Lippold, J. (2010). Characterization of Welding Fume from SMAW ElectrodesóPart II. *Welding Journal, 89*(4).

Speight, F., & Campbell, H. (1979). Fumes and gases in the welding environment. *American Welding Society, Miami, FL.*

Stephenson, D., Seshadri, G., & Veranth, J. (2003). Workplace exposure to submicron particle mass and number concentrations from manual arc welding of carbon steel. *AIHA Journal, 64*(4), 516-521.

Stern, R. (1977). *A Chemical, Physical and Biological Assay of Welding Fume. Part I: Fume Characteristics.* Paper presented at the Hungarian-Finnish-Italian-Scandinavian Symposium on Industrial Dust Problems, Helsinki, Finland.

Surya Narayana, D. S., Sundararajan, A. R., Subramanian, V., Manjula, B., & Vijaya Kumari, S. C. (1995). Chemical characteristics of stainless steel welding fumes. *Journal of Aerosol Science, 26*(1), 531-532.

Tandon, R., Ellis, J., Crisp, P., Baker, R., & Chenhall, B. (1986). Chemical investigation of welding fumes from hardfacing and HSLA-steel electrodes. *Weld. J., 65*(9).

Tandon, R., Payling, R., Chenhall, B., Crisp, P., Ellis, J., & Baker, R. (1985). Application of X-ray photoelectron spectroscopy to the analysis of stainless-steel welding aerosols. *Applications of Surface Science, 20*(4), 527-537.

Tandon, R. K., Crisp, P. T., Ellis, J., & Baker, R. S. (1982). Variations in the chemical composition and generation rates of fume from stainless steel electrodes under different a.c. arc welding conditions. *Australian Welding Research, 11*, 10-14.

Thomsen, V., Schatzlein, D., & Mercuro, D. (2003). Limits of detection in spectroscopy. *Spectroscopy, 18*(12), 112-114.

Vincent, J. (1985). On the practical significance of electrostatic lung deposition of isometric and fibrous aerosols. *Journal of Aerosol Science, 16*(6), 511-519.

Vincent, J. (1986). Industrial hygiene implications of the static electrification of workplace aerosols. *Journal of Electrostatics, 18*(2), 113-145.

Vincent, J. H., Johnston, A. M., Jones, A. D., & Mclathlan, C. Q. (1983). *Measurements of the static electrification of airborne dusts in workplaces.*: Institute of Occupational Medicine.

Virtanen, A., Marjamaki, M., Ristimaki, J., & Keskinen, J. (2001). Fine particle losses in electrical low-pressure impactor. *Journal of Aerosol Science, 32*(3), 389-401.

Voitkevich, V. G. (1995). *Welding Fumes: Formation, Properties and Biological Effects*. Cambridge, U.K.: Abington Publishing.

Wemmert, B. (1994). Fume - particles and gases. *Svetsaren, 48*(1), 7.

Worobiec, A., Stefaniak, E., Kiro, S., Oprya, M., Bekshaev, A., Spolnik, Z., et al. (2007). Comprehensive microanalytical study of welding aerosols with x ray and Raman based methods. *X Ray Spectrometry, 36*(5), 328-335.

Yamada, Y., Miyamoto, K., Tokonami, S., Shimo, M., & Yamasaki, K. (2000). *Experimental determination of attachment function of radon progeny on aerosol particles*. Paper presented at the 10th Congress of the International Radiation Protection Association.

Yoon, C., Paik, N., & Kim, J. (2003). Fume generation and content of total chromium and hexavalent chromium in flux-cored arc welding. *Annals of Occupational Hygiene, 47*(8), 671.

Yoon, C., Paik, N., Kim, J., & Chae, H. (2009). Total and Soluble Metal Contents in Flux-Cored Arc Welding Fumes. *Aerosol Science and Technology, 43*(6), 511-521.

Young, P., Sung, A., Traini, D., Kwok, P., Chiou, H., & Chan, H. (2007). Influence of humidity on the electrostatic charge and aerosol performance of dry powder inhaler carrier based systems. *Pharmaceutical Research, 24*(5), 963-970.

Zhitkovich, A. (2005). Importance of Chromium- DNA Adducts in Mutagenicity and Toxicity of Chromium (VI). *Chem. Res. Toxicol, 18*(1), 3-11.

Zimmer, A. (2002). The influence of metallurgy on the formation of welding aerosols. *Journal of Environmental Monitoring, 4*(5), 628-632.

Zimmer, A., Baron, P., & Biswas, P. (2002). The influence of operating parameters on number-weighted aerosol size distribution generated from a gas metal arc welding process. *Journal of Aerosol Science, 33*(3), 519-531.

Zimmer, A. T. (2002). The influence of metallurgy on the formation of welding aerosols. *J Environ Monit, 4*(5), 628-632.

Zimmer, A. T., Baron, P. A., & Biswas, P. (2002). The influence of operating parameters on number-weighted aerosol size distribution generated from a gas metal arc welding process. *Journal of Aerosol Science, 33*(3), 519-531.

Zimmer, A. T., & Biswas, P. (2001). Characterization of the aerosols resulting from arc welding processes. *Journal of Aerosol Science, 32*(8), 993-1008.

APPENDIX

TABLE XXXVIII: MASS CONCENTRATIONS ELPI EMISSION CHAMBER

Experiment #		3A		3B		4A		4B		Average	
Stage #	Particle Size	Filter ID	Mass Conc. (mg/m³)	Filter ID	Mass Conc. (mg/m³)	Filter ID	Mass Conc. (mg/m³)	Filter ID	Mass Conc. (mg/m³)	Mass Conc. (mg/m³)	SD (mg/m³)
1	0.028	zo950067	0.041	zo950087	0.031	JB-PTFE-25-051	0.047	ZO950051	0.032	0.04	0.0075
2	0.055	zo950068	0.028	zo950099	0.048	JB-PTFE-25-052	0.065	ZO950052	0.032	0.04	0.0168
3	0.094	zo950069	0.078	zo950098	0.086	JB-PTFE-25-053	0.049	ZO950053	0.069	0.07	0.0162
4	0.157	zo950071	0.178	zo950097	0.251	JB-PTFE-25-054	0.186	ZO950054	0.198	0.20	0.0328
5	0.266	zo950072	1.063	zo950096	1.462	JB-PTFE-25-055	1.107	ZO950055	1.233	1.22	0.1789
6	0.387	zo950073	3.377	zo950095	3.650	JB-PTFE-25-056	2.952	ZO950056	2.567	3.14	0.4761
7	0.622	zo950074	1.342	zo950094	1.889	JB-PTFE-25-057	1.255	ZO950057	1.199	1.42	0.3173
8	0.961	zo950075	0.263	zo950093	0.361	JB-PTFE-25-058	0.198	ZO950059	0.225	0.26	0.0713
9	1.62	zo950076	0.072	zo950092	0.100	JB-PTFE-25-059	0.065	ZO950060	0.087	0.08	0.0157
10	2.42	zo950077	0.047	zo950091	0.093	JB-PTFE-25-060	0.233	ZO950061	0.085	0.11	0.0814
11	4.05	zo950078	0.069	zo950090	0.045	JB-PTFE-25-061	0.036	ZO950062	0.074	0.06	0.0183
12	6.77	zo950079	0.066	zo950089	0.069	JB-PTFE-25-062	0.038	ZO950063	0.079	0.06	0.0174
13	10.04	zo950080	0.066	zo950088	0.034	JB-PTFE-25-063	0.045	ZO950064	0.066	0.05	0.0158
		Sum	6.689	Sum	8.118	Sum	6.275	Sum	5.946	6.76	0.9571

TABLE XXXIX: MASS CONCENTRATIONS MOUDI EMISSION CHAMBER

Experiment #		3A		3B		4A		4B		Average	
Stage #	Particle Size	Filter ID	Mass Conc. (mg/m^3)	Filter ID	Mass Conc. (mg/m^3)	Filter ID	Mass Conc. (mg/m^3)	Filter ID	Mass Conc. (mg/m^3)	Mass Conc. (mg/m^3)	SD (mg/m^3)
Backup	<0.056	t0930058	0.036	t0930067	0.022	JB-PTFE-37-019	0.020	JB-PTFE-37-022	0.020	0.02	0.0076
11	0.056	t0940251	0.037	t0940240	0.053	JB-PTFE-47-041	0.061	JB-PTFE-47-054	0.041	0.05	0.0111
10	0.100	t0940250	0.102	t0940252	0.129	JB-PTFE-47-040	0.058	JB-PTFE-47-053	0.051	0.08	0.0373
9	0.180	t0940249	0.686	t0940253	0.857	JB-PTFE-47-039	0.727	JB-PTFE-47-052	0.835	0.78	0.0827
8	0.320	t0940248	1.543	t0940254	1.179	JB-PTFE-47-038	1.458	JB-PTFE-47-051	1.150	1.33	0.1973
7	0.560	t0940247	1.706	t0940255	1.358	JB-PTFE-47-037	1.315	JB-PTFE-47-050	1.040	1.35	0.2733
6	1.00	t0940246	0.806	t0940257	0.589	JB-PTFE-47-036	0.235	JB-PTFE-47-049	0.353	0.50	0.2541
5	1.80	t0940245	0.138	t0940258	0.079	JB-PTFE-47-035	0.058	JB-PTFE-47-048	0.082	0.09	0.0342
4	3.20	t0940244	0.119	t0940259	0.027	JB-PTFE-47-034	0.076	JB-PTFE-47-047	0.109	0.08	0.0415
3	5.60	t0940243	0.039	t0940260	0.033	JB-PTFE-47-033	0.060	JB-PTFE-47-046	0.064	0.05	0.0152
2	10.0	t0940242	0.083	t0940270	0.057	JB-PTFE-47-032	0.052	JB-PTFE-47-045	-0.015	0.04	0.0420
1	18.0	t0940241	0.032	t0940256	0.102	JB-PTFE-47-031	0.061	JB-PTFE-47-044	0.076	0.07	0.0291
		Sum	5.327	Sum	4.487	Sum	4.182	Sum	3.805	4.45	0.6477

TABLE XL: MASS CONCENTRATIONS ELPI EXPOSURE CHAMBER

Experiment #		5A		5B		6A		6BR		Average	
Stage #	Particle Size	Filter ID	Mass Conc. (mg/m³)	Filter ID	Mass Conc. (mg/m³)	Filter ID	Mass Conc. (mg/m³)	Filter ID	Mass Conc. (mg/m³)	Mass Conc. (mg/m³)	SD (mg/m³)
1	0.028	zo950001	0.000	zo950025	0.062	JB-PTFE-25-001	0.061	ZO950111	0.016	0.03	0.0317
2	0.055	zo950002	0.206	zo950026	0.009	JB-PTFE-25-002	0.069	ZO950112	0.066	0.09	0.0838
3	0.094	zo950003	0.076	zo950027	0.044	JB-PTFE-25-003	0.066	ZO950113	0.064	0.06	0.0137
4	0.157	zo950004	0.076	zo950028	0.124	JB-PTFE-25-004	0.150	ZO950115	0.188	0.13	0.0469
5	0.266	zo950005	0.251	zo950029	0.372	JB-PTFE-25-005	0.560	ZO950116	1.474	0.66	0.5547
6	0.387	zo950006	0.710	zo950030	1.121	JB-PTFE-25-006	1.929	ZO950117	4.567	2.08	1.7325
7	0.622	zo950007	0.263	zo950031	0.447	JB-PTFE-25-007	0.747	ZO950118	2.625	1.02	1.0881
8	0.961	zo950008	0.057	zo950032	0.140	JB-PTFE-25-008	0.708	ZO950119	0.394	0.32	0.2930
9	1.62	zo950009	0.079	zo950033	0.083	JB-PTFE-25-009	0.346	ZO950120	0.103	0.15	0.1296
10	2.42	zo950010	0.101	zo950034	0.067	JB-PTFE-25-010	0.258	ZO950121	0.045	0.12	0.0964
11	4.05	zo950011	0.108	zo950035	0.048	JB-PTFE-25-011	0.251	ZO950122	0.066	0.12	0.0917
12	6.77	zo950012	0.084	zo950036	0.037	JB-PTFE-25-012	0.322	ZO950123	0.058	0.13	0.1326
13	10.04	zo950013	0.032	zo950037	0.060	JB-PTFE-25-013	0.211	ZO950124	0.034	0.08	0.0856
		Sum	2.042	Sum	2.612	Sum	5.678	Sum	9.701	5.01	3.5123

TABLE XLI: MASS CONCENTRATIONS MOUDI EXPOSURE CHAMBER

Experiment #		5A		5B		6A		6B		6BR		Average	
Stage #	Particle Size	Filter ID	Mass Conc. (mg/m³)	Filter ID	Mass Conc. (mg/m³)	Filter ID	Mass Conc. (mg/m³)	Filter ID	Mass Conc. (mg/m³)	Filter ID	Mass Conc. (mg/m³)	Mass Conc. (mg/m³)	SD (mg/m³)
Backup	<0.056	t093004 9	0.013	t093005 3	0.007	JB-PTFE-37-013	0.027	JB-PTFE-37-015	0.044	JB-PTFE-37-028	0.016	0.02	0.0146
11	0.056	t094022 0	-0.001	t094023 5	0.005	JB-PTFE-47-011	0.022	JB-PTFE-47-022	0.023	JB-PTFE-47-067	-0.030	0.00	0.0215
10	0.100	t094021 9	0.014	t094023 4	0.013	JB-PTFE-47-010	0.012	JB-PTFE-47-021	0.002	JB-PTFE-47-066	-0.016	0.01	0.0127
9	0.180	t094021 8	0.061	t094023 3	0.087	JB-PTFE-47-009	0.098	JB-PTFE-47-030	0.094	JB-PTFE-47-065	0.113	0.09	0.0193
8	0.320	t094021 7	0.135	t094023 2	0.169	JB-PTFE-47-008	0.293	JB-PTFE-47-029	0.241	JB-PTFE-47-064	0.443	0.26	0.1211
7	0.560	t094021 6	0.156	t094023 1	0.233	JB-PTFE-47-007	0.218	JB-PTFE-47-028	0.198	JB-PTFE-47-063	0.253	0.21	0.0369
6	1.00	t094021 5	0.064	t094023 0	0.035	JB-PTFE-47-006	0.008	JB-PTFE-47-020	0.025	JB-PTFE-47-062	0.029	0.03	0.0203
5	1.80	t094021 4	0.008	t094022 9	0.006	JB-PTFE-47-005	0.023	JB-PTFE-47-019	0.004	JB-PTFE-47-061	0.011	0.01	0.0076
4	3.20	t094021 3	-0.005	t094022 8	0.006	JB-PTFE-47-004	0.035	JB-PTFE-47-018	0.017	JB-PTFE-47-060	0.009	0.01	0.0148
3	5.60	t094021 2	0.008	t094022 7	0.007	JB-PTFE-47-003	-0.011	JB-PTFE-47-017	0.013	JB-PTFE-47-059	0.004	0.00	0.0090
2	10.0	t094021 1	0.023	t094022 5	0.012	JB-PTFE-47-002	0.001	JB-PTFE-47-016	0.021	JB-PTFE-47-058	0.027	0.02	0.0107
1	18.0	t094021 0	0.037	t094022 4	0.022	JB-PTFE-47-001	0.052	JB-PTFE-47-015	0.008	JB-PTFE-47-057	0.022	0.03	0.0170
		Sum	0.513	Sum	0.602	Sum	0.779	Sum	0.689	Sum	0.883	0.69	0.1451

TABLE XLII: ELPI EMISSION LOG-PROBABILITY PLOT DATA

Particle Size (um)	Conc. (mg/m3)	% of Total Mass	Cumulative Fraction	z-score
0.028	0.04	0.0055	0.0055	-2.540
0.055	0.04	0.0064	0.0119	-2.259
0.094	0.07	0.0104	0.0224	-2.007
0.157	0.20	0.0301	0.0525	-1.621
0.266	1.22	0.1800	0.2325	-0.731
0.387	3.14	0.4642	0.6967	0.515
0.622	1.42	0.2103	0.9069	1.322
0.961	0.26	0.0387	0.9457	1.604
1.62	0.08	0.0120	0.9577	1.724
2.42	0.11	0.0169	0.9746	1.953
4.05	0.06	0.0083	0.9829	2.117
6.77	0.06	0.0093	0.9922	2.418
10.04	0.05	0.0078	-	-
Total Mass Conc.	6.76			

TABLE XLIII: ELPI EXPOSURE LOG-PROBABILITY PLOT DATA

Particle Size (um)	Conc. (mg/m3)	% of Total Mass	Cumulative Fraction	z-score
0.028	0.03	0.0069	0.0069	-2.460
0.055	0.09	0.0175	0.0244	-1.970
0.094	0.06	0.0125	0.0369	-1.788
0.157	0.13	0.0268	0.0638	-1.524
0.266	0.66	0.1326	0.1963	-0.855
0.387	2.08	0.4157	0.6120	0.285
0.622	1.02	0.2038	0.8158	0.899
0.961	0.32	0.0648	0.8806	1.178
1.62	0.15	0.0305	0.9111	1.348
2.42	0.12	0.0235	0.9346	1.511
4.05	0.12	0.0236	0.9582	1.730
6.77	0.13	0.0250	0.9832	2.124
10.04	0.08	0.0168	-	-
Total Mass Conc.	5.01			

TABLE XLIV: MOUDI EMISSION LOG-PROBABILITY PLOT DATA

Particle Size (um)	Conc. (mg/m3)	% of Total Mass	Cumulative Fraction	z-score
0.028	0.02	0.0055	0.0055	-2.543
0.056	0.05	0.0108	0.0163	-2.136
0.1	0.08	0.0191	0.0354	-1.807
0.18	0.78	0.1744	0.2098	-0.807
0.32	1.33	0.2995	0.5093	0.023
0.56	1.35	0.3045	0.8137	0.892
1	0.50	0.1114	0.9251	1.440
1.8	0.09	0.0201	0.9452	1.600
3.2	0.08	0.0186	0.9638	1.797
5.6	0.05	0.0110	0.9748	1.957
10	0.04	0.0100	0.9848	2.165
18	0.07	0.0152	-	-
Total Mass Conc.	4.45			

TABLE XLV: MOUDI EXPOSURE LOG-PROBABILITY DATA

Particle Size (um)	Conc. (mg/m3)	% of Total Mass	Cumulative Fraction	z-score
0.028	0.02	0.0308	0.0308	-1.869
0.056	0.00	0.0056	0.0364	-1.794
0.1	0.01	0.0073	0.0437	-1.709
0.18	0.09	0.1306	0.1742	-0.938
0.32	0.26	0.3694	0.5437	0.110
0.56	0.21	0.3053	0.8489	1.032
1	0.03	0.0467	0.8956	1.257
1.8	0.01	0.0152	0.9108	1.346
3.2	0.01	0.0180	0.9288	1.467
5.6	0.00	0.0064	0.9352	1.516
10	0.02	0.0241	0.9593	1.742
18	0.03	0.0407	-	-
Total Mass Conc.	0.69			

TABLE XLVI: ICP-MS RESULTS - MOUDI EMISSION CHAMBER

Particle Size (um)	Na ($\mu g/m^3$)	K ($\mu g/m^3$)	Al ($\mu g/m^3$)	Ni ($\mu g/m^3$)	Ti ($\mu g/m^3$)	Fe ($\mu g/m^3$)	Mn ($\mu g/m^3$)	Cr ($\mu g/m^3$)
0.028	0.03	0.17	-0.01	0.01	0.00	0.21	0.03	0.12
0.056	0.00	2.01	0.27	0.18	0.03	1.89	0.27	0.58
0.1	3.97	17.51	0.42	1.80	0.60	6.79	2.46	4.82
0.18	42.63	143.24	4.19	6.18	8.55	44.06	24.57	29.68
0.32	69.85	243.85	8.33	6.11	15.98	66.36	43.40	41.52
0.56	289.18	271.81	11.15	5.40	20.22	53.56	48.50	42.72
1	38.50	132.98	5.24	3.03	10.93	36.37	24.11	20.26
1.8	4.98	17.86	1.12	0.59	3.82	6.92	3.75	3.14
3.2	2.06	8.26	1.12	0.43	4.51	5.22	2.04	1.90
5.6	0.68	3.26	0.79	0.41	3.59	3.80	1.07	1.22
10	0.81	3.80	1.59	0.72	9.53	7.02	1.46	2.60
18	0.44	2.50	1.33	0.57	7.41	5.18	1.15	2.26

TABLE XLVII: ICP-MS RESULTS ELPI EMISSION CHAMBER

Particle Size (um)	Na ($\mu g/m^3$)	K ($\mu g/m^3$)	Al ($\mu g/m^3$)	Ni ($\mu g/m^3$)	Ti ($\mu g/m^3$)	Fe ($\mu g/m^3$)	Mn ($\mu g/m^3$)	Cr ($\mu g/m^3$)
0.028	-1.61	1.61	0.08	0.58	0.08	1.61	0.32	0.60
0.055	-2.00	1.26	-0.29	0.63	-0.02	3.30	0.40	1.29
0.094	0.46	9.08	0.83	1.57	0.31	5.95	1.48	3.71
0.157	6.66	40.30	0.56	3.36	1.65	17.32	6.34	11.60
0.266	80.91	262.68	8.66	9.48	16.53	82.56	48.60	56.29
0.387	252.01	834.30	29.14	16.66	55.64	199.79	147.35	131.71
0.622	108.77	359.32	13.57	6.24	22.68	77.09	59.84	49.42
0.961	17.84	67.06	3.51	2.00	4.96	18.44	11.80	9.62
1.62	0.44	12.46	0.66	0.81	1.89	4.79	2.52	2.06
2.42	0.11	6.74	0.67	1.27	1.28	6.14	1.03	1.52
4.05	-1.91	6.21	0.40	0.91	2.41	3.97	1.43	1.33
6.77	-1.58	6.88	0.95	1.02	5.44	5.61	1.82	1.91
10.04	-2.99	1.26	0.88	0.65	1.52	4.50	0.40	6.32

TABLE XLVIII: ICP-MS RESULTS PCIS EMISSION CHAMBER

Particle Size (μm)	Na (μg/m³)	K (μg/m³)	Al (μg/m³)	Ni (μg/m³)	Ti (μg/m³)	Fe (μg/m³)	Mn (μg/m³)	Cr (μg/m³)
0.1	52.41	191.00	3.42	5.48	11.85	42.88	29.62	59.94
0.25	297.86	992.13	39.96	17.52	75.91	230.59	176.60	156.80
0.5	3.63	31.11	1.13	0.78	3.49	9.69	6.40	5.30
1	-3.23	10.18	0.28	-0.17	2.88	4.91	2.94	2.37
2.5	-4.59	5.34	9.78	-0.06	5.51	5.68	2.22	2.28

TABLE XLIX: ICP-MS RESULTS - MOUDI EXPOSURE CHAMBER

Particle Size (um)	Na ($\mu g/m^3$)	K ($\mu g/m^3$)	Al ($\mu g/m^3$)	Ni ($\mu g/m^3$)	Ti ($\mu g/m^3$)	Fe ($\mu g/m^3$)	Mn ($\mu g/m^3$)	Cr ($\mu g/m^3$)
0.028	0.08	0.02	0.00	0.00	0.00	0.01	0.00	0.06
0.056	-0.06	0.19	-0.02	0.05	0.10	0.13	0.04	0.18
0.1	0.24	1.25	0.06	0.77	0.03	1.87	0.25	1.13
0.18	3.48	13.88	0.44	2.18	0.63	10.36	2.54	4.55
0.32	8.23	30.29	0.96	2.09	1.87	14.56	6.07	6.67
0.56	11.78	43.10	1.38	1.90	2.64	18.31	8.44	7.85
1	2.58	9.16	0.34	0.55	0.58	4.39	1.94	1.92
1.8	0.01	1.14	0.05	0.08	0.14	0.74	0.17	0.24
3.2	0.04	1.19	0.10	0.12	0.29	1.05	0.14	0.29
5.6	-0.08	0.25	0.00	0.12	0.31	0.74	0.08	0.25
10	-0.04	0.21	0.26	0.38	0.72	2.43	0.17	0.64
18	0.17	0.49	0.51	0.44	2.19	3.15	0.38	1.14

TABLE L: ICP-MS RESULTS - ELPI EXPOSURE CHAMBER

Particle Size (um)	Na (μg/m³)	K (μg/m³)	Al (μg/m³)	Ni (μg/m³)	Ti (μg/m³)	Fe (μg/m³)	Mn (μg/m³)	Cr (μg/m³)
0.028	-0.61	0.29	0.24	0.11	0.83	0.78	0.18	0.53
0.055	1.69	0.87	0.61	0.62	0.07	3.91	0.15	0.91
0.094	1.09	3.19	0.33	2.14	0.20	5.46	0.70	2.62
0.157	3.66	11.15	0.20	4.23	0.55	13.96	2.79	6.04
0.266	16.97	45.70	1.90	5.48	3.21	30.63	11.00	13.65
0.387	62.61	184.28	7.38	7.11	13.15	61.53	38.66	34.36
0.622	23.94	64.06	2.85	2.11	4.55	21.93	12.82	10.78
0.961	9.56	12.92	0.76	0.98	0.81	6.88	2.27	2.39
1.62	5.48	2.22	0.14	0.27	0.30	1.50	0.32	0.44
2.42	10.00	2.70	0.06	0.41	0.23	1.63	0.18	0.40
4.05	-0.39	2.29	1.46	0.32	0.23	1.72	0.14	0.43
6.77	0.88	0.96	0.12	0.14	0.33	1.47	0.12	0.37
10.04	3.64	0.89	0.23	0.21	0.09	1.27	0.06	0.34

TABLE LI: ICP-MS RESULTS - PCIS IN EXPOSURE CHAMBER

Particle Size (μm)	Na (μg/m³)	K (μg/m³)	Al (μg/m³)	Ni (μg/m³)	Ti (μg/m³)	Fe (μg/m³)	Mn (μg/m³)	Cr (μg/m³)
0.1	18.41	60.03	1.53	3.16	3.98	19.36	10.36	13.29
0.25	107.72	322.17	14.64	5.37	24.01	78.54	60.50	47.02
0.5	8.21	38.75	2.41	0.28	3.29	13.98	7.47	6.55
1	-5.21	0.69	0.24	-0.83	0.34	1.23	0.30	0.30
2.5	-3.11	-0.42	3.21	-1.03	0.54	1.19	0.22	0.31

TABLE LII: ICP-MS RESULTS - PCIS OUT EXPOSURE CHAMBER

Particle Size (μm)	Na (μg/m³)	K (μg/m³)	Al (μg/m³)	Ni (μg/m³)	Ti (μg/m³)	Fe (μg/m³)	Mn (μg/m³)	Cr (μg/m³)
0.1	42.74	159.57	16.78	11.59	9.54	53.92	26.85	35.68
0.25	137.89	436.40	17.91	9.86	32.39	124.79	86.39	69.51
0.5	-4.61	6.89	-0.42	0.38	0.85	3.11	1.43	1.35
1	-6.07	1.34	0.31	-0.13	1.33	4.56	0.74	1.18
2.5	-4.91	3.23	0.35	0.69	4.24	6.85	1.37	2.19

VITA

John Daniel Breskey
University of Illinois at Chicago School of Public Health
Environmental and Occupational Health Sciences
2121 West Taylor Street, M/C 922, Chicago, IL 60612

EDUCATION

Ph.D. Candidate, ***University of Illinois at Chicago,*** Chicago, IL
Expected Graduation May 2011

M.S. Public Health, ***University of Illinois at Chicago***, Chicago, IL
May 2008

B.A. Degree Biology/Minor Sociology, ***Oberlin College***, Oberlin, OH
June 2002

EMPLOYMENT

2008 – Present: **Ph.D. Student and Research/Teaching Assistant,** University of Illinois at Chicago, School of Public Health, Department of Environmental and Occupational Health Sciences, Chicago, IL.

Thesis Title: "Ultrafine and Nano-Size Welding Fume Exposure Assessment: Size, Shape, and Chemistry."

2005 – 2008: **M.S. Student and Research Assistant,** University of Illinois at Chicago, School of Public Health, Department of Environmental and Occupational Health Sciences, Chicago, IL

Thesis Title: "Assessment of Inhaled Dose and Personal Exposure to Welding Fume Under Laboratory-Controlled Conditions."

2005 – 2006: **Safety Assistant,** University of Illinois at Chicago, Environmental Health and Safety Office, Chicago IL

2004 – 2005: **Regulatory Affairs Associate,** Dober Group, Midlothian, IL

2003 – 2004: **Quality Control Chemist,** Dober Group, Midlothian, IL

2002 – 2003: **Quality Control Chemist,** ChemCentral Corp., Bedford Park, IL

2000, 2002: **Laboratory Technician**, DesPlaines Valley Mosquito Abatement District, Lyons, IL, (Summer employment)

TEACHING EXPERIENCE

Teaching Assistant – EOHS 400 – Introduction to Environmental and Occupational Health Principles Course (Primary Instructors: Drs. An Li, Linda Forst, Milton Clark)
University of Illinois at Chicago, Chicago, IL
Fall Semester 2008, 2009, 2010

Teaching Assistant – EOHS 529 – Industrial Hygiene Laboratory II (Primary Instructor: Michael Selway)
University of Illinois at Chicago, Chicago IL
Summer Semester 2008, 2009, 2010

Teaching Assistant – EOHS 431 – Air Quality Management (Primary Instructor: Dr. Donna Kenski)
University of Illinois at Chicago, Chicago IL
Spring Semester 2008, 2009

Teaching Assistant – EOHS 438 – Air Quality Laboratory (Primary Instructor: Dr. Serap Erdal)
University of Illinois at Chicago, Chicago IL
Spring Semester 2008, 2009

Assistant Instructor – Lead Safety for Renovation, Repair, and Painting Course (Primary Instructor: Salvatore Cali)
OAI, Inc., Chicago IL
Spring 2010

Assistant Instructor – Lead Safe Work Practices for Weatherization Course (Primary Instructor: Salvatore Cali)
University of Illinois at Chicago, Chicago IL
Fall 2010

Primary Instructor – Sampling Methods for Criteria Pollutants
Air Pollution Training Institute, Indianapolis IN
June 2009

RESEARCH EXPERIENCE

2008 – Present: Ph.D. Dissertation Research – Ultrafine and Nano-Size Welding Fume Exposure Assessment: Size, Shape, and Chemistry
University of Illinois at Chicago, Chicago IL

May – December, 2009: Climate Change, Green Jobs and Healthy Workplaces
University of Illinois at Chicago, Chicago IL

April – October, 2009: Chicago Health and Environmental Exposure Recreation Study
University of Illinois at Chicago, Chicago IL

September, 2006 – January, 2008: Assessment of Inhaled Dose and Personal Exposure to Welding Fume under Laboratory-Controlled Conditions
University of Illinois at Chicago, Chicago, IL

July – October, 2007 and July – August, 2008: Size-fractionated and Total Dust/Lead Particulate Deposition and Exposure associated with Urban Housing Demolition
University of Illinois at Chicago, Chicago IL

AWARDS

Illinois Public Health Research Pre-Doctoral Fellowship, awarded by Center for Disease Control to select doctoral students pursuing dissertation research at the University of Illinois at Chicago, 2010

UIC-Institute for Environmental Safety and Policy Fellowship Recipient, awarded by IESP to select doctoral students conducting interdisciplinary research applicable to environmental public policy decision making, 2008

American Industrial Hygiene Foundation Scholarship Recipient, awarded by AIHF to select graduate students based on academic merit and active participation in the field of Industrial Hygiene, 2007

Michael Bruton Workplace Safety Foundation Scholarship Recipient, awarded to a single student in the UIC EOHS department with proven commitment to the field of occupational safety and health, 2006

National Safety Council Congress and Expo Scholarship Recipient, awarded by National Safety Council to graduate students pursuing a career in a safety discipline, 2006

NIOSH Industrial Hygiene Traineeship, University of Illinois at Chicago, 2005 to 2009

Science Scholar, Oberlin College, 1998 to 2002

PROFESSIONAL MEMBERSHIP/ACTIVITIES

UIC Industrial Hygiene Student Association, President (2009), (Treasurer, 2008)
International Society of Exposure Analysis (ISEA)
American Industrial Hygiene Association (AIHA)
American Society for Safety Engineers (ASSE)
Society for Risk Analysis (SRA)
Illinois Public Health Association (IPHA)

PUBLICATIONS

Mans, N. Z., Yurgionas, S. E., Garvin, M. C., Gary, R. E., Breskey, J. D., Galatias, A. C. and Ohajuruka, O. A. "West Nile Virus in Mosquitoes of Northern Ohio, 2001-2002." American Journal of Tropical Medicine and Hygiene. 70(5), 2004, pp. 562-565.

PRESENTATIONS

Breskey, J. "Overview of Environmental and Occupational Health Sciences." Invited speaker at Conference on Career Opportunities for Minorities in Public Health, University of Illinois at Chicago, Chicago, IL, October 15, 2010.

Breskey, J. and Erdal, S. "Characterization of Stainless Steel Welding Fume Particles Generated During Laboratory-Based Emission and Exposure Chamber Experiments." Poster presented at:
- American Industrial Hygiene Association, Chicago Chapter, Student Night, February 2011
- UIC Educational Resource Center Research Day, Chicago, IL, September 2010.
- *American Industrial Hygiene Conference and Expo, Denver, CO, June 2010.*

Breskey, J. "Opportunities for Doctoral Research in Public Health." Invited speaker for panel discussion at Conference on Career Opportunities for Minorities in Public Health, University of Illinois at Chicago, Chicago, IL, January 16, 2010.

Breskey, J. "Occupational Hygiene Topics in Steel Production." Invited speaker for Occupational Medicine Conference, University of Illinois at Chicago School of Medicine, January 13, 2010.

Breskey J. "NIOSH Educational Resource Centers and Graduate Studies in Occupational Health." Invited speaker for student seminar at Department of Health Sciences, Illinois State University, Bloomington, IL, November 20, 2009.

Breskey, J. "Risk Assessment for Nanomaterials and Nanoparticles." Invited speaker for course on Health Risks of Emerging Technologies, University of Illinois at Chicago, Chicago, IL, July 28, 2009.

Breskey, J. "Strategies for Controlling Exposure to Nanomaterials." Invited speaker for course on Health Risk of Emerging Technologies, University of Illinois at Chicago, Chicago, IL, July 30, 2009.

Breskey, J. and Erdal, S. "Assessment of Inhaled Concentration and Personal Exposure to Welding Fume under Laboratory-Controlled Conditions." Poster Presented at:
- American Industrial Hygiene Conference and Expo, Minneapolis, MN, June 2008.
- UIC SPH Research and Award Day, Chicago, IL, April 2008.
- AIHA Chicago Local Section Student Night, Countryside, IL, March 2008.

SPRINGER LICENSE
TERMS AND CONDITIONS

Mar 14, 2011

This is a License Agreement between John D Breskey ("You") and Springer ("Springer") provided by Copyright Clearance Center ("CCC"). The license consists of your order details, the terms and conditions provided by Springer, and the payment terms and conditions.

All payments must be made in full to CCC. For payment instructions, please see information listed at the bottom of this form.

License Number	2547130109379
License date	Nov 13, 2010
Licensed content publisher	Springer
Licensed content publication	JOM Journal of the Minerals, Metals and Materials Society
Licensed content title	Submicron particle chemistry: Vapor condensation analogous to liquid solidification
Licensed content author	Neil T. Jenkins
Licensed content date	Jun 1, 2003
Volume number	55
Issue number	6
Type of Use	Thesis/Dissertation
Portion	Figures
Author of this Springer article	No
Order reference number	
Title of your thesis / dissertation	Ultrafine and Nano-Size Welding Fume Exposure Assessment: Size, Shape and Chemical Characterization
Expected completion date	Mar 2011
Estimated size(pages)	200
Total	0.00 USD
Terms and Conditions	

Introduction

The publisher for this copyrighted material is Springer Science + Business Media. By clicking "accept" in connection with completing this licensing transaction, you agree that the following terms and conditions apply to this transaction (along with the Billing and Payment terms and conditions established by Copyright Clearance Center, Inc. ("CCC"), at the time that you opened your Rightslink account and that are available at any time at http://myaccount.copyright.com).

Limited License

With reference to your request to reprint in your thesis material on which Springer Science

and Business Media control the copyright, permission is granted, free of charge, for the use indicated in your enquiry. Licenses are for one-time use only with a maximum distribution equal to the number that you identified in the licensing process.

This License includes use in an electronic form, provided it is password protected or on the university's intranet, destined to microfilming by UMI and University repository. For any other electronic use, please contact Springer at (permissions.dordrecht@springer.com or permissions.heidelberg@springer.com)

The material can only be used for the purpose of defending your thesis, and with a maximum of 100 extra copies in paper.

Although Springer holds copyright to the material and is entitled to negotiate on rights, this license is only valid, provided permission is also obtained from the (co) author (address is given with the article/chapter) and provided it concerns original material which does not carry references to other sources (if material in question appears with credit to another source, authorization from that source is required as well). Permission free of charge on this occasion does not prejudice any rights we might have to charge for reproduction of our copyrighted material in the future.

Altering/Modifying Material: Not Permitted
However figures and illustrations may be altered minimally to serve your work. Any other abbreviations, additions, deletions and/or any other alterations shall be made only with prior written authorization of the author(s) and/or Springer Science + Business Media. (Please contact Springer at permissions.dordrecht@springer.com or permissions.heidelberg@springer.com)

Reservation of Rights
Springer Science + Business Media reserves all rights not specifically granted in the combination of (i) the license details provided by you and accepted in the course of this licensing transaction, (ii) these terms and conditions and (iii) CCC's Billing and Payment terms and conditions.

Copyright Notice:
Please include the following copyright citation referencing the publication in which the material was originally published. Where wording is within brackets, please include verbatim.
"With kind permission from Springer Science+Business Media: <book/journal title, chapter/article title, volume, year of publication, page, name(s) of author(s), figure number(s), and any original (first) copyright notice displayed with material>."

Warranties: Springer Science + Business Media makes no representations or warranties with respect to the licensed material.

Indemnity
You hereby indemnify and agree to hold harmless Springer Science + Business Media and CCC, and their respective officers, directors, employees and agents, from and against any and all claims arising out of your use of the licensed material other than as specifically authorized pursuant to this license.

No Transfer of License
This license is personal to you and may not be sublicensed, assigned, or transferred by you to any other person without Springer Science + Business Media's written permission.

No Amendment Except in Writing
This license may not be amended except in a writing signed by both parties (or, in the case of Springer Science + Business Media, by CCC on Springer Science + Business Media's behalf).

Objection to Contrary Terms
Springer Science + Business Media hereby objects to any terms contained in any purchase order, acknowledgment, check endorsement or other writing prepared by you, which terms are inconsistent with these terms and conditions or CCC's Billing and Payment terms and conditions. These terms and conditions, together with CCC's Billing and Payment terms and conditions (which are incorporated herein), comprise the entire agreement between you and Springer Science + Business Media (and CCC) concerning this licensing transaction. In the event of any conflict between your obligations established by these terms and conditions and those established by CCC's Billing and Payment terms and conditions, these terms and conditions shall control.

Jurisdiction
All disputes that may arise in connection with this present License, or the breach thereof, shall be settled exclusively by the country's law in which the work was originally published.

Other terms and conditions:

v1.2

Gratis licenses (referencing $0 in the Total field) are free. Please retain this printable license for your reference. No payment is required.

If you would like to pay for this license now, please remit this license along with your payment made payable to "COPYRIGHT CLEARANCE CENTER" otherwise you will be invoiced within 48 hours of the license date. Payment should be in the form of a check or money order referencing your account number and this invoice number RLNK10883114.
Once you receive your invoice for this order, you may pay your invoice by credit card. Please follow instructions provided at that time.

Make Payment To:
Copyright Clearance Center
Dept 001
P.O. Box 843006
Boston, MA 02284-3006

For suggestions or comments regarding this order, contact Rightslink Customer Support: customercare@copyright.com or +1-877-622-5543 (toll free in the US) or +1-978-646-2777.